Aerosol Chemistry Over Remote Oceanic Regions

Thesis by

Anne Marie Jorunn Johansen

In Partial Fulfillment of the Requirements

for the Degree of

Doctor of Philosophy

California Institute of Technology

Pasadena, California

1999

(Submitted April 28, 1999)

Acknowledgment

I thank my parents for the guidance that they have given me early in my life, without which the culmination of my schooling years would probably not have occurred in a PhD from Caltech.

Thanks are extended to my advisor, Prof. Michael R. Hoffmann, for his continued support and for giving me the freedom to participate in as many field sampling trips as I could imagine possible for the completion of this thesis. Thanks also to the members of my examinations committee, Profs. James J. Morgan, Glen R. Cass, and Janet G. Hering for their inputs.

I was fortunate to have overlapped some time in the lab with fellow students Simo Pehkonen, Ron Siefert and Sam Webb. Not only did we enjoy good times, but more importantly, they passed on valuable laboratory and field sampling experience to me. I would also like to express my appreciation for the rest of the helpful Hoffmann group, especially my thirsty friends Linda Weavers and Ralf Hoechemer. The instrumentation and computer assistance from of Peter Green and Janiv Dubowski are greatly appreciated.

The permanent presence of two wonderful persons, Elena Escot and Linda Scott, cheered up the endless hours spent in Keck Labs. I have also greatly enjoyed the company of my office mates, Veronica Blackwell, Jennie Stephens and Mariu Hernandez, without whom the last few months of my work may have been shortened, but only at the expense of many joyful moments and of mental sanity. My activities in Caltech's Club Latino have enabled me to meet some of my best friends, Douglas Varela, Roberto Zenit and Chantal Morgan, and last, but not least, my dearest friend Karina Montilla (now, Karina Edmonds).

Caltech and my research have taken me to many parts of the globe, from remote oceanic regions to Mexico, upstate New York, and local areas, but more importantly to the Caltech climbing wall, where I met my future husband, Timothy Ian Melbourne. His adventurous spirit did not allow for a dull moment during our years in Southern California. His support and that of his wonderful family was of tremendous significance.

Abstract

Atmospheric sampling of aerosol was carried out from ships during four separate month-long research cruises over remote oceanic regions. Three cruises took place in the Arabian Sea, during the inter-, SW- and NE-monsoons. An additional cruise was focused on the tropical North Atlantic Ocean. Identical sampling techniques were employed for all cruises. One high volume dichotomous virtual impactor and two low volume collectors were used to collect aerosol particles for the quantification of trace metals, anions and major cations. Ferrous iron concentrations were determined immediately after sample collection on board the ship using a ferrozine extraction technique. Data were analyzed by principal component, enrichment factor and weighted multiple linear regression analyses.

The mineralogical composition of aerosol collected over the Arabian Sea reflected that of an average of the earth's crust, while over the Atlantic Ocean, shale appeared to best represent the sampled mineral dust. With exception of the SW-monsoon samples, which were characterized by weak continental influences, the aerosol samples contained excess water-soluble non-sea-salt calcium that appeared to be of crustal origin, in the form of $CaCO_3$ or $CaSO_4$.

Ferrous iron concentrations accounted for 0.3, 1.3, and 0.5% of the total observed Fe during the inter- and NE-monsoons over the Arabian Sea, and over the Atlantic Ocean, respectively. Absolute Fe(II) concentrations were determined at 5.2, 9.8, and 3.1 $\mu g\ m^{-3}$ for the corresponding seasons, with most of the Fe(II) (> 80%) present in the fine fraction. Fe(II) did not exhibit a simple relationship with any of the sources indicating the complexity of iron redox reactions is this system.

Non-sea-salt sulfate (NSS-SO_4^{2-}) sources were identified and quantified with the use of multiple linear regression analyses. Biogenically-derived SO_4^{2-} contributed significant amounts of NSS-SO_4^{2-}, especially during the SW-monsoon, when anthropogenic sources were small. Biogenic SO_4^{2-}/methansulfonic acid (MSA) weight ratios were determined and found to be in agreement with reported literature values from pristine oceanic regions, varying from 6.8 at 24 °C to 17.7 at 28.9 °C.

Table of Contents

Acknowledgment iii

Abstract v

Table of Contents vii

List of Tables xiii

List of Figures xvi

1. Introduction 1-1

1.1 References 1-6

Figure 1-14

2. Chemical characterization of ambient aerosol collected during the southwest-monsoon and inter-monsoon seasons over the Arabian Sea: Labile-Fe(II) and other trace metals 2-1

2.1 Abstract 2-2

2.2 Introduction 2-4

2.3 Methods 2-8

2.3.1 Aerosol Collection 2-8

2.3.2 Labile-Fe(II) Measurements Performed Immediately After Sample Collection 2-9

2.3.3 Analysis Performed After the Cruise 2-9

2.3.4 Error Analysis 2-11

2.3.5 Statistical Analysis and Enrichment Factor Analysis 2-11

2.4 Results and Discussion 2-13

2.4.1 Cruise Tracks and Air Mass Trajectories 2-13

2.4.2 Total Elemental Concentrations 2-14

2.4.3 Fe(II) Concentrations 2-16

2.4.4 Enrichment Factors 2-19

2.4.5 Factor Analysis 2-21

2.5 Conclusions 2-26

2.6 References 2-28

2.7 Figure Captions 2-36

Tables 2-37

Figures 2-45

3. Chemical characterization of ambient aerosol collected during the southwest-monsoon and inter-monsoon seasons over the Arabian Sea: Anions and cations 3-1

3.1 Abstract 3-2

3.2 Introduction 3-4

3.3 Experimental 3-10

3.3.1 Sampling Location and Period 3-10

3.3.2 Aerosol Collection 3-11

3.3.3 Chemical Analysis 3-12

3.3.4 Statistical Analysis 3-13

3.4 Results and Discussion 3-15

3.4.1 SO_4^{2-} and MSA 3-15

3.4.1.1 Atmospheric Concentrations 3-15

3.4.1.2 Bio-SO_4^{2-}/MSA Ratio 3-16

3.4.1.3 Linear Regression 3-17

3.4.1.4 Temperature Dependence of the Bio-SO_4^{2-}/MSA Ratio 3-23

3.4.1.5 Sulfate Sources 3-25

3.4.2 Halogens 3-27

3.4.3 Organic Anions 3-33

3.4.4 Cations 3-36

3.4.5 Total Suspended Particulates (TSP) 3-40

3.5 Conclusions 3-42

3.6 References 3-45

3.7 Figure Captions 3-56

Tables 3-58

Figures 3-65

4. Chemical composition of aerosols collected over the tropical North Atlantic Ocean 4-1

4.1 Abstract 4-2

4.2 Introduction 4-3

4.3 Experimental 4-9

4.3.1 Sampling Location and Period 4-9

4.3.2 Aerosol Collection 4-11

4.3.3 Chemical Analyses 4-13

4.3.3.1 Fe(II) Analysis Performed On-board the Ship 4-13

4.3.3.2 Elemental Analysis 4-14

4.3.3.3 Ion Analysis and Gravimetric Determination 4-14

4.3.4 Statistical Analyses 4-15

4.4 Results 4-17

4.4.1 Total Suspended Particulates (TSP) 4-17

4.4.2 Trace Metals 4-17

4.4.3 Fe and Fe(II) 4-20

4.4.4 Anions 4-24

4.4.4.1 NSS-SO_4^{2-} and MSA 4-24

4.4.4.2 NO_3^- and Organic Acids 4-27

4.4.4.3 Halogens 4-29

4.4.5 Cations 4-31

4.4.5.1 Na^+, K^+, Mg^{2+} and Ca^{2+} 4-31

4.4.5.2 NH_4^+ and Acid Neutralization 4-33

4.5 Discussion 4-36

4.5.1 Mineral Aerosol 4-36

4.5.2 Sea-salt Aerosol 4-47

4.5.3 SO_4^{2-} Contributions 4-52

4.5.4 Fe(II) 4-60

4.6 Conclusions 4-63

4.7 References 4-67

4.8 Figure Captions 4-85

Tables 4-88

Figures 4-98

5. Chemical composition of aerosols collected over the Arabian Sea during the northeast-monsoon period 5-1

5.1 Abstract 5-2

5.2 Introduction 5-4

5.3 Experimental 5-11

5.3.1 Sample Location and Period 5-11

5.3.2 Aerosol Collection 5-12

5.3.3 Chemical Analyses 5-13

5.3.3.1 Fe(II) Analysis Performed On-board the Ship 5-13

5.3.3.2 Elemental Analysis 5-14

5.3.3.3 Ion Analyses 5-14

5.3.4 Statistical Analyses 5-15

5.4 Results and Discussion 5-17

5.4.1 Air Mass Origins and Characteristics 5-17

5.4.2 Trace Metals 5-19

5.4.3 Fe and Fe(II) 5-27

5.4.4 Anions 5-30

5.4.4.1 NSS-SO_4^{2-} and MSA 5-30

5.4.4.2 NO_3^- 5-36

5.4.4.3 Cl^- 5-37

5.4.5 Cations 5-40

5.4.5.1 NH_4^+ 5-40

5.4.5.2 Na^+, K^+, Mg^{2+}, and Ca^{2+} 5-42

5.5 Conclusions 5-45

5.6 References 5-49

5.7 Figure Captions 5-59

Tables 5-63

Figures 5-73

6. Summary **6-1**

List of Tables

Chapter 2

Table 1. Sequential extraction procedure for measuring labile fractions of ferrous iron (Fe(II)) collected on the coarse and fine HVDVI filters. 2-37

Table 2. Strong acid digestion method for HVDVI. 2-38

Table 3. Aerosol sample collection times and positions. 2-39

Table 4. Enrichment factor for a series of elements based on their total concentration. 2-40

Table 5. Element Abundances in Ultramafic Rock and Crustal Average. 2-41

Table 6. Principal components extracted from inter-monsoon and southwest-monsoon data. 2-42

Table 7. Factor analysis statistics for data presented in Table 6. 2-43

Table 8. Sector sampling system operation. 2-44

Chapter 3

Table 1. Aerosol sample collection times and positions. 3-58

Table 2. Atmospheric anion and cation concentrations during inter- and SW-monsoons. 3-59

Table 3. M32/3-Inter-monsoon. Model outputs from weighted linear least squares regression. 3-60

Table 4. M32/5-SW-monsoon. Model outputs from weighted linear least squares regression. 3-61

Table 5. M32/5-SW-monsoon, three outliers. Model outputs from weighted linear least squares regression. 3-62

Table 6. Varimax rotated component matrix for inter-monsoon samples. 3-63

Table 7. Varimax rotated component matrix for SW-monsoon samples. 3-64

Chapter 4

Table 1. Aerosol sample collection times and positions. 4-88

Table 2. Average, minimum and maximum atmospheric trace metal concentrations in coarse, fine and total aerosol fractions. 4-89

Table 3. Varimax rotated principal component matrix. Trace metals. 4-90

Table 4. Varimax rotated principal component matrix. Trace metals and ions. 4-91

Table 5. Average, minimum and maximum atmospheric anion and cation concentrations in coarse, fine and total aerosol fractions. 4-93

Table 6. Enrichment factors assuming continental bulk composition according to Taylor and McLennan [1985]. 4-94

Table 7. Enrichment factors assuming shale composition according to Turekian and Wedepohl [1961]. 4-95

Table 8. Model outputs from weighted linear regressions with coarse, fine and total SO_4^{2-} as dependent variable. 4-96

Table 9. Model outputs from weighted linear regressions with coarse and fine non-bio-SO_4^{2-} as independent variable. 4-97

Chapter 5

Table 1. Aerosol sampling collection times and positions. 5-62

Table 2. Average, minimum and maximum atmospheric trace metal concentrations in coarse, fine and total aerosol fractions. 5-63

Table 3. Varimax rotated component matrix. Trace metals. 5-64

Table 4. Enrichment factors for the coarse aerosol fraction relative to Al, assuming continental bulk composition according to McLennan and Taylor [1985]. 5-65

Table 5. Enrichment factors for fine aerosol fraction relative to Al, assuming continental bulk composition according to McLennan and Taylor [1985]. 5-66

Table 6. Enrichment factors for total aerosol relative to Al, assuming continental bulk composition according to McLennan and Taylor [1985]. 5-67

Table 7. Varimax rotated principal component matrix. Trace metals and ions. 5-68

Table 8. Average, minimum and maximum atmospheric anion and cation concentrations in coarse, fine and total aerosol fractions. 5-70

Table 9. Weighted multiple linear regression outputs for coarse SO_4^{2-} fractions as dependent variable. 5-71

Table 10. Weighted multiple linear regression outputs for fine SO_4^{2-} fractions as dependent variable. 5-72

List of Figures

Chapter 1

Figure 1. 1-14

Chapter 2

Figure 1. Five-day air mass back trajectories for four different elevations (based on pressure) above sea level. 2-45

Figure 2. Total suspended particulates (TSP) over the Arabian Sea during the inter- and southwest-monsoons. 2-46

Figure 3. Concentration plots for (a) Al, (b) Fe, (c) Na, (d) Mn, (e) V, (f) Pb, (g) Cr, (h) Mo, and (i) Cu. 2-47

Figure 4. Labile-Fe(II) concentrations for the (a) fine, (b) coarse, and (c) total aerosol fractions during the inter-monsoon. 2-49

Figure 5. Percentage of $Fe(II)_{total,labile}$ to Fe_{total} for the fine, coarse, and total aerosol fractions during the inter-monsoon. 2-50

Figure 6. Factor score plots for the first seven principal components shown in Table 6. 2-51

Chapter 3

Figure 1. Five day air mass back trajectories at four different final elevations (based on pressure) above sea level. 3-65

Figure 2. Sulfur species during inter- and SW-monsoons. 3-66

Figure 3. NSS-SO_4^{2-} versus Pb (a) and NO_3^- (b) during inter- and SW-monsoons. 3-67

Figure 4. Observed and predicted SO_4^{2-} versus sample. 3-68

Figure 5. Bio-SO_4^{2-}/MSA weight ratio as a function of the average daily air temperature. 3-69

Figure 6. Total anion and total cation charges versus sample, inter- and SW-monsoon data. 3-70

Figure 7. Br^-, SS-Br^- (a), and Cl^-, SS-Cl^- (b) during inter- and SW-monsoons, versus sample. 3-71

Figure 8. Cl^- deficit, anthropogenic-SO_4^{2-}+NO_3^-, and NO_3^- versus sample, inter- and SW-monsoon data. 3-72

Figure 9. Anion minus cation charges versus Cl^- deficit during inter- and SW-monsoons. 3-73

Figure 10. Organic anions versus sample: (a) acetate, (b) glycolate, (c) formate, (d) malonate, and (e) oxalate. 3-74

Figure 11. NH_4^+ versus sample during inter- and SW-monsoons. 3-75

Figure 12. Na (a), K (b), Mg (c), and Ca (d) as detected with IC and ICP-MS versus inter- and SW-monsoon samples. 3-76

Figure 13. Average relative contribution of major components to total suspended material collected during inter- and SW-monsoons. 3-77

Chapter 4

Figure 1. Six day air mass back trajectory calculations at five different final elevations above sea level. 4-98

Figure 2. Total suspended particulates (TSP) vs. sample ID. 4-99

Figure 3. Coarse and fine fraction trace metal concentrations vs. sample ID. for Al (a), Zn (b), and Na (c). 4-100

Figure 4. Fe(II) concentrations vs. sample ID. 4-101

Figure 5. Relative Fe(II) concentrations (in % of total Fe) vs. sample ID. for coarse, fine and total Fe(II). 4-102

Figure 6. Relative amount Fe(II) released in the sequential extraction steps for coarse (a) and fine (b) fractions. 4-103

Figure 7. Sea-salt and NSS-SO_4^{2-} contributions in coarse and fine fractions vs. sample ID. 4-104

Figure 8. MSA concentrations in coarse and fine fractions vs. sample ID. 4-105

Figure 9. NO_3^- concentrations in coarse and fine fractions vs. sample ID. 4-106

Figure 10. Oxalate concentrations in coarse and fine fractions vs. sample ID. 4-107

Figure 11. Halogen concentrations in coarse and fine fractions vs. sample ID. 4-108

Figure 12. (a) Cl^- deficit vs. sample ID. (b) neq mineral acid concentrations vs. Cl^- deficit in coarse fraction, and (c) neq mineral acid concentrations vs. Cl^- deficit in fine fraction. 4-109

Figure 13. Water-soluble SS- and NSS- fractions of Na^+ (a), K^+ (b), Mg^{2+} (c), and Ca^{2+} (d), in coarse and fine fractions vs. sample ID. 4-110

Figure 14. (a) NH_4^+ and (b) $NH_4^+/NSS\text{-}SO_4^{2-}$ vs. sample ID., and (c) $NH_4^+/NSS\text{-}SO_4^{2-}$ vs. $NSS\text{-}SO_4^{2-}$ in fine fraction and fine and coarse combined (total). 4-111

Figure 15. (a) $(NH_4^+ + NSS\text{-}Ca^{2+})/NSS\text{-}SO_4^{2-}$ vs. sample ID. (b) $(NH_4^+ + NSS\text{-}Ca^{2+})/NSS\text{-}SO_4^{2-}$ vs. $NSS\text{-}SO_4^{2-}$ in fine fraction and fine and coarse combined (total). 4-112

Figure 16. ICP-MS and IC determined concentrations of (a) Na, (b) K, (c) Mg, and (d) Ca vs. sample ID. in coarse and fine fractions. 4-113

Figure 17. Air temperature vs. sample ID. 4-114

Figure 18. Model predictions for SO_4^{2-}. 4-115

Figure 19. $NH_4^+/NSS\text{-}SO_4^{2-}$ (a) and $(NH_4^+ + NSS\text{-}Ca^{2+})/NSS\text{-}SO_4^{2-}$ (b) vs. $Fe(II)_{total,5minFZ}$ concentrations in fine fraction and fine and coarse combined (total). 4-116

Figure 20. $Fe(II)_{total,5minFZ}$ in fine fraction vs. MSA. 4-117

Chapter 5

Figure 1. Five day air mass back trajectory calculations at five different final elevations (based on pressure) above sea level. 5-73

Figure 2. a) Average wind speed vs. sample ID.; b) Average true wind direction vs. sample ID. 5-75

Figure 3. Air temperature and relative humidity vs. sample ID. 5-76

Figure 4. Coarse and fine fraction trace metal concentrations vs. sample ID. for Al (a), Pb (b), Na (c), Fe (d), and Ca (e). 5-77

Figure 5. Factor scores for the crustal (a) and other (b) principal components extracted in the principal component analysis from Table 7. 5-78

Figure 6. ICP-MS and IC determined concentrations of (a) Na, (b) K, (c) Mg, and (d) Ca vs. sample ID. in coarse and fine fractions. 5-79

Figure 7. Fe(II) concentrations vs. sample ID. (a) Fe(II) in the coarse fraction, (b) Fe(II) in the fine fraction, and (c) total Fe(II) released after 5 min in ferrozine. 5-80

Figure 8. Relative Fe(II) concentrations (in % of total Fe) vs. sample ID. for coarse, fine and total Fe(II). 5-81

Figure 9. Relative amount Fe(II) released in the sequential extraction steps for coarse (a) and fine (b) fractions. 5-82

Figure 10. SS- and NSS-SO_4^{2-} contributions in coarse and fine fractions vs. sample ID. 5-83

Figure 11. MSA concentrations in coarse and fine fractions vs. sample ID. 5-84

Figure 12. NO_3^- concentrations on coarse and fine fractions vs. sample ID. 5-85

Figure 13. (a) Cl^- concentrations and (b) Cl^- deficits in coarse and fine fractions vs. sample ID. 5-86

Figure 14. (a) neq mineral acid concentrations vs. Cl^- deficit in coarse fraction, and (b) fine fraction. 5-87

Figure 15. (a) NH_4^+ and (b) NH_4^+/NSS-SO_4^{2-} vs. sample ID. 5-88

Figure 16. Water-soluble SS- and NSS- fractions of (a) Na^+, (b) K^+, (c) Mg^{2+}, and (d) Ca^{2+} in coarse and fine fractions vs. sample ID. 5-89

1. Introduction

This thesis is a compilation of four individual but analogously performed ship-board studies on the chemistry of atmospheric aerosols collected over remote oceanic regions. Three month-long research cruises were carried out over the Arabian Sea during different seasons of the Indian monsoon, while a one-month cruise took place over the tropical North Atlantic Ocean. The first two data sets, from the inter- and the SW-monsoons of 1995, over the Arabian Sea, are presented in the second and third chapters. In the second chapter I present and discuss the trace-metal chemistry and in the third chapter the chemistry of the anions and cations. The subsequent cruises, over the Atlantic Ocean in 1996 and over the Arabian Sea during the NE-monsoon of 1997, are presented in separate chapters. All chapters are written and formatted for publication in the *Journal of Geophysical Research* and as such are accompanied by their own introductory and conclusions sections. Since the background information given in chapters 2 through 5 is specific and quite extensive, following is a more broad overview of the motivations for this study.

The chemistry of ambient aerosols, which are complex mixtures of minerals, sea-salt and organic compounds and their interaction with gas molecules is still poorly understood [*Andreae and Crutzen*, 1997; *Keene et al.*, 1998]. Basic knowledge on their detailed composition and ambient reactivity is needed. Furthermore, information on the abundance of atmospheric particulate species over the remote open oceans is scarce due to the seasonal and spatial variability in atmospheric aerosol loading [*Jickells*, 1995]. Daily sampling over extensive periods of time, on the order of years, would be necessary to adequately characterize the chemical composition of the marine aerosol; however, such long sampling programs are normally impossible at sea on research cruises. Thus, any atmospheric

sampling carried out over any part of the remote oceans counts as a valuable addition to the existing sparse data. This data is sought to shed light on a major problem pursued in both oceanic and atmospheric science which is to understand long term changes in the environment.

One important issue is to determine the effect of increased atmospheric concentrations and fluxes of nutrients and trace metals exceeding the natural background levels as a result of human interference, such as the input of pollutants from fossil fuel burning and the increased entrainment of mineral dust as a consequence of the disruption of soils by changing land use in arid and subarid regions, such as deforestation and denaturalization. The effect of changing atmospheric concentrations is not only of biogeochemical importance but also of importance in the debate about global climate change.

Traditional budgets and residence time estimates for trace metals and nutrients in the oceans have been based on riverine fluxes and have ignored atmospheric and other inputs [*Jickells*, 1995]. It seems that the atmospheric inputs are a significant source of at least some trace elements to many parts of the ocean [*Chester et al.*, 1993; *Duce and Tindale*, 1991; *Marin and Duce*, 1989a; *Marin and Duce*, 1989b; *Zhuang et al.*, 1990]. Studies have found Fe to be a rate-limiting nutrient to phytoplankton growth in certain regions of the open ocean [*Cooper et al.*, 1996; *DiTullio et al.*, 1993; *Kolber et al.*, 1994; *Martin et al.*, 1994; *Martin and Fitzwater*, 1988; *Martin et al.*, 1991; *Paerl et al.*, 1994; *Price et al.*, 1994]. It is clear that the gross flux of aeolian iron could control the oceanic iron cycle, and thereby affect the biogeochemical cycles of C and S. However, not much is known about the chemical state of the iron in the aerosols or the ocean, and, specifically, whether the iron is in a from that can be utilized readily by marine phytoplankton [*Hudson et al.*, 1992; *Hudson and Morel*, 1990;

Hudson and Morel, 1993]. Speciation and photochemical reactions of iron in surface and atmospheric waters have been the subject of many investigations [*Duce and Tindale*, 1991; *Faust and Zepp*, 1993; *Graedel et al.*, 1985; *King et al.*, 1995; *Kuma et al.*, 1996; *Litter et al.*, 1991; *Miller and Bruland*, 1994; *Millero et al.*, 1991; *Millero et al.*, 1995; *Moffett and Zika*, 1987a; *O'Sullivan et al.*, 1995; *Pehkonen et al.*, 1993; *Siefert et al.*, 1994; *Spokes and Liss*, 1995; *Sulzberger et al.*, 1990; *Suter et al.*, 1991; *Voelker and Sedlak*, 1995; *Waite and Morel*, 1984; *Wehrli et al.*, 1989; *Weschler et al.*, 1986; *Zhang and Terada*, 1994; *Zhuang et al.*, 1990], but gaps still exist in the understanding of the different physico-chemical forms of oceanic iron [*Wells et al.*, 1995].

One focus of this thesis is the quantification and characterization of the oxidation states of iron in the aerosol particles that are transported from the continents to the open oceans before they are settled out. During atmospheric transport an aerosol may be subject to repeated wetting and drying cycles during cloud formation and dissipation, which can result in increased solubility due to acids attacking the aluminosilicate lattice structure of clays in the aerosol. Only a few relevant studies exist on the dissolution chemistry of metals from marine aerosols [*Guieu et al.*, 1994; *Spokes et al.*, 1994; *Sunda and Huntsman*, 1994; *Zhu et al.*, 1992; *Zhu et al.*, 1993; *Zhu et al.*, 1997; *Zhuang and Duce*, 1993; *Zhuang et al.*, 1990; *Zhuang et al.*, 1992a; *Zhuang et al.*, 1992b; *Zhuang et al.*, 1995]. In general, a small percentage of the total iron in the aerosol phase appears to be present in the form of more soluble Fe(II) species. The amount of Fe(II) present in aerosol seems to vary with the transport history of the air parcel.

During the inter-monsoon of 1995, atmospheric Fe(II) concentrations over the Indian Ocean [*Siefert et al.*, 1999] appeared to correlate significantly with the surface abundance of *Trichodesmium* spp. determined by Capone et al. [*Capone et al.*, 1997]. In Figure 1a, the

observed *Tichodesmium* abundance is plotted in conjunction with the wind speed, since it is only during low wind conditions that this phytoplankton rises to the surface in order to fixate N_2 from the atmosphere. For comparison, Fe(II) in both coarse and fine fractions is plotted in stacked bars in Figure 1b. *Trichodemsium* is a N_2-fixating planktonic cyanobacterium that is reliant on adequate Fe availability for the mediation of nitrogen uptake [*Paerl et al.*, 1994].

Iron is not the only trace metal of importance that reaches the open ocean via atmospheric transport. Copper [*Moffett*, 1995; *Moffett and Zika*, 1983; *Sedlak and Hoigné*, 1993; *Xue et al.*, 1991; *Xue and Sigg*, 1993], zinc, manganese [*Guieu et al.*, 1994; *Moffett*, 1994; *Sunda and Huntsman*, 1994; *Waite and Szymczak*, 1993; *Xyla et al.*, 1992], nickel and cobalt have also been studied individually or in combination [*Graedel et al.*, 1986; *Graedel et al.*, 1985; *Kersten et al.*, 1991; *Moffett and Ho*, 1996; *Sedlak and Hoigné*, 1993; *Sedlak and Hoigné*, 1994; *Spokes et al.*, 1994; *Spokes and Liss*, 1995; *Weschler et al.*, 1986] in both aerosols and surface waters.

In a larger context, the mineral aerosol containing this array of metals not only affects the ocean biology but also weather and global climate, directly and indirectly. The direct effect is a result of the scattering of sunlight by dust particles, which, although less effective in scattering light compared to sulfate aerosol, are present at much greater abundance in certain regions [*Andreae*, 1996; *Li et al.*, 1996]. Charlson and colleagues have suggested that aerosols have an indirect effect through a climate feedback loop produced by the oxidation of dimethylsulfide (DMS) [*Charlson et al.*, 1987]. DMS is excreted by most phytoplankton species and escapes to the air where it is oxidized to sulfate and methane sulfonate (MSA) aerosol. Sulfate aerosol produced from DMS serves as cloud-condensation nuclei (CCN) and can participate in the earth's radiation balance through the formation of clouds [*Andreae et al.*, 1995; *Ayers and Gras*, 1991; *Turner et al.*, 1996]. Zhuang et al. [*Zhuang et al.*, 1992b]

carried this concept further by suggesting a positive feedback loop between the production of DMS and dissolution of Fe(II) derived from aerosol deposited in the marine environment.

In summary, in the 4 main chapters of this thesis I present and discuss unique field observations from several parts of the open ocean in the context of bioegeochemistry and global climate. Measurements are interpreted with the aid of a series of different statistical analysis methods and discussed in relation to previously reported investigations performed in the same regions.

1.1 References

Andreae, M.O., Raising dust in the greenhouse, *Nature*, *380*, 389-390, 1996.

Andreae, M.O., and P.J. Crutzen, Atmospheric aerosols: Biogeochemical sources and role in atmorpheric chemistry, *Science*, *276*, 1052-1058, 1997.

Andreae, M.O., W. Elbert, and S.J. de Mora, Biogenic sulfur emissions and aerosols over the tropical South Atlantic. 3. Atmospheric dimethylsulfide, aerosols and cloud condensation nuclei, *J. Geophys. Res.*, *100*, 11,335-11,356, 1995.

Ayers, G.P., and J.L. Gras, Seasonal relationship between cloud condensation nuclei and aerosol methanesulphonate in marine air, *Nature*, *353*, 834-835, 1991.

Capone, D.G., A. Subramaniam, J.P. Montoya, M. Voss, C. Humborg, A.M. Johansen, R.L. Siefert, and E.J. Carpenter, An extensive bloom of the N_2-fixing cyanobacterium *Trichodesmium* erythraeum in the Central Arabian Sea, *Mar. Ecol. Prog. Ser.*, *172*, 281-292, 1997.

Charlson, R.J., J.E. Lovelock, M.O. Andreae, and S.G. Warren, Oceanic phytoplankton, atmospheric sulphur, cloud albedo and climate, *Nature*, *326*, 655-661, 1987.

Chester, R., K.J.T. Murphy, F.J. Lin, A.S. Berry, G.A. Bradshaw, and P.A. Corcoran, Factors controlling the solubilities of trace metals from non-remote aerosols deposited to the sea surface by the 'dry' deposition mode, *Mar. Chem.*, *42*, 107-126, 1993.

Cooper, D.J., A.J. Watson, and P.D. Nightingale, Large decrease in ocean-surface CO2 fugacity in response to in situ iron fertilization, *Nature*, *383*, 511-514, 1996.

DiTullio, G.R., D.A. Hutchins, and K.W. Bruland, Interaction of iron and major nutrients controls phytoplankton growth and species composition in the tropical North Pacific Ocean, *Limnol. Oceanogr.*, *38* (3), 495-508, 1993.

Duce, R.A., and N.W. Tindale, Atmospheric transport of iron and its deposition in the ocean, *Limnol. Ocean.*, *36* (8), 1715-1726, 1991.

Faust, B.C., and R.G. Zepp, Photochemistry of aqueous iron(III)-polycarboxylate complexes: roles in the chemistry of atmospheric and surface waters, *Environ. Sci. Technol.*, *27*, 2517-2522, 1993.

Graedel, T.E., M.L. Mandich, and C.J. Weschler, Kinetic model studies of atmospheric droplet chemistry 2. Homogeneous transition metal chemistry in raindrops, *J. Geophys. Res.*, *91*, 5205-5221, 1986.

Graedel, T.E., C.J. Weschler, and M.L. Mandich, Influence of transition metal complexes in atmospheric droplet acidity, *Nature*, *317*, 240-242, 1985.

Guieu, C., R. Duce, and R. Arimoto, Dissolved input of manganese to the ocean: Aerosol source, *J. Geophys. Res.*, *99*, 18,789-18,800, 1994.

Hudson, R.J.M., D.T. Covault, and F.M.M. Morel, Investigations of iron coordination and redox reactions in seawater using ^{59}Fe radiometry and ion-pair solvent extraction of amphiphilic iron complexes, *Mar. Chem.*, *38*, 209-235, 1992.

Hudson, R.J.M., and F.M.M. Morel, Iron transport in marine phytoplankton: Kinetics of cellular and medium coordination reactions, *Limnol. Ocean.*, *35* (5), 1002-1020, 1990.

Hudson, R.J.M., and F.M.M. Morel, Trace metal transport by marine microorganisms: implications of metal coordination kinetics, *Deep-Sea Res.*, *40* (1), 129-150, 1993.

Jickells, T., Atmospheric inputs of metals and nutrients to the oceans: their magnitude and effects, *Mar. Chem.*, *48*, 199-214, 1995.

Keene, W.C., R. Sander, A.A.P. Pszenny, R. Vogt, P.J. Crutzen, and J.N. Galloway, Aerosol pH in the marine boundary layer: A review and model evaluation, *J. Aerosol Sci.*, *29* (3), 339-356, 1998.

Kersten, M., M. Kriews, and U. Förster, Partitioning of trace metals released from polluted marine aerosols in coastal seawater, *Mar. Chem.*, *36*, 165-182, 1991.

King, W.D., H.A. Lounsbury, and F.J. Millero, Rates and mechanism of Fe(II) oxidation at nanomolar total iron concentrations, *Environ. Sci. Technol.*, *29* (3), 818-824, 1995.

Kolber, Z.S., R.T. Barber, K.H. Coale, S.E. Fitzwater, R.M. Greene, K.S. Johnson, S. Lindley, and P.G. Falkowski, Iron limitation of phytoplankton photosynthesis in the equatorial Pacific Ocean, *Nature*, *371*, 145-149, 1994.

Kuma, K., J. Nichioka, and K. Matsunaga, Controls on iron(III) hydroxide solubility in seawater: The influence of pH and natural organic chelators, *Limnol. Oceanogr.*, *41* (3), 396-407, 1996.

Li, X., H. Maring, D. Savoie, K. Voss, and J.M. Prospero, Dominance of mineral dust in aerosol light-scattering in the North Atlantic trace winds, *Nature*, *380*, 416-418, 1996.

Litter, M.I., E.C. Baumgartner, G.A. Urrutia, and M.A. Blesa, Photodissolution of iron oxides. 3. Interplay of photochemical and thermal processes in maghemite/caboxylic acid systems, *Environ. Sci. Technol.*, *25* (11), 1907-1913, 1991.

Marin, H.B., and R.A. Duce, The impact of atmospheric aerosols on trace-metal chemistry in open ocean surface seawater. 2. aluminum, *Earth Planet Sci. Lett.*, *84* (4), 381-392, 1989a.

Marin, H.B., and R.A. Duce, The impact of atmospheric aerosols on trace-metal chemistry in open ocean surface seawater. 2. copper, *J. Geophys. Res.*, *94*, 1039-1045, 1989b.

Martin, J.H., K.H. Coale, K.S. Johnson, S.E. Fitzwater, R.M. Gordon, and ....., Testing the iron hypothesis in ecosystems of the equatorial Pacific Ocean, *Nature*, *371*, 123-129, 1994.

Martin, J.H., and S.F. Fitzwater, Iron deficiency limits phytoplankton growth in the north-east Pacific subarctic, *Nature*, *331*, 341-342, 1988.

Martin, J.H., R.M. Gordon, and S.E. Fitzwater, The case of iron, *Limnol. Oceanogr.*, *36* (8), 1793-1802, 1991.

Miller, L.A., and K.W. Bruland, Determination of copper speciation in marine waters by competitive ligand equilibration/liquid-liquid extraction: an evaluation of the technique, *Anal. Chim. Acta*, *284*, 573-586, 1994.

Millero, F.J., S. Sotolongo, D.J. Stade, and C.A. Vega, Effect of ionic interactions on the oxidation of Fe(II) with H_2O_2 in aqueous solutions, *J. Solution Chem.*, *20* (11), 1079-1092, 1991.

Millero, F.J., W. Yao, and J. Aicher, The speciation of Fe(II) and Fe(III) in natural waters, *Mar. Chem.*, *50*, 21-39, 1995.

Moffett, J.W., The relationship between cerium and manganese oxidation in the marine environment, *Limnol. Ocean.*, *39* (6), 1309-1318, 1994.

Moffett, J.W., Temporal and spatial variability of copper complexation by strong chelators in the Sargasso Sea, *Deep-Sea Res.*, *42* (8), 1273-1295, 1995.

Moffett, J.W., and J. Ho, Oxidation of cobalt and manganese in seawater via a common microbially catalyzed pathway, *Geochim. Cosmochim. Acta*, *60* (18), 3415-3424, 1996.

Moffett, J.W., and R.G. Zika, Oxidation kinetics of Cu(I) in seawater: Implications for its existence in the marine environment, *Mar. Chem.*, *13*, 239-251, 1983.

Moffett, J.W., and R.G. Zika, Reaction kinetics of hydrogen peroxide with copper and iron in seawater, *Environ. Sci. Technol.*, *1* (8), 804-810, 1987a.

O'Sullivan, D.W., A.K. Hanson Jr., and D.R. Kester, Stopped flow luminol chemiluminescence determination of Fe(II) and reducible iron in seawater at subnanomolar levels, *Mar. Chem.*, *49*, 65-77, 1995.

Paerl, H.W., L.E. Prufert-Bebout, and C. Guo, Iron-stimulated N_2 fixation and growth on natural and cultured populations of the planktonic marine cyanobacteria *Trichodesmium* spp., *Appl. Environ. Microbiol.*, *60* (3), 1044-1047, 1994.

Pehkonen, S.O., R. Siefert, Y. Erel, S. Webb, and M. Hoffmann, Photoreduction of iron oxyhydroxides in the presence of important atmospheric organic compounds, *Environ. Sci. Technol.*, *27* (10), 2056-2062, 1993.

Price, N.M., B.A. Ahner, and F.M.M. Morel, The equatorial Pacific Ocean: Grazer-controlled phytoplankton populations in an iron-limited ecosystem, *Limnol. Oceanogr.*, *39* (3), 520-534, 1994.

Sedlak, D.L., and J. Hoigné, The role of copper and oxalate in the redox cycling of iron in atmospheric waters, *Atmos. Environ.*, *27A* (14), 2173-2185, 1993.

Sedlak, D.L., and J. Hoigné, Oxidation of S(IV) in atmospheric water by photooxidants and iron in the presence of copper, *Environ. Sci. Technol.*, *28* (11), 1898-1906, 1994.

Siefert, R.L., A.M. Johansen, and M.R. Hoffmann, Chemical characterization of ambient aerosol collected during the southwest- and inter-monsoon seasons over the Arabian Sea: Labile-Fe(II) and other trace metals, *J. Geophys. Res.*, *104* (3511-3526), 1999.

Siefert, R.L., S.O. Pehkonen, Y. Erel, and M.R. Hoffmann, Iron photochemistry of aqueous suspensions of ambient aerosol with added organic acids, *Geochim. Cosmochim. Acta*, *58* (15), 3271-3279, 1994.

Spokes, L.J., T.D. Jickells, and B. Lim, Solubilisation of aerosol trace metals by cloud processing: A laboratory study, *Geochim. Cosmochim. Acta*, *58* (15), 3281-3287, 1994.

Spokes, L.J., and P.S. Liss, Photochemically induced redox reactions in seawater, I. Cations, *Mar. Chem.*, *49*, 201-213, 1995.

Sulzberger, B., J.L. Schnoor, R. Giovanoli, J.G. Hering, and J. Zobrist, Biogeochemistry of iron in an acidic lake, *Aquat. Sci.*, *52* (1), 56-74, 1990.

Sunda, W.G., and S.A. Huntsman, Photoreduction of manganese oxides in seawater, *Mar. Chem.*, *46*, 133-152, 1994.

Suter, D., S. Banwart, and W. Stumm, Dissolution of hydrous iron(III) oxides by reductive mechanisms, *Langmuir*, *7*, 809-813, 1991.

Turner, S.M., P.D. Nightingale, L.J. Spokes, M.I. Liddicoat, and P.S. Liss, Increased dimethyl sulphide concentrations in sea water from *in situ* iron enrichment, *Nature*, *383*, 513-517, 1996.

Voelker, B.M., and D.L. Sedlak, Iron reduction by photoproduced superoxide in seawater, *Mar. Chem.*, *50*, 93-102, 1995.

Waite, D.T., and F.M.M. Morel, Coulometric study of the redox dynamics of iron in seawater, *Anal. Chem.*, *56*, 787-792, 1984.

Waite, D.T., and R. Szymczak, Manganese dynamics in surface waters of the Eastern Caribbean, *J. Geophys. Res.*, *98*, 2361-2369, 1993.

Wehrli, B., B. Sulzberger, and W. Stumm, Redox processes catalyzed by hydrous oxide surfaces, *Chem. Geol.*, *78*, 167-179, 1989.

Wells, M.L., N.M. Price, and K.W. Bruland, Iron chemistry in seawater and its relationship to phytoplankton: a workshop report, *Mar. Chem.*, *48*, 157-182, 1995.

Weschler, C.J., M.L. Mandich, and T.E. Graedel, Speciation, photosensitivity, and reactions of transition metal ions in atmospheric droplets, *J. Geophys. Res.*, *91*, 5189-5204, 1986.

Xue, H., M.d.L.S. Gonçalves, M. Reutlinger, L. Sigg, and W. Stumm, Copper(I) in fogwater: Determination and interactions with sulfite, *Environ. Sci. Technol.*, *25* (10), 1716-1722, 1991.

Xue, H., and L. Sigg, Free cupric ion concentration and Cu(II) speciation in a eutrophic lake, *Limnol. Ocean.*, *38*, 1200-1213, 1993.

Xyla, A., B. Sulzberger, G.W. Luther III, J.G. Hering, P. Van Cappellen, and W. Stumm, Reductive dissolution of manganese(III,IV) (hydr)oxides by oxalate: The effect of pH and light, *Langmuir*, *8*, 95-103, 1992.

Zhang, L.-P., and K. Terada, Spectrophotometric determination of iron(II) in sea water after preconcentration by sorption of its 3-(2-pyridyl)-5,6-bis(4-phenylsulphonic acid)-1,2,4-triazine complex with poly(chlorotrifluoroethylene) resin, *Anal. Chim. Acta*, *293*, 311-318, 1994.

Zhu, X., J.M. Prospero, F.J. Millero, D.L. Savoie, and G. Brass, The solubility of ferric ion in marine mineral aerosol solutions at ambient realtive humidities, *Mar. Chem.*, *38*, 91-107, 1992.

Zhu, X., J.M. Prospero, D.L. Svoie, F.J. Millero, R.G. Zika, and E.S. Saltzman, Photoreduction of iron(III) in marine mineral aerosol solutions, *J. Geophys. Res.*, *98*, 9039-9046, 1993.

Zhu, X.R., J.M. Prospero, and F.J. Millero, Diel variability of soluble Fe(II) and soluble total Fe in North African dust in the trade winds at Barbados, *J. Geophys. Res.*, *102*, 21,297-21,305, 1997.

Zhuang, G., and R.A. Duce, The adsorption of dissolved iron on marine aerosol particles in surface waters of the open ocean, *Deep-Sea Res.*, *40* (7), 1413-1429, 1993.

Zhuang, G., R.A. Duce, and D.R. Kester, The dissolution of atmospheric iron in surface seawater of the open ocean, *J. Geophys. Res.*, *95*, 16,207-16,216, 1990.

Zhuang, G., Z. Yi, and R.A. Duce, Chemistry of iron in marine aerosols, *Global Biogeochem. Cycles*, *6* (2), 161-173, 1992a.

Zhuang, G., Z. Yi, R.A. Duce, and P.R. Brown, Link between iron and sulphur cycles suggested by detection of Fe(II) in remote marine aerosols, *Nature*, *355*, 537-539, 1992b.

Zhuang, G., Z. Yi, and G.T. Wallace, Iron(II) in rainwater, snow, and surface seawater from a coastal environment, *Mar. Chem.*, *50*, 41-50, 1995.

Figure 1

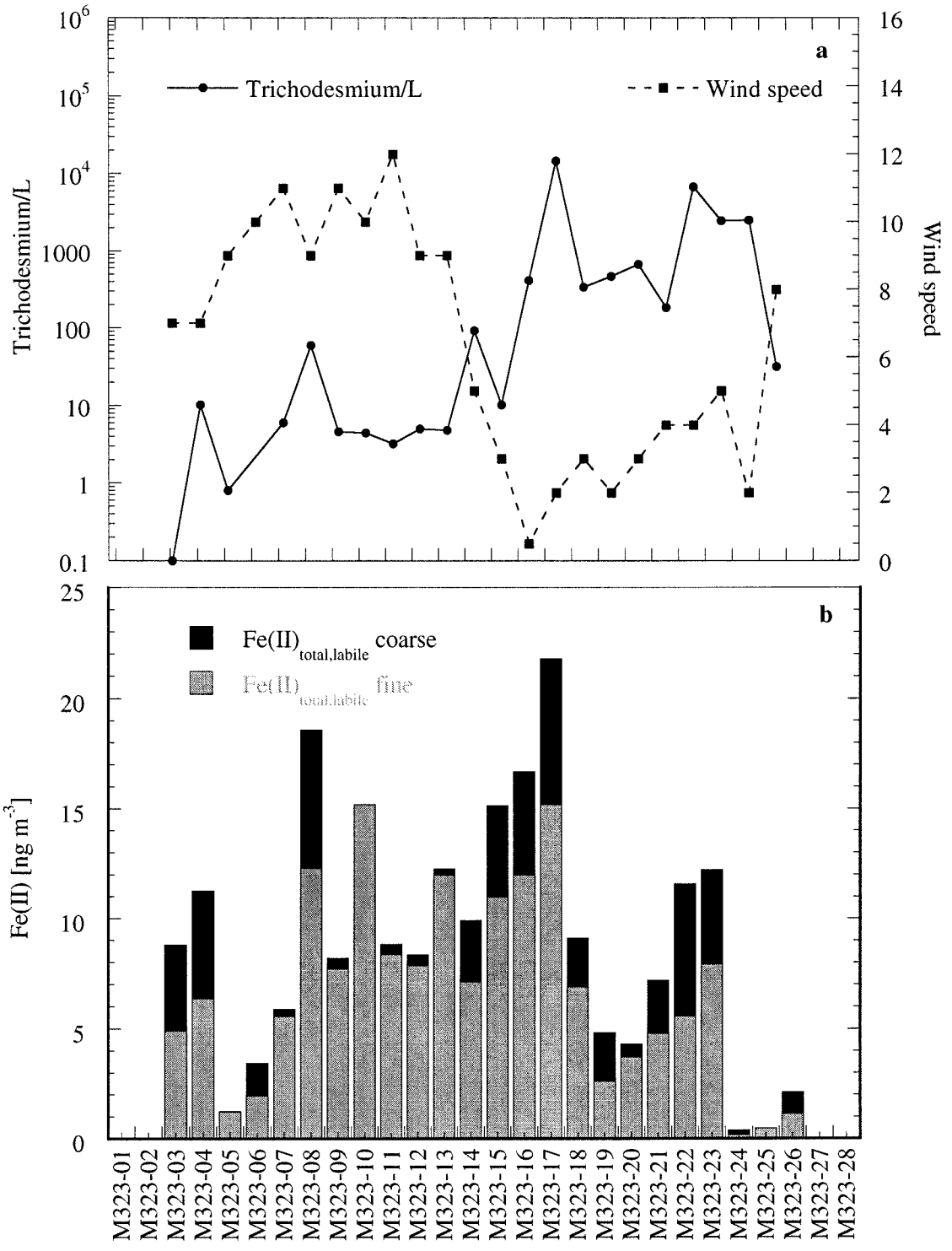

(a) Trichodesmium surface abundance and (b) labile Fe(II) concentrations observed during the inter-monsoon of 1995 over the Arabian Sea.

Chapter 2

Chemical characterization of ambient aerosol collected during the southwest-monsoon and inter-monsoon seasons over the Arabian Sea: Labile-Fe(II) and other trace metals

[Ronald L. Siefert, Anne M. Johansen, and Michael R. Hoffmann, *Journal of Geophysical Research*, 104, 3511-3526, 1999]

2.1 Abstract

Atmospheric deposition of iron (Fe) to certain regions of the oceans is an important nutrient source of Fe to the biota, and the ability of the biota to uptake Fe is dependent on the speciation of the Fe. Therefore, understanding the speciation of Fe in the atmosphere is critical to understanding the role of Fe as a nutrient source in surface ocean waters. Labile ferrous iron (Fe(II)) concentrations as well as total concentrations for Fe and other important trace metals, cations and anions, were determined over the Arabian Sea for two non-consecutive months during 1995.

Ambient aerosol samples were collected during the Indian Ocean inter- and southwest monsoon seasons over the Arabian Sea. Sampling took place aboard the German research vessel Meteor in the months of May (leg M32/3; inter-monsoon) and July/August (leg M32/5; southwest monsoon). Both cruise tracks followed the 65th E meridian, travelling for 30 days each (from north to south during leg M32/3 and from south to north during leg M32/5).

A high-volume dichotomous virtual impactor (HVDVI) with an aerodynamic cutoff size of 3 μm was used to collect the fine and coarse aerosol fractions for metal analysis. A low volume collector (LVC) was used to collect aerosol samples for anion and cation analysis. The analysis for labile-Fe(II) was done immediately after sample collection to minimize any possible Fe redox reactions which might occur during sample storage. The analytical procedure involved filter extraction in a formate/formic acid buffered solution at pH 4.2 followed by colorimetric quantification of soluble Fe(II). Metals, anions and cations were analysed after the cruise. Total atmospheric aqueous-labile-Fe(II) concentrations during the inter-monsoon were between 4.75 ng m^{-3} and < 0.4 ng m^{-3}, of which most (> 80%) was present in the fine fraction (< 3.0 μm). During the southwest monsoon, atmospheric aqueous-labile-Fe(II) concentrations were

consistently below the detection limit (< 0.34 ng m^{-3} to < 0.089 ng m^{-3}, depending on the volume of air sampled).

Air mass back trajectories (5 day, three-dimensional) showed that air masses sampled during the southwest monsoon had advected over the open Indian Ocean, while air masses sampled during the inter-monsoon had advected over northeast Africa, the Saudi Arabian peninsula, and southern Asia. These calculations were consistent with the results of the statistical analysis performed on the dataset which showed that the variance due to crustal species during the inter-monsoon samples was greater than the variance due to crustal species during the southwest monsoon. The factor scores for the crustal components were also greater when the back trajectories had advected over the nearby continental masses. Principal component analysis was also performed with the inter-monsoon samples where aqueous labile Fe(II) was above the detection limit. Aqueous labile Fe(II) did not correlate well with other species, indicating possible atmospheric processing of the iron during advection.

2.2 Introduction

A knowledge of the detailed chemical speciation of metals in atmospheric aerosols is important to understanding their role in atmospheric chemistry (cloud chemistry) and their fate in surface ocean waters after deposition. Once deposited in the ocean, metal speciation is critical to assessing the ability of marine biota to utilize atmospherically-derived trace elements as micronutrients [*Hudson and Morel*, 1990; *Hudson and Morel*, 1993; *Morel et al.*, 1991; *Wells et al.*, 1994; *Wells et al.*, 1995]. Recent studies have found Fe to be a rate-limiting nutrient to primary phytoplankton growth in certain regions of the open ocean [*Martin and Gordon*, 1988; *Ditullio et al.*, 1993; *Kolber et al.*, 1994; *Martin et al.*, 1994; *Price et al.*, 1994]; and the speciation of Fe is critical to the rate of Fe uptake by phytoplankton. Overall, a knowledge of the speciation of trace-metals in atmospheric deposition and the subsequent speciation changes upon introduction to marine waters is important to the assessment of the ability of marine biota to utilize atmospherically-derived elements.

The source of metals to cloudwater is from "dry" aerosol serving as cloud condensation nuclei or by impaction processes between the “dry” interstitial aerosol and the cloudwater droplets. Aqueous chemistry occurring in the cloudwater, in the presence of light and in a complex matrix, alters the speciation and reactivity of these metals. Several first-row transition metals are thought to play a major role in the redox cycle of sulfur and organic compounds in the troposphere, as well as controlling free radical production in clouds [*Conklin and Hoffmann*, 1988a; *Conklin and Hoffmann*, 1988b; *Faust and Hoffmann*, 1986; *Graedel et al.*, 1986; *Hoffmann and Jacob*, 1984; *Jacob et al.*, 1989; *Jacob and Hoffmann*, 1983; *Kotronarou and Sigg*, 1993; *Martin and Hill*, 1987; *Siefert et al.*, 1994; *Weschler et al.*, 1986; *Xue et al.*, 1991; *Zhuang et al.*, 1992b; *Zuo and Hoigné*, 1992]. Both Mn and Fe can catalyze the oxidation of

S(IV) by oxygen and together they have a synergistic effect [*Berglund and Elding*, 1995; *Berglund et al.*, 1993; *Conklin and Hoffmann*, 1988b; *Faust and Allen*, 1994; *Kraft and Van Eldik*, 1989; *Martin and Good*, 1991; *Martin et al.*, 1991]. Sedlak and Hoigné [*Sedlak and Hoigné*, 1993; *Sedlak and Hoigné*, 1994] have investigated the redox cycling of Fe and Cu in the presence of oxalate, and its implications on sulfur oxidation. The photoredox chemistry of Fe(III)-hydroxy and Fe(III)-oxalato complexes with the production of Fe(II) and oxidants ($OH^{\bullet}$, $HO_2^{\bullet}/O_2^{\bullet-}$) has also been studied [*Faust and Hoigné*, 1990; *Zuo and Hoigné*, 1992]. Zuo *et al.* [*Zuo and Hoigné*, 1994] studied the photochemical decomposition of oxalic, glyoxalic and pyruvic-acid catalyzed by iron in atmospheric waters.

Modeling studies have also looked at transition metal redox chemistry in cloudwater [*Jacob et al.*, 1989; *Matthijsen et al.*, 1995; *Seigneur and Constantinou*, 1995]. Jacob *et al.* [*Jacob et al.*, 1989] modeled the accumulation of pollutants observed over Bakersfield, CA, and found iron to be important for the catalytic oxidation of S(IV), while Matthijsen *et al.* [*Matthijsen et al.*, 1995] used a cloud model to investigate the effect of Fe and Cu on tropospheric ozone. In addition, Fe(III) has been shown to be an important reductant of Cr(VI) to Cr(III) in cloudwater [*Seigneur and Constantinou*, 1995].

Many investigators have determined the occurrence, particle-size distribution and sources of transition metals in the atmosphere [*Galloway et al.*, 1982; *Lantzy and Mackenzie*, 1979; *Nriagu and Davidson*, 1986; *Nriagu,* 1989; *Puxbaum*, 1991]. But only a few studies have investigated the speciation or reactivity of trace metals in cloudwater [*Behra and Sigg*, 1990; *Erel et al.*, 1993; *Kotronarou and Sigg*, 1993; *Xue et al.*, 1991] or in ambient aerosol [*Kopcewicz and Kopcewicz*, 1991; *Kopcewicz and Kopcewicz*, 1992; *Siefert et al.*, 1994; *Siefert et al.*, 1996; *Spokes et al.*, 1994; *Zhu et al.*, 1993; *Zhuang et al.*, 1992b]. Some of these studies have investigated the speciation of Fe in ambient aerosols by determining: 1) the concentration of

Fe(II) [*Zhu et al.*, 1993; *Zhuang et al.*, 1992a], 2) the concentration of soluble Fe [*Spokes et al.*, 1994; *Zhu et al.*, 1993], 3) the mineral form of the Fe through Mossbauer spectroscopy [*Kopcewicz and Kopcewicz*, 1991; *Kopcewicz and Kopcewicz*, 1992] and the photoreactivity of the iron [*Siefert et al.*, 1996].

Iron, which is one of the most abundant elements in the earth's crust, is present primarily as various Fe(II) and Fe(III) species [*Taylor and McLennan*, 1985]. Particulate Fe is transferred to the atmosphere by wind, volcanic activity, and through anthropogenic sources [*Cass and McRae*, 1983; *Gomes and Gillette*, 1993; *Seinfeld*, 1986]. Total Fe concentrations in tropospheric aerosols range from: 0.6 to 4160 ng/m^3 in remote areas, 55 to 14500 ng/m^3 in rural areas and 21 to 32820 ng/m^3 in urban areas [*Schroeder et al.*, 1987], and cloudwater concentrations range from 0.4 μM to 424 μM [*Behra and Sigg*, 1990; *Fuzzi et al.*, 1988; *Jacob et al.*, 1985; *Munger et al.*, 1983; *Waldman et al.*, 1982].

Previous studies have investigated the aerosol over the Indian Ocean. Chester *et al.* [*Chester et al.*, 1991] studied the distributions of aerosol trace metals over the Indian Ocean. Samples were collected during the northeast monsoon period off the coast of Oman, and in the Tropical Southern Indian Ocean where there were no large-scale up-wind continental sources. They found strong latitudinal variations in the chemical signatures of aerosols over the Indian Ocean. Savoie *et al.* [*Savoie et al.*, 1987] collected aerosol samples in the northwestern Indian Ocean and found significant variations in nitrate and NSS-sulfate concentrations which were a consequence of the variation in the impact of continentally derived aerosol.

The purpose of this study was to determine the chemical composition of ambient aerosol in both the fine and coarse aerosol fractions during the inter-monsoon and southwest monsoon periods over the Arabian Sea. Specific attention was given to the speciation of Fe in the ambient aerosol by conducting labile-Fe(II) measurements immediately after sample collection during the

cruise. The chemical characterization of the aerosol was used to investigate sources and other factors which control both total and labile Fe concentrations. The relationship between atmospheric labile-Fe(II) and marine biological acitivity, which was measured concurrently during the cruise, was also investigated.

2.3 Methods

2.3.1 Aerosol Collection

Ambient aerosol samples were collected using two collector types: 1) a high volume dichotomous virtual impactor (HVDVI) [*Solomon et al.*, 1983] and 2) a low volume collector (LVC). Two size fractions ($D_{p,50}$ = 3.0 μm) were collected with the HVDVI, which were used to analyze for total elemental composition and Fe(II). This collector was constructed out of polycarbonate with nylon screws in order to minimize trace metal contamination, and had a total flow rate of 335 ± 15 l min^{-1}. The fine and coarse sample fractions were collected on two 90 millimeter diameter Teflon filters (Gelman Zefluor, 1 μm pore size). Two LVCs, running at a flow rate of 27 l min^{-1} each, were used to collect aerosol samples for cation and anion analysis. The LVC consisted of an inverted high density polyethylene 2 liter bottle, serving as a rain shield, inside of which was placed a Nucleopore polycarbonate filter holder loaded with a Gelman Zefluor filter (47 mm in diameter). The aerosol collectors and lab equipment were acid-cleaned before use by following similar procedures as outlined by *Patterson and Settle* [*Patterson and Settle*, 1976] employing ultra-pure acids from Seastar Chemicals (Sidney, B.C., Canada) and 18.2 MΩ-cm Milli-Q UV water. The collectors were also cleaned periodically in the field by wiping the surfaces clean with KimWipes wetted with Milli-Q UV water. Filters were stored in acid-cleaned polystyrene petri dishes taped shut with Teflon tape, placed inside two plastic bags and stored in a refrigerator during the cruise. After the cruise the filters were sent back to Caltech (via air-freight) and stored in a freezer until analysis.

A sector sampling system was used to simultaneously control all of the aerosol collectors. The system was configured to allow collection of ambient aerosol samples only when the relative wind direction was ±90° off the bow during the inter-monsoon cruise and ±60° off the bow

during the southwest monsoon cruise. The sector sampling system was not in operation during the first 12 samples of the inter-monsoon cruise and therefore the aerosol collectors were manually controlled. This resulted in 6 of the 12 samples during this time to have collected aerosol "out of sector" (see Discussion section for further details). Usually, 24 hour averaged aerosol samples were collected (the actual sampling duration varied depending on the ship's cruise track during the collection period).

2.3.2 Labile Fe(II) Measurements Performed Immediately After Sample Collection

Several fractions of labile Fe(II), in both the fine and coarse particles collected on the two HVDVI filters, were determined by a sequential extraction procedure. These measurements were initiated immediately (within 1 hour) after sample collection in order to minimize any changes in Fe oxidation state due to possible redox reactions occurring during sample storage. Table 1 outlines the sequential extraction procedure. Three labile fractions of Fe were quantified using the procedure: 1) aqueous-labile-Fe(II) ($Fe(II)_{aq,labile}$), 2) 5-minute Ferrozine-labile-Fe(II) ($Fe(II)_{FZ,5min}$), and 3) 22 hour Ferrozine-labile-Fe(II) ($Fe(II)_{FZ,22hr,labile}$). Total labile iron Fe(II) ($Fe(II)_{total,labile}$) is defined as the sum of these three fractions. Fe(II) concentrations were determined colorimetrically by complexation with ferrozine [*Stookey*, 1970; *Carter*, 1971] and subsequent absorption measurements using a portable spectrophotometer (Shimadzu UV-1201).

2.3.3 Analysis Performed After the Cruise

Total concentrations for 31 elements (Na, Mg, Al, K, Ca, Sc, Ti, V, Cr, Mn, Fe, Ni, Cu, Zn, Ge, As, Se, Mo, Ru, Cd, Sn, Sb, Cs, Ba, La, Ce, Sm, Eu, Hf, Pb and Th) were measured in

both the coarse and fine fractions of the atmospheric aerosol (using the filters from the HVDVI). The method included a strong acid digestion of the aerosol samples, and subsequent analysis using inductively coupled plasma mass spectrometry (ICP-MS) with a Hewlett-Packard 4500 instrument. The same samples were also analyzed on a Perkin Elmer / Sciex 6000 ICP-MS for 17 elements (Na, Mg, Al, K, Ca, Ti, V, Cr, Mn, Fe, Ni, Cu, Zn, Cd, Sb, Ba and Pb) for quality control. Table 2 outlines the strong acid digestion technique. Indium and Bismuth were used as internal standards. Analysis of multiple isotopes was done for Mg (isotopes 24, 25, 26), Ca (isotopes 43 and 44), Ti (isotopes 47 and 48), Cr (isotopes 52 and 53), Fe (isotopes 54 and 57), Ni (isotopes 60, 61 and 62), Cu (isotopes 63 and 65), Zn (isotopes 66, 67 and 68), Ge (isotopes 69, 72 and 73), Mo (isotopes 96 and 97), Sn (isotopes 117, 118 and 119), Ba (isotopes 135 and 137), Sm (isotopes 147 and 149), Eu (isotopes 151 and 153) and Hf (isotopes 177, 178 and 179). These redundant measurements were made to check for possible interference problems.

Total atmospheric aerosol concentrations of organic anions (formate, acetate, glycolate, oxalate, succinate, malonate, maleate, fumarate, citrate), inorganic anions (sulfate, nitrate, nitrite, phosphate, chloride, bromide) and cations (sodium, calcium, magnesium, ammonium) were measured using the filters from the LVCs. The procedure included an ion extraction method, similar to Derrick and Moyers [*Derrick and Moyers*, 1981], followed by separation and quantification with ion-chromatography. The ion-chromatograph used was a Dionex BIO-LC with the capabilty of switching between anion and cation modes. Anions were separated and eluted with a PAX-500 anion column (Dionex) in gradient mode with a NaOH eluent, while the cations were eluted isocratically with HCl from a IonPac CS10 cation column. Although the anions data will be used in the present paper to perform the statistical analysis mentioned below, the IC data will be treated in greater detail in a separate paper.

Total suspended particulate concentrations were determined by measuring the mass of atmospheric aerosols collected on the LVC filters and knowing the volume of air sampled. The weighing procedure involved equilibrating the filters to air at 21°C and a relative humidity of 50% overnight and then weighing (these were the same conditions used to pre-weigh the filters). This weighing technique is similar to the one followed by *Ligocki et al.* [*Ligocki et al.*, 1993].

2.3.4 Error Analysis

Errors accompanying data in the table and plots are estimated by propagating the uncertainty of every parameter in the calculation that led to the final concentration. This included the volume of air sampled (10% estimated error), cutting and extracting the filter (10% estimated error), and the precision of the analytical instrument. The standard deviation for the ICP-MS is calculated about the weighted linear regression of the calibration curve. The detection limits were defined as three times the standard deviation of the blank (95% confidence level) divided by the slope of the calibration curve.

2.3.5 Statistical Analysis and Enrichment Factor Analysis

In addition to interpreting the data based on an element's enrichment compared to a crustal tracer [*Taylor and McLennan*, 1985], a multivariate statistical analysis was performed using SPSS software. In a principal component analysis the correlation matrix of the observed variables is utilized to reduce the number of those observed variables by linearly combining them into a smaller set of independent variables, called the principal components. These principal components are orthogonal to each other and can be rotated in space in order to simplify

interpretation of the data set. The common type of rotation used for this type of study is varimax rotation, during which othogonality of the principal components is retained.

2.4 Results and Discussion

2.4.1 Cruise Tracks and Air-Mass Back Trajectories

Four examples of five day air-mass back-trajectories (AMBTs) for both the M32/3 and M32/5 cruise legs are presented in Figure 1. AMBTs were obtained for all days for both cruise legs; however, the two AMBTs displayed for each of the cruises are representative of the meteorological conditions encountered. The cruise track for the appropriate leg is shown in Figure 1 as a solid line. Figure 1 (a) and (b) are AMBTs for M32/3 (inter-monsoon) which began in Oman and ended in the Seychelles, and Figure 1 (c) and (d) are AMBTs for M32/5 (southwest monsoon) which began in the Seychelles and ended in Oman. Each plot traces four different AMBTs which correspond to different initial elevations (based on pressure) at the initial position. The vertical motion of each AMBT is shown in the graph at the bottom of each diagram in Figure 1. Each symbol in the diagrams represents a period of 6 hours.

During the northern part of M32/3 (inter-monsoon, Figure 1(a)), air-masses generally came from continental sources including Africa, the Middle East, and Asia, while the southern portion of the same cruise was characterized by slower moving (observe the closely spaced points) "oceanic" air-masses (Figure 1(b)) which had not recently advected over any continental land masses.

The southwest monsoon was dominated by strong southwest winds blowing open ocean air-masses towards the northeastern part of Africa. These air-masses did not reach the continent before being sampled during the southern part of the cruise (Figure 1(c)). However, during the northern portion of the same cruise (Figure 1(d)), some of the higher elevation back trajectories did advect over continental land masses, thereby possibly entraining crustal material. This pattern of persistent high-speed air current, in the form of a system of low-level jet streams in the

vicinity of the western Indian Ocean during the northern summer, named the Findlater Jet [*Findlater*, 1969], also leads to major areas of upwelling in the ocean off of the coast of Somalia, which has been the subject for many areas of research.

2.4.2 Total Elemental Concentrations

The mass of total suspended particulates (TSP) was determined with the filters originating from the two low volume collectors; therefore, two data points per sampling interval are represented in Figure 2. Note the higher average during the southwest monsoon, when strong winds break the ocean surface, increasing the amount of sea spray droplets reaching the collector. More evidence for this statement follows below.

The x-axis of this and all the plots to follow represent both a spatial and temporal scale. Both cruise tracks were almost identical but proceeded in opposite directions, on a spatial scale, the left and right-hand sides of the plots represent Oman, while the center is in proximity to the equator. Simultaneously, the left side of the plot represents the inter-monsoon while the right represents the southwest monsoon. Vertical lines in Figures 2, 3 and 6 depicts this break in the data set. Labels on the x-axes are sample identifications. Table 3 lists the collection intervals and locations (taken at mid point in time of the interval) for each aerosol sample.

Total concentrations of Na, Mg, Al, K, Ca, Sc, Ti, V, Cr, Mn, Fe, Ni, Cu, Zn, Ge, As, Se, Mo, Ru, Cd, Sn, Sb, Cs, Ba, La, Ce, Sm, Eu, Hf, Pb and Th were determined in both the fine and coarse fractions of the ambient aerosol. Only the elements for which most of the concentrations in the samples were above detection limit are discussed further. Plots in Figure 3 represent the atmospheric concentrations in both the fine and coarse fractions of the more noteworthy elements.

A general observation from Figure 3 is that most of the metals, except for the sea salt tracer sodium (Figure 3(c)), are present at much greater abundance during the inter-monsoon when air-masses originated over contintental masses. The crustal component is typically traced by aluminium (Figure 3(a)), and shows that, as expected, the crustal contribution to the total aerosol loadings is highest during the inter-monsoon season. Of special interest is the distribution between the fine and coarse fractions. Since crustal material suspended in the atmosphere is mechanically derived, its characteristic particle diameter is >1μm. Due to the 3 μm cut off of the HVDVI, we observe a considerable Al contribution in both size fractions, where the amount in the coarse fraction should dominate in closer proximity to the aerosol source. The larger the mass of a particle and the lower the wind speeds, the faster will be the removal of the aerosol from the atmosphere by dry deposition processes. This feature is well represented in Figure 3(a); samples M32/3-21 through M32/3-23 (see also AMBT in Figure 1(b)) were taken near the equator during very low winds where air-masses had traveled a substantial amount of time (>5 days) over the ocean before being sampled. The same finger print of the three fine fraction samples can be recognized in Figures 3(b) for Fe, 3(d) for Mn, 3(g) for Cr and somewhat in 3(e) for V, indicating those elements to have a common origin. The origin of these elements will be discussed in the statistical analysis below.

Another interesting feature is the large fine contribution of lead (see Figure 3(f)) to its total atmospheric concentration, especially during the first half for the inter-monsoon cruise. Lead is a common fuel additive still used in Africa and Asia and can therefore serve as a tracer for the anthropogenic contribution of the total aerosol collected over the Arabian Sea. Because combustion processes produce sub-micron sized particles, we observe the enrichment of lead predominantly in the fine fraction.

Vanadium is another combustion tracer, which is inherent in crude oils and varies strongly with the region from where the oil was extracted. The heavier the oil, the higher the vanadium content. The R/V Meteor used diesel generators and electric engines ("diesel-electric") for its propulsion system. And diesel is a very light distillate fuel, compared with the heavy fuel oils used by most ocean-going freighters and tankers. Thus, we expect most of the vanadium in the samples to be comprised of an underlying crustal component plus a sporadic contribution from upwind encountered freight ships along the cruise track. The spikes in the fine V fraction observed during the southwest monsoon (the right half of Figure 3(e)) coincides with our steaming in the area of well defined and busy shipping lanes on the Arabian Sea.

2.4.3 Fe(II) Concentrations

Three labile fractions of Fe(II) were measured immediately after aerosol collection in both the coarse and fine aerosol fractions. Table 1 describes the sequential extraction procedure resulting in the measurements of $Fe(II)_{aq,labile}$ $Fe(II)_{FZ,5min,labile}$ and $Fe(II)_{FZ,22hr,labile}$. The sum of these three labile fractions is $Fe(II)_{total,labile}$. In the discussion we will focus on the $Fe(II)_{aq,labile}$ and $Fe(II)_{total,labile}$, for both aerosol size fractions. These fractions were selected since they best represent the minimum ($Fe(II)_{aq,labile}$) and maximum ($Fe(II)_{total,labile}$) amount of Fe(II) which would be expected to be dissolved into the aqueous-phase upon activation of the aerosol into cloud drops (excluding reductive dissolution processes). Only labile Fe(II) results from the inter-monsoon (M32/3) are available since all the extractions during the southwest monsoon were below detection limit. The results are presented in Figures 4 and 5. Two samples are missing at either end of the cruise; at the beginning, due to the development of the extraction procedure, and

at the end, due to the early disassembly of the laboratory equipment in preparation for disembarkation.

Concentrations of Fe(II) in both the fine and coarse fractions are presented in the stacked bar plots in Figure 4. The measurement for $Fe(II)_{FZ,22hr,labile}$ was started using sample M323-08 for the fine fraction, and M323-13 for the coarse fraction, due to the development of the labile Fe(II) extraction method during the first part of inter-monsoon cruise. Therefore, both the fine $Fe(II)_{total,labile}$ and the coarse $Fe(II)_{total,labile}$ are potentially biased low during the first 7 and 12 samples, respectively.

From Figure 4 we see that overall more than 80% of the $Fe(II)_{total,labile}$ was present in the fine fraction. These observations may indicate the presence of two different sources and/or a different weathering history of the two aerosol size fractions. Iron in the coarse size fraction is probably associated with crustal material. And this Fe is expected to be bound in alumino-silicate minerals, which would not be susceptible to chemical weathering on the time scale of atmospheric aerosols. However, some fraction of the crustal material may also include clay materials and iron oxides which would be more susceptible to chemical weathering and the release of Fe(II). Aerosol in the fine fraction is usually comprised of secondary aerosol and primary aerosol from pollution sources; however due to the 3 μm cutoff size in the HVDVI, we are also probably collecting crustal elements in the fine fraction. Overall, a greater fraction of the iron in the fine fraction is probably from pollution sources (e.g., combustion of fossil fuels) than in the coarse fraction. And the pollution sources may produce more labile forms of Fe such as iron-oxyhydroxides. Smaller particles can also be suspended in the atmosphere much longer [*Arimoto and Duce*, 1986; *Rojas et al.*, 1993] than larger particles, allowing them to undergo chemical transformation when subjected to repeated "wet" and "dry" cycles. This cycling could also result in an increase in labile Fe(II) to total Fe.

Figure 5 represents the percentages of $Fe(II)_{total,labile}$ to total Fe (determined by ICP-MS) for the fine and coarse size fractions as well as for the total (the bars represent calculated ranges based on the detection limits of the measurements). Overall, never more than 4% of the total Fe is released as Fe(II) after 22 hours of extraction. However, a greater percentage of $Fe(II)_{total,labile}$ to total Fe is observed in the fine aerosol fraction for almost all of the samples. Zhu *et al.* [*Zhu et al.*, 1993] observed $Fe(II)_{labile}/Fe_{total}$ fractions in four Barbados aerosol samples of 0.87, 0.92, 0.47 and 0.53% which were similar to our observations. Zhuang *et al.* [*Zhuang et al.*, 1992b] observed higher $Fe(II)_{labile}/Fe_{total}$ fractions: 2.2% to 49% in marine aerosol samples collected over the central North Pacific and Barbados (see [*Zhu et al.*, 1993] for a correction of [*Zhuang et al.*, 1992b] results). These higher fractions, compared to our observations on the Arabian Sea, may be the result of increased cloud processing of the aerosol in the central North Pacific and Barbados. However, in the studies by both Zhu *et al.* [*Zhu et al.*, 1993] and Zhuang *et al.* [*Zhuang et al.*, 1992b] the time between the collection and analysis was considerable, possibly enough to change oxidation states; whereas, in this study, analysis was performed immediately (within 1 hour) after sample collection (which took approximately 24 hours). In addition, their extraction techniques were performed in acidic solutions.

Another interesting observation is the increase of $Fe(II)_{total,labile}$ to total Fe in the coarse fraction for samples M32/3-21 through M32/3-23 (shown as a lower limit using the detection limit for total Fe); this corresponds to the same three samples with the large fine Fe contribution seen in Figure 3(b). There is no obvious explanation for these observations. Furthermore, it seems to be against common expectations, the air masses sampled had traveled over long periods of time during which the aerosol was probably subjected to considerable weathering, photoreductively increasing its relative Fe(II) content [*Faust and Hoigné*, 1990; *Zuo and Hoigné*, 1992]. Concurrently, however, the selective removal of the larger aerosol fraction, due to their

faster settling velocities, results in a large decrease in the coarse aerosol loadings, while the fine fraction is not affected in the same way. Unless the coarse side of the collector collects some fraction of the fine particles which are heavily enriched in Fe(II), there seems to be a mechanism by which Fe(II) is enriched more selectively in the coarse than in the fine aerosol fraction. This could be explained by sequential cloud processing which may affect aerosols of distinct size and composition in different ways.

Although our research focused on atmospheric particulate matter, the primary focus of the cruise was the investigation of nutrient fluxes (primarily nitrogen species) in the water column and its role on biological productivity. One major observation during the cruise was an extensive bloom of the N_2-fixing Cyanobacterium, *Trichodesmium erythraeum* [*Capone et al.*, 1998]. In addition, the ability of Trichodesmium erythraeum to sequester new nitrogen makes it an important component of biological productivity in the Central Arabian Sea, which is oligotrophic. The enzyme, which is responsible for nitrogen fixation in *Trichodesmium erythraeum,* has relatively large amounts of Fe in its chemical structure. Therefore, correlations between atmospheric labile-Fe(II) and *Trichodesmium erythraeum* were investigated (for more details see Capone et al. [1998]). We observed a correlation between labile-Fe(II) and *Trichodesmium erythraeum*; however, the evidence is not conclusive.

2.4.4 Enrichment Factors

Enrichment factors (EF) were determined [*Zoller et al.*, 1974; *Duce et al.*, 1975] for a series of elements using their total (fine plus coarse fractions) atmospheric concentrations. The enrichment of an element is defined as $EF(X) = (X/Al)_{air}/(X/Al)_{crust}$. Crustal averages from Taylor [*Taylor and McLennan*, 1985] were used as a reference using Al as the crustal tracer. The values

are listed in Table 4. The closer the value to 1, the stronger the indication that that specific element in the sample was associated with the crustal component of the aerosol.

Iron seems to be predominantly of crustal origin during the southwest monsoon (M325), while during the inter-monsoon (M323), over a third of the samples are enriched (>2), suggesting another source of Fe, especially in the first half of that cruise. EFs for Mn reveal the same relative enrichment pattern as Fe, however, at lower values. This resemblance is clearly visible when comparing the Fe and Mn plots in Figure 3(b) and (d), respectively. Cr, Cu, Zn, Mo and Sn are also elements which are enriched above normal when Fe and Mn are enriched. Although the reason for these enrichments is not clear, two speculated sources of these enrichments may be contamination (e.g., ship exhaust), or a natural source of these elements. One potential natural source which may explain the enrichment observations is ultramafic rock which has an elemental profile which is generally consistent with the observed enrichments. Ultramafic rock is made up of ferromagnesian minerals (olivine and pyroxene), which, as the name suggests, contain higher than normal concentrations of iron and manganese. These types of rocks are associated with the earth's mantle, of which a piece, known as the Samail ophiolite formation [*Hess*, 1989], is residing on the coast of Oman. Table 5 lists the composition of a typical ultramafic rock and that of the crustal average used in determining the above enrichment factors. In order to directly compare the EFs in Table 4 with the elemental content of the ultramafic rock, the elemental concentrations of the ultramafic rock were normalized with regard to the crustal average, in the same manner as the EF were determined. Thus, the third column denotes the enrichment of a typical ultramafic rock over the crustal average. Assuming all the aerosol in a sample was made up of this ultramafic rock, one should observe the maximum EF for an element in that sample (Table 4) to match the value in column 3 in Table 5. The elements in bold in Table 5 are the highly enriched ones; Mn, Fe, Cr and Ni, in ascending order. The observed Fe and Mn

enrichments during the inter-monsoon are roughly consistent with ultramafic rock; however, the observed Cr enrichments are over an order of magnitude lower than what Table 5 predicts. Overall, a natural source of the enriched Fe and Mn during the inter-monsoon samples could not be identified with any strong confidence.

Vanadium enrichment during the southwest monsoon is, as mentioned in the previous section, attributable to a sporadic external source from the combustion of heavy fuel oil. Vanadium enrichment is not observed during the inter-monsoon cruise. However this does not rule out the possibility of contamination of the aerosol samples from sampling the ships exhaust since the R/V Meteor uses diesel which is lighter than fuel oil and therefore has much less V. The enrichment of Pb throughout all the samples indicates a steady transport of anthropogenic matter from the continents to the open ocean, where the values increase with the proximity to land masses.

Chester *et al.* [*Chester et al.*, 1991] studied the aerosol composition over the Indian Ocean during the northeast- and southwest monsoons. As expected, crustal components in the aerosol loadings were small during the southwest monsoon. The wind direction during the northeast-monsoon blows air from Pakistan and northern India over the Arabian Sea, thus representing different sources than the ones sampled during this study, making it difficult to compare the finger print of the different components.

2.4.5 Factor Analysis

Principal component analysis, also called factor analysis, serves to simplify the interpretation of a large data set by reducing the number of observed variables. The correlation matrix for the data set is used to combine those variables which correlate strongly into

independent variables, resulting in a smaller set of orthogonal variables that describe the total variance of the data almost as well as the original set of variables. These new variables, called principal components or factors, usually represent the distinct sources by which the sampled aerosol is composed. This identification of different sources is essential to the knowledge of the detailed chemical composition as well as to estimating the potential for chemical transformation of the aerosol during its residence time in the atmosphere. In the presence of a contamination source which contributes significantly to the variance of the data set, a factor with those characteristics will emerge for the analysis. However, this is only the case, if the source's chemical composition contributes significantly to the variance of the dataset. This will be discussed in further detail below.

The first principal component analysis was performed using the measurements from both cruises. The inter-monsoon and southwest monsoon measurements were combined for this analysis since the potential sources, deduced from the AMBTs, for both the cruises will be the same, due to the relatively large sampling area covered. The observed variables used in the analysis were the fine and coarse elemental compositions, the total anion and cation concentrations, and the wind speed. Only those measurement with most of the values above the detection limit were included in the analysis. Table 6 lists the result obtained from the factor analysis (employing varimax rotation), and Table 7 lists the analysis statistics for the same analysis. Missing data points (e.g., variables below the detection limit) were replaced by the average value of the detection limit for the variable. Table 6 shows all the extracted components with an eigenvalue greater than one. The extracted components in Table 6 describe 87.3% of the total variance of the data set, of which over half (63.9%) is accounted for by the first three components. Figure 6 displays the factor scores for each factor plotted against the sample

number. Since factor scores are the weight of each factor in a sample, the curves in Figure 6 show the relative contribution of each component in every sample in terms of variance.

The results in Table 6 are interpreted by how close the correlation coefficient is to 1. The closer a value is to 1, the better it correlates with that specific component. Several elements in one component that exhibit values close to 1 correlate with each other. To ease the reading of this table, correlation coefficients greater than 0.5 were printed in bold. Thus, Factor 1 is characterized by a coarse crustal component, due to the high correlation with coarse aluminium and the high correlation coefficients with other elements in the coarse fraction which also had enrichment factors close to one in Table 4 (Ba, Ce, La, Sc, and Zn). Factor 2 displays the same character as Factor 1, however, for the fine fraction. The reason for these two distinct crustal components is probably due to the different removal rates of these distinct size fractions. Qualitative evidence for this can be seen by noticing the greater variation in the factor loadings for the crustal fine component (Figure 6(b)) towards the later part of the inter-monsoon cruise, compared to the greater variation in the factor loadings for the crustal coarse component (Figure 6(a)) earlier during the inter-monsoon cruise where the advection of the crustal aerosol from the source regions was less. These two crustal components predominate the variance during the inter-monsoon, as can be seen in Figure 6 and Table 7. Factor 3 has high correlation coefficients with species associated with sea salt, including several anions (i.e., Cl^-, MSA, SO_4^{2-}) and cations (i.e., Na^+, K^+, Mg^{2+}). Factor 3 also has a high correlation coefficient with wind speed. Sea spray is produced by stronger winds, which were typical during the southwest monsoon, and result in the larger factor scores of this component in Figure 6(c).

Factor 4 (Figure 6(d)) contributed only 8.8% to the total variance and has high correlation coefficients for Ga Zn Fl^- and NH_4^+. Factor 4 has one peak on top of an underlying decline during the beginning of the inter-monsoon followed by one more peak at the end of the inter-

monsoon and two more at the beginning of the southwest monsoon cruise. The source of the elements in Factor 4 are not known. However, the NH_4^+ trend in factor 4 is consistent with the fact that the predominant sources of ammonia to the atmosphere are terrestrial (>80%) [*Schlesinger and Hartley*, 1992], and the factor 4 loadings (Figure 6(d)) are higher when the AMBTs showed less advection time from terrestrial sources. Of special interest are Factors 5 & 6 (Figure 6(e & f)) since they describe a major source of Fe and Mn. These factors are also more predominant during the beginning of the inter-monsoon cruise. The last Factor (Figure 6(g)) has no elements with a correlation coefficient greater than 0.5.

In the case of an additional crustal source, of ultramafic nature, as considered in the enrichment factor section, we would expect to find one component characterized by the same elements as depicted in Table 5 (Cr, Mn, Fe and Ni), unless some elements are preferentially enriched over others during the weathering process of an ultramafic rock. Unfortunately, Cr was not used for this principal component analysis since many of the measurements were below the detection limit for the southwest monsoon, and Ni was also omitted because of the contamination problem described before. Overall, there is no clear evidence from this principal component analysis or the enrichment factor analysis of the presence of an additional ultramafic crustal source.

Contamination of the samples may be a reason for some of the components and the large enrichment factors observed for some elements. Anthropogenic sources from the continents, such as smelting operations, cannot be excluded. The potential of having sampled the Meteor's exhaust plume was substantial during 6 of the first 12 samples during the inter-monsoon cruise, when the sector-sampling system was not working properly. Table 8 summarizes the sector sampling system operation during this time including the time the aerosol samplers collected out of sector and if the ship plume passed over the collectors. Due to the burning of relatively trace

metal free Diesel fuel, the direct assignment of one of the unknown factors to be representative of the Diesel contribution is difficult.

Throughout the cruise, a considerable amount of different kinds of waste was incinerated. Incineration took place on a sporadic time scale and included old paints and old oil. Due to the wide range of different materials burned, the exhaust may have varied its chemical fingerprint from incident to incident, making it impossible to be detected as a single and simple component in the factor analysis. Paints used on the Meteor contained Zn, Ti, Pb, Cr, Ba and Fe. Note that every one of the 11 paints used on the Meteor only contains one or two of these metals. The chance for having sampled some of these metals from the incinerator may exist. A slight chance of sampling the plume will always exist during the maneuvering of the ship as drifters are being put out or taken in, even though the sector-sampling system is working correctly.

Factor analysis was also performed using only the inter-monsoon samples and including the $Fe(II)_{aq,labile,FINE}$ measurements. The results for this factor analysis were nearly identical to the previous factor analysis and are therefore not shown. The $Fe(II)_{aq,labile,FINE}$ had a 0.67 correlation coefficient for the "crustal coarse" component, a 0.28 correlation coefficient for the "crustal fine" component and a 0.35 correlation coefficient for the "sea salt" component. Overall, $Fe(II)_{aq,labile,FINE}$ did not load exclusively (have a high corrrelation coefficient) on any of the components. The inclusion of $Fe(II)_{aq,labile,FINE}$ also did not result in a new component since it probably has a relatively low contribution to the total variance. It is also interesting that the $Fe(II)_{aq,labile,FINE}$ correlated best with the crustal iron in the coarse fraction and not the fine fraction. Overall, the results indicate that $Fe(II)_{aq,labile,FINE}$ concentrations cannot be predicted from other elements (including total iron) and that other processes including atmospheric reactions are influencing the $Fe(II)_{aq,labile,FINE}$ concentrations.

2.5 Conclusions

Ambient aerosol samples were collected and analyzed for trace metals, anions, cations and three labile-Fe(II) fractions during the inter- and southwest monsoon periods of 1995 over the Arabian Sea aboard the German research vessel Meteor (Meteor Cruise 32). Enrichment factor and principal component analyses revealed the major sources of variances to the aerosol composition to be of crustal nature during the inter-monsoon, while most of the variance during the southwest monsoon was accounted for by the sea salt component. These findings were in agreement with the back-trajectory analysis done for both crusies. A few of the highly enriched (enriched over the crustal average) elements (e.g., Mn, Mo, Fe) were discussed in greater detail. An ultramafic crustal nature as a source of these enriched elements was not completely ruled out; however, their source could also be from an anthropogenic source or from contamination source from the ship.

Total atmospheric aqueous-labile-Fe(II) concentrations during the inter-monsoon were between 4.75 ng m^{-3} and < 0.4 ng m^{-3}. In contrast, during the southwest monsoon the labile-Fe(II) concentrations were consistently below detection limit (< 0.34 ng m^{-3} to < 0.089 ng m^{-3}, depending on the volume of air sampled). The total labile-Fe(II) represented only a small fraction (< 4%) of the total Fe. The sequential extraction procedure also revealed that most of the labile-Fe(II) (> 80%) was released from the fine fraction (< 3 μm) than from the coarse fraction (> 3 μm). This may have important implications on the bioavailability of iron once it reaches surface waters.

Acknowledgments Special thanks are extended to the crew of the FS Meteor for their help. We also thank Prof. J. J. Morgan (Caltech) and Prof. M. O. Andreae (Max Planck Institute for Chemistry, Mainz, Germany) for helpful discussions. Support for this research has been provided by a grant from the National Science Foundation, Division of Atmospheric Sciences, Atmospheric Chemistry Section (ATM 9015775; ATM 9303024). This research was also sponsored by the U.S. Department of Energy, Office of Energy Research, Environmental Sciences Division, Office of Health and Environmental Research, under appointment to the Graduate Fellowships for Global Change administered by Oak Ridge Institute for Science and Education.

2.6 References

Arimoto, R., and R. A. Duce, Dry deposition models and the air/sea exchange of trace elements, *J. Geophys. Res.*, *91* (D2), 2787-2792, 1986.

Behra, P., and L. Sigg, Evidence for redox cycling of iron in atmospheric water droplets, *Nature*, *344* (6265), 419-421, 1990.

Berglund, J., and L.I. Elding, Manganese-catalyzed autooxidation of dissolved sulfur-dioxide in the atmospheric aqueous-phase, *Atmos. Environ.*, *29* (12), 1379-1391, 1995.

Berglund, J., S. Fronaeus, and L.I. Elding, Kinetics and mechanism for manganese-catalyzed oxidation of sulfur(IV) by oxygen in aqueous-solution, *Inorg. Chem.*, *32* (21), 4527-4538, 1993.

Capone, D.G., A. Subramaniam, J.P. Montoya, M. Voss, C. Humborg, A.M. Johansen, R.L. Siefert, and E.J. Carpenter, An extensive bloom of the N_2-fixing Cyanobacterium *Trichodesmium erythraeum* in the Central Arabian Sea, *Marine Ecology Progress Series*, *172*, 281-292, 1998.

Carter, P., Spectrophotometric determination of serum iron at the submicrogram level with a new reagent (ferrozine), *Anal. Biochem.*, *40*, 450-458, 1971.

Cass, G. R., and G. J. McRae, Source-receptor reconciliation of routine air monitoring data for trace metals: An emission inventory assisted approach, *Environ. Sci. Technol.*, *17* (3), 129-139, 1983.

Chester, R., A. S. Berry, and K. J. T. Murphy, The distributions of particulate atmospheric trace metals and mineral aerosols over the Indian Ocean, *Marine. Chem.*, *34*, 261-290, 1991.

Conklin, M. H., and M. R. Hoffmann, Metal ion-sulfur(IV) chemistry. 2. Kinetic studies of the redox chemistry of copper(II)-sulfur(IV) complexes, *Environ. Sci. Technol.*, *22*, 891-898, 1988a.

Conklin, M. H., and M. R. Hoffmann, Metal ion-sulfur(IV) chemistry. 3. Thermodynamics and kinetics of transient iron(III)-sulfur(IV) complexes, *Environ. Sci. Technol.*, *22*, 899-907, 1988b.

Derrick, M., and J. Moyers, Precise and sensitive water soluble ion extraction method for aerosol samples collected on polytetrafluoroethylene filters, *Anal. Lett.*, *14* (A19), 1637-1652, 1981.

Ditullio, G. R., D. A. Hutchins, and K. W. Bruland, Interaction of iron and major nutrients controls phytoplankton growth and species composition in the tropical North Pacific Ocean, *Limnol. & Ocean.*, *38* (3), 495-508, 1993.

Duce, R. A., G. L. Hoffman, and W. H. Zoller, Atmospheric trace metals at remote northern and southern hemisphere sites: Pollution or natural, *Science*, *187*, 59-61, 1975.

Erel, Y., S. O. Pehkonen, and M. R. Hoffmann, Redox chemistry of iron in fog and stratus clouds, *J. Geophys. Res. A.*, *98* (D10), 18423-18434, 1993.

Faure, G., *Principles and Applications of Inorganic Geochemistry*, Mac-millan, Indianapolis, Ind., 1991.

Faust, B.C., and J.M. Allen, Sunlight-initiated partial inhibition of the dissolved iron(III)-catalyzed oxidation of S(IV) species by molecular-oxygen in aqueous-solution, *Atmospheric Environment*, *28* (4), 745-748, 1994.

Faust, B. C., and M. R. Hoffmann, Photoinduced reductive dissolution of alpha-Fe_2O_3 by bisulfite, *Environ. Sci. Technol.*, *20*, 943-948, 1986.

Faust, B. C., and J. Hoigné, Photolysis of Fe(III)-hydroxy complexes as sources of OH radicals in clouds, fog and rain, *Atmos. Environ.*, *24A* (1), 79-89, 1990.

Findlater, J., A major low-level air current near the Indian Ocean during the northern summer, *Quarternary Journal R. Meteorological Society*, *95*, 362-380, 1969.

Fuzzi, S., G. Orsi, G. Nardini, M. C. Facchini, E. McLaren, and M. Mariotti, Heterogeneous processes in the Po Valley radiation fog, *J. Geophys. Res. A.*, *93* (ND9), 11141-11151, 1988.

Galloway, J. N., J. D. Thornton, S. A. Norton, H. L. Volchok, and R. A. N. Mclean, Trace-metals in atmospheric deposition - A review and assessment, *Atmos. Environ.*, *16*, 1677-1700, 1982.

Gomes, L., and D. A. Gillette, A comparison of characteristics of aerosol from dust storms in central Asia with soil derived dust from other regions, *Atmos. Environ.*, *27* (16), 2539-2544, 1993.

Graedel, T. E., M. L. Mandich, and C. J. Weschler, Kinetic model studies of atmospheric droplet chemistry, 2. Homogenous transition metal chemistry in raindrops, *J. Geophys. Res.*, *91*, 5205-5221, 1986.

Hess, P. C., *Origins of igneous rocks*, Harvard Univ. Press, Cambridge, MA, 1989.

Hoffmann, M. R., and D. J. Jacob, Kinetics and mechanism of the catalytic oxidation of dissolved SO_2 in atmospheric droplets: Free radical, polar and photoassisted pathways, in *SO_2, NO, NO_2 Oxidation Mechanisms: Atmospheric Considerations*, edited by J.G. Calvert, pp. 101-172, Butterworth Publishers, Boston, 1984.

Hudson, R. J. M., and F. M. M. Morel, Iron transport in marine phytoplankton: Kinetics of cellular and medium coordination reactions, *Limnol. Ocean.*, *35* (5), 1002-1020, 1990.

Hudson, R. J. M., and F. M. M. Morel, Trace-metal transport by marine microorganisms: Implications of metal coordination kinetics, *Deep Sea Res.*, *40*, 129-150, 1993.

Jacob, D. J., E. W. Gottlieb, and M. J. Prather, Chemistry of the polluted boundary layer, *J. Geophys. Res.*, *94*, 12975-13002, 1989.

Jacob, D. J., and M. R. Hoffmann, A dynamic model for the production of H^+, NO_3^-, and SO_4^{2-} in urban fog, *J. Geophys. Res.*, *88* (NC11), 6611-6621, 1983.

Jacob, D. J., J. M. Waldman, J. W. Munger, and M. R. Hoffmann, Chemical composition of fogwater collected along the California coast, *Environ. Sci. Technol.*, *19* (8), 730-736, 1985.

Kolber, Z. S., R. T. Barber, K. H. Coale, S. E. Fitzwater, R. M. Greene, K. S. Johnson, S. Lindley, and P. G. Falkowski, Iron limitation of phytoplankton photosynthesis in the equatorial Pacific Ocean, *Nature*, *371* (6493), 145-149, 1994.

Kopcewicz, B., and M. Kopcewicz, Mossbauer study of iron-containing atmospheric aerosols, *Struct. Chem.*, *2* (3-4), 303-312, 1991.

Kopcewicz, B., and M. Kopcewicz, Seasonal variations of iron concentration in atmospheric aerosols, *Hyperfine Interactions*, *71* (1-4), 1457-1460, 1992.

Kotronarou, A., and L. Sigg, SO2 Oxidation in atmospheric water: role of Fe(II) and effect of ligands, *Environ. Sci. & Technol.*, *27* (13), 2725-2735, 1993.

Kraft, J., and R. Van Eldik, Kinetics and mechanism of the iron(III)-catalyzed autooxidation of sulfur(IV) oxides in aqueous-solution .2. Decomposition of transient iron(III) sulfur(IV) complexes, *Inorg. Chem.*, *28* (12), 2306-2312, 1989.

Lantzy, R. J., and F. T. Mackenzie, Atmospheric trace metals: Global cycles and assessment of Man's impact, *Geochim. et Cosmochim. Acta*, *43*, 511-523, 1979.

Ligocki, M. P., L. G. Salmon, T. Fall, M. C. Jone, W. W. Nazaroff, and G. R. Cass, Characteristics of airborne particles inside southern California museums, *Atmos. Environ.*, *27(5)*, 697-711, 1993.

Martin, J. H., K. H. Coale, K. S. Johnson, S. E. Fitzwater, R. M. Gordon, S. J. Tanner, C. N. Hunter, V. A. Elrod, J. L. Nowicki, T. L. Coley, R. T. Barber, S. Lindley, A. J. Watson, K. Van Scoy, C. S. Law, M. I. Liddicoat, R. Ling, T. Stanton, J. Stockel, C. Collins, A. Anderson, R. Bidigare, M. Ondrusek, M. Latasa, F. J. Millero, K. Lee, W. Yao, J. Z. Zhang, G. Friederich, C. Sakamoto, F. Chavez, K. Buck, Z. Kolber, R. Greene, P. Falkowski, S. W. Chisholm, F. Hoge, R. Swift, J. Yungel, S. Turner, P. Nightingale, A. Hatton, P. Liss, and N. W. Tindale, Testing the

iron hypothesis in ecosystems of the equatorial Pacific Ocean, *Nature*, *371* (6493), 123-129, 1994.

Martin, J. H., and R. M. Gordon, Northeast Pacific iron distributions in relation to phytoplankton productivity, *Deep Sea Res. A.*, *35* (2), 177-196, 1988.

Martin, L.R., and T.W. Good, Catalyzed oxidation of sulfur dioxide in solution: The iron-manganese synergism, *Atmospheric Environment*, *25* (10), 2395-2399, 1991.

Martin, L. R., and H. W. Hill, The iron catalyzed oxidation of sulfur: Reconciliation of the literature rates, *Atmos. Environ.*, *21*, 1487-1490, 1987.

Martin, L.R., M.W. Hill, A.F. Tai, and T.W. Good, The iron catalyzed oxidation of sulfur(IV) in aqueous-solution: Differing effects of organics at high and low pH, *J. Geophys. Res.*, *96* (ND2), 3085-3097, 1991.

Matthijsen, J., P. J. H. Builtjes, and D. L. Sedlak, Cloud model experiments of the effect of iron and copper on tropospheric ozone under marine and continental conditions, *Meteorol. Atmos. Phys.*, *57*, 43-60, 1995.

Morel, F. M. M., R. J. M. Hudson, and N. M. Price, Limitation of productivity by trace-metals in the sea, *Limnol. Oceanogr.*, *36* (8), 1742-17455, 1991.

Munger, J. W., J. M. Waldman, D. J. Jacob, and M. R. Hoffmann, Fogwater chemistry in an urban atmosphere, *J. Geophys. Res.*, *88* (NC9), 5109-5121, 1983.

Nriagu, J. O., A global assessment of natural sources of atmospheric trace metals, *Nature*, *338*, 47-49, 1989.

Nriagu, J. O., and C. I. Davidson, Toxic metals in the atmosphere, in *Advances in environmental science and technology*, Wiley, New York, 1986.

Patterson, C. C., and D. M. Settle, The reduction of orders of magnitude errors in lead analysis of biological materials and natural waters by evaluating and controlling the extent and sources of

industrial lead contamination introduced during sampling, collecting, handling and analysis, *National Bureau of Standards, Special Publication*, *422*, 321-351, 1976.

Price, N. M., B. A. Ahner, and F. M. M. Morel, The equatorial Pacific Ocean - grazer controlled phytoplankton populations in an iron limited ecosystem, *Limnol. & Ocean.*, *39* (3), 520-534, 1994.

Puxbaum, H., Metal compounds in the atmosphere, in *Metals and their compounds in the environment*, edited by E. Merian, pp. 257-286, VCH Publishers, 1991.

Rojas, C. R., R. E. Van Grieken, and R. Laane, Comparison of three dry deposition models applied to field measurements in the southern bight of the North Sea, *Atmos. Environ.*, *27A* (3), 363-370, 1993.

Savoie, D. L., J. M. Prospero, and R. T. Nees, Nitrate, non-sea-salt sulfate, and mineral aerosol over the Northwestern Indian Ocean, *J. Geophys. Res.*, *92* (D1), 933-942, 1987.

Schlesinger, W. H., and A. E. Hartley, A global budget for atmospheric NH_3, *Biogeochemistry*, *15* (3), 191-211, 1992.

Schroeder, W. H., M. Dobson, D. M. Kane, and N. D. Johnson, Toxic trace elements associated with airborne particulate matter: A review, *J. Air Pollut. Control Assoc.*, *37* (11), 1267-1285, 1987.

Sedlak, D. L., and J. Hoigné, The role of copper and oxalate in the redox cycling of iron in atmospheric waters, *Atmos. Environ.*, *27*, 2173-2185, 1993.

Sedlak, D. L., and J. Hoigné, Oxidation of S(IV) in atmospheric water by photooxidants and iron in the presence of copper, *Environ. Sci. & Technol.*, *28*, 1898-1906, 1994.

Seigneur, C., and E. Constantinou, Chemical kinetic mechanism for atmospheric chromium, *Environ. Sci. Technol.*, *29*, 222-231, 1995.

Seinfeld, J. H., *Atmospheric Chemistry and Physics of Air Pollution*, 738 pp., Wiley, New York, 1986.

Siefert, R. L., S. O. Pehkonen, Y. Erel, and M. R. Hoffmann, Iron photochemistry of aqueous suspensions of ambient aerosol with added organic acids, *Geochim. et Cosmochim. Acta*, *58* (15), 3271-3279, 1994.

Siefert, R. L., S. M. Webb, and M. R. Hoffmann, Determination of photochemically available iron in ambient aerosol, *J. Geophys. Res.*, *101*, 14441-14449, 1996.

Solomon, P. A., J. L. Moyers, and R. A. Fletcher, High-volume dichotomous virtual impactor for the fractionation and collection of particles according to aerodynamic size, *Aerosol Sci. & Technol.*, *2*, 455-464, 1983.

Spokes, L. J., T. D. Jickells, and B. Lim, Solubilisation of aerosol trace metals by cloud processing: A laboratory study, *Geochim. et Cosmochim. Acta*, *58* (15), 3281-3287, 1994.

Stookey, L. L., Ferrozine- a new spectrophotometric reagent for iron, *Anal. Chem.*, *42* (7), 119-781, 1970.

Taylor, S. R., and S. M. McLennan, *The continental crust: its composition and evolution*, 9-52 pp., Blackwell Scientific Publications, London, 1985.

Turekian, K. K., and K. H. Wedepohl, Distribution of the elements in some major units of the Earth's crust, *Geol. Soc. Am. Bull.*, *72*, 175-192, 1961.

Vinogradov, A. P., Average contents of chemical elements in the principal types of igneous rocks of the Earth's crust, *Geochemistry*, *7*, 641-664, 1962.

Waldman, J. M., J. W. Munger, D. J. Jacob, R. C. Flagan, J. J. Morgan, and M. R. Hoffmann, The chemical composition of acid fog, *Science*, *218* (4573), 677-680, 1982.

Wells, M. L., N. M. Price, and K. W. Bruland, Iron limitation and the cyanobacterium synechococcus in equatorial pacific waters, *Limnol. Ocean.*, *39* (6), 1481-1486, 1994.

Wells, M. L., N. M. Price, and K. W. Bruland, Iron chemistry in seawater and its relationship to phytoplankton: a workshop report, *Marine Chem.*, *48*, 157-182, 1995.

Weschler, C. J., M. L. Mandich, and T. E. Graedel, Speciation, photosensitivity, and reactions of transition metal ions in atmospheric droplets, *J. Geophys. Res.*, *91*, 5189-5204, 1986.

Xue, H. B., M. D. S. Goncalves, M. Reutlinger, L. Sigg, and W. Stumm, Copper(I) in fogwater: determination and interactions with sulfite, *Environ. Sci. & Technol.*, *25* (10), 1716-1722, 1991.

Zhu, X. R., J. M. Prospero, D. L. Savoie, F. J. Millero, R. G. Zika, and E. S. Saltzman, Photoreduction of iron(III) in marine mineral aerosol solutions, *J. Geophys. Res. A.*, *98* (ND5), 9039-9046, 1993.

Zhuang, G., Z. Yi, R. A. Duce, and P. R. Brown, The chemistry of iron in marine aerosols, *Global Biogeochem. Cycles*, *7* (3), 711, 1992a.

Zhuang, G., Z. Yi, R. A. Duce, and P. R. Brown, Link between iron and sulfur cycles suggested by detection of Fe(II) in remote marine aerosols, *Nature*, *355* (6360), 537-539, 1992b.

Zoller, W. H., R. A. Gordon, and R. A. Duce, Atmospheric concentrations and sources of trace metals at the South Pole, *Science*, *183*, 198-200, 1974.

Zuo, Y., and J. Hoigné, Formation of hydrogen peroxide and depletion of oxalic acid in atmospheric water by photolysis of iron(III)-oxalato compounds, *Environ. Sci. Technol.*, *26* (5), 1014-1022, 1992.

Zuo, Y. G., and J. Hoigné, Photochemical decomposition of oxalic, glyoxalic and pyruvic-acid catalyzed by iron in atmospheric waters., *Atmos. Environ.*, *28* (7), 1231-1239, 1994.

2.7 Figure Captions

Figure 1. Five day air-mass back trajectories for four different elevations (based on pressure) above sea level for: a) May 13, 1995, 18:00 UTC, b) May 31, 1995, 18:00 UTC, c) July 23, 1995, 18:00 UTC and d) August 5, 1995, 18:00 UTC.

Figure 2. Total Suspended Particulates (TSP) over the Arabian Sea during the inter- and southwest monsoons.

Figure 3. Concentration plots for (a) Al (m/z = 27), (b) Fe (m/z = 57), (c) Na (m/z = 23), (d) Mn (m/z = 55), (e) V (m/z = 51), (f) Pb (m/z = 208), (g) Cr (m/z = 53), (h) Mo (m/z = 95), and (I) Cu (m/z = 65). Represented are both coarse and fine fractions. Left-hand side of the dividing line indicates inter-monsoon while the right-hand side represents the southwest monsoon.

Figure 4. Labile Fe(II) concentrations for the fine, coarse and total aerosol fractions during the inter-monsoon (no data for the southwest monsoon is presented since all the measurements were below the detection limit).

Figure 5. Percentage of $Fe(II)_{total,labile}$ to Fe_{total} for the fine, coarse and total aerosol fractions during the inter-monsoon (no data for the southwest monsoon is presented since all the measurements were below the detection limit).

Figure 6. Factor score plots for the first seven principal components shown in Table 6.

Table 1. Sequential extraction procedure for measuring labile fractions of ferrous iron (Fe(II)) collected on the coarse and fine HVDVI filters.

Step	Description
1	cut a 47 mm diameter piece of the 90 mm filter using a ceramic knife and a polycarbonate die
2	place filter cut in a Teflon jar
3	"wet" the filter cut by adding approximately 0.1 ml (in 0.01 ml increments) of ethanol
4	add 20 ml of formate buffer solution (pH = 4.2, $[formate]_{total}$ = 500 μM) to the jar
5	place Teflon grid on top of filter to keep it submerged, and gently swirl solution periodically
6	after 30 minutes remove 5 ml aliquot and filter (using a 0.2 μm cellulose acetate syringe filter)
7	place filtered aliquot in spectrophotometric cell (5 cm path length, semi-low volume)
8	measure absorbance, ABS(background)
9	add 0.1 ml of ferrozine solution ([ferrozine] = 6.1 mM) to spectrophotometeric cell and mix
10	measure absorbance, ABS(extraction #1): $Fe(II)_{aq,labile}$
11	rinse spectrophotometer cell
12	add 0.3 ml of ferrozine soloution to remaining 15 ml of solution in jar and gently swirl solution
13	after 5 minutes remove 5 ml aliquot and filter (using a 0.2 μm cellulose acetate syringe filter)
14	place filtered aliquot in spectrophotometric cell
15	measure absorbance, ABS(extraction #2): $Fe(II)_{FZ,5min,labile}$
16	rinse spectrophotometer cell
17	let extraction solution stand overnight (periodically swirling solution)
18	measure absorbance, ABS(extraction #3): $Fe(II)_{FZ,22hr,labile}$

Table 2. Strong acid digestion method for HVDVI.

Step	Description
1	cut a piece from the 90 mm filter using a ceramic knife and a polycarbonate die
2	place filter cut in 10 ml Teflon vial
3	add 1 g concentrated HNO_3 and 1 g concentrated HF to the vial
4	place Teflon grid on top of filter to keep it submerged, and cap vial
5	place vial on shaker table, and set temperature to 50 °C
6	shake vial at 50 °C overnight (> 12 hours)
7	remove filter cut and Teflon grid from vial
8	rinse filter cut and grid with ~ 1 g H_20, with rinse solution falling into vial
9	evaporate solution in vial to dryness (purging vial with N_2 gas)
10	add 0.5 g HNO_3 to vial and shake for 1/2 hour
11	add 9.5 g H_2O to vial
12	analyze solution using ICP-MS

Table 3. Aerosol sample collection times and positions.

Label	Start Date/Time UTC	Stop Date/Time UTC	Latitude ° North	Longitude ° East
M32/3_01	05/09/95 09:16	05/09/95 17:26	16.3	65.0
M32/3_02	05/09/95 17:50	05/10/95 04:15	16.7	65.0
M32/3_03	05/10/95 06:40	05/10/95 12:00	18.0	65.0
M32/3_04	05/10/95 13:00	05/11/95 02:21	18.0	65.0
M32/3_05	05/11/95 02:40	05/11/95 07:15	18.0	65.0
M32/3_06	05/11/95 14:10	05/11/95 23:30	18.1	65.0
M32/3_07	05/12/95 04:15	05/12/95 22:30	18.1	65.0
M32/3_08	05/13/95 04:30	05/13/95 22:00	18.1	65.0
M32/3_09	05/14/95 03:10	05/14/95 22:15	18.1	65.0
M32/3_10	05/15/95 03:20	05/15/95 22:30	18.1	65.0
M32/3_11	05/16/95 03:15	05/16/95 16:55	18.1	65.0
M32/3_12	05/17/95 03:21	05/18/95 03:10	18.1	65.0
M32/3_13	05/18/95 03:35	05/19/95 03:05	16.9	65.0
M32/3_14	05/19/95 03:20	05/20/95 03:15	14.3	65.0
M32/3_15	05/20/95 03:35	05/21/95 03:10	11.5	65.0
M32/3_16	05/21/95 03:35	05/22/95 03:10	10.0	65.0
M32/3_17	05/22/95 03:20	05/23/95 03:15	10.0	65.0
M32/3_18	05/23/95 03:30	05/24/95 03:15	10.0	65.0
M32/3_19	05/24/95 03:25	05/25/95 03:15	10.0	65.0
M32/3_20	05/25/95 03:30	05/26/95 03:25	10.0	65.0
M32/3_21	05/26/95 03:35	05/27/95 03:15	9.9	65.0
M32/3_22	05/27/95 03:35	05/28/95 03:20	9.5	65.0
M32/3_23	05/28/95 03:35	05/29/95 03:15	7.5	65.0
M32/3_24	05/29/95 03:30	05/30/95 03:20	4.5	65.0
M32/3_25	05/30/95 04:00	05/30/95 21:00	3.0	65.0
M32/3_26	05/31/95 03:40	06/01/95 03:00	2.9	65.0
M32/3_27	06/01/95 07:25	06/01/95 21:55	1.4	65.0
M32/3_28	06/02/95 04:55	06/02/95 11:55	0.0	65.0
M32/5_01	07/16/95 09:10	07/17/95 10:19	0.0	65.0
M32/5_02	07/18/95 04:46	07/20/95 10:25	1.5	65.0
M32/5_03	07/20/95 10:43	07/21/95 04:02	3.1	65.0
M32/5_04	07/21/95 11:37	07/22/95 14:15	6.0	65.0
M32/5_05	07/24/95 01:02	07/25/95 02:40	10.0	65.0
M32/5_06	07/26/95 04:09	07/26/95 13:15	13.0	65.0
M32/5_07	07/26/95 23:57	07/28/95 11:15	14.5	64.7
M32/5_08	07/28/95 11:47	07/30/95 00:21	15.2	63.5
M32/5_09	07/30/95 00:33	07/31/95 04:05	16.1	62.0
M32/5_10	07/31/95 04:23	08/01/95 04:12	16.7	60.7
M32/5_11	08/01/95 04:30	08/02/95 03:14	17.1	59.8
M32/5_12	08/02/95 03:30	08/03/95 04:02	17.6	58.7
M32/5_13	08/03/95 04:27	08/04/95 05:15	18.4	57.5
M32/5_14	08/04/95 05:31	08/05/95 03:09	18.6	57.2
M32/5_15	08/05/95 03:22	08/06/95 13:57	18.4	57.3
M32/5_16	08/06/95 14:11	08/07/95 13:00	18.0	58.5
M32/5_17	08/07/95 13:52	08/08/95 10:09	17.4	59.6
M32/5_18	08/08/95 10:20	08/09/95 14:07	16.4	61.0
M32/5_19	08/09/95 23:29	08/11/95 03:41	16.2	61.5
M32/5_20	08/11/95 03:54	08/11/95 23:56	16.0	62.0

Table 4. Enrichment factors for a series of elements based on their total concentration. Inter (M323) and southwest (M325) -monsoon samples. (BDL = below detection limit)

Sample	EF(Sc)	EF(Ti)	EF(V)	EF(Cr)	EF(Mn)	EF(Fe)	EF(Cu)	EF(Zn)	EF(Mo)	EF(Sb)	EF(Cs)	EF(Ba)	EF(La)	EF(Ce)
M323-01	1.1	1.5	1.7	5.5	0.9	0.8	8.6	21.3	134.9	200.0	6.2	1.8	2.4	2.6
M323-02	BDL	1.0	1.4	5.8	0.5	BDL	8.1	19.8	99.7	149.1	8.6	1.7	2.5	3.1
M323-03	2.9	3.9	2.6	79.4	0.8	BDL	12.3	88.3	272.7	153.2	BDL	1.6	2.2	2.5
M323-04	0.5	0.9	1.0	1.3	3.8	8.5	13.2	11.8	BDL	60.2	6.0	2.0	2.3	2.8
M323-05	0.7	1.0	1.2	3.0	3.3	7.0	46.4	8.5	125.6	147.6	6.9	2.1	2.1	2.7
M323-06	0.6	1.0	0.9	3.1	9.4	19.6	82.3	5.3	BDL	93.3	4.4	2.0	1.6	2.0
M323-07	5.2	0.9	1.1	1.8	3.3	6.3	105.9	5.9	30.3	49.4	5.7	1.9	2.5	2.7
M323-08	0.6	0.9	0.9	1.3	1.5	2.4	10.9	4.4	13.4	29.9	5.6	1.9	2.2	2.4
M323-09	0.7	1.0	0.9	1.5	2.5	4.5	58.7	5.7	12.5	39.7	5.6	1.9	2.4	2.6
M323-10	0.6	1.0	0.9	2.0	1.6	2.4	8.7	4.2	19.7	27.4	5.8	1.9	1.8	2.1
M323-11	0.6	0.9	0.9	1.6	2.6	4.8	28.8	4.0	28.0	38.2	5.5	1.8	1.7	1.9
M323-12	0.6	1.1	0.9	1.3	1.9	3.0	119.8	7.8	24.2	33.8	5.6	2.0	2.3	2.6
M323-13	0.6	1.0	0.9	1.3	1.3	2.3	5.7	4.3	16.0	29.0	5.0	2.0	1.8	2.1
M323-14	0.8	1.4	1.1	1.6	1.3	1.7	6.9	3.8	BDL	24.0	5.8	2.6	1.3	1.7
M323-15	0.7	1.1	1.1	1.3	1.1	1.4	51.8	3.3	BDL	20.9	4.8	2.1	2.5	2.7
M323-16	0.7	1.1	0.9	1.3	0.9	1.2	6.6	3.5	BDL	20.4	5.0	2.1	2.1	2.4
M323-17	0.7	1.1	0.9	1.4	1.1	1.4	4.0	3.1	BDL	23.2	4.9	2.1	2.6	2.7
M323-18	0.7	1.1	1.4	1.7	0.7	0.9	3.8	4.2	BDL	22.0	5.2	2.1	2.0	2.6
M323-19	0.9	1.1	1.0	2.2	0.8	0.6	10.1	4.6	BDL	24.6	9.0	2.2	2.1	2.5
M323-20	1.1	1.3	1.4	2.4	0.6	0.8	3.4	6.1	57.1	38.7	6.2	2.1	2.3	2.5
M323-21	1.0	1.3	1.0	1.1	1.0	0.9	3.9	2.7	BDL	13.7	12.2	2.7	1.1	1.6
M323-22	0.7	1.0	1.0	1.3	0.7	0.7	1.8	3.6	BDL	39.1	9.6	2.1	2.0	2.3
M323-23	1.1	1.1	1.1	1.3	0.9	0.8	3.2	2.9	BDL	29.8	11.4	2.3	1.1	1.7
M323-24	BDL	1.0	1.0	10.5	BDL	BDL	9.7	5.8	BDL	BDL	BDL	1.5	1.8	2.0
M323-25	BDL	BDL	BDL	BDL	BDL	BDL	BDL	BDL	BDL	BDL	BDL	BDL	BDL	BDL
M323-26	BDL	BDL	BDL	BDL	BDL	BDL	BDL	BDL	BDL	BDL	BDL	BDL	BDL	BDL
M323-27	BDL	BDL	BDL	BDL	BDL	BDL	BDL	BDL	BDL	BDL	BDL	BDL	BDL	BDL
M323-28	40.5	9.1	BDL	190.3	BDL	2.3	271.4	160.9	6567.1	BDL	BDL	2.7	5.6	8.7
M325-01	BDL	14.9	BDL	103.0	BDL	0.9	95.4	51.5	761.5	BDL	BDL	1.7	1.3	1.8
M325-02	0.6	1.1	BDL	BDL	0.8	0.9	9.2	20.5	BDL	BDL	BDL	2.0	2.1	3.0
M325-03	1.1	1.4	BDL	BDL	0.9	1.0	21.6	11.9	BDL	BDL	BDL	1.9	2.4	2.7
M325-04	1.6	1.8	6.2	BDL	0.7	1.2	28.1	39.1	BDL	BDL	BDL	2.0	3.4	49.7
M325-05	3.1	1.2	2.2	BDL	0.7	0.8	16.0	6.1	BDL	BDL	BDL	1.7	2.1	2.5
M325-06	7.5	1.1	4.5	BDL	0.5	0.9	30.6	17.8	BDL	BDL	BDL	1.5	1.9	2.0
M325-07	9.1	1.5	3.7	19.2	0.5	1.0	33.5	17.2	346.3	BDL	BDL	1.6	1.7	2.1
M325-08	1.9	1.0	3.2	BDL	0.6	0.7	13.4	5.7	41.7	BDL	BDL	1.4	1.6	2.1
M325-09	0.8	1.3	2.3	9.0	0.7	0.9	11.5	6.5	BDL	BDL	BDL	1.2	1.9	2.6
M325-10	1.9	1.0	1.1	20.7	0.8	1.0	13.0	8.4	416.1	BDL	BDL	1.2	2.3	2.4
M325-11	2.0	1.1	1.3	BDL	0.8	0.9	9.2	4.1	BDL	BDL	BDL	1.3	2.2	2.7
M325-12	1.3	1.0	1.3	BDL	0.7	0.8	9.4	5.1	BDL	BDL	BDL	1.1	2.0	2.4
M325-13	3.9	1.0	3.0	BDL	0.7	0.8	12.0	5.3	BDL	BDL	BDL	1.2	1.8	2.2
M325-14	4.1	1.2	4.4	BDL	0.7	0.8	26.0	9.5	BDL	BDL	BDL	1.2	1.9	2.4
M325-15	3.5	1.1	4.5	2.8	0.7	0.8	17.3	6.1	50.1	BDL	3.8	1.4	2.3	2.7
M325-16	13.0	1.5	2.5	BDL	0.7	0.8	25.7	12.4	107.0	BDL	BDL	1.2	1.9	2.1
M325-17	9.2	1.4	2.9	BDL	0.6	0.8	31.2	21.9	BDL	BDL	BDL	1.2	1.7	1.9
M325-18	2.1	1.3	1.7	6.3	0.7	0.9	13.9	9.5	BDL	BDL	BDL	1.3	3.2	4.2
M325-19	0.8	1.2	1.0	BDL	0.7	0.8	7.6	3.9	BDL	BDL	3.6	1.3	1.9	2.3
M325-20	1.1	1.3	1.7	5.8	0.8	0.9	10.2	5.3	60.7	BDL	4.6	1.5	2.2	2.6

Table 5. Elemental abundances in ultramafic rock and crustal average.

Element (ppm unless otherwise noted)	Ultramafic[a]	Crustal average[b]	EF of ultramafic rock compared to crustal average
Mg (%)	23.2	3.2	50.8
Al (%)	1.2	8.4	1.0
Si (%)	19.8	26.8	5.17
K (%)	0.017	0.9	0.13
Sc	10	30	2.3
Ti	300	5300	0.4
V	40	230	1.2
Cr	**1800**	**185**	**68.1**
Mn	**1560**	**1400**	**7.80**
Fe (%)	**9.64**	**7.06**	**9.56**
Co	175	29	42
Ni	**2000**	**105**	**133**
Cu	15	75	1.4
Zn	40	80	3.5
Sr	5.5	260	0.1
Mo	0.3	1	2.1
Sn	0.5	2.5	1.4
La	1.3	16	0.6
Ce	3.5	33	0.7
Pb	0.5	8	0.4
Th	0.0045	3.5	0.0090

[a][*Faure*, 1991; *Turekian and Wedepohl*, 1961; *Vinogradov*, 1962]
[b][*Taylor and McLennan*, 1985]

Table 6. Principal components extracted from inter-monsoon and southwest monsoon data.

Component	1	2	3	4	5	6	7
Variable	Crustal Coarse	Crustal Fine	Sea Salt	Ga Zn Fl NH_4^+	Fe Mn Coarse	Cu Fe Mn Fine	Other
AL27_C	**0.92**	0.28	0.00	0.04	0.17	0.14	0.03
AL27_F	0.27	**0.92**	-0.20	0.05	0.08	0.12	0.03
BA137_C	**0.94**	0.24	-0.05	0.05	0.15	0.12	0.02
BA137_F	0.17	**0.91**	-0.26	0.01	0.04	0.11	0.01
CA44_C	**0.90**	0.14	0.13	0.03	0.25	0.24	0.07
CA44_F	0.23	**0.89**	0.00	-0.11	0.13	0.04	-0.15
CE140_C	**0.94**	0.26	-0.06	0.02	-0.01	0.11	-0.02
CE140_F	0.44	**0.76**	-0.19	0.10	0.13	0.18	0.07
CU65_C	**0.57**	0.20	-0.01	-0.05	0.33	-0.13	0.49
CU65_F	0.27	0.05	0.07	0.04	0.12	**0.78**	-0.17
EU153_C	**0.94**	0.15	-0.06	0.08	0.04	0.11	0.00
EU153_F	**0.52**	**0.68**	-0.14	-0.01	0.09	0.12	0.03
FE57_C	0.41	0.14	-0.02	0.09	**0.84**	0.16	0.03
FE57_F	0.28	0.23	-0.03	0.12	**0.53**	**0.71**	-0.07
GA69_C	-0.02	-0.12	-0.12	**0.88**	0.22	-0.10	-0.03
GA69_F	-0.03	-0.14	-0.14	**0.87**	0.22	0.10	0.00
K39_C	**0.83**	0.02	0.44	0.00	0.10	0.10	-0.01
K39_F	-0.03	**0.84**	0.30	-0.08	0.02	0.14	-0.01
LA139_C	**0.94**	0.27	-0.05	0.04	-0.02	0.09	0.00
LA139_F	**0.52**	**0.74**	-0.15	0.13	0.16	0.20	0.07
MG26_C	**0.75**	0.00	**0.51**	0.14	0.20	0.16	0.10
MG26_F	0.11	**0.67**	**0.62**	-0.20	0.16	0.05	-0.01
MN55_C	**0.52**	0.14	0.00	0.07	**0.78**	0.16	0.02
MN55_F	0.30	0.45	-0.06	0.12	0.46	**0.68**	-0.02
NA23_C	0.34	-0.24	**0.73**	0.13	0.03	0.07	0.06
NA23_F	-0.19	-0.02	**0.84**	-0.26	-0.01	-0.03	0.01
PB208_C	0.32	**0.66**	-0.27	0.01	-0.07	-0.11	-0.42
PB208_F	**0.59**	0.36	0.00	0.45	0.14	0.33	0.17
SC45_C	**0.84**	0.10	-0.03	0.12	0.25	-0.07	-0.04
SC45_F	-0.03	0.31	-0.06	0.15	-0.17	**0.79**	0.18
TH232_C	**0.93**	0.27	-0.07	0.10	-0.03	0.11	-0.03
TI47_C	**0.95**	0.23	-0.05	0.01	0.12	0.10	0.03
TI47_F	0.11	**0.80**	-0.14	0.43	-0.06	0.08	0.15
V51_F	0.32	**0.76**	-0.08	0.36	0.02	0.17	0.31
ZN66_C	**0.81**	0.35	-0.15	0.11	0.19	-0.10	-0.16
ZN66_F	0.04	0.20	0.14	**0.80**	-0.13	0.14	0.26
Wind Speed	-0.23	-0.21	**0.78**	-0.03	0.25	0.04	0.06
ACETATE	**0.71**	0.05	-0.08	0.02	0.08	-0.21	0.49
CHLORIDE	-0.12	-0.15	**0.94**	-0.19	-0.02	-0.10	-0.02
FLUORIDE	0.41	0.18	-0.04	**0.74**	-0.13	-0.08	-0.25
FORMATE	0.11	0.08	0.49	0.23	**0.73**	-0.04	0.10
MSA	-0.05	-0.15	**0.81**	0.04	-0.05	-0.04	0.27
NITRATE	**0.53**	**0.64**	-0.22	0.24	0.02	0.04	-0.02
OXALATE	**0.50**	0.39	**0.57**	0.24	0.13	0.13	-0.10
SULFATE	0.48	0.41	**0.66**	0.18	-0.13	0.02	0.03
Ca^{2+}	**0.65**	**0.59**	0.15	-0.02	0.13	0.10	-0.09
K^+	0.11	0.05	**0.85**	0.10	0.06	0.04	-0.09
Mg^{2+}	0.00	-0.08	**0.95**	-0.08	-0.02	0.00	-0.11
Na^+	-0.12	-0.17	**0.94**	-0.16	-0.05	-0.06	-0.07
NH_4^+	0.11	0.18	-0.05	**0.76**	0.06	0.18	-0.05

Table 7. Factor analysis statistics for data presented in Table 6.

Factor	Eigenvalue	% of Variance	Cumulative %
1	14.2	28.4	28.4
2	9.4	18.8	47.2
3	8.3	16.7	63.9
4	4.4	8.8	72.7
5	3.2	6.3	79.0
6	2.9	5.8	84.8
7	1.2	2.4	87.3

Table 8. Sector sampling system operation.

Sample	Time Out of Sector (minutes)	% Time Out of Sector	Ship Plume Passed Over Samplers
M323-1	0	0.0%	NO
M323-2	0	0.0%	NO
M323-3	0	0.0%	NO
M323-4	30	3.7%	YES
M323-5	20	2.9%	YES
M323-6	10	1.8%	YES
M323-7	0	0.0%	NO
M323-8	0	0.0%	NO
M323-9	30	2.5%	YES
M323-10	0	0.0%	NO
M323-11	60	7.3%	YES
M323-12	10	0.7%	YES
M323-13	*sector sampler system now in operation (M323: ± 90°, M325: ± 60°)*		

Figure 1

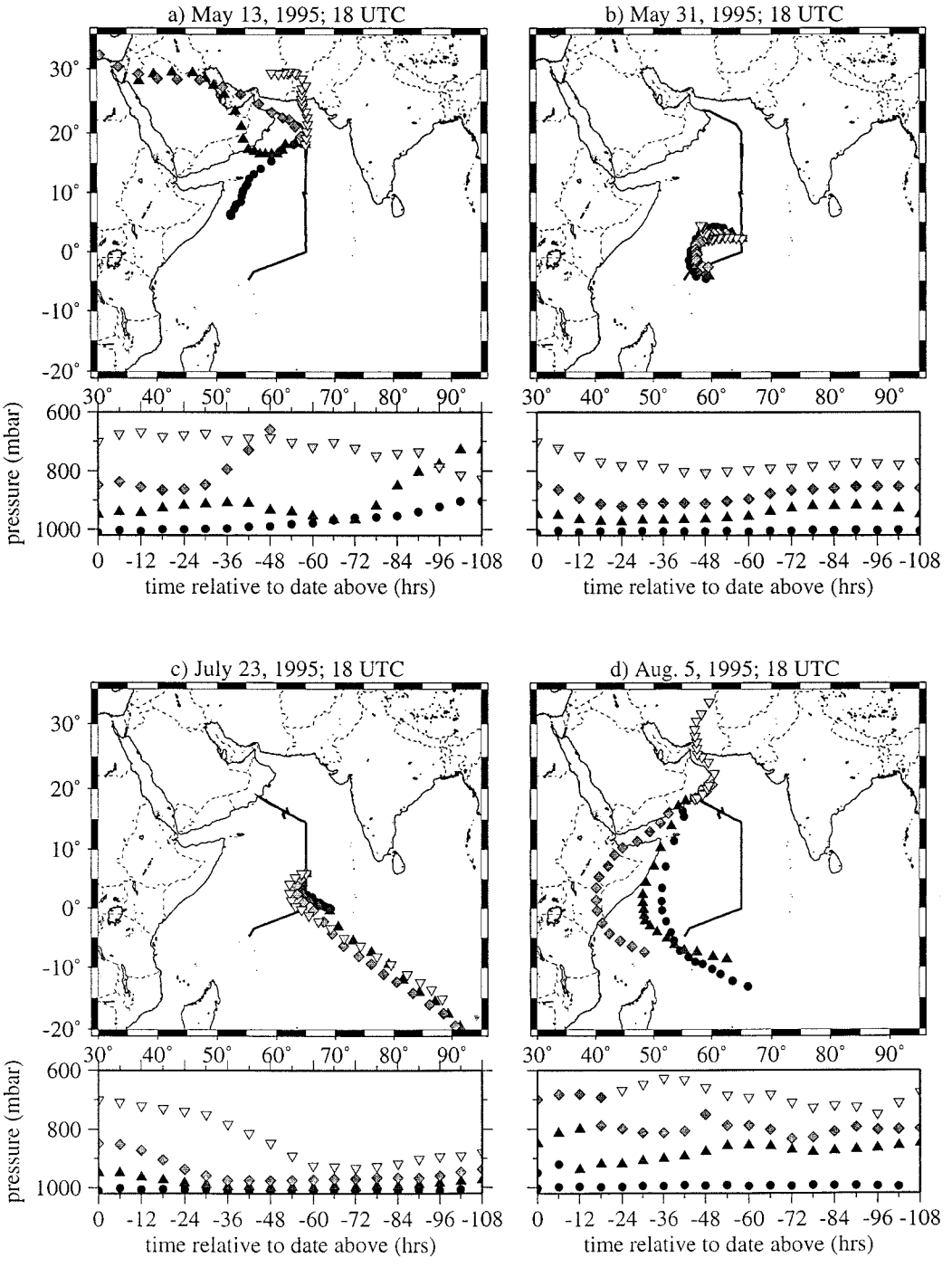
a) May 13, 1995; 18 UTC
b) May 31, 1995; 18 UTC
c) July 23, 1995; 18 UTC
d) Aug. 5, 1995; 18 UTC
30°
20°
10°
0°
-10°
-20°
30° 40° 50° 60° 70° 80° 90°
pressure (mbar)
600
800
1000
0 -12 -24 -36 -48 -60 -72 -84 -96 -108
time relative to date above (hrs)

Figure 2

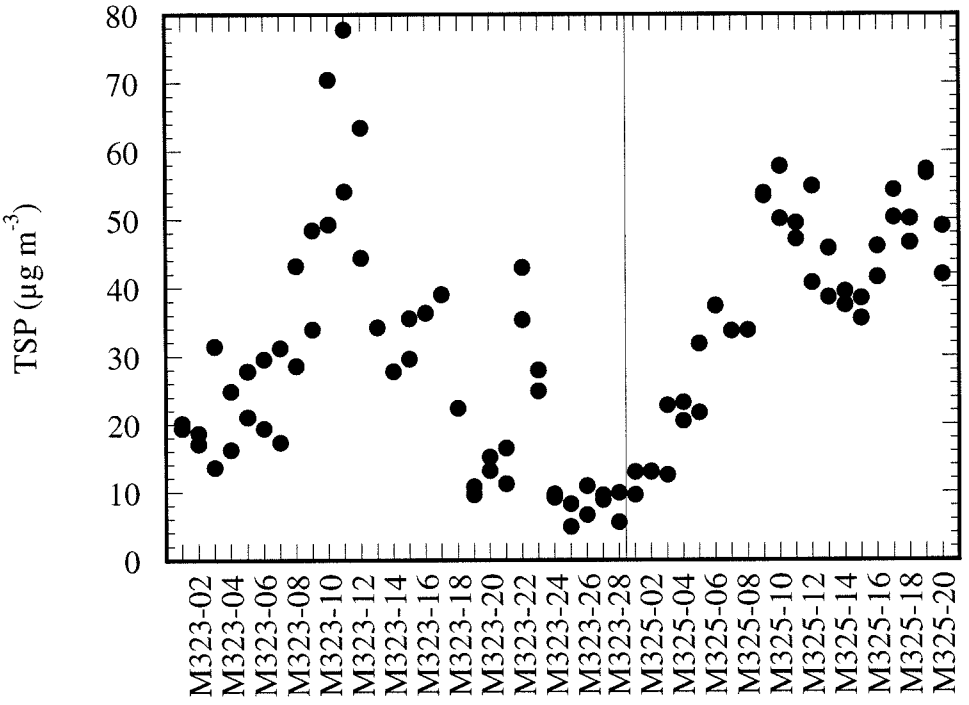
TSP (µg m-3)
80
70
60
50
40
30
20
10
0
M323-02
M323-04
M323-06
M323-08
M323-10
M323-12
M323-14
M323-16
M323-18
M323-20
M323-22
M323-24
M323-26
M323-28
M325-02
M325-04
M325-06
M325-08
M325-10
M325-12
M325-14
M325-16
M325-18
M325-20

Figure 3

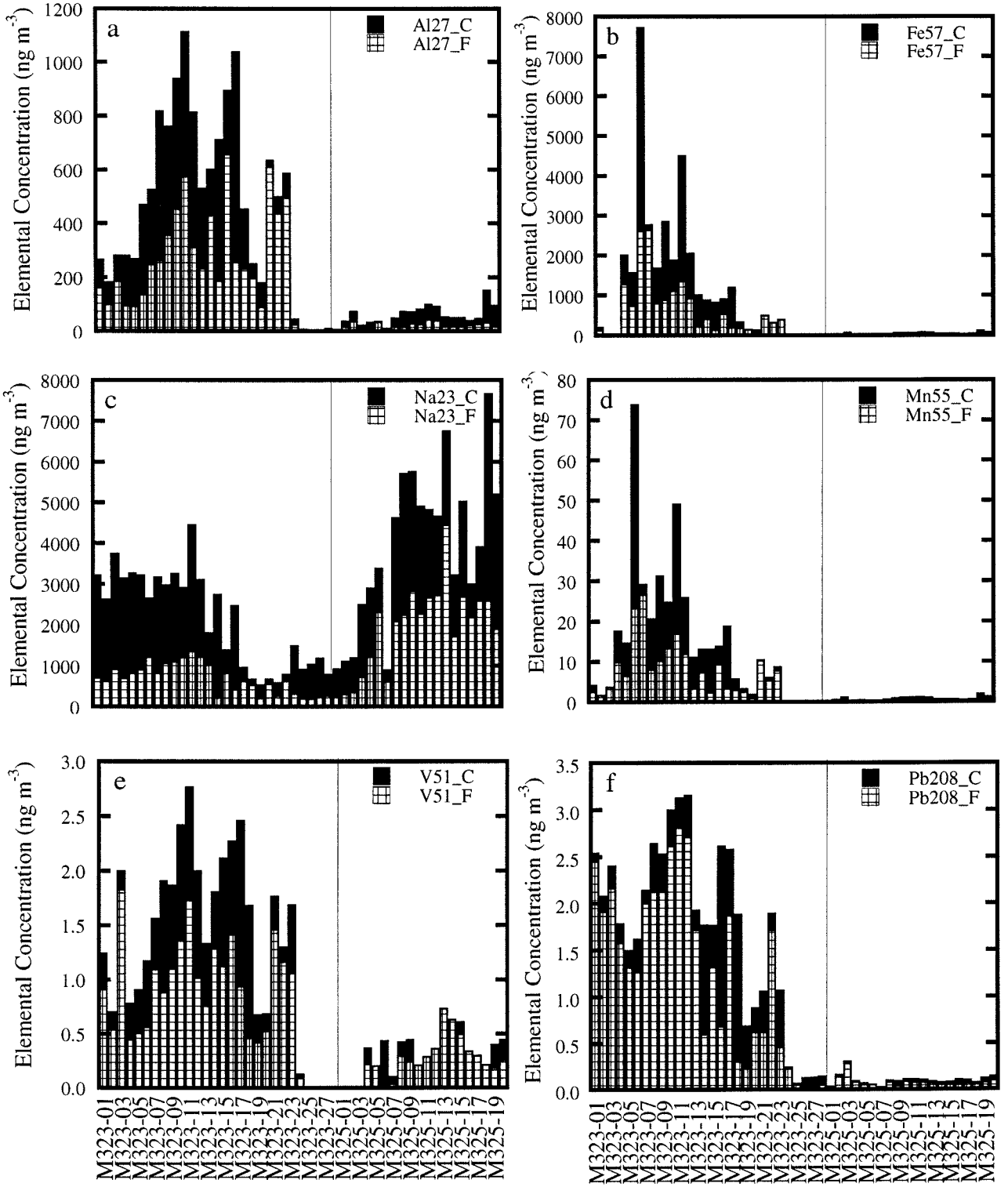
a
Al27_C
Al27_F
Elemental Concentration (ng m-3)
b
Fe57_C
Fe57_F
c
Na23_C
Na23_F
d
Mn55_C
Mn55_F
e
V51_C
V51_F
f
Pb208_C
Pb208_F
M323-01
M323-03
M323-05
M323-07
M323-09
M323-11
M323-13
M323-15
M323-17
M323-19
M323-21
M323-23
M323-25
M323-27
M325-01
M325-03
M325-05
M325-07
M325-09
M325-11
M325-13
M325-15
M325-17
M325-19

Figure 3 (continued)

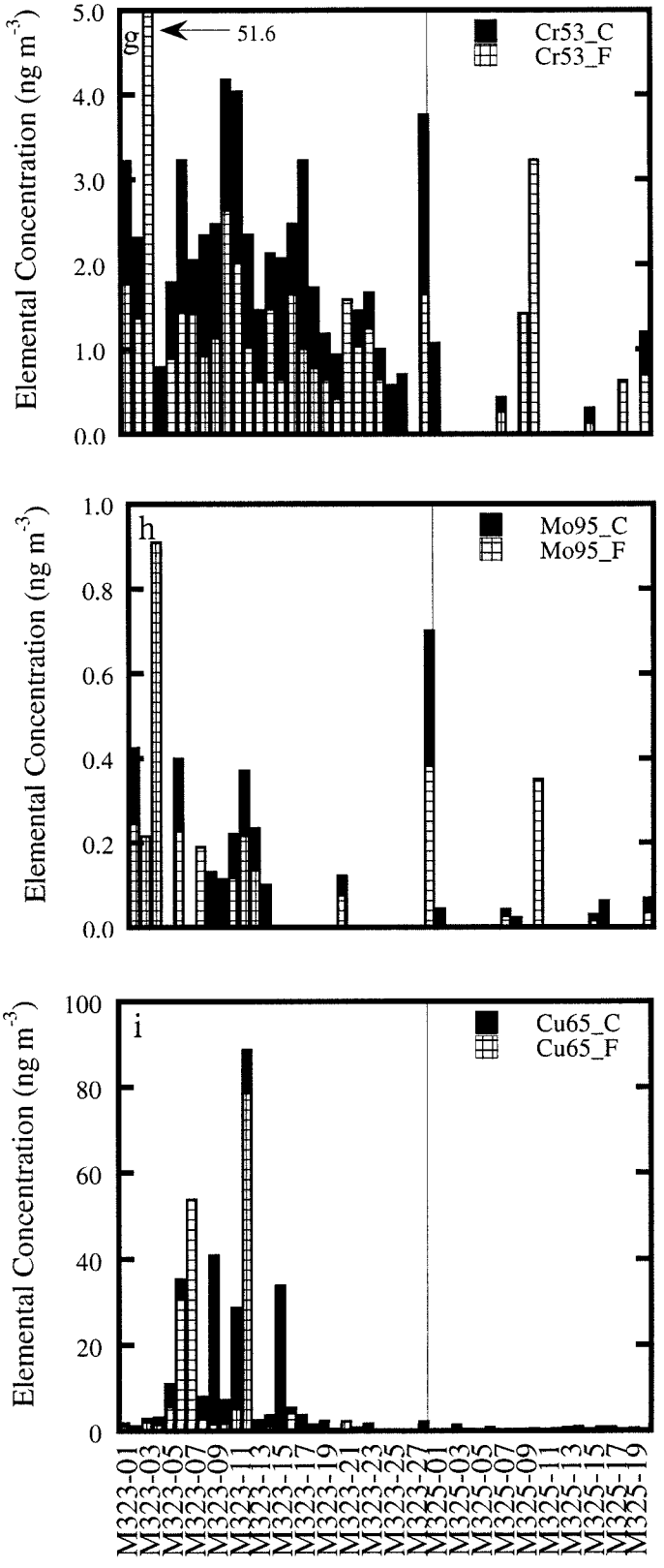

Figure 4

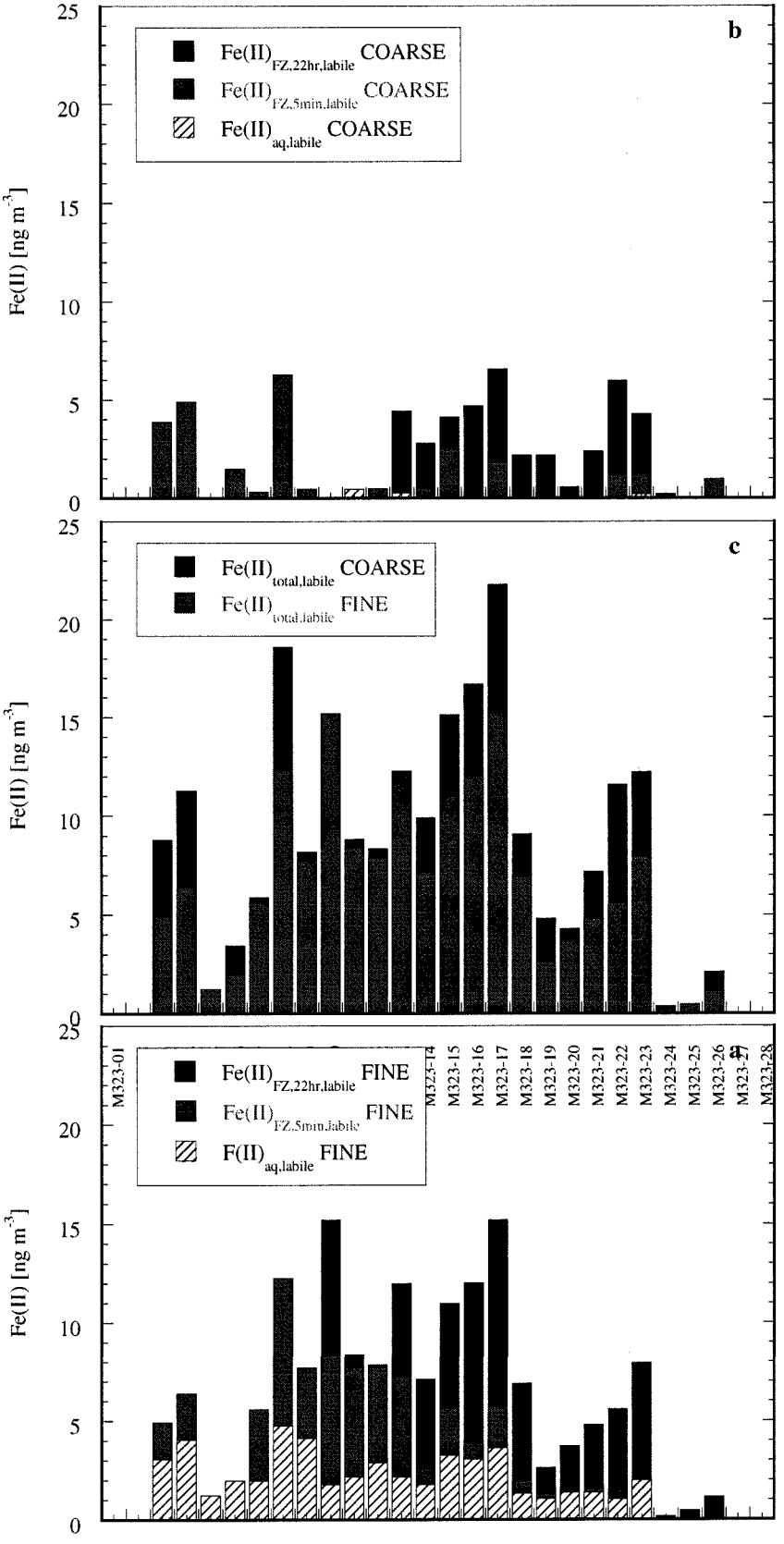
b
Fe(II)FZ,22hr,labile COARSE
Fe(II)FZ,5min,labile COARSE
Fe(II)aq,labile COARSE
Fe(II) [ng m-3]
c
Fe(II)total,labile COARSE
Fe(II)total,labile FINE
Fe(II) [ng m-3]
a
Fe(II)FZ,22hr,labile FINE
Fe(II)FZ,5min,labile FINE
F(II)aq,labile FINE
Fe(II) [ng m-3]
M323-01
M323-14
M323-15
M323-16
M323-17
M323-18
M323-19
M323-20
M323-21
M323-22
M323-23
M323-24
M323-25
M323-26
M323-27
M323-28

Figure 5

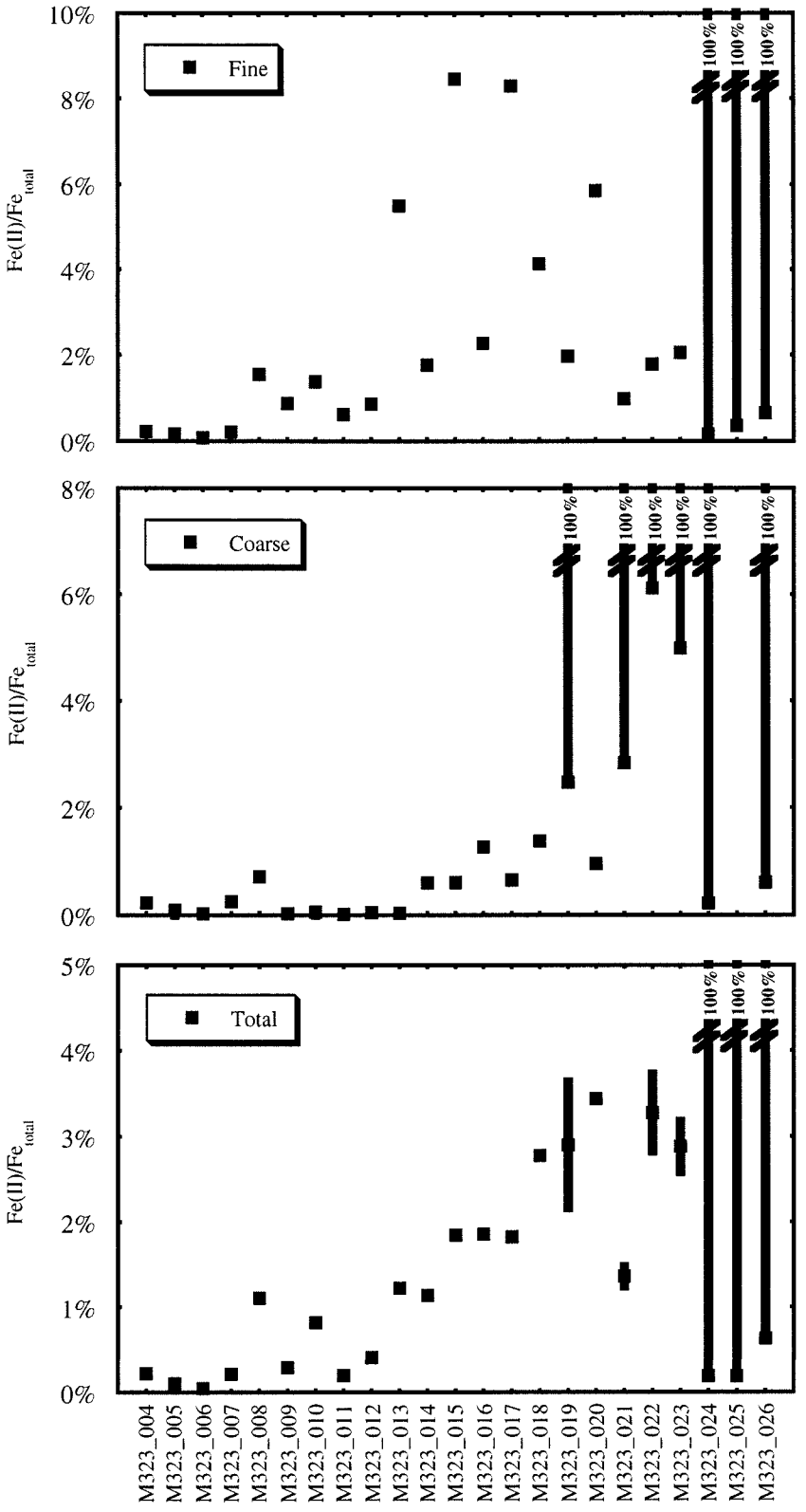
Fine
Coarse
Total
Fe(II)/Fe$_{total}$
10%
8%
6%
4%
2%
0%
5%
3%
1%
100%
M323_004
M323_005
M323_006
M323_007
M323_008
M323_009
M323_010
M323_011
M323_012
M323_013
M323_014
M323_015
M323_016
M323_017
M323_018
M323_019
M323_020
M323_021
M323_022
M323_023
M323_024
M323_025
M323_026

Figure 6

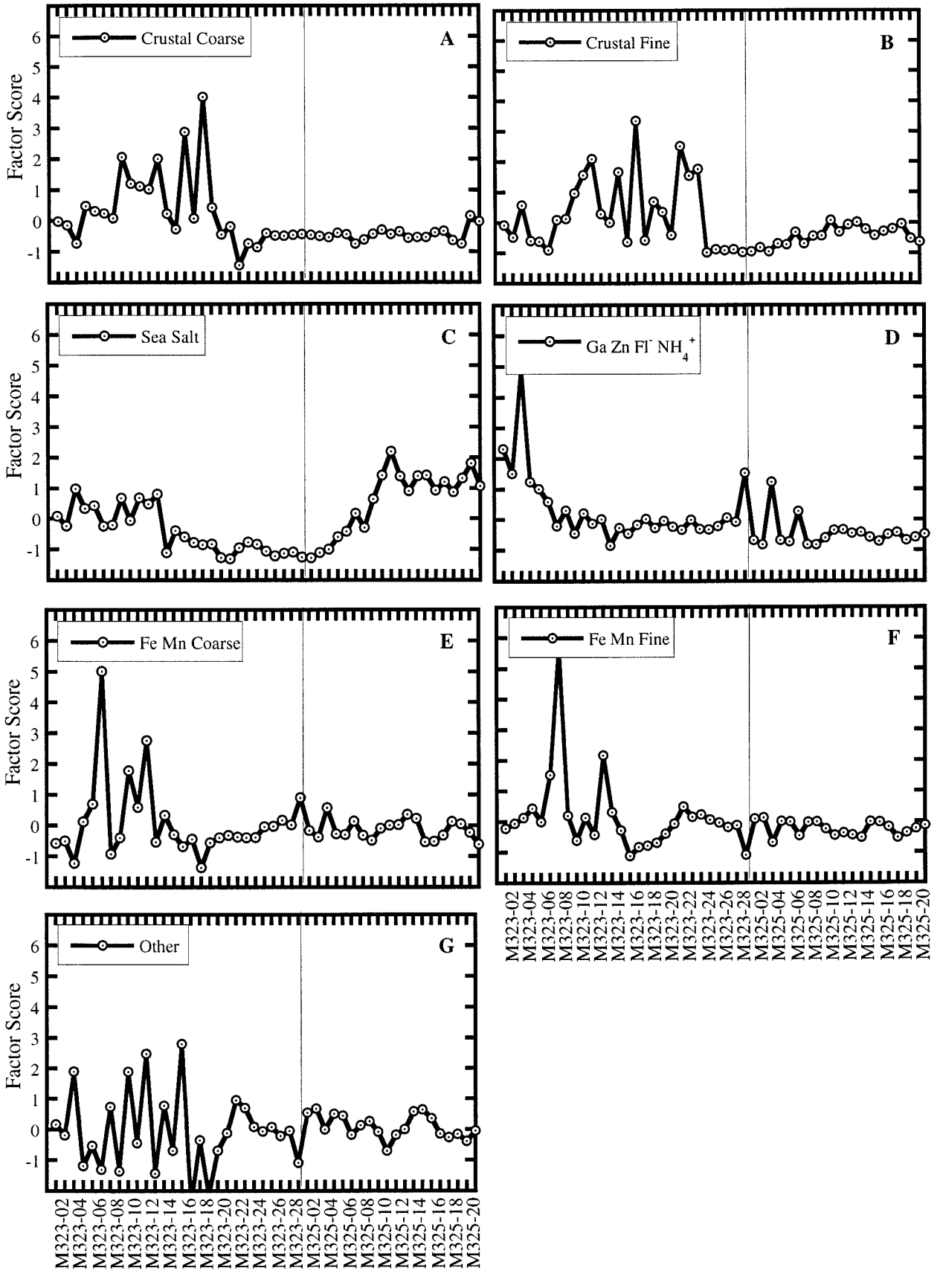
Crustal Coarse
A
Crustal Fine
B
Sea Salt
C
Ga Zn Fl⁻ NH4+
D
Fe Mn Coarse
E
Fe Mn Fine
F
Other
G
Factor Score
6
5
4
3
2
1
0
-1
M323-02
M323-04
M323-06
M323-08
M323-10
M323-12
M323-14
M323-16
M323-18
M323-20
M323-22
M323-24
M323-26
M323-28
M325-02
M325-04
M325-06
M325-08
M325-10
M325-12
M325-14
M325-16
M325-18
M325-20

Chapter 3

Chemical characterization of ambient aerosol collected during the southwest-monsoon and inter-monsoon seasons over the Arabian Sea: Anions and cations

[Anne M. Johansen, Ronald L. Siefert, and Michael R. Hoffmann, accepted to the *Journal of Geophysical Research* with minor revisions]

3.1 Abstract

Ambient aerosol samples were collected over the Northern Indian Ocean during two one-month-long research cruises (German R/V Meteor) that took place during the inter- (May) and SW-monsoon (July/August) of 1995. A high volume and two small volume collectors were used to collect samples, which were subsequently analyzed for ferrous iron, 32 elements, and anions and cations. The present paper focuses on the bulk aerosol material, the ions, while utilizing some of the trace metal data that was presented in more detail in our previous paper [*Siefert et al.*, 1999]. Data is analyzed and interpreted with the aid of principal component and multiple linear regression analyses. Inter-monsoon samples were strongly influenced by continental material, both of crustal and anthropogenic origin. The crustal component (24.5 ± 13% of the total suspended particulate mass (TSP), 6.0 ± 4.4 μg m^{-3})) contained 3.2% gypsum ($CaSO_4$). While more than half of the TSP (21.2 ± 9.6 μg m^{-3}) during the SW-monsoon was sea-salt derived due to the strong winds prevailing during this season, only 1.7 ± 1.1% (0.7 ± 0.4 μg m^{-3}) was found to be of crustal origin. Sulfate (SO_4^{2-}) sources were determined and quantified with linear regression analyses utilizing specific tracers for the independent variables. Lead (Pb) was found to be a more reliable surrogate for anthropogenic SO_4^{2-} compared to nitrate (NO_3^-) during the relatively polluted inter-monsoon. Soluble calcium (Ca^{2+}) served as the tracer for gypsum, and methane sulfonate (MSA) served as the tracer for biogenically derived SO_4^{2-} during both seasons. Based on this analysis, 75% of the non-sea-salt sulfate (NSS-SO_4^{2-}) (0.8 ± 0.2 μg m^{-3}, representing ~ 2.4% of TSP) was found to be of biogenic origin during the SW-monsoon with the remaining 25% of anthropogenic origin. During the inter-monsoon NSS-SO_4^{2-} accounted for 2.1 ± 1.2 μg m^{-3} (~ 9.2% of TSP) and had a composition that was 65% anthropogenic, 21% biogenic, and

14% gypsum derived. Linear regression analyses revealed that the bio-SO_4^{2-}/MSA weight ratios appear to be consistent with the temperature dependence proposed by Hynes et al. [*Hynes et al.*, 1986]. In this case the yield of SO_4^{2-} increased relative to MSA with an increase in temperature. Three samples during the SW-monsoon, near the coast of Oman, showed lower temperatures, due to coastal upwelling, than the rest of the samples; at 24 °C the bio-SO_4^{2-}/MSA weight ratio was 6.8 ± 0.5. The remainder of the SW-monsoon samples were collected at an average temperature of 27.2 °C, for which the bio-SO_4^{2-}/MSA weight ratio was 13.5 ± 4.4. At an average temperature of 28.9 °C during the inter-monsoon sampling gave a ratio of 17.7 ± 4.8. These observations indicate a temperature-dependence factor between 24 and 29 °C of 2.2 (i.e., a 2.2 increase in the ratio of bio-SO_4^{2-}/MSA with every degree temperature increase). Cl^- deficits determined during both seasons appear to indicate that distinctly different mechanisms govern the observed depletion of Cl^- in each season.

3.2 Introduction

The chemistry of ambient aerosols, which are complex mixtures of minerals, sea-salt and organic compounds and their interaction with gas molecules is still poorly understood [*Andreae and Crutzen*, 1997; *Keene et al.*, 1998]. Basic information on their detailed composition and ambient reactivity is still needed. The present study is part of a large set of field observations collected to shed light on the chemical composition of atmospheric aerosol particles in different marine environments. Aerosol samples discussed in this study were initially described in our first paper in this series [*Siefert et al.*, 1999] in terms of their trace metal composition and the labile-Fe(II) concentrations. In this paper, we focus our attention on the bulk aerosol composition.

Non-sea-salt sulfate (NSS-SO_4^{2-}) particles in the sub-micrometer size range serve as cloud condensation nuclei (CCN) and influence the radiation balance of the atmosphere [*Charlson et al.*, 1987]. Extensive efforts have been focused on elucidation of the chemical and physical processes that lead to NSS-SO_4^{2-} particle formation from anthropogenic and biogenic sulfur sources. Biogenic sources of sulfur that contribute to NSS-SO_4^{2-} are particularly important in the marine boundary layer of remote oceanic regions [*Charlson et al.*, 1987; *Berresheim et al.*, 1993; *Andreae et al.*, 1995].

Sea-salt particles may act as seeds for the uptake and oxidation of sulfur gases and deposition of condensable sulfate vapors [*Keene et al.*, 1998; *McInnes et al.*, 1994]. Sea-salt may also strongly influence the oxidative properties of aerosol particles in the marine boundary layer through the production of halogen radicals [*Fan and Jacob*, 1992; *Finlayson-Pitts et al.*, 1989; *Graedel and Keene*, 1995; *Keene et al.*, 1996; *Pszenny et al.*, 1993; *Sander and Crutzen*, 1996; *Vogt et al.*, 1996]. These transient radical oxidants may have an effect on

biogenically emitted gases known to be the source of sulfate and organic aerosol particles over the oceans.

The primary organosulfur compound emitted to the atmosphere is dimethyl sulfide (CH_3SCH_3, DMS) [*Bates et al.*, 1992]. The reactions of DMS with hydroxy radical ($OH^\bullet$) and nitrate radical ($NO_3^\bullet$) are the initial steps in a complex chemical mechanism leading to the formation of NSS-SO_4^{2-} aerosol particles and other sulfur-containing reaction products, such as methanesulfonic acid (CH_3SO_3H, MSA) [*Hynes et al.*, 1986; *Yin et al.*, 1986]. Hynes et al. [*Hynes et al.*, 1986] suggested that temperature determines the relative contributions of the OH-addition and H-abstraction pathways of the initial oxidation step of DMS with $OH^\bullet$, whereby fixing the NSS-SO_4^{2-}/MSA ratio at a given temperature. MSA is easily sampled using filters since it partitions readily into the particle phase due to its low vapor pressure. As a consequence, MSA has been considered a quasi-conservative tracer for the marine biogenic NSS-SO_4^{2-} component. Thus, a simple relationship has been sought between the NSS-SO_4^{2-}derived from DMS and MSA, that would prove to be useful for estimating the biogenic yield of SO_4^{2-} important to the DMS-cloud-climate relationship. Kinetic studies on the oxidation of DMS have been critically reviewed [*Berresheim et al.*, 1995; *Turnipseed and Ravishankara*, 1993; *Yin et al.*, 1990]. A summary is given below in conjunction with newer studies on this topic.

A series of recent laboratory [*Barone et al.*, 1995; *Barone et al.*, 1996; *Sørensen et al.*, 1996; *Turnipseed et al.*, 1996] and modeling studies [*Ayers et al.*, 1996; *Barone et al.*, 1995; *Kerminen et al.*, 1998a] on the kinetics of the DMS reaction with $OH^\bullet$ and $NO_3^\bullet$ indicate that the NSS-SO_4^{2-}/MSA ratio observed in natural environments is the result of a complex array of reactions involving numerous radical and non-radical intermediates. It

seems that the key branching points required to explain the field observations of DMS oxidation have not been determined. Furthermore, the reaction of DMS with $NO_3^{\bullet}$, which becomes of importance during night-time and in northern winters due to the relatively lower $OH^{\bullet}$ concentrations, will also lead to the products MSA and SO_2 [*Berresheim et al.*, 1995; *Koga and Tanaka*, 1996]. In a model simulation study by Kerminen et al. [*Kerminen et al.*, 1998a], the NSS-SO_4^{2-}/MSA weight ratio seemed to be sensitive to the relative yields of oxidation products from the DMS-$OH^{\bullet}$ and DMS-$NO_3^{\bullet}$ reactions, as well as by any factor influencing SO_2 to sulfate conversion in clouds, such as the size distribution of particles, the abundance of sea-salt and anthropogenic particles, and SO_2 entrainment from the free troposphere. Furthermore, NO_x ($NO + NO_2$) concentrations have been found to influence the yields of MSA, $DMSO_2$ (dimethyl sulfone, $CH_3SO_2CH_3$), DMSO (dimethyl sulfoxide, CH_3SOCH_3) and SO_2 [*Patroescu et al.*, 1999], thus further complicating the NSS-SO_4^{2-}/MSA ratio.

Nevertheless, a multitude of field studies reveal that the NSS-SO_4^{2-} formation from DMS oxidation is more efficient at higher temperatures than the formation of MSA [*Bates et al.*, 1992; *Berresheim et al.*, 1989; *Berresheim et al.*, 1991; *Bürgermeister and Georgii*, 1991; *Prospero et al.*, 1991; *Pszenny et al.*, 1989; *Saltzman et al.*, 1985; *Saltzman et al.*, 1983; *Savoie and Prospero*, 1989; *Savoie and Prospero*, 1994; *Savoie et al.*, 1992; *Savoie et al.*, 1989]. Reported values for the NSS-SO_4^{2-}/MSA weight ratio vary from 870, observed over the China Sea [*Gao et al.*, 1996] to 3, observed in Antarctica [*Berresheim et al.*, 1989; *Pszenny et al.*, 1989]. Typical ratios for mid to low latitudes are between 14 and 20 [*Berresheim et al.*, 1991; *Bürgermeister and Georgii*, 1991; *Saltzman et al.*, 1985; *Saltzman et al.*, 1983; *Savoie and Prospero*, 1989; *Savoie and Prospero*, 1994] while they range from

3 to 6 for high latitude summers [*Allen et al.*, 1997; *Berresheim et al.*, 1989; *Bürgermeister and Georgii*, 1991; *Prospero et al.*, 1991; *Pszenny et al.*, 1989; *Savoie et al.*, 1992]. It is of interest to note that reported NSS-SO_4^{2-}/MSA weight ratios outside the typical ranges indicated above [*Allen et al.*, 1997; *Ayers and Gras*, 1991; *Bates et al.*, 1992; *Berresheim et al.*, 1991; *Gao et al.*, 1996; *Saltzman et al.*, 1983; *Savoie et al.*, 1989] were not corrected for NSS-SO_4^{2-} contributions of other origin than biogenic. Even for those studies, that were chosen in locations minimally impacted by continentally derived material, evidence exists for the long range transport of aeolian dust and man-made pollutants [*Berresheim et al.*, 1991; *Savoie and Prospero*, 1989; *Savoie et al.*, 1992]. About 25% of the NSS-SO_4^{2-} in Mawson, Antarctica [*Savoie et al.*, 1992] has been associated with the anthropogenic tracer NO_3^-, while that percentage falls to 20% during some seasons over the North Pacific [*Savoie and Prospero*, 1989]. In addition to this background anthropogenic NSS-SO_4^{2-} component, gypsum ($CaSO_4$) has been detected in association with silicate material in the atmosphere in several regions of the world's oceans [*Andreae et al.*, 1986; *Esteve et al.*, 1997; *Hoornaert et al.*, 1996; *Savoie et al.*, 1987; *van Malderen et al.*, 1996; *Zhou and Tazaki*, 1996]. Neglecting these additional NSS-SO_4^{2-} sources may lead to a bias in the NSS-SO_4^{2-}/MSA ratios, especially in locations and seasons with low DMS emissions. In these cases, the resulting weak biogenic signal becomes more susceptible to perturbations by non-marine sources.

In order to estimate a more accurate DMS derived NSS-SO_4^{2-}/MSA ratio the continental component should be extracted from the total NSS-SO_4^{2-}. This requires the simultaneous sampling of conservative tracers that serve as surrogates for continental material of both anthropogenic and crustal nature. By performing a multivariate linear

regression analysis, coefficients can be extracted that describe the dependence of the observed NSS-SO_4^{2-} on the independent tracers. A simple linear regression was used by Savoie and coworkers [*Savoie and Prospero*, 1994; *Savoie et al.*, 1992] with NO_3^- or Sb as tracers for anthropogenic material. However, NO_3^- is not a strict conservative tracer since it is thermodynamically more effectively incorporated into the sea-salt aerosol particle due to HNO_3 scavenging [*Seinfeld and Pandis*, 1997]. The extent of HNO_3 scavenging will therefore depend on the aerosol particle composition.

Additional difficulties in comparing data from distinct groups arise from the variety of sampling techniques employed, such as the use of different collector types that result in the collection of particles within different size ranges. MSA has been found to be distributed on larger particles, presumably as a function of aerosol surface area while NSS-SO_4^{2-} is typically associated with submicrometer particles [*Kerminen et al.*, 1997; *Pszenny*, 1992; *Qian and Ishizaka*, 1993; *Quinn et al.*, 1993; *Saltzman et al.*, 1983]. For example, Ayers et al. [*Ayers et al.*, 1997; *Ayers et al.*, 1991] collected only submicrometer aerosol particles and, as a consequence, the bulk of the MSA mass in the atmosphere was not sampled. This sampling bias will lead to larger than normal NSS-SO_4^{2-}/MSA ratios.

In addition to gas phase DMS oxidation by known oxidants ($OH^\bullet$ and $NO_3^\bullet$), photochemically produced reactive halogens in the marine boundary layer have recently been proposed as important reaction initiators [*Andreae and Crutzen*, 1997; *Keene et al.*, 1996; *Vogt et al.*, 1996]. Keene et al. [*Keene et al.*, 1996] and Andreae and Crutzen [*Andreae and Crutzen*, 1997] believe that DMS oxidation by Cl atoms could provide a significant additional sink that would resolve discrepancies between measured and modeled DMS budget analysis [*Chin et al.*, 1996].

Atmospheric chloride (Cl^-) chemistry in the marine boundary layer has been the subject of many investigations. Chloride concentrations observed in the field are typically below expected values deduced from sea-salt ratios. Chloride deficits of up to 90% have been reported [*Graedel and Keene*, 1995; *Keene et al.*, 1990]. The largest deficits occur as marine air intersects with more polluted air masses [*Sturges and Shaw*, 1993]. It was widely assumed that the only significant mechanism by which sea-salt is dechlorinated involves acidification of the aerosol by H_2SO_4 and HNO_3, with subsequent volatilization of HCl [*Duce and Hoffmann*, 1976; *Duce et al.*, 1973; *Sturges and Barrie*, 1988]. However, a large number of studies have found that the extent of dechlorination of the aerosol cannot be explained only by HCl displacement reactions involving mineral acids [*Graedel and Keene*, 1995; *Graedel and Keene*, 1996; *Keene et al.*, 1996; *Keene et al.*, 1990]. Experimental evidence [*Finlayson-Pitts*, 1983; *Finlayson-Pitts et al.*, 1989; *Graedel and Keene*, 1995; *Keene et al.*, 1990; *Pszenny et al.*, 1993; *Vogt et al.*, 1996] reveals the existence of highly reactive Cl gases (Cl_2, HOCl, $ClNO_2$, NOCl, BrCl) which photolyze or hydrolyze readily to from reactive Cl. Reactive Cl can initiate photochemical reactions in an analogous manner to $OH^\bullet$ and have major consequences for the oxidation of hydrocarbons and DMS [*Keene et al.*, 1996; *Keene et al.*, 1990; *Langer et al.*, 1996; *Pszenny et al.*, 1993; *Sander and Crutzen*, 1996; *Stickel et al.*, 1992; *Vogt et al.*, 1996]. Vogt et al. [*Vogt et al.*, 1996] found in their model calculations that about 40% of the SO_2 scavenged by the aerosol is oxidized by HOCl, increasing the amount of S(IV) oxidized in sea-salt aerosol by 0.4 to 0.8. This result implies that additional SO_2 oxidation on pre-existing particles will reduce the formation of new CCN and therefore the feedback between greenhouse warming, oceanic DMS emissions and increased cloud albedo.

3.3 Experimental

3.3.1 Sampling Location and Period

Samples were collected over the Arabian Sea during two separate month-long cruises on the R/V Meteor funded by the German Indian Ocean JGOFS project. Meteor32/3 (M32/3) initiated in Muscat, Oman (58.3° E, 23.8° N), and ended in Mahe, Seychelles (55.5° E, 4.5° S), cruising for the whole month of May of 1995, while Meteor32/5 (M32/5) backtracked M32/3's path, during the latter half of July and the first half of August of the same year. For most of the time, both the cruises tracked the 65th E meridian. The month of May, during which M32/3 took place, is typically characterized by no predominant weather pattern over the Northern Indian Ocean. It is the end of the transition time between the NE- (also, winter-) and the SW-monsoon (also, summer-monsoon) and is therefore called the inter-monsoon. M32/5 took place during the SW-monsoon. Daily three-dimensional isentropic air mass back trajectory calculations were provided by the German Weather Service. Figure 1 depicts two representative meteorological conditions per cruise. For each of these plots, four trajectories representing different final elevations at time of arrival are traced with dots that are separated by 6 hours. Trajectory calculations go back 4.5 days.

During the northern part of M32/3 (inter-monsoon), air masses advected over Africa, the Middle East, and/or Asia (Figure 1a) while the southern portion of the same cruise was characterized by slower moving marine air masses coming from the open ocean (Figure 1b). Strong SW winds dominated meteorological conditions during the SW-monsoon as shown in Figures 1c and 1d. All air masses originated from the open ocean, and with exception for a few higher elevation air masses in the latter half of the cruise, most of the air masses during the SW-monsoon did not have contact with continental land. This pattern of persistent high-

speed air current, in the form of a system of low-level jet streams in the vicinity of the western Indian Ocean during the northern summer, named Findlater Jet [*Findlater*, 1969], also leads to major areas of upwelling in the ocean off of the coast of Somalia, which was observed during the M32/5 cruise.

3.3.2 Aerosol Collection

Ambient aerosol samples were collected with two collector types. One high volume dichotomous virtual impactor (HVDVI) served for the collection of trace metals in two size fractions, described in detail in Siefert et al. [*Siefert et al.*, 1999]. Two low volume collectors, running at a flow rate of 27 l/min were used to collect aerosol samples for anion, cation, and gravimetric analyses, to be presented in this study. For the low volume collectors inverted high density polyethylene 2 liter bottles served as rainshields for the Nucleopore polycarbonate filter holders which were loaded with acid cleaned 47 mm diameter Gelman Zefluor filters (1 μm poresize).

A sector sampling system controlled the operation of all the pumps, thereby stopping collection of all aerosol collectors simultaneously when wind speed or wind direction were out of sector. The data logger was programmed to shut the pumps off when the wind speed was = 0 m s^{-1} and when the relative wind direction was ±90° off of the bow of the ship during the inter-monsoon and ±60° during the SW-monsoon.

In general, samples represent daily averages, but due to the ship's cruise track actual sampling duration may vary. Exact sampling intervals for each sample are listed in Table 1.

Due to the sampling characteristics of the HVDVI, approximately 10% of the fine particles end up on the coarse particle filter. All reported coarse concentrations have been corrected for this sampling artifact.

3.3.3 Chemical Analysis

Labile ferrous iron was analyzed spectrophotometrically on the high volume filters immediately after sample collection on board the ship; see Siefert et al. [*Siefert et al.*, 1999] for details. Filter samples for anion and cation analyses were refrigerated in cleaned petri dishes until they were analyzed after the research cruise.

Elemental analysis of 31 elements (Na, Mg, Al, K, Ca, Sc, Ti, V, Cr, Mn, Fe, Ni, Cu, Zn, Ge, As, Se, Mo, Ru, Cd, Sn, Sb, Cs, Ba, La, Ce, Sm, Eu, Hf, Pb, and Th) was performed on the high volume filters with an ICP-MS (Inductively Coupled Mass Spectrometer). Methods and results of this analysis are presented in Siefert et al. [*Siefert et al.*, 1999], but some of the metal abundance data will be used in here.

For the ion analyses, the 47 mm diameter low volume filters were first wetted with approximately 0.2 ml ethanol then extracted overnight in 10 ml MQ water. Anions were separated and quantified with a Dionex Bio LC ion chromatograph using a OmniPac Pax-500 separator column and the corresponding guard column. A AMMS-II anion micromembrane suppressor ensured the lowest possible background noise levels and detection limits. Organic and inorganic anions were eluted with a gradient pump and a combination of 3 eluents (1 mM NaOH, 200 mM NaOH, 5% MeOH) whereby the NaOH concentration was ramped from an initial 0.75 mM to a final 80.35 mM while the MeOH component remained constant at 1.24%. All anions eluted within 30 minutes of running time, but 9 additional

minutes were required to re-equilibrate the column to the same initial conditions after every run. Inorganic anions detected for were fluoride, chloride, nitrite, bromide, nitrate and sulfate while the organic anions were acetate, glycolate, formate, methanesulfonate, malonate, and oxalate. Propionate, pyruvate, succinate, fumarate, phthalate, phosphate and citrate were only present at non-detectable concentrations.

Cations were separated and quantified isocratically on the same Bio LC chromatograph with IonPac CS10 analytical and guard columns and a 40 mM HCl eluent. Sodium, ammonium, potassium, magnesium, and calcium concentrations were determined.

Daily average total suspended particulate (TSP) mass was determined by difference in filter weights (equilibrated to 21 °C and 50% RH) before and after collection.

3.3.4 Statistical Analysis

All concentrations are accompanied by their standard deviation calculated through propagation of error in every parameter used. The estimated errors in the volume of air sampled, in the filter section cut, in the volume of the extraction solution, etc., were assumed at 10%. The detection limits were determined as the mean of the blanks plus three times the standard deviation. Average concentrations are reported in conjunction with the standard deviation inthe sample population collected.

Principal component analysis (by SPSS, [*SPSS*, 1997]) was performed on the whole data set, including the metals, to learn about the source characteristics that made up the sampled aerosol material. In a principal component analysis, the correlation matrix of the observed variables is examined to reduce the number of descriptive variables by linearly combining the observed ones into a smaller set of independent variables, the principal

components. The principal components are orthogonal to each other and can be rotated in space to simplify interpretation of the data set. A common type of rotation is the Varimax rotation, during which orthogonality is retained. All principal components in the present study are Varimax rotated.

A principal component in this study represents a source, such as crustal material, sea-salt, anthropogenic pollutants, etc. An observed variable will display a number close to 1 if it correlates with the principal component, thus two variables with numbers close to 1 in one component correlate with each other. For example, the crustal component will exhibit values close to 1 for Al and other crustal elements, while the sea-salt component will exhibit values close to 1 for variables that are characteristic for sea-salt, such as Na^+, Cl^-, and wind speed.

3.4 Results and Discussion

3.4.1 SO_4^{2-} and MSA

3.4.1.1 Atmospheric Concentrations

Particulate SO_4^{2-} and MSA are determined as described in the experimental section above. NSS-SO_4^{2-} is estimated by subtracting sea-salt SO_4^{2-} from the total SO_4^{2-}, where the sea-salt component is inferred from Na^+ concentrations and the constant SO_4^{2-}/Na^+ ocean water ratio (0.252, from [*Millero and Sohn*, 1992]). Total and NSS-SO_4^{2-} are plotted in Figure 2a. The format of this plot is analogous to the rest of the concentration-vs.-sample plots in this study; samples are plotted as a function of time, inter-monsoon samples to the left, and SW-monsoon samples to the right of the vertical line that represents the equator. Thus, the abscissa is a temporal as well as a spatial variable, where each sample, in general, represents one day. Sampling duration and location for each sample are specified in Table 1.

The SO_4^{2-} data shows stronger anthropogenic sulfate inputs during the inter-monsoon, especially early in the cruise when closer to continental landmasses, as compared to the SW-monsoon. Strong winds during the SW-monsoon produced high loadings of sea-salt aerosol; therefore, a larger sea-salt component to total SO_4^{2-} is observed during that season. Table 2 lists the average, maximum and minimum concentrations of all anions and cations during both seasons. Sodium, a tracer for sea-salt, is larger by a factor of 2.5 during the SW-monsoon compared to the inter-monsoon.

Figure 2b shows the particulate MSA concentrations. Concentrations decrease over the oligotrophic waters located near the equator and during the SW-monsoon, while the MSA concentrations reach a maximum in the coastal upwelling regions off the coast of Oman due to increased biologic activity (samples M32/5_13, 14, and 15). This elevated biologic

productivity was also recorded by Bange et al. [*Bange et al.*, 1996] based on increased $N_2O(g)$ emissions from the ocean.

3.4.1.2 Bio-SO_4^{2-}/MSA ratio

NSS-SO_4^{2-} is defined as the total-SO_4^{2-} minus the sea-salt-SO_4^{2-} (SS-SO_4^{2-}). In other words, it is the remainder of SO_4^{2-} after correcting for the sea-salt contribution. However, this NSS-SO_4^{2-} remainder can be comprised of a series of additional components. It is only in the rare case when no other than biogenic sources are present that all NSS-SO_4^{2-} is derived from the oxidation of biogenically emitted S-gases. Linear regression analyses, described in the next section, and the large Ca^{2+} concentrations reveal the presence of gypsum as a SO_4^{2-} source in the inter-monsoon samples. Thus, to prevent all ambiguity, the following definitions are introduced here:

$$\text{total-}SO_4^{2-} = SO_4^{2-} = \text{SS-}SO_4^{2-} + \text{bio-}SO_4^{2-} + \text{anthr-}SO_4^{2-} + \text{gyp-}SO_4^{2-} \quad (1)$$

therefore,

$$\text{NSS-}SO_4^{2-} = SO_4^{2-} - \text{SS-}SO_4^{2-} = \text{bio-}SO_4^{2-} + \text{anthr-}SO_4^{2-} + \text{gyp-}SO_4^{2-}, \quad (2)$$

where SS-SO_4^{2-}, bio-SO_4^{2-}, anthr-SO_4^{2-}, and gyp-SO_4^{2-} represent the sea-salt, biogenic, anthropogenic, and gypsum contributions, respectively. Of special interest is the biogenic contribution, bio-SO_4^{2-}, and not the NSS-SO_4^{2-}.

A strong anthropogenic SO_4^{2-} component during the inter-monsoon contributes to a relatively high value for NSS-SO_4^{2-}. The resulting inflated NSS-SO_4^{2-}/MSA ratio would misrepresent the biogenic contribution if the anthropogenic fraction were neglected and not properly determined. In Figure 2c, NSS-SO_4^{2-} concentrations are plotted against observed MSA concentrations. The slope of the least squares fit through the inter-monsoon data set reveals a large NSS-SO_4^{2-}/MSA weight ratio (60 ± 10) in close agreement with other studies

performed in areas impacted heavily by continental sulfur emissions [*Allen et al.*, 1997; *Berresheim et al.*, 1991; *Saltzman et al.*, 1983; *Savoie et al.*, 1989]. A more reasonable value during the SW-monsoon (14 ± 3) is consistent with other observations from comparable parts of the remote open ocean [*Bürgermeister and Georgii*, 1991; *Gao et al.*, 1996; *Saltzman et al.*, 1985; *Saltzman et al.*, 1983; *Savoie and Prospero*, 1989; *Savoie and Prospero*, 1994]. The three samples collected near the Omani coast, which displayed larger than average MSA concentrations, are plotted but excluded from the linear regression and will be considered separately.

Note that low concentration samples from the inter-monsoon, in the left bottom corner of the plot, fall on a line with the SW-monsoon samples. Back trajectories of these samples indicate no recent contact with continental landmasses and can therefore be considered "clean" of anthropogenic and crustal material. Thus, it is justified to believe that the NSS-SO_4^{2-}/MSA weight ratio of ~14 in the present case is a good estimate of the biogenically derived sulfur in this region. Nevertheless, following is a methodical statistical procedure that deconvolutes the observed total-SO_4^{2-} to reveal all its sources and their relative contributions, and to unveil the truly biogenic fraction, especially for the "dirty" inter-monsoon samples.

3.4.1.3 Linear Regression

General

Several weighted multiple linear regression analyses are performed on each data set (inter-, SW-monsoon, and the three SW-monsoon "outliers") where SO_4^{2-} is the dependent variable and the independent variables are other carefully selected atmospheric species. Each conceivable source of SO_4^{2-} is represented by a tracer, i.e., an independent variable, where

the coefficient by which the tracer is multiplied is a measure of the extent to which SO_4^{2-} is related to that given variable after removing the effect of all the other variables. The coefficients are called partial regression coefficients and denoted b_i in the regression analysis. The standardized regression coefficients ($\beta_I = b_i(s_x/s_y)$) can be directly compared with each other, and are used as indicators of relative importance of the various sources in determining the value of SO_4^{2-}.

There are several objective ways of testing the significance of a regression and the significance of each chosen variable. From the analysis of variance (ANOVA) output of the linear regression, F, the ratio of the regression and residual mean squares, is a measure of the strength of the relationship in the data (for a more detailed description refer to *Biostatistical Analysis* by Zar [*Zar*, 1996]). If F for the regression is significant, then each of the partial regression coefficients in a multiple regression equation may be submitted to an analogous test. Here the student t-test is performed on the partial regression coefficients. However, in general, a significant F value in testing the dependence of Y (here, SO_4^{2-}) on all X's will be associated with significance of some of the b's being concluded by the t-test; but it is possible to have a significant F without any significant t's, or even significant t's without significant F. The latter situations often indicate a high degree of correlation between the several independent variables.

In the present study, multiple models are run with different numbers and combinations of variables due to the availability of a large set of variables (anions, cations, and metals [*Siefert et al.*, 1999]). By examination of the residual mean squares (R^2), the F's, and t's, as described above, those regressions and variables with the optimal conditions were

retained. A few of the models for each data set are discussed in an attempt to show the objectiveness of the final choice of model.

Inter-monsoon (M32/3)

Table 3 displays the ANOVA output, coefficients and additional statistical information for four linear regressions for the 27 inter-monsoon samples. Na^+ was included as the sea-salt tracer and served as an additional test of the model, since the exact ratio is known (0.252, from [*Millero and Sohn*, 1992]) and thus expected to coincide with the partial regression coefficient for Na^+ in the analysis. MSA represents the biogenic SO_4^{2-} contribution. The existence of an anthropogenic component is known but the tracer needs a careful selection due to its crucial effect on the outcome of the model. Comparison of models 3 and 4 in Table 3, where the input differences are the choice of the anthropogenic tracer, Pb and NO_3^-, respectively, shows that model 3 is the better regression model, and that Pb is the better variable (Vanadium, not shown, did not qualify) according to the t-test and ANOVA output. In addition, the standardized coefficients (0.108 for NO_3^- as opposed to 0.482 for Pb) indicate the stronger dependence of Pb on SO_4^{2-}. The relative difference in the resulting bio-SO_4^{2-}/MSA weight ratio between the two models (35.7 in model 4, as opposed to 17.7 in model 3) shows how misleading the results would have been, if NO_3^- were chosen as the anthropogenic tracer.

The plots shown in Figure 3 confirm the choice of Pb over NO_3^- as the optimal anthropogenic tracer for the inter-monsoon samples; the correlation between Pb and NSS-SO_4^{2-}, as depicted in Figure 3a, is considerably higher than between NO_3^- and NSS-SO_4^{2-}, shown in Figure 3b.

An additional SO_4^{2-} source was detected during the inter-monsoon in association with enriched soluble Ca. Calcium as detected by the IC (Ca^{2+}) for these samples was found on average to be enriched 12 times over concentrations expected from the sea-salt tracer Na^+. ICP-MS analysis revealed varying crustal enrichments of NSS-Ca of up to a factor of five over the crustal tracer Al. These crustal enrichment calculations are based on several assumptions that are explained in more detail below. In Figure 12d, the IC and ICP-MS Ca data for each sample is presented, whereby the stacked bars add up to measured total ICP-MS Ca concentrations. Note the large non-sea-salt, non-crustal fraction for Ca (in green) during the inter-monsoon.

Gypsum ($CaSO_4$) has been found in aerosols associated with crustal material [*Andreae et al.*, 1986; *Esteve et al.*, 1997; *Hoornaert et al.*, 1996; *Zhou and Tazaki*, 1996] and in aerosols collected over the Indian Ocean by Savoie et al. [*Savoie et al.*, 1987]. Therefore, NSS-Ca^{2+} (corrected for the sea-salt-Ca^{2+} estimated from soluble Na^+) was included in the linear regression analysis to portray this crustal-SO_4^{2-} contribution, denoted gyp-SO_4^{2-}.

Model 1, which is presented in Table 3 includes all the above mentioned tracers, Na^+, MSA, Pb, and NSS-Ca^{2+}, in addition to Al. Aluminum is added to check if the gypsum component is associated with the crustal component, thus indicating a common source. The t-test for Al in Model 1 shows a conditional probability, that a relationship as strong as the one observed in the data would be present if the null hypothesis were true, of 85%. This implies that Al can be taken out of the model, but it does not exclude the possibility of inter-correlation between the two variables of interest. Thus, when taking out one of the variables at a time, we observe that both Al (not shown) and NSS-Ca^{2+} are pertinent parameters for the

crustal contribution of SO_4^{2-}. The statistical output reveals that the better regression includes NSS-Ca^{2+}, however, as shown in Models 2 and 3. We conclude that gypsum and the other crustal component, traced by Al, most likely have a common source. Furthermore, a possible explanation for the better fit obtained with NSS-Ca^{2+} is that it was derived from IC analyses and the low volume samples, as were SO_4^{2-}, Na^+ and MSA, while Al was determined with ICP-MS and from the high volume filters. However, a differential effect of collection and analysis methods on concentrations does not apply for the preference of Pb as anthropogenic tracer over NO_3^-. Thus, most likely, more than one factor determines the concentration of gypsum in the aerosol particles. This is further discussed in the next section.

In addition, the constant can be eliminated from Model 2 since it is negligible. With these considerations, Model 3 appears to be the best representation of the inter-monsoon data set. Model 3 provides a sea-salt coefficient that is close to the expected 0.252 for ocean water, and a bio-SO_4^{2-}/MSA weight ratio of 17.7 ± 4.8 for the biogenic SO_4^{2-} contribution during the inter-monsoon of 1995.

SW-monsoon

An analogous statistical analysis procedure is performed on samples from the SW-monsoon. Three of the total of 20 samples from this season are considered separately due to the increased biological activity near the coast of Oman for those three samples.

The remote oceanic origin of most of the air masses sampled during the SW-monsoon resulted in fewer detectable SO_4^{2-} sources compared to the inter-monsoon. Nevertheless, we choose to start with the same variables in model 1 of Table 3 for the inter-monsoon data set. Several of the independent variables, such as MSA, in Model 1 of Table 4 fail the t-test.

However, after removal of the crustal components Al and NSS-Ca^{2+}, as Model 2 indicates, MSA becomes more important, while the constant approaches zero, and the SS-SO_4^{2-}/Na^+ coefficient moves closer to the expected constant in ocean water (0.252). The apparent negative correlation of NSS-Ca^{2+} with SO_4^{2-}, deduced from the negative coefficient in Model 1, is most likely the result of the error associated with the small remaining NSS-Ca^{2+} concentrations after the large sea-salt component was subtracted from Ca^{2+}. Evaluation of the t-tests in Model 2 allows for the safe elimination of the constant and Pb. In Model 3, the sea-salt coefficient is near the expected value of 0.252. Even though the anthropogenic component was best represented by Pb during the inter-monsoon, NO_3^- appears to be a better tracer during the SW-monsoon. A possible reason for this is that the Pb signal during the SW-monsoon is very weak, and thus more prone to errors. Nevertheless, the fact that NO_3^- does not serve as a tracer for anthropogenic SO_4^{2-} during the inter-monsoon, when continental pollution is greater and sea-salt less abundant in the atmosphere, is evidence that it cannot be used unequivocally as a tracer as such.

The bio-SO_4^{2-}/MSA weight ratio valid over most of the Arabian Sea during the SW-monsoon is 13.5 ± 4.4, which is very close to the first estimate (14 ± 3), when no correction for the small anthropogenic contribution was made.

The three remaining samples from the SW-monsoon that were collected over coastal upwelling regions seem to display a much smaller bio-SO_4^{2-}/MSA ratio than the rest of the samples. A linear regression through three sample points is not reliable; in fact, if we retain the same variables as above, no degree of freedom to perform a regression is left and the solution is unique. However, by subtracting from the total-SO_4^{2-} the known sea-salt component and the inferred (from the other SW-monsoon samples) anthropogenic

component, a total of two degrees of freedom are obtained. A regression of this data set through the origin provides a bio-SO_4^{2-}/MSA ratio of 6.8 ± 0.5, as shown in the model output in Table 5.

3.4.1.4 Temperature Dependence of the Bio-SO_4^{2-}/MSA Ratio

Although the oxidation of DMS yielding MSA and bio-SO_4^{2-} appears to depend on the interplay of a series of factors [*Berresheim et al.*, 1995; *Kerminen et al.*, 1998a; *Koga and Tanaka*, 1996; *Turnipseed et al.*, 1996], the only relevant variable measured in the present study is temperature. Thus, following is a simple attempt to find a temperature dependence in the bio-SO_4^{2-}/MSA weight ratio while assuming that the other variables remain unchanged.

Hynes et al. [*Hynes et al.*, 1986] proposed that the bio-SO_4^{2-}/MSA ratio should be temperature dependent. In an attempt to find such a dependence, Bates et al. [*Bates et al.*, 1992] consolidated all published data (up to 1991) and plotted them as a function of air temperature. Although the compiled data exhibits considerable scatter, it seems to indicate that the SO_4^{2-} production is favored at elevated temperatures. This effect should produce larger bio-SO_4^{2-}/MSA ratios at higher temperatures, as proposed by Hynes et al. [*Hynes et al.*, 1986].

The scatter in the plot presented by Bates et al. may partly be due to different aerosol size fractions sampled by the different groups. This may result in skewed ratios since MSA has been found to be distributed on larger particles, presumably as a function of aerosol surface area while NSS-SO_4^{2-} is typically associated with submicrometer particles [*Kerminen et al.*, 1997; *Pszenny*, 1992; *Qian and Ishizaka*, 1993; *Quinn et al.*, 1993; *Saltzman et al.*, 1983]. Furthermore, in regions where the biogenic SO_4^{2-} is very small, e.g., in colder

climates, the ratio will be susceptible to perturbations by even a modest non-marine back ground SO_4^{2-}.

As a consequence, only a small number of studies can be compared directly with our data set. These include data from the remote South Pacific, Antarctica, and Tasmania, that represent samples based on the collection of aerosol particles from pollution free air masses over all size ranges. This data is plotted together with our current results in Figure 5 as a function of air temperature. Filled squares represent the bio-SO_4^{2-}/MSA ratios extracted from linear regression analyses for the inter-monsoon, SW-monsoon, and the three "outliers" collected in coastal upwelling regions during the SW-monsoon. Air temperatures averaged 28.9 ± 0.6 °C during the inter-monsoon, 27.2 ± 1.3 °C during the SW-monsoon, and 24.0 ± 1.7 °C in the coastal upwelling regions near the coast of Oman. Standard deviations for the ratio are estimated in the linear regression analysis, and are thus not directly comparable to standard deviations calculated from a population of samples as practiced in the literature data plotted. Three data points obtained at temperatures above 20 °C are clearly consistent with the Hynes et al. [*Hynes et al.*, 1986] proposition of higher SO_4^{2-} production at higher air temperatures (e.g., one-degree temperature gain leads to a 2.2 increase in the ratio).

Barone and coworkers [*Barone et al.*, 1995; *Barone et al.*, 1996; *Turnipseed et al.*, 1996] have shown in their laboratory experiments that the branching between abstraction and addition reactions of DMS with $OH^{\bullet}$ cannot explain the large temperature dependence of the biog-SO_4^{2-}/MSA ratio. They concluded that the key branching point to explain the field observations in DMS oxidation has yet to be determined but that it most likely involves the oxidation of $CH_3S^{\bullet}$ to CH_3SO_x.

On the other hand, by fitting the data to an exponential temperature dependency we do observe a flattening out at lower temperatures, comparable to what has been observed in other studies, although these latter ratios obtained at low temperatures may be elevated by the presence of uncorrected background SO_4^{2-} contributions. Anthropogenic SO_4^{2-} is known to undergo long range transport and may, therefore, be present at low concentrations in remote areas, such as the South Pacific and Antarctica. However, in the studies by other investigators included in Figure 5 no measures were taken to correct for the possible influence of an anthropogenic SO_4^{2-} component. Furthermore, literature values for ratios at the elevated temperatures (from the South Pacific) were not reported with daily average temperatures, thus, temperatures are assumed to be 26 ± 1 °C. Inferring from the strong temperature dependence in our data points, correct temperature ranges may have positioned those two data point in a different place.

In summary, bio-SO_4^{2-}/MSA ratios over the Arabian Sea as determined by linear regression analysis reveal a significant temperature dependence, which seems to be independent of season.

3.4.1.5 Sulfate Sources

The standardized coefficients in a linear regression are a measure of the relative contribution of each component to the total-SO_4^{2-}. Thus, from Tables 2 and 3, the biogenic contributions account for ~16 and ~24% during the inter- and SW-monsoons, respectively, while the corresponding numbers for anthropogenic contributions are ~50 and ~8%. Sea-salt makes up the bulk SO_4^{2-} during the SW-monsoon (68%) and 23% during the inter-monsoon. While gypsum does not appear to be present during the SW-monsoon, ~11% of the SO_4^{2-} during the inter-monsoon is attributed to gypsum.

The source of NSS-Ca^{2+} in the form of gypsum appears to be clearly crustal in nature since it correlates strongly with the crustal signatures in the principal component analysis presented in Table 6 (component 1 and 3). Several land-based sources may contribute to the $CaSO_4$. Limestone, $CaCO_3$, weathers to form an external crust of gypsum, $CaSO_4$:

$$CaCO_3(s) + SO_2(g) + H_2O + 1/2O_2 \rightarrow CaSO_4(s) + H_2CO_3 \quad (3)$$

The most likely such crustal sources are evaporite deposits and gypsiferous soils known to exist in some regions of the Thar (India), and the deserts of Iran and Arabia [*Savoie et al.*, 1987]. Savoie et al. [*Savoie et al.*, 1987] found that if all the NSS-Ca were derived from gypsum, then the gypsum accounted for ~10 to 50% of the total mean NSS-SO_4^{2-} on the northeastern air masses collected over the Indian Ocean. In the present case, gypsum, as determined by linear regression, accounted for 8.1 ± 7.0% (ranging from 0 to 23.3%) of the NSS-SO_4^{2-}. This is in close agreement with observations by Savoie et al., although our samples included "clean" samples from near the equator and samples representative of air masses from the northwest.

Gypsum has also been found to be the product of the reaction between acid sulfates and silicate minerals brought together by in-cloud processes [*Andreae et al.*, 1986]. Since our samples are enriched in Ca, over what is expected from the average crustal composition [*Taylor and McLennan*, 1985], this process may play a minor role in the final gypsum concentration.

NSS-Ca^{2+} does not appear to correlate with Al: This may be due to a combination of effects that may have led to a differential distribution of gypsum and the other crustal component. For example, the aerosol particles may have been differently sized, and/or the air parcels may have undergone distinctly different weathering cycles. Hopke et al. [*Hopke*,

1985] noted that $CaSO_4$ is associated with the combustion of coal, oil, and fuel and that $CaCO_3$ is present in dust from metallurgical plants and cement plants. Although the data is inconclusive at this point, the apparent Ca enrichment may be a result of a combination of the above sources.

Results from the linear regression analyses are presented in conjunction with field observations in Figure 4. The model predictions of each source for every sample are plotted in stacked bars overlain by the dotted line representing the observed total-SO_4^{2-}. Correspondence between predicted and measured total-SO_4^{2-} is quite strong, especially during the SW-monsoon. The most noticeable discrepancies during the inter-monsoon are possibly due to an over prediction of the gyp-SO_4^{2-} component from the presence of other Ca^{2+} sources, such as $CaCO_3$. Anion and cation equivalent charges are plotted in Figure 6. During the inter-monsoon cation charges are typically in surplus, thus, to maintain electroneutrality a negative charge concentration corresponding to this positive surplus needs to be present. The most likely anion in this case, which is not detectable by IC, is CO_3^{2-}. Thus, any non-gypsum NSS-Ca^{2+} is assumed to be in the form of $CaCO_3$ and presented as such in subsequent sections.

3.4.2 Halogens

Principal component analyses on the inter- and SW-monsoon data sets, Tables 5 and 6, respectively, reveal that Cl^- and, to a lesser degree, Br^- correlate with the sea-salt component. Due to low F^- concentrations, 5.0 ± 2.8 and 2.1 ± 1.3 ng m^{-3}, for inter- and SW-monsoons, respectively, associated errors amount to 10 to 30%, which is sufficiently large to exclude the F^- from any further discussion.

Recent investigations show evidence that in addition to HCl, highly reactive Cl gases such as Cl_2, HOCl, $ClNO_2$, and BrCl may also volatilize from sea-salt aerosol [*Fan and Jacob*, 1992; *Graedel and Keene*, 1995; *Graedel and Keene*, 1996; *Langer et al.*, 1996; *Sander and Crutzen*, 1996; *Vogt et al.*, 1996]. Photolysis of these gases during the daytime produces atomic Cl with potential implications for the atmospheric lifetimes of alkanes, methyl halides, and DMS [*Keene et al.*, 1996].

The measured Br^- (plotted in solid in Figure 7a) is near the detection limit (i.e., ~ 15 ng m^{-3}, depending on air volume sampled) throughout the whole inter-monsoon season and for half of the SW-monsoon samples. The hatched bars in Figure 7a represent the expected sea-salt derived Br^- concentrations calculated indirectly from measured Na^+ concentrations (according to Br^-/Na^+ sea-salt ratios in Millero [*Millero and Sohn*, 1992]). Although the error bars are of considerable magnitude, it is apparent that Br^- is fully depleted, corresponding to a 100% Br^- deficit, in most of the samples. The samples with measurable levels of Br^- occurred during the SW-monsoon with average observed Br^- deficits of 51 ± 16% compared to the expected amount if Br^- were derived only from sea-salt.

Bromine has been studied in conjunction with the dramatic tropospheric ozone loss shortly after polar sunrise in the Arctic [*Barrie et al.*, 1988; *Bottenheim et al.*, 1990]. Bromine has been proposed in an autocatalytic reaction cycle involving transfer from the aerosol phase to gas phase as a principal free radical chain carrier that leads to O_3 destruction [*Fan and Jacob*, 1992; *McConnell et al.*, 1992; *Vogt et al.*, 1996]. Vogt et al. [*Vogt et al.*, 1996] also presented a model for an autocatalytic pathway for the production of reactive bromine and chlorine species in the pristine MBL involving the release of volatile species (Br_2, Cl_2, BrCl) from the particle phase:

$$H^+ + Br^- + HOBr \rightarrow Br_2(g) + H_2O \quad (4)$$

$$H^+ + Cl^- + HOCl \rightarrow Cl_2(g) + H_2O \quad (5)$$

$$H^+ + Cl^- + HOBr \rightarrow BrCl(g) + H_2O \quad (6)$$

This led to particle phase depletion of the halides, where the bromide deficit amounted to 90% and the chloride to 1%.

Chloride vs. time (and location) is shown in Figure 7b in which the measured Cl^- is compared to the expected Cl^- concentrations that were based on the observed Na^+ abundance and the ratio of Cl^-/Na^+ is sea-salt [*Millero and Sohn*, 1992]. Although not as obvious as in the case of Br^-, the observed Cl^- is generally (42 out of 48 samples) below what would have been expected from the measured Na^+ values assuming there is no additional source of Cl^- other than sea-salt. The percentage Cl^- deficit ranges from slightly negative to 32%, whereby the largest values are encountered during the relatively more polluted inter-monsoon season. These observations are in close agreement with results obtained from other open ocean regions [*Graedel and Keene*, 1995, and references therein].

Cl^- deficits have typically been found to correlate with the proximity to continental landmasses and thus assumed to depend on the concentrations of anthropogenic pollutants such as SO_4^{2-} and NO_3^-. In heavily polluted air masses, losses of particulate Cl^- approaching 100% have been reported. Based on these observations it has been widely assumed that Cl^- is solely released due to the thermodynamically favorable displacement reaction between mineral acids (H_2SO_4, HNO_3) and HCl:

$$2NaBr(s) + H_2SO_4 \rightarrow Na_2SO_4 + 2HBr(g) \quad (7)$$

$$NaBr(s) + HNO_3 \rightarrow NaNO_3 + HBr(g) \quad (8)$$

$$2NaCl(s) + H_2SO_4 \rightarrow Na_2SO_4 + 2HCl(g) \quad (9)$$

$$NaCl(s) + HNO_3 \rightarrow NaNO_3 + HCl(g) \quad (10)$$

Kerminen et al. [*Kerminen et al.*, 1998b] also found MSA and oxalate to replace Cl^- from supermicron sea-salt particles. However, since concentrations of latter two species are typically much lower than NO_3^- and SO_4^{2-} combined, the Cl^- released in this way should be negligible in our case.

The average Cl^- deficit during the SW-monsoon amounts to 3.5 ± 6.3% and increases by a factor of 4.3 to 15 ± 9% during the inter-monsoon. In this particular case, the absolute deficit only increases by a factor of 1.3 (from 507 to 660 ng m^{-3}). This value is considerably lower than the analogous factors that describe the increase of absolute concentrations of typical pollutants, such as Pb, anthropogenic-SO_4^{2-}, and NO_3^-, which are commonly used to trace the anthropogenic contribution to the air mass. Pb concentrations increase by a factor of 18 from the SW- to the inter-monsoon, while anthopogenic-SO_4^{2-} (as determined by multivariate linear regression analysis above) increases by a factor of 7.5, and NO_3^- by 2.6. If the Cl^- deficit is assumed to be solely due to HCl displacement via reactions involving strong mineral acids such as H_2SO_4 and HNO_3 aerosol [*McInnes et al.*, 1994; *Sturges and Barrie*, 1988], we should observe a relative deficit increase from the SW- to the inter-monsoon comparable to the relative increase of Pb, anthropogenic-SO_4^{2-} and NO_3^-. This inter-comparison is justifiable since the Cl^- deficit does not reach 100% in any one of the samples, thus indicating that the extent of the above displacement reactions is not limited by the Cl^- concentration in the aerosol phase. Although the three anthropogenic tracers do not seem to behave in the same manner, they all display values for their concentration increases that are larger than the relative Cl^- deficit increase. These observations suggest that additional mechanism(s) contribute to the Cl^- deficit, and that these mechanism(s) play a

significant role especially during the SW-monsoon, when pollutants are present at very low concentrations and the sea-salt contribution is predominant.

For visualization, the absolute deficit is plotted in Figure 8 in conjunction with the summed up molar equivalents of NO_3^- and SO_4^{2-} (i.e., $[NO_3^-]+2x[SO_4^{2-}]$). Error bars for the deficit are relatively large due to the subtraction of two large numbers, especially during the SW-monsoon, when the sea-salt contribution is 2.5 times that encountered during the inter-monsoon. Nevertheless, seasonal distinctions in the data set can be recognized. Although the Cl^- deficit during the inter-monsoon is typically within the range of the anthropogenic pollutants plotted, no obvious correlation between the two is observed. This may be due to some amount of externally mixed anthropogenic and sea-salt particles. However, most NO_3^- and some NSS-SO_4^{2-} is expected to be associated with the sea-salt particles [*Bassett and Seinfeld*, 1984; *Berresheim et al.*, 1991; *Huebert et al.*, 1996; *Keene et al.*, 1998; *McInnes et al.*, 1994; *Naik et al.*, 1991; *O'Dowd et al.*, 1997; *Savoie and Prospero*, 1982; *Sievering et al.*, 1990; *Sisterson*, 1989] and thus available for Cl^- depletion. Different observations are made during the SW-monsoon, when the Cl^- deficit ranges from negative to large positive values that do not match concentrations of anthropogenic pollutants. Even if all the particles were internally mixed during the SW-monsoon, there would not be enough NO_3^- and NSS-SO_4^{2-} available to account for the large Cl^- deficit observed. Thus, there may be an indication of different prevalent mechanisms during each of the seasons.

Principal component analyses presented in Tables 5 and 6 reconfirm the poor correlation between the observed Cl^- deficit on one hand and the anthropogenic-SO_4^{2-} and NO_3^- on the other, for both the inter- and the SW-monsoon, respectively. During the inter-monsoon, the Cl^- deficit does not seem to correlate with any of the major principal

components and appears isolated in component 6 of Table 6. On the other hand, during the SW-monsoon, the Cl^- deficit seems to correlate with the charge difference observed between anions and cations, in component 4 of Table 7. The discrepancy between the summations of measured anionic and cationic charges is most likely due to species that are undetectable by the IC, such as H^+ and CO_3^{2-}. Total anion and cation charges are plotted simultaneously in Figure 6.

Volatilized Cl^- in the form of HCl from acid displacement reactions with H_2SO_4 and/or HNO_3 would have been replaced by the corresponding $SO_4^{2-}$and NO_3^- anions and thus been detected by IC. On the other hand, the alternative idea for the release of Cl in the form of reactive species, such as HOCl, $ClNO_2$, and BrCl, may not be replaced by a detectable anion. If no other significant source of CO_3^{2-} (e.g., in the form of calcite) is present in the aerosol phase as is the case during the SW-monsoon, it is conceivable that the charge difference may become a measure of the extent of Cl^- released in this form.

A correlation between the Cl^- deficit and the apparent charge difference during the "clean" SW-monsoon is apparent in Figure 9, where the absolute concentration difference between anion and cation charges is plotted as a function of Cl^- deficit. Error bars are relatively large due to repeated propagation of error for every calculation; nonetheless, a distinct difference in behavior between the scattered inter-monsoon and the aligned SW-monsoon samples is apparent.

In summary, observations seem to indicate that Cl^- released by acid displacement reactions does not adequately describe the observed Cl^- deficits for the two sampling seasons. While the acid displacement reaction most likely is of some importance during the more

highly polluted inter-monsoon, this reaction seems negligible during the sea-salt influenced SW-monsoon, when Cl^- deficits are observed but anthropogenic inputs are minimal.

3.4.3 Organic Anions

Increased interest in organic anions in the atmosphere stems from the hygroscopicity of these ions. Organic aerosols have been shown active in the formation of CCN comparable to some inorganic aerosols [*Cruz and Pandis*, 1998; *Matsumoto et al.*, 1997]. Novakov and Penner [*Novakov and Penner*, 1993] found that organic aerosol mass dominated the total mass in nucleation mode in a marine site known to be influenced by anthropogenic emissions. Even though in summation the organic anions may amount to only a minute fraction of the total ions in atmospheric aerosol, they may be relevant to the formation of new particles in the atmosphere. Furthermore, organic anions have been shown to play a major role in photochemically reducing insoluble Fe(III) to release soluble Fe(II) [*Faust and Zepp*, 1993; *Pehkonen et al.*, 1993; *Siefert et al.*, 1994]. This is a topic of interest in our preceding paper [*Siefert et al.*, 1999] where soluble Fe(II) was determined over the ocean in the context of the iron-hypothesis [*Martin et al.*, 1994; *Martin and Fitzwater*, 1988; *Martin et al.*, 1991].

In the present samples, organic anions represent only 3.1 ± 2.2 wt% (2.2 ± 2.2 mol%) of all the anions analyzed during the inter-monsoon, while the corresponding numbers for the SW-monsoon are 1.5 ± 0.6 wt% (0.8 ± 0.4 mol%). Since no simultaneous CNN measurements were undertaken during this sampling program, this data cannot be interpreted in light of findings presented above. Instead, further discussion will focus on the relative distribution and sources of each of the organic anions measured.

In Figure 10, acetate, glycolate, formate, malonate and oxalate are plotted as a function of sample for both the inter- and the SW-monsoon seasons. Acetic and formic acids are typically more abundant in the aqueous and gaseous phases than in aerosol particles. As a result, one may expect introduction of sampling artifacts during collection as these gaseous species may be trapped on the cake of sea-salt formed on the filter. Thus, their measured aerosol concentrations may not be easily interpretable. In an attempt to determine their sources, both acetate and formate are included in the principal component analyses in Tables 5 and 6, for the inter- and SW-monsoons, respectively.

During the inter-monsoon, acetate shows some correlation with the coarse crustal component, which, based on the scores for Pb, V, NO_3^- and NSS-SO_4^{2-}, is also found to include some fraction of anthropogenic material. Similar observations are made during the SW-monsoon where acetate correlates slightly with the fine crustal component, which also includes some anthropogenic material; in addition it correlates with component 6, which is pure anthropogenic. Thus, indications are that acetic acid is anthropogenically derived, but this does not exclude the presence of other, weaker sources that remain undetected by principal component analysis. Of special interest is that acetate anti-correlates with the Cl^- deficit in samples from both the inter- and SW-monsoons. No explanation can be given for that.

In contrast, formate correlates somewhat with the sea-salt component during both seasons. In addition, formate seems associated with anthropogenic emissions, since it correlates with components in the two seasons that carry anthropogenic signatures: the iron component (5) during the inter-monsoon, which was determined in our previous paper [*Siefert et al.*, 1999] to possibly be contamination from the ship's plume, and the fine crustal

component during the SW-monsoon, which includes an anthropogenic fraction. Thus, formate may have a biogenic source, similar to MSA, in addition to an anthropogenic one.

Malonate and Oxalate are both dicarboxylic acids, which due to the presence of two carboxylic groups, are less volatile and are mostly present in the particle phase in the ambient atmosphere. Oxalic acid has been observed to be the dominant dicarboxylic acid in many urban areas [*Kawamura and Ikushima*, 1993, and references therein], and was found to be produced secondarily in the atmosphere by photochemically induced reactions involving organic precursors. Kawamura and Ikushima's [*Kawamura and Ikushima*, 1993] suggests that diacids once produced in the atmosphere are further oxidized to result in smaller diacids, leading to the accumulation of oxalic acid. Thus, we expect oxalic acid to correlate with the anthropogenic component. The principal component analysis reveals that oxalate is mainly associated with the sea-salt during both seasons, comparable to formate. In addition, during the inter-monsoon oxalate also correlates with the fine crustal component that carries an anthropogenic fingerprint, as mentioned above, and during the SW-monsoon, with component 6, the anthropogenic one. Thus, besides the anthropogenic source, other factors, such as the aerosol residence time in the air and the aerosol matrix composition, may play important roles in the final oxalate concentrations measured during both seasons.

Malonate displays a different behavior from oxalate. It correlates with the coarse crustal component during the inter-monsoon, but with the sea-salt and the MSA component during the SW-monsoon. Thus, malonate seems to have a biogenic source, especially during the SW-monsoon.

In summary, carboxylic acids over the Arabian Sea during the inter- and SW-monsoons seem to be of both anthropogenic and biogenic nature. Because carboxylic acids

may be directly emitted as well as produced from organic precursors, their measured concentrations also become a function of parameters such as the residence time in the atmosphere and the presence of precursors and reactive species. Once formed, carboxylic acids are removed from the atmosphere mainly by dry and wet deposition, this is due to their weak reactivity in the atmosphere. All these factors play a role in determining the final concentration of carboxylic acids, thus determining their sources based on the principal component analysis is not conclusive.

3.4.4 Cations

Water-soluble fractions of Na^+, K^+, Mg^{2+}, Ca^{2+}, and NH_4^+ were quantified by IC. NH_3 is mainly released in conjunction with agriculture and farming, but over the oceans, some NH_3 is biogenically derived. Gaseous NH_3 reacts with sulfate aerosol particles thereby neutralizing the aerosol. Since both NH_3 and anthropogenically derived SO_4^{2-} are transported from the continents to the ocean, NH_4^+ is expected to vary in conjunction with anthr-SO_4^{2-}. However, during the inter-monsoon, which is heavily influenced by continental sources, such a correlation is not obvious, instead, NH_4^+ seems to correlate with the sea-salt component in the principal component analysis in Table 6. A plot of concentration vs. sample for NH_4^+ during the inter-monsoon, Figure 11, shows increased NH_4^+ concentrations with continental proximity; nevertheless, no relationship between anthr-SO_4^{2-} and NH_4^+ is found. The larger concentrations observed near the coast may be due to the combination of increased NH_3 production in near-shore environments and the short lifetime of NH_3 [*Schlesinger and Hartley*, 1992].

The NH_4^+/anthr-SO_4^{2-} equivalent mole ratio (anthr-SO_4^{2-} is determined in the linear regression analysis above) during the inter-monsoon varies between 0.2 and 5.0 (average value: 1.8 ± 1.2). This indicates that most of the anthr-$SO4^{2-}$ is neutralized by NH_3. Both $(NH_4)_2SO_4$ and some NH_4HSO_4 are expected present in these aerosol particles. In the cases where the ratios is larger than 2, more NH_3 is assimilated by the particle than necessary for full neutralization. When such surplus of NH_4^+ is detected the formation and maintenance of particulate NH_4NO_3 may become possible. However, due to the high temperatures encountered in the present samples, at which NH_4NO_3 becomes thermodynamically unstable, its presence is highly unlikely. Instead, biogenically derived SO_4^{2-} may be considered to add acidity to the aerosol and therefore be neutralized by available NH_3. The equivalent mole ratio of NH_4^+/(anthr+bio)-SO_4^{2-} also varies from 0.2 to 5.0 (average value: 1.1 ± 0.9). The neutralization capacity of calcite, which was taken as the remaining NSS-Ca^{2+}, after subtracting the gypsum contribution determined in the linear regression, increases the ratio (now, (NH_4^+ + $CaCO_3$)/(anthr+bio)-SO_4^{2-}) to an average of 2.1 ± 0.9.

During the SW-monsoon average NH_4^+ concentrations (46 ± 32 ng m^{-3}) are lower by more than a factor of 6 compared to the inter-monsoon, and NH_4^+ correlates strongly with the fine crustal component in the principal component analysis in Table 7. Since this fine crustal component includes an anthropogenic signal, it is likely that the NH_4^+ originates from the continents. The SW-monsoon is characterized by clean marine air masses, with a relatively large input of biognically derived SO_4^{2-}. Thus, the small quantities of NH_3 will not suffice for neutralization of both anthropogenic and biogenic SO_4^{2-}. This is revealed in the small equivalent mole ratio NH_4^+/(anthr+bio)-SO_4^{2-} observed during this season: it varies from 0.1 to 1.0 with an average of 0.3 ± 0.2. Thus, most of the SO_4^{2-} during this season seems to be

present as H_2SO_4 and HSO_4^{2-}. If the measured NSS-Ca2+ is assumed to be calcite, the additional neutralization capability results in a ratio of $(NH_4^+ + CaCO_3)/(anthr+bio)\text{-}SO_4^{2-}$ of 0.5.

Na^+, K^+ and Mg^{2+} are usually expected to be conservative tracers of sea-salt, while Ca^{2+} may have additional sources, such as continentally derived gypsum or oceanic $CaCO_3$. However, as Keene et al. [*Keene et al.*, 1986] illustrated, the correct choice for the sea-salt tracer needs to be carefully evaluated. They conclude from their database that Na^+ or Mg^{2+} are the best tracers, but that the specific data set has to be evaluated and the element with the lower concentration relative to sea-salt picked.

Figure 12 depicts the 4 cations, as dotted lines, in conjunction with concentrations for the same elements determined with ICP-MS and from the high volume collector filters. Initial focus is on the dotted lines. Comparing these lines in the 4 plots reveals the similarity between Na^+ (plot a) and Mg^{2+} (plot b), especially during the SW-monsoon, when high wind speeds (up to 16 m s^{-1}, with 11 m s^{-1} average, as opposed to 7 m s^{-1} average during the inter-monsoon) are responsible for elevated abundance of sea-salt particles in the atmosphere. Since Mg^{2+} seems to exhibit slightly larger concentrations during the inter-monsoon compared to Na^+, relative to sea-salt, Na^+ is assumed the better sea-salt tracer. The same reasoning holds true for the ICP-MS data, presented in stacked bars.

Thus, after accounting for the crustal contribution to Na (ICP-MS), using Al as the tracer and average crustal concentrations from Taylor and McLennan [*Taylor and McLennan*, 1985], the rest of Na is assumed to be sea-salt derived. This SS-Na is further utilized to estimate sea-salt contributions of Mg, K, and Ca, based on sea-salt concentrations by Millero

[*Millero and Sohn*, 1992]. In this manner, sea-salt, crustal, and remaining (denoted "other"), contributions to Na, Mg, K, and Ca are determined and plotted in stacked bars in Figure 12.

When comparing the total concentrations of Na, Mg, K, and Ca with the corresponding ions in plots a, b, c, and d, respectively, in Figure 12, one has to keep in mind that the two data sets are derived from two different collectors and two different analysis techniques. Furthermore, the strong acid digestion performed for samples analyzed by ICP-MS assures a comprehensive inclusion of the elements independent of their initial form. Thus, the water soluble fraction is a portion of the total concentration as determined by ICP-MS. If collector efficiencies were identical, the dotted line, representing the soluble fraction, would necessarily fall within the concentrations determined by ICP-MS; however, this is not the case. The discrepancy is less during the inter-monsoon than during the SW-monsoon, most probably as a function of wind speed. It is conceivable that at larger wind speeds the high volume dichotomous virtual impactor is less efficient in collecting the large particles, which are typically composed of sea-salt. Thus, during the SW-monsoon, when sources other than sea-salt are scarce, the dotted line, representing the soluble fraction is above the stacked bars.

Ca, in Figure 12d, displays a very different pattern compared to the other 3 elements. While the signature during the SW-monsoon is similar to the other 3 metals, during the inter-monsoon, both the Ca^{2+} and the total Ca concentrations are larger by a factor of 6 compared to what would be expected if Ca behaved similar to the other elements. After subtracting the crustal and sea-salt components, as explained above, the remaining ICP-MS Ca (represented in green stacked bars) is substantial and mostly present in the coarse size fraction (> 3 μm); furthermore, this extra Ca must be water soluble since the same enrichment is observed for

Ca^{2+}. Thus, indications are that this extra Ca is present in the form of gypsum, possibly carried directly from gypsiferous continental soils [*Esteve et al.*, 1997; *Hoornaert et al.*, 1996; *Savoie et al.*, 1987; *Zhou and Tazaki*, 1996] and/or formed during transport from in-cloud processing of crustal material [*Andreae et al.*, 1986].

The presence of additional K and Mg, not accounted for by the sea-salt or the crustal components, may partly be an artifact introduced by assuming an average crustal composition, which may not be representative of this area.

3.4.5 Total Suspended Particulates (TSP)

Total suspended particulates (TSP) are determined on the low volume filters. The average TSP amounts to 25 ± 13 μg m^{-3} and 38 ± 14 μg m^{-3}, during the inter- and SW-monsoons, respectively. As depicted in Figure 13a and 13b, more than 50% of the suspended mass during the SW-monsoon is sea-salt derived, while it amounts to 39% during the inter-monsoon, respectively.

The crustal component is determined based on ICP-MS results deduced from the high volume samples. As indicated in the previous section, sampling efficiencies between the low and the high volume collectors vary considerably during strong winds, i.e., SW-monsoon, and seemingly affecting the larger particles more strongly. Thus, the crustal component as presented in Figure 13 is an underestimate of what is probably present on the low volume filters. This low estimate for crustal material during the SW-monsoon amounts to 1.7 ± 1.1% of the TSP. The fact that 40% of the TSP remains unaccounted for indicates that some large crustal particles may not have been collected by the high volume collector. A similar, less

pronounced effect, is observed during the inter-monsoon, when 21 ± 13% of the TSP appears to be crustal and 17% remains unattributed.

Gypsum contributions are determined from the outcome of the linear regression analysis that resolved the different SO_4^{2-} sources. The remaining NSS-Ca^{2+} is assumed to be present as $CaCO_3$. While gypsum was not found during the SW-monsoon, 3.2 ± 2.1% of the TSP during the inter-monsoon can be attributed to gypsum.

Anthropogenic and biogenic SO_4^{2-} fractions are also extracted from the linear regression analysis, and, when combined, they account for ~7% and ~2.4% of the measured TSP during inter- and SW-monsoon, respectively. Finally, organic anions, which are also measured by IC from the low volume filters, make up only 1.0 ± 0.7% of the TSP during the inter-monsoon and 0.5 ± 0.2% during the SW-monsoon.

3.5 Conclusions

Aerosol sampling over the Indian Ocean show that the inter-monsoon period is characterized by strong anthropogenic and crustal signatures, while the SW-monsoon is characterized by clean remote marine air masses. Strong winds appear to be responsible for the upwelling of nutrient rich water near the coast of Oman, which explain the relatively larger biogenically derived MSA concentrations during this season. Linear regression analysis shows that 75% of NSS-SO_4^{2-} is of biogenic origin during the SW-monsoon, while during the inter-monsoon this number falls to 21%. In addition to an anthropogenic component of NSS-SO_4^{2-} during both seasons (inter-monsoon: 65%, SW-monsoon: 8%), gypsum is found to be present in the inter-monsoon samples. If this added gypsum contribution (14%) to the total SO_4^{2-} had not been detected, the additional SO_4^{2-} would have been assumed to be of biogenic origin.

Multiple linear regression analyses show that NO_3^- is not a conservative tracer for anthropogenic-SO_4^{2-} during the inter-monsoon; however, Pb correlates highly with anthr-SO_4^{2-}. The observed bio-SO_4^{2-}/MSA weight ratios are: 17.7 ± 4.8 during the inter-monsoon, at 28.9 ± 0.6 °C; 13.5 ± 4.4 during the SW-monsoon, at 27.2 ± 1.3 °C; and 6.8 ± 0.5 in the upwelling region during the SW-monsoon, at 24.0 ± 1.7 °C. An attempt is made in defining a simple temperature dependence for the bio-SO_4^{2-}/MSA ratio. Although a series of other variables may influence this ratio, the observed temperature dependence is in agreement with that proposed by Hynes et al. [*Hynes et al.*, 1986]: an increase in the ratio with temperature. Comparable data by Saltzman and coworkers [*Saltzman et al.*, 1985; *Saltzman et al.*, 1983] display slightly larger ratios, since the data was not corrected for background SO_4^{2-}.

The chloride depletion observed in the samples seem to indicate that during the SW-monsoon, Cl is released in the from of reactive Cl species, in agreement with evidence from a number of investigators [*Finlayson-Pitts*, 1983; *Finlayson-Pitts et al.*, 1989; *Graedel and Keene*, 1995; *Keene et al.*, 1990; *Pszenny et al.*, 1993; *Vogt et al.*, 1996]. Reactive Cl is believed to initiate photochemical reactions in an analogous manner to $OH^{\bullet}$ which would have major consequences for the oxidation of hydrocarbons and DMS, as proposed by several studies [*Keene et al.*, 1996; *Keene et al.*, 1990; *Langer et al.*, 1996; *Pszenny et al.*, 1993; *Sander and Crutzen*, 1996; *Stickel et al.*, 1992; *Vogt et al.*, 1996]. However, our results appear to indicate no apparent differential effect in the yield of bio-SO_4^{2-} and MSA as a function of Cl chemistry in the marine boundary layer.

Acknowledgments. The authors wish to thank Drs. Meinrat O. Andreae and Hermann W. Bange of the Max Planck Institute of Biogeochemistry in Mainz, Germany, for assistance with the Meteor 32/3 and 32/5 cruises, which were sponsored by the German Joint Global Ocean Flux Study (JGOFS) project. Appreciation is also extended to the helpful and lively crew of the R/V Meteor. Research support was provided by the National Science Foundation and by the Environment Now Foundation. Their support is greatly appreciated.

3.6 References

Allen, A.G., A.L. Dick, and B.M. Davidson, Sources of atmospheric methanesulphonate, non-sea-salt sulphate, nitrate and related species over the temperate South Pacific, *Atmos. Environ.*, *31* (2), 191-205, 1997.

Andreae, M.O., R.J. Charlson, H.S. Bruynseels, R. Van Grieken, and W. Maenhaut, Internal mixture of sea salt, silicates, and excess sulfate in marine aerosols, *Science*, *232*, 1620-1623, 1986.

Andreae, M.O., and P.J. Crutzen, Atmospheric aerosols: Biogeochemical sources and role in atmorpheric chemistry, *Science*, *276*, 1052-1058, 1997.

Andreae, M.O., W. Elbert, and S.J. de Mora, Biogenic sulfur emissions and aerosols over the tropical South Atlantic. 3. Atmospheric dimethylsulfide, aerosols and cloud condensation nuclei, *J. Geophys. Res.*, *100*, 11,335-11,356, 1995.

Ayers, G.P., J.M. Cainey, R.W. Gillett, and J.P. Ivey, Atmospheric sulphur and cloud condensation nuclei in marine air in the Southern Hemisphere, *Philos. Trans. R. Soc. London, B*, *352* (1350), 203-211, 1997.

Ayers, G.P., J.M. Cainey, H. Granek, and C. Leck, Dimethylsulfide oxidation and the ratio of methanesulfonate to non sea-salt sulfate in the marine aerosol, *J. Atmos. Chem.*, *25*, 307-325, 1996.

Ayers, G.P., and J.L. Gras, Seasonal relationship between cloud condensation nuclei and aerosol methanesulphonate in marine air, *Nature*, *353*, 834-835, 1991.

Ayers, G.P., J.P. Ivey, and R.W. Gillett, Coherence between seasonal cycles of dimethyl sulphide, methanesulphonate and sulphate in marine air, *Nature*, *349*, 404-406, 1991.

Bange, H.W., S. Rapsomanikis, and M.O. Andreae, Nitrous oxide emissions from the Arabian Sea, *Geophys. Res. Lett.*, *23* (22), 3175-3178, 1996.

Barone, S.B., A.A. Turnipseed, and A.R. Ravishankara, Role of adducts in the atmospheric oxidation of dimethyl sulfide, *Faraday Discuss.*, *100*, 39-54, 1995.

Barone, S.B., A.A. Turnipseed, and A.R. Ravishankara, Reaction of OH with dimethyl sulfide (DMS). 1. Equilibrium constant for OH + DMS reaction and the kinetics of the OH•DMS + O_2 reaction, *J. Phys. Chem.*, *100*, 14694-14702, 1996.

Barrie, L.A., J.W. Bottenheim, R.C. Schnell, P.J. Crutzen, and R.A. Rasmussen, Ozone destruction and photochemical reactions at polar sunrise in the lower Arctic atmosphere, *Nature*, *334*, 138-141, 1988.

Bassett, M.E., and J.H. Seinfeld, Atmospheric equilibrium model of sulfate and nitrate aerosols-II. Particle size analysis, *Atmos. Environ.*, *18* (6), 1163-1170, 1984.

Bates, T.S., J.A. Calhoun, and P.K. Quinn, Variations in the methanesulfonate to sulfate molar ratio in submicrometer marine aerosol particles over the South Pacific Ocean, *J. Geophys. Res.*, *97*, 9859-9865, 1992.

Berresheim, H., M.O. Andreae, G.P. Ayers, and R.W. Gillett, Distribution of Biogenic Sulfur Compounds, *ACS Symposium Series*, *393*, 352-366, 1989.

Berresheim, H., M.O. Andreae, G.P. Ayers, R.W. Gillett, J.T. Merrill, V.J. Davis, and W.L. Chameides, Airborne measurements of dimethylsulfide, sulfur dioxide, and aerosol ions over the Southern Ocean South of Australia, *J. Atmos. Chem.*, *10*, 341-370, 1990.

Berresheim, H., M.O. Andreae, R.L. Iverson, and S.M. Li, Seasonal variations of dimethylsulfide emissions and atmospheric sulfur and nitrogen species over the western north Atlantic Ocean, *Tellus*, *43B*, 353-372, 1991.

Berresheim, H., F.L. Eisele, D.J. Tanner, L.M. McInnes, D.C. Ramsey-Bell, and D.S. Covert, Atmospheric sulfur chemistry and cloud condensation nuclei (CCN) concentrations over the northeastern Pacific coast, *J. Geophys. Res.*, *98*, 12,701-12,711, 1993.

Berresheim, H., P. Wine, and D. Davis, Sulfur in the atmosphere, in *Composition, Chemistry, and Climate of the Atmosphere*, edited by H. Singh, pp. 251-307, Van Nostrand Reinhold, New York, 1995.

Bottenheim, J.W., L.A. Barrie, E. Atlas, L.E. Heidt, H. Niki, R.A. Rasmussen, and P.B. Shepson, Depletion of lower tropospheric ozone during Arctic spring: the polar sunrise experiment 1988, *J. Geophys. Res.*, *95*, 18,555-18,568, 1990.

Bürgermeister, S., and H.-W. Georgii, Distribution of methanesulfonate, nss-sulfate and dimethylsulfide over the Atlantic and the North Sea, *Atmos. Environ.*, *25A* (3/4), 587-595, 1991.

Charlson, R.J., J.E. Lovelock, M.O. Andreae, and S.G. Warren, Oceanic phytoplankton, atmospheric sulphur, cloud albedo and climate, *Nature*, *326*, 655-661, 1987.

Chin, M., D.J. Jacob, G.M. Gardner, M.S. Foreman-Fowler, and P.A. Spiro, A global three-dimensional model of tropospheric sulfate, *J. Geophys. Res.*, *101*, 18,667-18,690, 1996.

Cruz, C.N., and S.N. Pandis, The effect of organic coatings on the cloud condensation nuclei activation of organic atmospheric aerosols, *J. Geophys. Res.*, *103*, 13,111-13,123, 1998.

Duce, R.A., and E.J. Hoffmann, Chemical fractionation at the air/sea interface, *Annu. Rev. Earth Planet. Sci.*, *4*, 187-228, 1976.

Duce, R.B., W.H. Zoller, and J.L. Moyers, Particulate and gaseous halogens in the Antarctic atmosphere, *J. Geophys. Res.*, *78*, 7802-7811, 1973.

Esteve, V., J. Rius, L.E. Ochando, and J.M. Amigó, Quantitative X-ray diffraction phase analysis of coarse airborne particulate collected by cascade impactor sampling, *Atmos. Environ.*, *31* (23), 3963-3967, 1997.

Fan, S.-M., and D.J. Jacob, Surface ozone depletion in Arctic spring sustained by bromine reactions on aerosol, *Nature*, *359*, 522-524, 1992.

Faust, B.C., and R.G. Zepp, Photochemistry of aqueous iron(III)-polycarboxylate complexes: roles in the chemistry of atmospheric and surface waters, *Environ. Sci. Technol.*, *27*, 2517-2522, 1993.

Findlater, J., A major low-level air current near the Indian Ocean during the northern summer, *Quart. J. R. Meteorol. Soc.*, *95*, 362-380, 1969.

Finlayson-Pitts, B.J., Reaction of NO_2 with NaCl and atmospheric implications of NOCl formation, *Nature*, *306*, 676-677, 1983.

Finlayson-Pitts, B.J., M.J. Ezell, and J.N. Pitts Jr., Formation of chemically active chlorine compounds by reactions of atmospheric NaCl particles with gaseous N_2O_5 and $ClONO_2$, *Nature*, *337*, 241-244, 1989.

Gao, Y., R. Arimoto, R.A. Duce, L.Q. Chen, M.Y. Zhou, and D.Y. Gu, Atmospheric non-sea-salt sulfate, nitrate and methanesulfonate over the China Sea, *J. Geophys. Res.*, *101*, 12,601-12,611, 1996.

Graedel, T.E., and W.C. Keene, Tropospheric budget of reactive chlorine, *Global Biogeochem. Cycles*, *9* (1), 47-77, 1995.

Graedel, T.E., and W.C. Keene, The budget and cycle of Earth's natural chlorine, *Pure Appl. Chem.*, *68* (9), 1689-1697, 1996.

Hoornaert, S., H. van Malderen, and R. van Grieken, Gypsum and other calcium-rich aerosol particles above the North Sea, *Environ. Sci. Technol.*, *30*, 1515-1520, 1996.

Hopke, P.K., Appendix: Selected Source Profiles, in *Receptor Modeling in Environmental Chemistry*, pp. 267-314, John Wiley & Sons, Inv., 1985.

Huebert, B.J., L. Zhuang, S. Howell, K. Noone, and B. Noone, Sulfate, nitrate, methanesulfonate, chloride, ammonium, and sodium measurements from ship, island, and aircraft during the Atlantic Stratocumulus Transition Experiment/Marine Aerosol Gas Exchange, *J. Geophys. Res.*, *101*, 4413-4423, 1996.

Hynes, A.J., P.H. Wine, and D.H. Semmes, Kinetics and mechanism of OH reactions with organic sulfides, *J. Phys. Chem.*, *90*, 4148-4156, 1986.

Kawamura, K., and K. Ikushima, Seasonal changes in the distribution of dicarboxylic acids in the urban atmosphere, *Environ. Sci. Technol.*, *27*, 2227-2235, 1993.

Keene, W.C., D.J. Jacob, and S.-M. Fan, New Directions: Reactive chlorine: A potential sink for dimethylsulfide and hydrocarbons in the marine boundary layer, *Atmos. Environ.*, *30* (6), i-iii, 1996.

Keene, W.C., A.A.P. Pszenny, J.N. Galloway, and M.E. Hawley, Sea-salt corrections and Interpretation of constituent ratios in marine precipitation, *J. Geophys. Res.*, *91*, 6647-6658, 1986.

Keene, W.C., A.A.P. Pszenny, D.J. Jacob, R.A. Duce, J.N. Galloway, J.J. Schultz-Tokos, H. Sievering, and J.F. Boatman, The geochemical cycling of reactive chlorine through the marine troposphere, *Global Biogeochem. Cycles*, *4* (4), 407-430, 1990.

Keene, W.C., R. Sander, A.A.P. Pszenny, R. Vogt, P.J. Crutzen, and J.N. Galloway, Aerosol pH in the marine boundary layer: A review and model evaluation, *J. Aerosol Sci.*, *29* (3), 339-356, 1998.

Kerminen, V.-M., M. Aurela, R.E. Hillamo, and A. Virkkula, Formation of particulate MSA: Deductions from size distribution measurements in the Finnish Arctic, *Tellus*, *49B*, 159-171, 1997.

Kerminen, V.-M., R.E. Hillamo, and A.S. Wexler, Model simulations on the variability of particulate MSA to non-sea-salt sulfate ratio in the marine atmosphere, *J. Atmos. Chem.*, *30*, 345-370, 1998a.

Kerminen, V.-M., K. Teinilä, R. Hillamo, and T. Pakkanen, Substitution of chloride in sea-salt particles by inorganic and organic anions, *J. Aerosol Sci.*, *29* (8), 929-942, 1998b.

Koga, S., and H. Tanaka, Simulations of seasonal variations of sulfur compounds in the remote marin atmosphere, *J. Atmos. Chem.*, *23*, 163-192, 1996.

Langer, S., B.T. McGovney, B.J. Finlayson-Pitts, and R.M. Moore, The dimethyl sulfide reaction with atomic chlorine and its implications for the budget of methyl chloride, *Geophys. Res. Lett.*, *23* (13), 1661-1664, 1996.

Martin, J.H., K.H. Coale, K.S. Johnson, S.E. Fitzwater, R.M. Gordon, and ....., Testing the iron hypothesis in ecosystems of the equatorial Pacific Ocean, *Nature*, *371*, 123-129, 1994.

Martin, J.H., and S.F. Fitzwater, Iron deficiency limits phytoplankton growth in the north-east Pacific subarctic, *Nature*, *331*, 341-342, 1988.

Martin, J.H., R.M. Gordon, and S.E. Fitzwater, The case of iron, *Limnol. Oceanogr.*, *36* (8), 1793-1802, 1991.

Matsumoto, K., H. Tanaka, I. Nagao, and Y. Ishizaka, Contribution of particulate sulfate and organic carbon to cloud condensation nuclei in the marine atmosphere, *Geophys. Res. Lett.*, *24* (6), 655-658, 1997.

McConnell, J.C., G.S. Henderson, L. Barrie, J. Bottenheim, H. Niki, C.H. Langford, and E.M.J. Templeton, Photochemical bromine production implicated in Arctic boundary -layer ozone depletion, *Nature*, *355*, 150-152, 1992.

McInnes, L.M., D.S. Covert, P.K. Quinn, and M.S. Germani, Measurements of chloride depletion and sulfur enrichment in individual sea-salt particles collected from the remote marine boundary layer, *J. Geophys. Res.*, *99*, 8257-8268, 1994.

Millero, F.J., and M.L. Sohn, *Chemical Oceanography*, CRC Press, 1992.

Naik, M.S., L.T. Khemani, G.A. Momin, P.S. Prakasa Rao, and P.D. Safai, Origin of calcium in marine aerosol over the Arabian Sea near the west coast of India, *J. Aerosol Sci.*, *22* (3), 365-372, 1991.

Novakov, T., and J.E. Penner, Large contribution of organic aerosols to cloud-condensation nuclei concentrations, *Nature*, *365*, 823-826, 1993.

O'Dowd, C., M.H. Smith, I.E. Consterdine, and J.A. Lowe, Marine aerosol, sea-salt, and the marine sulphur cycle: A short review, *Atmos. Environ.*, *31* (1), 73-80, 1997.

Patroescu, I.V., I. Barnes, K.H. Becker, and N. Mihalopoulos, FT-IR product study of the OH-initiated oxidation of DMS in the presence of NOx, *Atmos. Environ.*, *33*, 25-35, 1999.

Pehkonen, S.O., R. Siefert, Y. Erel, S. Webb, and M. Hoffmann, Photoreduction of iron oxyhydroxides in the presence of important atmospheric organic compounds, *Environ. Sci. Technol.*, *27* (10), 2056-2062, 1993.

Prospero, J.M., D.L. Savoie, E.S. Saltzman, and R. Larsen, Impact of oceanic sources of biogenic sulphur on sulphate aerosol concentrations at Mawson, Antarctica, *Nature*, *350*, 221-223, 1991.

Pszenny, A.A.P., Particle size distributions of methanesulfonate in the tropical Pacific marine boundary layer, *J. Atmos. Chem.*, *14*, 273-284, 1992.

Pszenny, A.A.P., A.J. Castelle, and J.N. Galloway, A study of the sulfur cycle in the Antarctic marine boundary layer, *J. Geophys. Res.*, *94*, 9818-9839, 1989.

Pszenny, A.A.P., W.C. Keene, D.J. Jacob, S. Fan, J.R. Maben, M.P. Zetwo, M. Springer-Young, and J.N. Galloway, Evidence of inorganic chlorine gases other than hydrogen chloride in marine surface air, *Geophys. Res. Lett.*, *20* (8), 699-702, 1993.

Qian, G.-W., and Y. Ishizaka, Electron microscope studies of methane sulfonic acid in individual aerosol particles, *J. Geophys. Res.*, *98*, 8459-8470, 1993.

Quinn, P.K., D.S. Covert, T.S. Bates, V.N. Kapustin, D.C. Ramsey-Bell, and L.M. McInnes, Dimethylsulfide/cloud condensation nuclei/climate system: Relevant size-resolved measurements of the chemical and physical properties of atmospheric aerosol particles, *J. Geophys. Res.*, *98*, 10,411-10,427, 1993.

Saltzman, E.S., D.L. Savoie, J.M. Prospero, and R.G. Zika, Atmospheric methanesulfonic acid and non-sea-salt sulfate at Fanning and American Samoa, *Geophys. Res. Lett.*, *12* (7), 437-440, 1985.

Saltzman, E.S., D.L. Savoie, R.G. Zika, and J.M. Prospero, Methane sulfonic acid in the marine atmosphere, *J. Geophys. Res.*, *88*, 10,897-10,902, 1983.

Sander, R., and P.J. Crutzen, Model study indicating halogen activation and ozone destruction in polluted air masses transported to the sea, *J. Geophys. Res.*, *101*, 9121-9138, 1996.

Savoie, D.L., and J.M. Prospero, Particle size distribution of nitrate and sulfate in the marine atmosphere, *Geophys. Res. Lett.*, *9* (10), 1207-1210, 1982.

Savoie, D.L., and J.M. Prospero, Comparison of oceanic and continental sources of non-sea-salt sulphate over the Pacific Ocean, *Nature*, *339*, 685-687, 1989.

Savoie, D.L., and J.M. Prospero, Non-sea-salt sulfate and methansulfonate at American Samoa, *J. Geophys. Res.*, *99*, 3587-3596, 1994.

Savoie, D.L., J.M. Prospero, R.J. Larsen, and E.S. Saltzman, Nitrogen and sulfur species in aerosols at Mawson, Antarctica, and their relationship to natural radionuclides, *J. Atmos. Chem.*, *14*, 181-204, 1992.

Savoie, D.L., J.M. Prospero, and R.T. Nees, Nitrate, non-sea-salt sulfate, and mineral aerosol over the northwestern Indian Ocean, *J. Geophys. Res.*, *92*, 933-942, 1987.

Savoie, D.L., J.M. Prospero, and E.S. Saltzman, Non-sea-salt sulfate and nitrate in trade wind aerosols at Barbados: Evidence for long-range transport, *J. Geophys. Res.*, *94*, 5,069-5,080, 1989.

Schlesinger, W.H., and A.E. Hartley, A global budget for atmospheric NH_3, *Biogeochem.*, *15*, 191-211, 1992.

Seinfeld, J.H., and S.N. Pandis, *Atmospheric Chemistry and Physics: From Air Pollution to Climate Change*, John Wiley & Sons, Inc., 1997.

Siefert, R.L., A.M. Johansen, and M.R. Hoffmann, Chemical characterization of ambient aerosol collected during the southwest- and inter-monsoon seasons over the Arabian Sea: Labile-Fe(II) and other trace metals, *J. Geophys. Res.*, *104* (3511-3526), 1999.

Siefert, R.L., S.O. Pehkonen, Y. Erel, and M.R. Hoffmann, Iron photochemistry of aqueous suspensions of ambient aerosol with added organic acids, *Geochim. Cosmochim. Acta*, *58* (15), 3271-3279, 1994.

Sievering, H., G. Ennis, E. Gorman, and C. Nagamoto, Size distribution and statistical analysis of nitrate, excess sulfate, and chloride deficit in the marine boundary layer during GCE/CASE/WATOX, *Global Biogeochem. Cycles*, *4* (4), 395-405, 1990.

Sisterson, D.L., A method for evaluation of acidic sulfate and nitrate in precipitation, *Water, Air, and Soil Pollut.*, *43*, 61-72, 1989.

Sørensen, S., H. Falbe-Hansen, M. Mangoni, J. Hjorth, and N.R. Jensen, Observation of DMSO and $CH_3S(O)OH$ from the gas phase reaction between DMS and OH, *J. Atmos. Chem.*, *24*, 299-315, 1996.

SPSS, SPSS for Windows, SPSS Inc., Chicago, 1997.

Stickel, R.E., J.M. Nicovich, Z. Zhao, and P.H. Wine, Kinetic and mechanistic study of the reaction of atomic chlorine with dimethyl sulfide, *J. Phys. Chem.*, *96*, 9875-9883, 1992.

Sturges, W.T., and L.A. Barrie, Chlorine, bromine and iodine in Arctic aerosols, *Atmos. Environ.*, *22* (6), 1179-1194, 1988.

Sturges, W.T., and G.E. Shaw, Halogens in aerosol in central Alaska, *Atmos. Environ.*, *27A* (17/18), 2969-2977, 1993.

Taylor, S.R., and S.M. McLennan, *The Continental Crust: Its Composition and Evolution*, Blackwell Scientific Publ., Oxford, England, 1985.

Turnipseed, A.A., S.B. Barone, and A.R. Ravishankara, Reaction of OH with Dimethyl Sulfide. 2. Products and Mechanism, *J. Phys. Chem.*, *100*, 14703-14713, 1996.

Turnipseed, A.A., and A.R. Ravishankara, The atmospheric oxidation of dimethyl sulfide: elementary steps in a complex mechanism, in *Dimethylsulfide: Oceans, Atmosphere and Climate*, edited by G.R.a.G. Angeletti, pp. 185-196, Kluwer Acad. Publ., Norwell, Mass., 1993.

van Malderen, H., R. van Grieken, T. Khodzher, V. Obolkin, and V. Potemkin, Composition of individual aerosol particles above Lake Baikal, Siberia, *Atmos. Env.*, *30* (9), 1453-1465, 1996.

Vogt, R., P.J. Crutzen, and R. Sander, A mechanism for halogen release in the remote marine boundary layer, *Nature*, *383*, 327-330, 1996.

Yin, F., D. Grosjean, and J.H. Seinfeld, Analysis of atmopheric photooxidation mechanisms for organosulfur compounds, *J. Geophys. Res.*, *91*, 14417-14438, 1986.

Yin, F., D. Grosjean, and J.H. Seinfeld, Photooxidation of dimethyl sulfide and dimethyl disulfide. I: mechanism development, *J. Atmos. Chem.*, *11*, 309-364, 1990.

Zar, J.H., *Biostatistical Analysis*, Prentice-Hall, Inc., Upper Saddle River, New Jersey, 1996.

Zhou, G., and K. Tazaki, Seasonal variation of gypsum in aerosol and its effect on the acidity of wet precipitation on the Sea side of Japan, *Atmos. Environ.*, *30* (19), 3301-3308, 1996.

3.7 Figure Captions

Figure 1. Five-day air mass back trajectories at four different final elevations (based on pressure) above sea level for: a) May 13, 1995, b) May 31, 1995, c) July 23, 1995, and d) August 5, 1995.

Figure 2. Sulfur species during inter- and SW-monsoons: SO_4^{2-}, NSS-SO_4^{2-} (a) and MSA (b) versus sample; NSS-SO_4^{2-} versus MSA (c).

Figure 3. NSS-SO_4^{2-} versus Pb (a) and versus NO_3^- (b) during inter- and SW-monsoons.

Figure 4. Observed (dotted line) and predicted (stacked bars) SO_4^{2-} versus sample. Stacked bars represent the various sources, which proportions were determined with linear regression analysis.

Figure 5. Bio-SO_4^{2-}/MSA weight ratios as a function of the average daily air temperature. Figure includes data from this study (filled squares) and from literature (open circles) [*Berresheim et al.*, 1989 (1); *Berresheim et al.*, 1990 (3); *Pszenny et al.*, 1989 (2); *Saltzman et al.*, 1985 (5); *Saltzman et al.*, 1983 (4)]

Figure 6. Total anion (dotted line) and total cation (solid line) charges versus sample, inter- and SW-monsoon data.

Figure 7. Br^-, SS-Br^- (a), and Cl^-, SS-Cl^- (b) during inter- and SW-monsoons, versus sample.

Figure 8. Cl^- deficit, anthropogenic-SO_4^{2-}+NO_3^-, and NO_3^- versus sample, inter- and SW-monsoon data.

Figure 9. Anion minus cations charges versus Cl^- deficit during inter- (open squares) and SW-monsoons (filled diamonds).

Figure 10. Organic anions versus sample: (a) acetate, (b) glycolate, (c) formate, (d) malonate, and (e) oxalate.

Figure 11. NH_4^+ versus sample during inter- and SW-monsoons.

Figure 12. Na (a), K (b), Mg (c), and Ca (d) as detected with IC (dotted lines) and ICMPS (stacked bars) versus inter- and SW-monsoon samples. See text for description on how proportions of stacked bars were determined.

Figure 13. Average relative contribution of major components to total suspended material collected during inter- (a) and SW-monsoons (b).

Table 1. Aerosol sample collection times and positions.

Label	Start Date/Time UTC	Stop Date/Time UTC	Latitude ° North	Longitude ° East
M32/3_01	05/08/95 09:16	05/08/95 17:26	16.3	65.0
M32/3_02	05/08/95 17:50	05/09/95 04:15	16.7	65.0
M32/3_03	05/09/95 06:40	05/09/95 12:00	18.0	65.0
M32/3_04	05/09/95 13:00	05/10/95 02:21	18.0	65.0
M32/3_05	05/10/95 02:40	05/10/95 07:15	18.0	65.0
M32/3_06	05/10/95 14:10	05/10/95 23:30	18.1	65.0
M32/3_07	05/11/95 04:15	05/11/95 22:30	18.1	65.0
M32/3_08	05/12/95 04:30	05/12/95 22:00	18.1	65.0
M32/3_09	05/13/95 03:10	05/13/95 22:15	18.1	65.0
M32/3_10	05/14/95 03:20	05/14/95 22:30	18.1	65.0
M32/3_11	05/15/95 03:15	05/15/95 16:55	18.1	65.0
M32/3_12	05/16/95 03:21	05/17/95 03:10	18.1	65.0
M32/3_13	05/17/95 03:35	05/18/95 03:05	16.9	65.0
M32/3_14	05/18/95 03:20	05/19/95 03:15	14.3	65.0
M32/3_15	05/19/95 03:35	05/20/95 03:10	11.5	65.0
M32/3_16	05/20/95 03:35	05/21/95 03:10	10.0	65.0
M32/3_17	05/21/95 03:20	05/22/95 03:15	10.0	65.0
M32/3_18	05/22/95 03:30	05/23/95 03:15	10.0	65.0
M32/3_19	05/23/95 03:25	05/24/95 03:15	10.0	65.0
M32/3_20	05/24/95 03:30	05/25/95 03:25	10.0	65.0
M32/3_21	05/25/95 03:35	05/26/95 03:15	9.9	65.0
M32/3_22	05/26/95 03:35	05/27/95 03:20	9.5	65.0
M32/3_23	05/27/95 03:35	05/28/95 03:15	7.5	65.0
M32/3_24	05/28/95 03:30	05/29/95 03:20	4.5	65.0
M32/3_25	05/29/95 04:00	05/29/95 21:00	3.0	65.0
M32/3_26	05/30/95 03:40	05/31/95 03:00	2.9	65.0
M32/3_27	05/31/95 07:25	05/31/95 21:55	1.4	65.0
M32/3_28	06/01/95 04:55	06/01/95 11:55	0.0	65.0
M32/5_01	07/15/95 09:10	07/16/95 10:19	0.0	65.0
M32/5_02	07/17/95 04:46	07/19/95 10:25	1.5	65.0
M32/5_03	07/19/95 10:43	07/20/95 04:02	3.1	65.0
M32/5_04	07/20/95 11:37	07/21/95 14:15	6.0	65.0
M32/5_05	07/23/95 01:02	07/24/95 02:40	10.0	65.0
M32/5_06	07/25/95 04:09	07/25/95 13:15	13.0	65.0
M32/5_07	07/25/95 23:57	07/27/95 11:15	14.5	64.7
M32/5_08	07/27/95 11:47	07/29/95 00:21	15.2	63.5
M32/5_09	07/29/95 00:33	07/30/95 04:05	16.1	62.0
M32/5_10	07/30/95 04:23	07/31/95 04:12	16.7	60.7
M32/5_11	07/31/95 04:30	08/01/95 03:14	17.1	59.8
M32/5_12	08/01/95 03:30	08/02/95 04:02	17.6	58.7
M32/5_13	08/02/95 04:27	08/03/95 05:15	18.4	57.5
M32/5_14	08/03/95 05:31	08/04/95 03:09	18.6	57.2
M32/5_15	08/04/95 03:22	08/05/95 13:57	18.4	57.3
M32/5_16	08/05/95 14:11	08/06/95 13:00	18.0	58.5
M32/5_17	08/06/95 13:52	08/07/95 10:09	17.4	59.6
M32/5_18	08/07/95 10:20	08/08/95 14:07	16.4	61.0
M32/5_19	08/08/95 23:29	08/10/95 03:41	16.2	61.5
M32/5_20	08/10/95 03:54	08/10/95 23:56	16.0	62.0

Table 2. Atmospheric anion and cation concentrations during inter- and SW-monsoons. Average (± standard deviation), minimum, and maximum concentrations (in ng m^{-3} unless otherwise indicated), and number of samples. (BDL = Below detection limit)

Species	Inter-monsoon				SW-monsoon			
	Average ± SD	Min.	Max.	No. sampl.	Average ± SD	Min.	Max.	No. sampl.
F^-	5.1 ± 2.8	1.5	10.3	28	2.1 ± 1.3	0.7	5.6	20
Cl^- (μg m^{-3})	4.1 ± 2.3	1.2	7.9	28	11.1 ± 4.8	2.5	18.3	20
NO_2^-	7.2 ± 8.7	BDL	28.7	28	18.6 ± 1.7	BDL	51.5	20
Br^-	0.5 ± 0.2	BDL	6.8	28	12.7 ± 13.9	BDL	34.1	20
NO_3^- (μg m^{-3})	1.23 ± 0.41	0.60	2.18	28	0.46 ± 0.12	0.23	0.64	20
SO_4^{2-} (μg m^{-3})	2.74 ± 1.47	0.49	5.24	28	2.44 ± 0.86	0.72	3.94	20
NSS-SO_4^{2-} (μg m^{-3})	2.08 ± 1.21	0.11	4.27	28	0.80 ± 0.18	0.38	1.13	20
Acetate	86.0 ± 174.8	BDL	734.6	28	19.5 ± 10.7	4.9	51.7	20
Glycolate	3.4 ± 4.1	BDL	13.0	28	8.7 ± 4.6	2.8	16.2	20
Formate	20.4 ± 19.0	4.6	73.6	28	21.1 ± 13.8	4.9	46.3	20
MSA	27.0 ± 15.3	BDL	62.1	28	51.3 ± 18.4	25.6	98.9	20
Malonate	56.1 ± 96.4	BDL	278.4	28	31.9 ± 32.1	BDL	84.7	20
Oxalate	88.5 ± 43.7	14.7	175.1	28	69.3 ± 35.8	18.2	179.2	20
Na^+ (μg m^{-3})	2.6 ± 1.4	0.9	5.4	28	6.5 ± 2.9	1.3	11.2	20
NH_4^+	290.5 ± 194.9	45.4	774.2	28	46.4 ± 31.5	21.6	154.6	20
K^+	175.7 ± 105.2	54.2	415.1	28	271.8 ± 144.5	BDL	571.3	20
Mg^{2+} (μg m^{-3})	0.31 ± 0.17	0.09	0.66	28	0.66 ± 0.30	0.10	1.09	20
Ca^{2+} (μg m^{-3})	1.06 ± 0.91	0.01	2.94	28	0.41 ± 0.25	0.03	0.87	20

Table 3. M32/3- Inter-monsoon. Model outputs from weighted linear least squares regressions with SO_4^{2-} being the dependent variable in all cases. Concentrations in units ng m^{-3}. 27 data points.

	Model summary Analysis of Variance				Unstandardized Coefficients		Standardized Coefficients			95% Confidence Interval for b	
Model #	**R^2**	**F**	**Sig.**	**Independent Variables**	**b_i**	**std. error**	**β_i**	**t**	**Sig.**	**Lower Bound**	**Upper Bound**
1	0.971	141.654	0.000	(constant)	26.859	128.870		0.201	0.843	-251.567	305.850
				MSA	17.489	133.884	0.222	3.444	0.002	6.929	28.048
				Na^+	0.251	0.056	0.254	4.501	0.000	0.135	0.367
				Al	-0.086	0.437	-0.230	-0.197	0.846	-0.994	0.822
				Pb	773.499	123.788	0.541	6.249	0.000	516.069	1030.930
				NSS-Ca^{2+}	0.334	0.158	0.218	2.110	0.047	0.005	0.663
2	0.971	185.147	0.000	(constant)	20.443	126.996		0.161	0.874	-242.931	283.817
				MSA	17.613	4.927	0.224	3.575	0.002	7.396	27.830
				Na^+	0.253	0.053	0.256	4.734	0.000	0.142	0.364
				Pb	761.153	104.407	0.532	7.290	0.000	544.626	977.681
				NSS-Ca^{2+}	0.309	0.090	0.201	3.424	0.002	0.122	0.495
3	**0.996**	**1395.823**	**0.000**	**MSA**	**17.699**	**4.793**	**0.190**	**3.693**	**0.001**	**7.783**	**27.614**
				Na^+	**0.256**	**0.049**	**0.248**	**5.243**	**0.000**	**0.155**	**0.357**
				Pb	**763.381**	**101.271**	**0.482**	**7.538**	**0.000**	**553.885**	**972.877**
				NSS-Ca^{2+}	**0.310**	**0.088**	**0.118**	**3.535**	**0.002**	**0.129**	**0.491**
4	0.987	434.410	0.000	MSA	35.719	7.251	0.383	4.926	0.000	20.720	50.719
				Na^+	0.319	0.087	0.309	3.678	0.001	0.140	0.499
				NO_3^-	0.280	0.195	0.108	1.438	0.164	-0.123	0.683
				NSS-Ca^{2+}	0.693	0.139	0.264	4.997	0.000	0.406	0.980

Table 4. M32/5- SW-monsoon. Model outputs from weighted linear least squares regressions with SO_4^{2-} being the dependent variable in all cases. Concentrations in units ng m^{-3}. 17 data points.

	Model summary Analysis of Variance				Unstandardized Coefficients		Standardized Coefficients			95% Confidence Interval for b	
Model #	**R^2**	**F**	**Sig.**	**Independent Variables**	**b_i**	**std. error**	**β_i**	**t**	**Sig.**	**Lower Bound**	**Upper Bound**
1	0.990	218.041	0.000	(constant)	264.514	165.401		1.599	0.138	-99.530	628.558
				MSA	3.848	6.120	0.039	0.629	0.542	-9.622	17.317
				Na^+	0.307	0.025	1.070	12.489	0.000	0.252	0.361
				Al	1.119	1.432	0.044	0.781	0.451	-2.033	4.271
				Pb	841.968	613.618	0.070	1.372	0.197	-508.596	2192.531
				NSS-Ca^{2+}	-0.882	0.326	-0.155	-2.709	0.020	-1.599	-0.165
2	0.983	129.105	0.000	(constant)	2.253	310.946		0.007	0.994	-701.155	705.661
				MSA	13.832	8.629	0.137	1.603	0.143	-5.689	33.353
				Na^+	0.248	0.029	0.863	8.549	0.000	0.182	0.313
				Pb	-201.701	938.192	-0.017	-0.215	0.835	-2324.037	1920.636
				NO_3^-	0.502	0.532	0.062	0.943	0.370	-0.701	1.704
3	**0.998**	**1520.912**	**0.000**	**MSA**	**13.495**	**4.407**	**0.245**	**3.062**	**0.011**	**3.795**	**23.195**
				Na^+	**0.251**	**0.016**	**0.687**	**15.641**	**0.000**	**0.216**	**0.287**
				NO_3^-	**0.443**	**0.299**	**0.086**	**1.484**	**0.166**	**-0.214**	**1.101**

Table 5. M32/5- SW-monsoon, three outliers. Model outputs from weighted linear least squares regressions with nss-nonanthrop.-SO_4^{2-} being the dependent variable in all cases. Concentrations in units ng m^{-3}. Three data points.

	Model summary Analysis of Variance				Unstandardized Coefficients		Standardized Coefficients			95% Confidence Interval for b	
Model #	**R^2**	**F**	**Sig.**	**Independent Variables**	**b**	**std. error**	**β**	**t**	**Sig.**	**Lower Bound**	**Upper Bound**
1	**0.991**	**214.169**	**0.005**	**MSA**	**6.802**	**0.465**	**0.995**	**14.635**	**0.005**	**4.802**	**8.802**

Table 6. Varimax rotated component matrix for inter-monsoon samples.

						Cumulative %		89.7%
	% variance	47.2	15.1	8.5	7.2	5.8	3.9	2.2
	Sampling/ Analysis techniques	**1 coarse crustal**	**2 sea salt**	**3 fine crustal**	**4**	**5 Fe**	**6 Cl- deficit**	**7**
Al coarse	HVDVI/ICPMS	**0.944**	0.203	0.185	-0.016	0.099	0.002	0.039
Al fine	HVDVI/ICPMS	0.297	-0.042	**0.916**	0.113	0.094	-0.056	0.131
Ca coarse	HVDVI/ICPMS	**0.917**	0.292	0.143	0.030	0.193	0.040	0.028
Ca fine	HVDVI/ICPMS	0.334	0.138	**0.776**	0.362	0.262	-0.035	0.086
Fe coarse	HVDVI/ICPMS	0.385	0.224	0.061	0.031	**0.791**	-0.119	-0.041
Fe fine	HVDVI/ICPMS	0.180	0.321	0.220	-0.136	**0.763**	0.184	0.198
K coarse	HVDVI/ICPMS	**0.871**	0.451	0.048	-0.028	0.062	0.046	0.011
K fine	HVDVI/ICPMS	0.070	0.030	**0.901**	-0.005	0.117	0.086	0.132
Mg coarse	HVDVI/ICPMS	**0.757**	**0.594**	0.068	-0.101	0.182	-0.082	-0.005
Mg fine	HVDVI/ICPMS	0.350	0.354	**0.742**	0.292	0.265	-0.051	0.122
Na coarse	HVDVI/ICPMS	0.366	**0.872**	-0.119	-0.164	0.041	-0.082	-0.100
Na fine	HVDVI/ICPMS	0.189	**0.701**	0.438	0.110	0.362	0.115	0.141
Pb coarse	HVDVI/ICPMS	**0.699**	-0.054	**0.469**	-0.134	0.022	0.011	0.057
Pb fine	HVDVI/ICPMS	0.459	**0.645**	0.489	-0.099	0.019	0.001	-0.009
Ti coarse	HVDVI/ICPMS	**0.959**	0.119	0.152	-0.002	0.052	0.013	-0.005
Ti fine	HVDVI/ICPMS	0.010	0.139	**0.857**	-0.135	-0.095	-0.014	-0.127
V coarse	HVDVI/ICPMS	**0.913**	0.157	0.308	0.007	0.078	-0.018	0.022
V fine	HVDVI/ICPMS	0.358	0.194	**0.830**	-0.143	0.012	0.003	-0.104
Ca^{2+}	Low Vol. Coll./IC	**0.720**	0.225	**0.506**	0.247	0.037	-0.107	0.232
NSS-Ca^{2+}	Low Vol. Coll./IC	**0.723**	0.172	**0.513**	0.253	0.029	-0.118	0.232
K^+	Low Vol. Coll./IC	0.438	**0.796**	0.283	0.216	0.117	-0.036	-0.089
Mg^{2+}	Low Vol. Coll./IC	0.424	**0.823**	0.219	0.121	0.113	0.053	0.180
Na^+	Low Vol. Coll./IC	0.222	**0.926**	0.064	0.010	0.137	0.095	0.108
NH_4^+	Low Vol. Coll./IC	-0.303	0.517	0.271	-0.587	-0.011	-0.098	-0.163
NO_2^-	Low Vol. Coll./IC	-0.024	**0.647**	-0.105	-0.284	0.327	0.113	-0.254
NO_3^-	Low Vol. Coll./IC	**0.600**	-0.114	**0.681**	0.189	-0.073	-0.017	-0.188
SO_4^{2-}	Low Vol. Coll./IC	**0.505**	**0.711**	0.454	-0.061	0.053	-0.062	-0.046
NSS-SO_4^{2-}	Low Vol. Coll./IC	**0.547**	**0.588**	**0.534**	-0.077	0.024	-0.104	-0.089
NO_3^-+anthr-SO_4^{2-}	Low Vol. Coll./IC	**0.607**	0.439	**0.625**	-0.027	-0.007	-0.024	-0.041
MSA	Low Vol. Coll./IC	0.088	**0.764**	0.279	-0.399	0.096	-0.307	-0.137
Cl^-	Low Vol. Coll./IC	0.220	**0.927**	0.075	0.028	0.154	-0.042	0.094
Cl^- deficit	Low Vol. Coll./IC	0.153	**0.589**	-0.013	-0.086	0.006	**0.737**	0.138
% Cl^- deficit	Low Vol. Coll./IC	-0.098	-0.305	-0.030	-0.103	-0.028	**0.849**	-0.112
Cat.-An. charges	Low Vol. Coll./IC	0.487	0.189	0.349	0.226	0.017	0.278	0.596
Br^-	Low Vol. Coll./IC	0.219	0.421	0.196	**0.537**	-0.132	0.381	-0.063
F^-	Low Vol. Coll./IC	0.222	0.534	-0.006	-0.251	-0.423	0.135	-0.443
Acetate	Low Vol. Coll./IC	**0.558**	0.000	0.033	-0.022	0.042	-0.637	-0.385
Formate	Low Vol. Coll./IC	0.019	**0.529**	0.140	0.194	**0.666**	-0.175	-0.185
Glycolate	Low Vol. Coll./IC	-0.048	-0.103	0.108	**0.842**	0.069	-0.209	0.062
Malonate	Low Vol. Coll./IC	**0.771**	0.118	0.269	0.356	0.026	-0.141	-0.338
Oxalate	Low Vol. Coll./IC	**0.508**	**0.660**	0.440	-0.038	0.097	0.039	0.114
windspeed ($m\ s^{-1}$)	ships met. Data	-0.324	**0.735**	-0.021	0.404	0.313	-0.005	0.105
Relative Humidity	ships met. Data	-0.313	**0.528**	-0.279	0.253	0.358	-0.130	0.321

Table 7. Varimax rotated component matrix for SW-monsoon samples.

						Cumulative %		92.1%
	% variance	47.6	15.8	9.6	7.1	5.4	3.6	3.1
	Sampling/ Analysis techniques	**1 sea salt**	**2 coarse crustal**	**3 fine crustal**	**4 Cl-deficit**	**5 MSA, V**	**6 anthrop.**	**7**
Al coarse	HVDVI/ICPMS	0.219	**0.914**	0.221	0.064	0.137	0.122	-0.043
Al fine	HVDVI/ICPMS	0.325	0.237	**0.836**	-0.029	0.220	0.204	0.078
Ca coarse	HVDVI/ICPMS	0.348	**0.869**	0.130	0.219	0.199	0.084	0.053
Ca fine	HVDVI/ICPMS	**0.670**	0.272	0.498	0.252	0.367	0.012	-0.050
Fe coarse	HVDVI/ICPMS	0.179	**0.930**	0.200	0.018	0.112	0.147	-0.035
Fe fine	HVDVI/ICPMS	0.250	0.148	**0.837**	-0.045	0.081	0.342	0.114
K coarse	HVDVI/ICPMS	0.356	**0.891**	0.040	0.100	0.133	0.034	0.128
K fine	HVDVI/ICPMS	**0.815**	0.211	0.376	0.113	0.222	0.085	0.083
Mg coarse	HVDVI/ICPMS	0.383	**0.846**	-0.018	0.147	0.226	0.106	0.153
Mg fine	HVDVI/ICPMS	**0.828**	0.253	0.307	0.094	0.312	0.016	0.135
Na coarse	HVDVI/ICPMS	0.360	**0.880**	-0.039	0.109	0.153	0.036	0.177
Na fine	HVDVI/ICPMS	**0.829**	0.267	0.296	0.067	0.305	-0.031	0.111
Pb coarse	HVDVI/ICPMS	0.382	**0.736**	0.061	-0.177	-0.221	-0.078	-0.127
Pb fine	HVDVI/ICPMS	-0.256	0.168	**0.449**	-0.331	0.013	**0.636**	-0.038
Ti coarse	HVDVI/ICPMS	0.046	**0.954**	0.115	-0.025	-0.004	0.064	-0.132
Ti fine	HVDVI/ICPMS	0.083	0.170	**0.863**	-0.357	0.011	0.022	-0.099
V coarse	HVDVI/ICPMS	0.010	0.290	0.314	-0.154	0.037	-0.104	0.848
V fine	HVDVI/ICPMS	0.268	0.013	0.253	-0.058	**0.896**	0.074	0.073
Ca^{2+}	Low Vol. Coll./IC	**0.669**	**0.439**	0.334	0.323	0.263	0.007	-0.239
NSS-Ca^{2+}	Low Vol. Coll./IC	0.430	**0.438**	0.480	0.356	0.321	-0.044	-0.340
K^+	Low Vol. Coll./IC	**0.842**	0.343	-0.006	0.354	0.107	0.108	-0.001
Mg^{2+}	Low Vol. Coll./IC	**0.882**	0.361	0.081	0.179	0.168	0.004	-0.050
Na^+	Low Vol. Coll./IC	**0.886**	0.352	0.090	0.214	0.133	0.045	-0.021
NH_4^+	Low Vol. Coll./IC	-0.056	-0.146	**0.803**	0.382	0.067	0.057	0.214
NO_2^-	Low Vol. Coll./IC	0.189	-0.098	-0.047	0.305	-0.360	0.253	0.692
NO_3^-	Low Vol. Coll./IC	0.284	0.137	**0.440**	-0.073	0.299	**0.683**	0.018
SO_4^{2-}	Low Vol. Coll./IC	**0.898**	0.353	0.063	0.117	0.133	0.140	0.025
NSS-SO_4^{2-}	Low Vol. Coll./IC	0.664	0.247	-0.071	-0.319	0.092	0.490	0.210
NO_3^- + anthr-SO_4^{2-}	Low Vol. Coll./IC	0.281	0.158	**0.476**	-0.082	0.023	**0.694**	0.060
MSA	Low Vol. Coll./IC	0.408	0.157	-0.002	-0.003	**0.836**	0.144	-0.087
Cl^-	Low Vol. Coll./IC	**0.897**	0.362	0.114	0.101	0.151	0.032	-0.044
Cl^- deficit	Low Vol. Coll./IC	0.423	0.134	-0.095	**0.811**	-0.036	0.104	0.131
% Cl^- deficit	Low Vol. Coll./IC	**0.507**	0.051	-0.304	**0.703**	0.090	-0.273	0.136
Cat.-An. charges	Low Vol. Coll./IC	0.271	0.166	0.043	**0.904**	0.040	-0.103	-0.049
Br^-	Low Vol. Coll./IC	**0.526**	0.260	0.273	0.047	0.352	-0.228	-0.483
F^-	Low Vol. Coll./IC	0.106	-0.164	**0.728**	-0.469	-0.022	0.176	0.280
Acetate	Low Vol. Coll./IC	-0.065	-0.017	0.399	-0.638	-0.037	**0.433**	0.282
Formate	Low Vol. Coll./IC	**0.453**	0.290	**0.726**	0.079	-0.029	0.074	-0.139
Glycolate	Low Vol. Coll./IC	0.333	0.186	**0.681**	-0.263	0.263	0.224	-0.177
Malonate	Low Vol. Coll./IC	0.417	0.318	0.232	0.275	**0.669**	0.087	-0.291
Oxalate	Low Vol. Coll./IC	**0.651**	0.334	0.175	0.322	0.058	**0.477**	0.097
windspeed ($m\ s^{-1}$)	ships met. Data	**0.823**	-0.084	0.312	0.150	0.202	0.136	-0.103
Relative Humidity	ships met. Data	**0.513**	0.320	-0.062	0.070	**0.688**	-0.045	-0.293

Figure 1

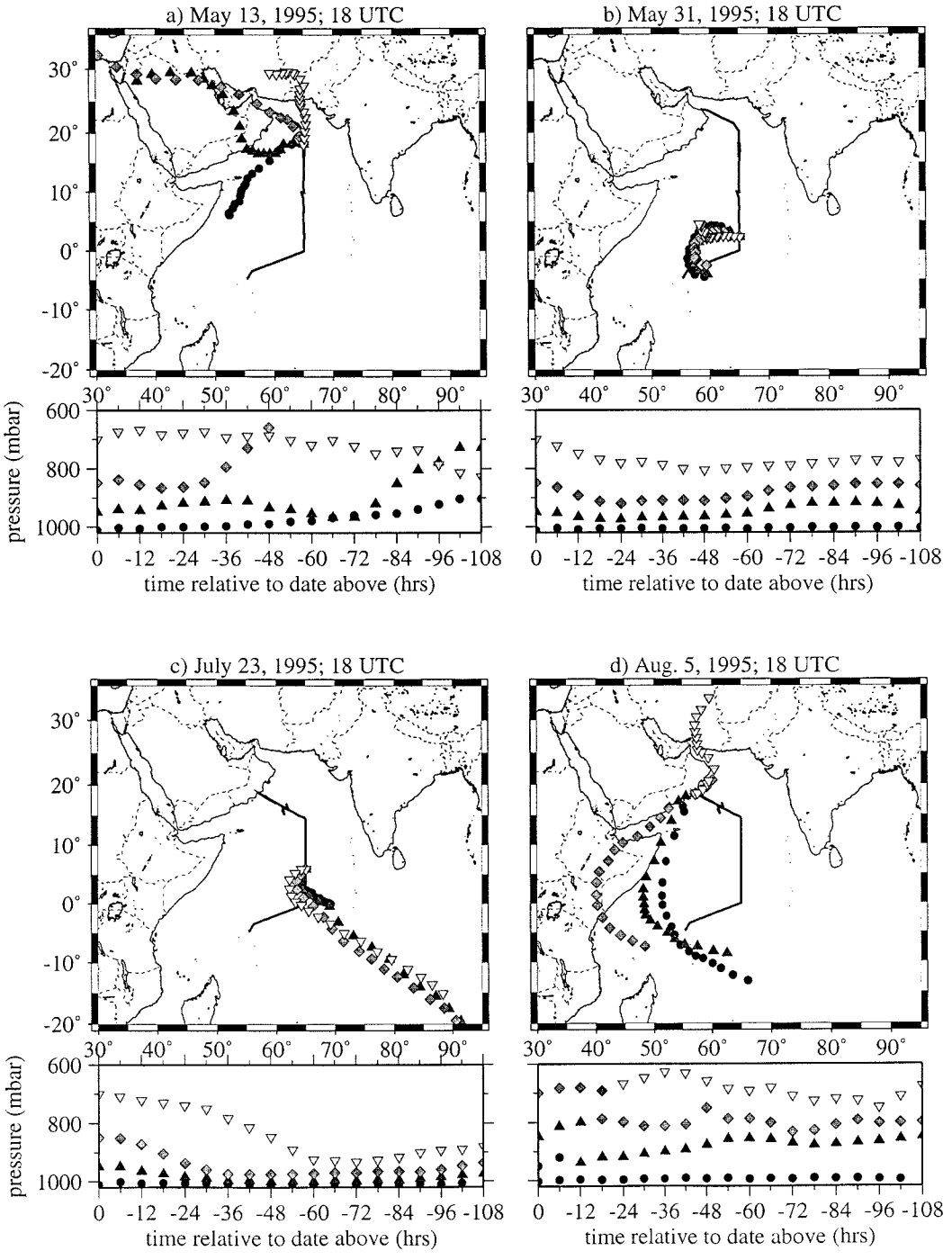
a) May 13, 1995; 18 UTC
b) May 31, 1995; 18 UTC
c) July 23, 1995; 18 UTC
d) Aug. 5, 1995; 18 UTC
30°
20°
10°
0°
-10°
-20°
30° 40° 50° 60° 70° 80° 90°
pressure (mbar)
600
800
1000
0 -12 -24 -36 -48 -60 -72 -84 -96 -108
time relative to date above (hrs)

Figure 2

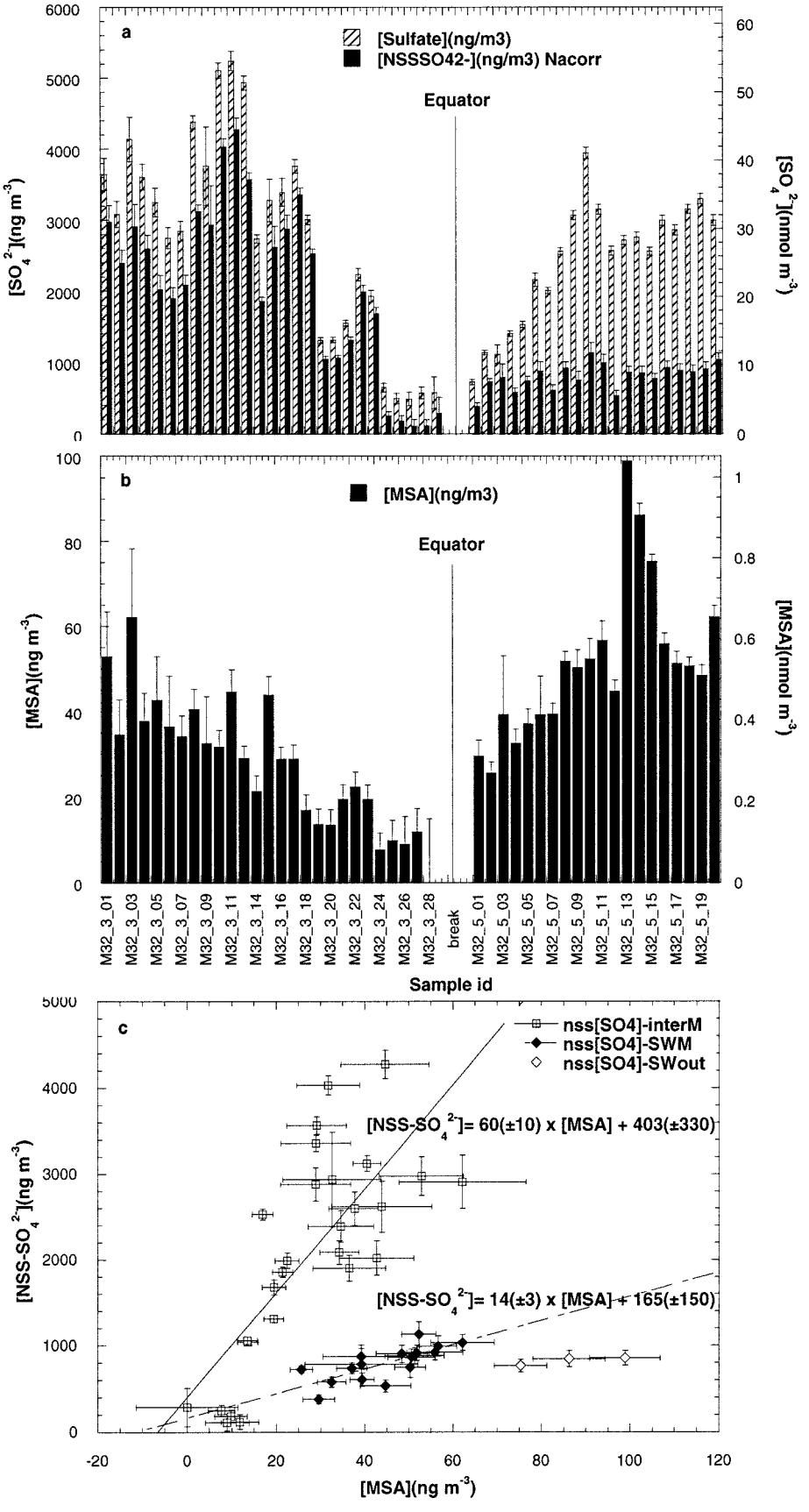
a
[Sulfate](ng/m3)
[NSSSO42-](ng/m3) Nacorr
Equator
[SO4 2-](ng m-3)
[SO4 2-](nmol m-3)
b
[MSA](ng/m3)
Equator
[MSA](ng m-3)
[MSA](nmol m-3)
M32_3_01
M32_3_03
M32_3_05
M32_3_07
M32_3_09
M32_3_11
M32_3_14
M32_3_16
M32_3_18
M32_3_20
M32_3_22
M32_3_24
M32_3_26
M32_3_28
break
M32_5_01
M32_5_03
M32_5_05
M32_5_07
M32_5_09
M32_5_11
M32_5_13
M32_5_15
M32_5_17
M32_5_19
Sample id
c
nss[SO4]-interM
nss[SO4]-SWM
nss[SO4]-SWout
[NSS-SO4 2-]= 60(±10) x [MSA] + 403(±330)
[NSS-SO4 2-]= 14(±3) x [MSA] + 165(±150)
[NSS-SO4 2-](ng m-3)
[MSA](ng m-3)

Figure 3

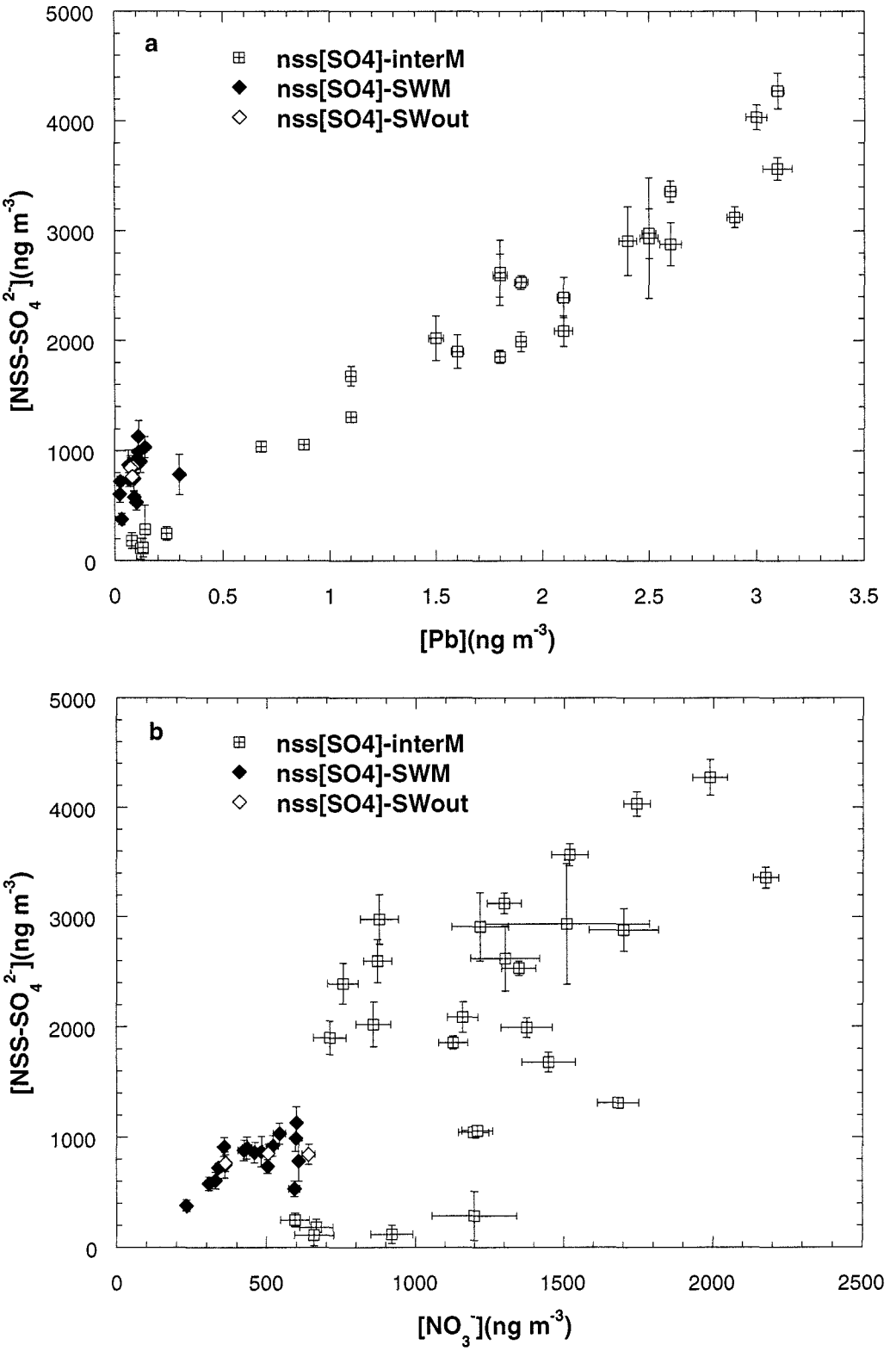
a
nss[SO4]-interM
nss[SO4]-SWM
nss[SO4]-SWout
[NSS-SO4 2-](ng m-3)
[Pb](ng m-3)
0
1000
2000
3000
4000
5000
0
0.5
1
1.5
2
2.5
3
3.5
b
nss[SO4]-interM
nss[SO4]-SWM
nss[SO4]-SWout
[NSS-SO4 2-](ng m-3)
[NO3-](ng m-3)
0
500
1000
1500
2000
2500

Figure 4

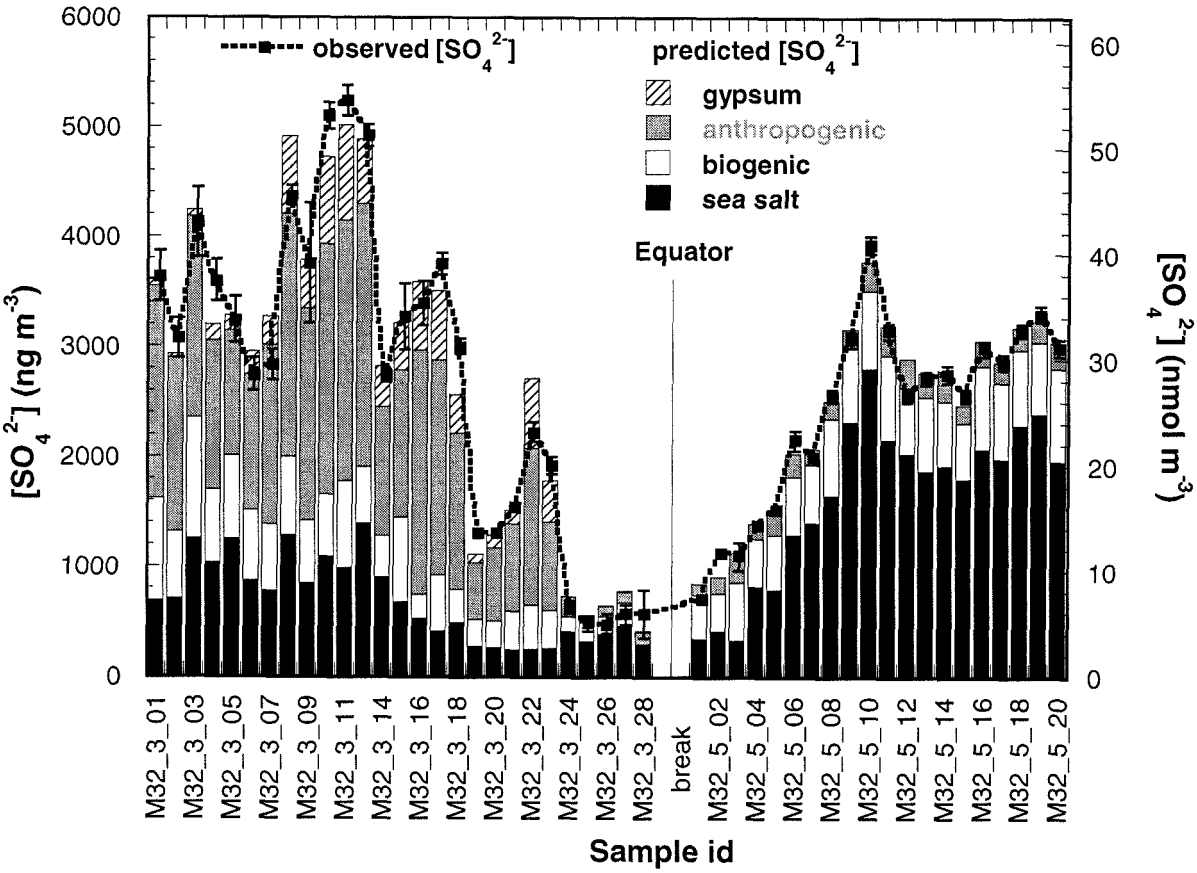
observed [SO4 2-]
predicted [SO4 2-]
gypsum
anthropogenic
biogenic
sea salt
Equator
[SO4 2-] (ng m-3)
[SO4 2-] (nmol m-3)
Sample id
M32_3_01
M32_3_03
M32_3_05
M32_3_07
M32_3_09
M32_3_11
M32_3_14
M32_3_16
M32_3_18
M32_3_20
M32_3_22
M32_3_24
M32_3_26
M32_3_28
break
M32_5_02
M32_5_04
M32_5_06
M32_5_08
M32_5_10
M32_5_12
M32_5_14
M32_5_16
M32_5_18
M32_5_20

Figure 5

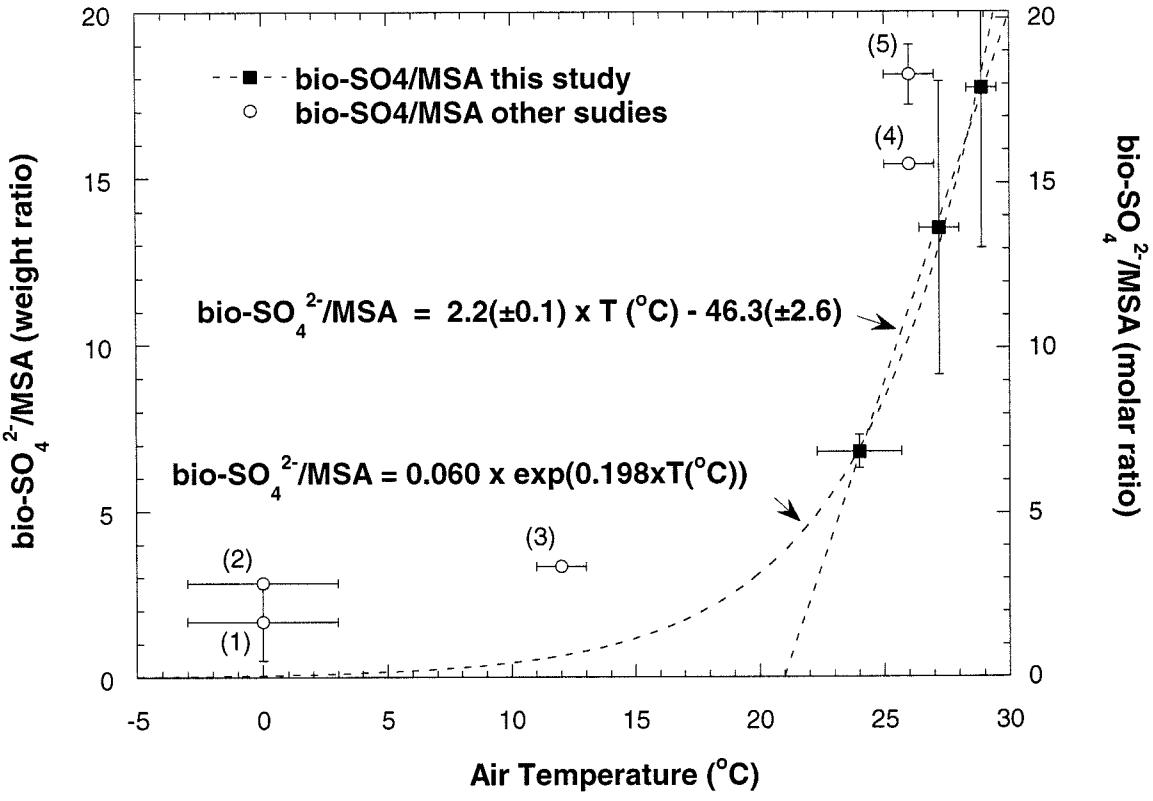
bio-SO4/MSA this study
bio-SO4/MSA other sudies
bio-SO4 2-/MSA = 2.2(±0.1) x T (°C) - 46.3(±2.6)
bio-SO4 2-/MSA = 0.060 x exp(0.198xT(°C))
(1)
(2)
(3)
(4)
(5)
bio-SO4 2-/MSA (weight ratio)
bio-SO4 2-/MSA (molar ratio)
Air Temperature (°C)
0
5
10
15
20
-5
0
5
10
15
20
25
30

Figure 6

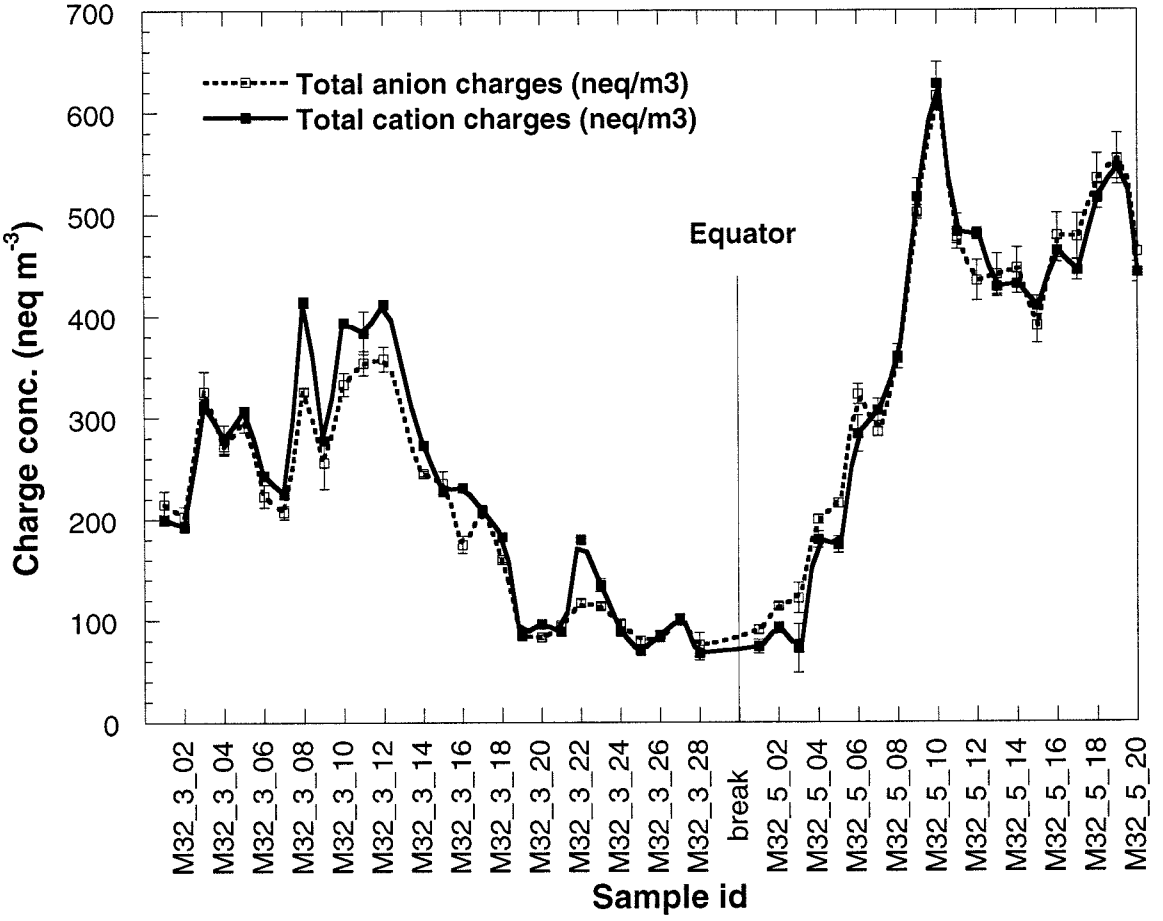
Total anion charges (neq/m3)
Total cation charges (neq/m3)
Equator
Charge conc. (neq m-3)
700
600
500
400
300
200
100
0
M32_3_02
M32_3_04
M32_3_06
M32_3_08
M32_3_10
M32_3_12
M32_3_14
M32_3_16
M32_3_18
M32_3_20
M32_3_22
M32_3_24
M32_3_26
M32_3_28
break
M32_5_02
M32_5_04
M32_5_06
M32_5_08
M32_5_10
M32_5_12
M32_5_14
M32_5_16
M32_5_18
M32_5_20
Sample id

Figure 7

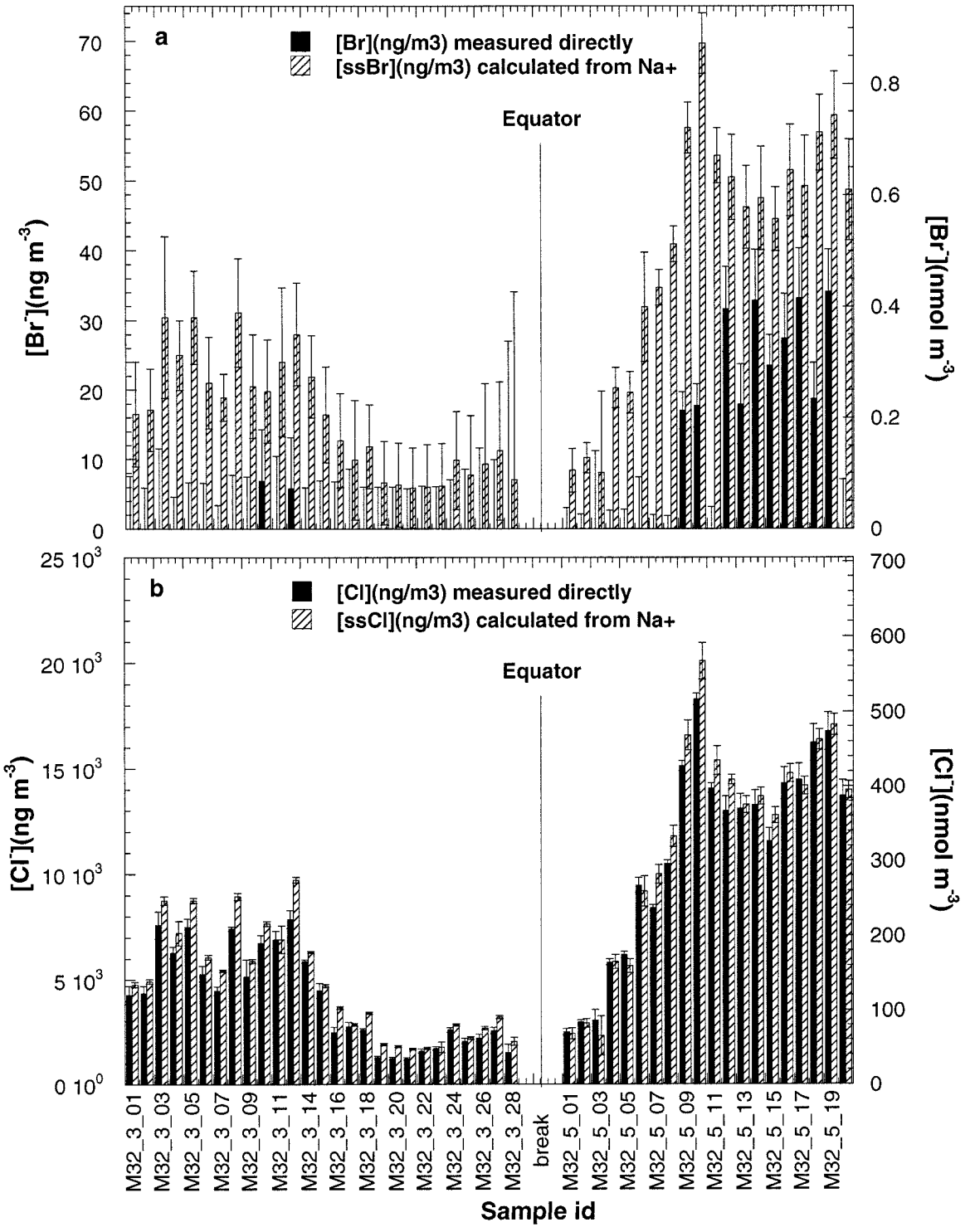
a
[Br](ng/m3) measured directly
[ssBr](ng/m3) calculated from Na+
Equator
[Br⁻](ng m⁻³)
[Br⁻](nmol m⁻³)
b
[Cl](ng/m3) measured directly
[ssCl](ng/m3) calculated from Na+
Equator
[Cl⁻](ng m⁻³)
[Cl⁻](nmol m⁻³)
M32_3_01
M32_3_03
M32_3_05
M32_3_07
M32_3_09
M32_3_11
M32_3_14
M32_3_16
M32_3_18
M32_3_20
M32_3_22
M32_3_24
M32_3_26
M32_3_28
break
M32_5_01
M32_5_03
M32_5_05
M32_5_07
M32_5_09
M32_5_11
M32_5_13
M32_5_15
M32_5_17
M32_5_19
Sample id

Figure 8

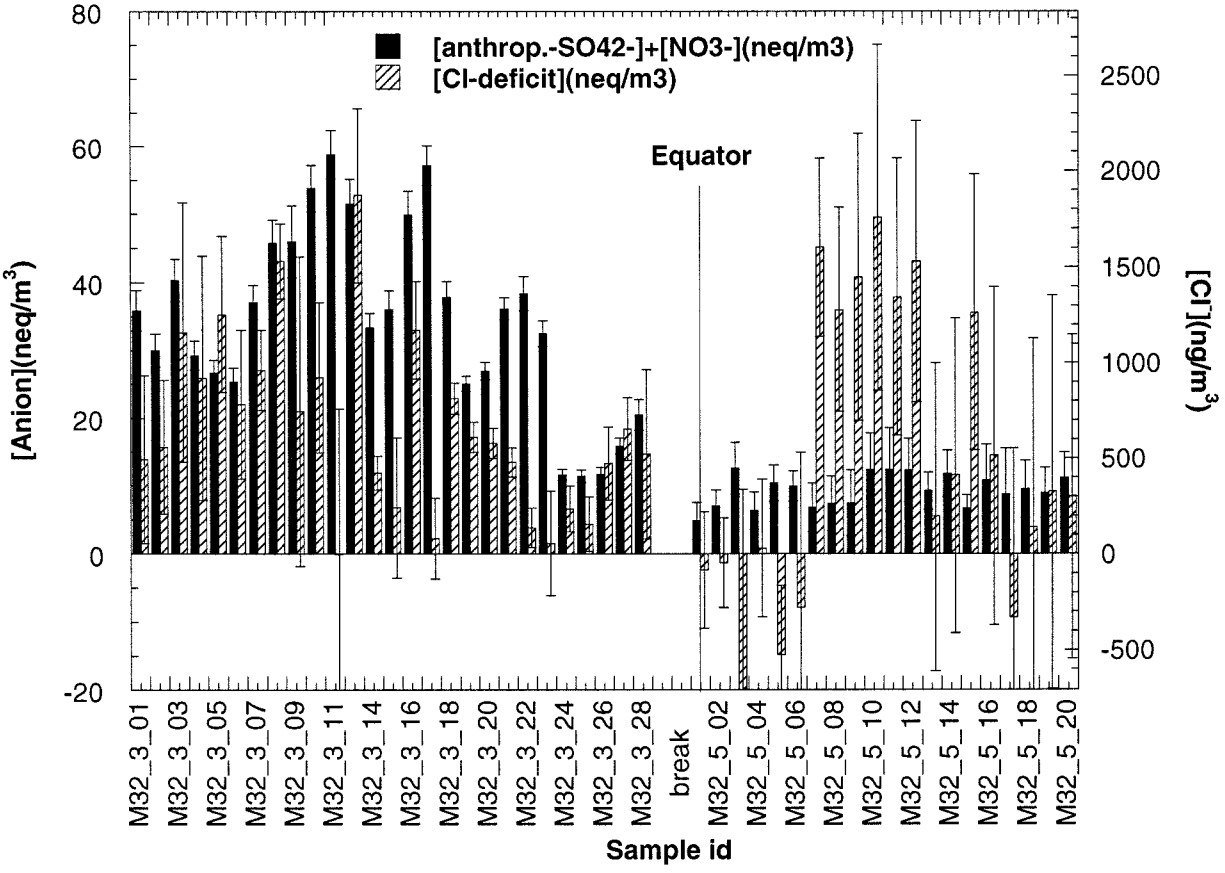
[anthrop.-SO42-]+[NO3-](neq/m3)
[Cl-deficit](neq/m3)
Equator
[Anion](neq/m3)
[Cl-](ng/m3)
Sample id
M32_3_01
M32_3_03
M32_3_05
M32_3_07
M32_3_09
M32_3_11
M32_3_14
M32_3_16
M32_3_18
M32_3_20
M32_3_22
M32_3_24
M32_3_26
M32_3_28
break
M32_5_02
M32_5_04
M32_5_06
M32_5_08
M32_5_10
M32_5_12
M32_5_14
M32_5_16
M32_5_18
M32_5_20

Figure 9

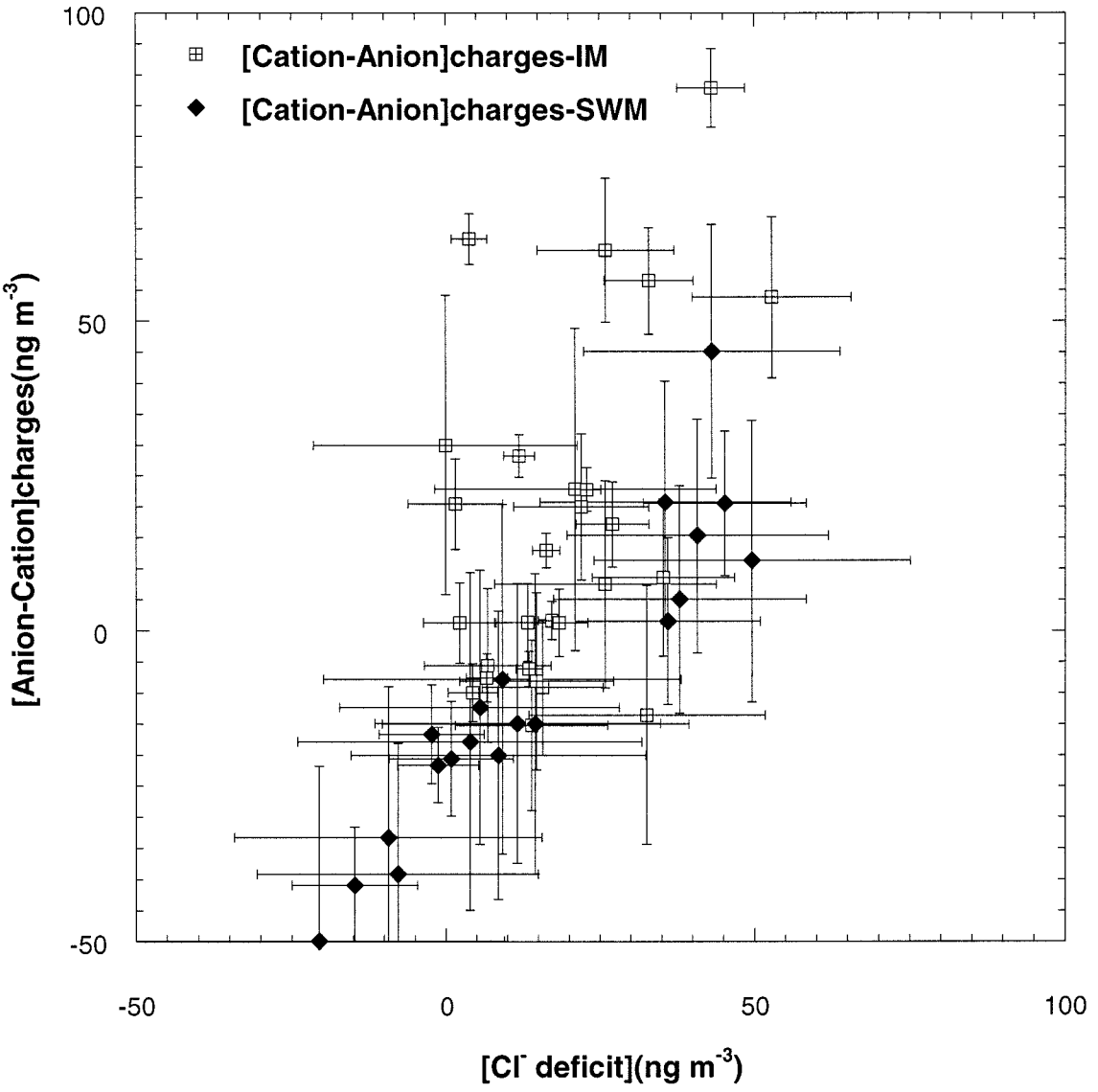
[Cation-Anion]charges-IM
[Cation-Anion]charges-SWM
[Anion-Cation]charges(ng m-3)
[Cl- deficit](ng m-3)
100
50
0
-50
-50
0
50
100

Figure 10

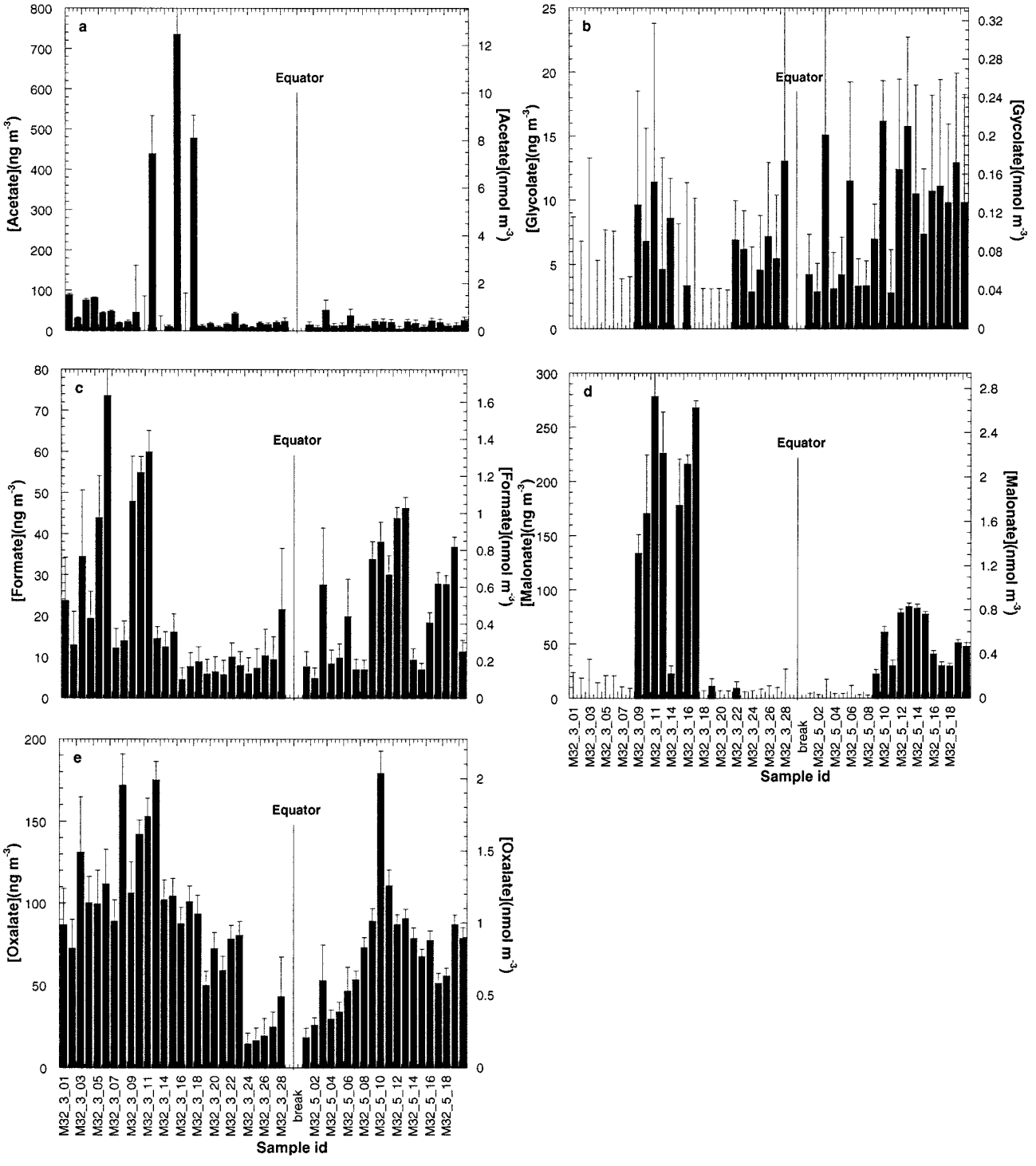
a
Equator
[Acetate](ng m-3)
[Acetate](nmol m-3)
b
Equator
[Glycolate](ng m-3)
[Glycolate](nmol m-3)
c
Equator
[Formate](ng m-3)
[Formate](nmol m-3)
d
Equator
[Malonate](ng m-3)
[Malonate](nmol m-3)
e
Equator
[Oxalate](ng m-3)
[Oxalate](nmol m-3)
M32_3_01
M32_3_03
M32_3_05
M32_3_07
M32_3_09
M32_3_11
M32_3_14
M32_3_16
M32_3_18
M32_3_20
M32_3_22
M32_3_24
M32_3_26
M32_3_28
break
M32_5_02
M32_5_04
M32_5_06
M32_5_08
M32_5_10
M32_5_12
M32_5_14
M32_5_16
M32_5_18
Sample id

Figure 11

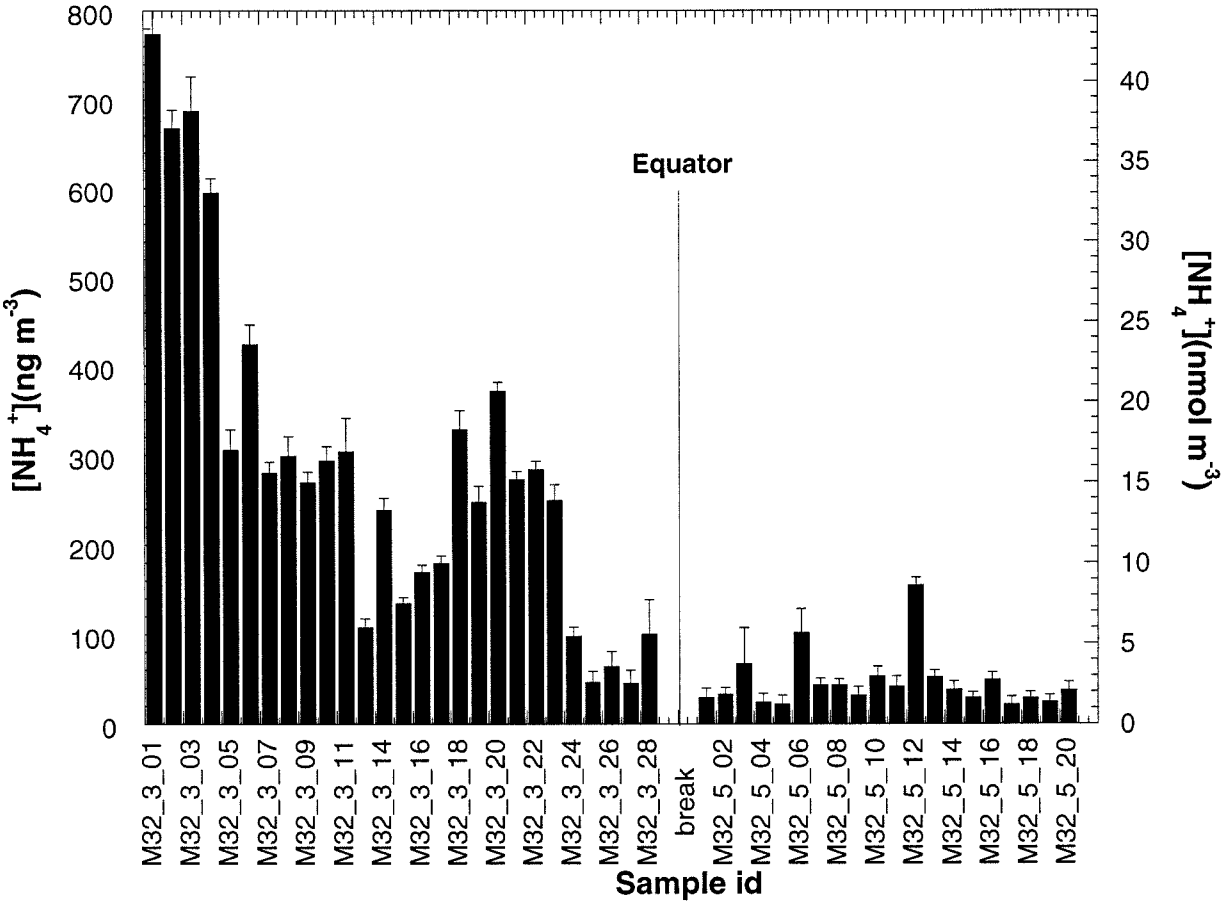
800
700
600
500
400
300
200
100
0
[NH4+](ng m-3)
40
35
30
25
20
15
10
5
0
[NH4+](nmol m-3)
Equator
M32_3_01
M32_3_03
M32_3_05
M32_3_07
M32_3_09
M32_3_11
M32_3_14
M32_3_16
M32_3_18
M32_3_20
M32_3_22
M32_3_24
M32_3_26
M32_3_28
break
M32_5_02
M32_5_04
M32_5_06
M32_5_08
M32_5_10
M32_5_12
M32_5_14
M32_5_16
M32_5_18
M32_5_20
Sample id

Figure 12

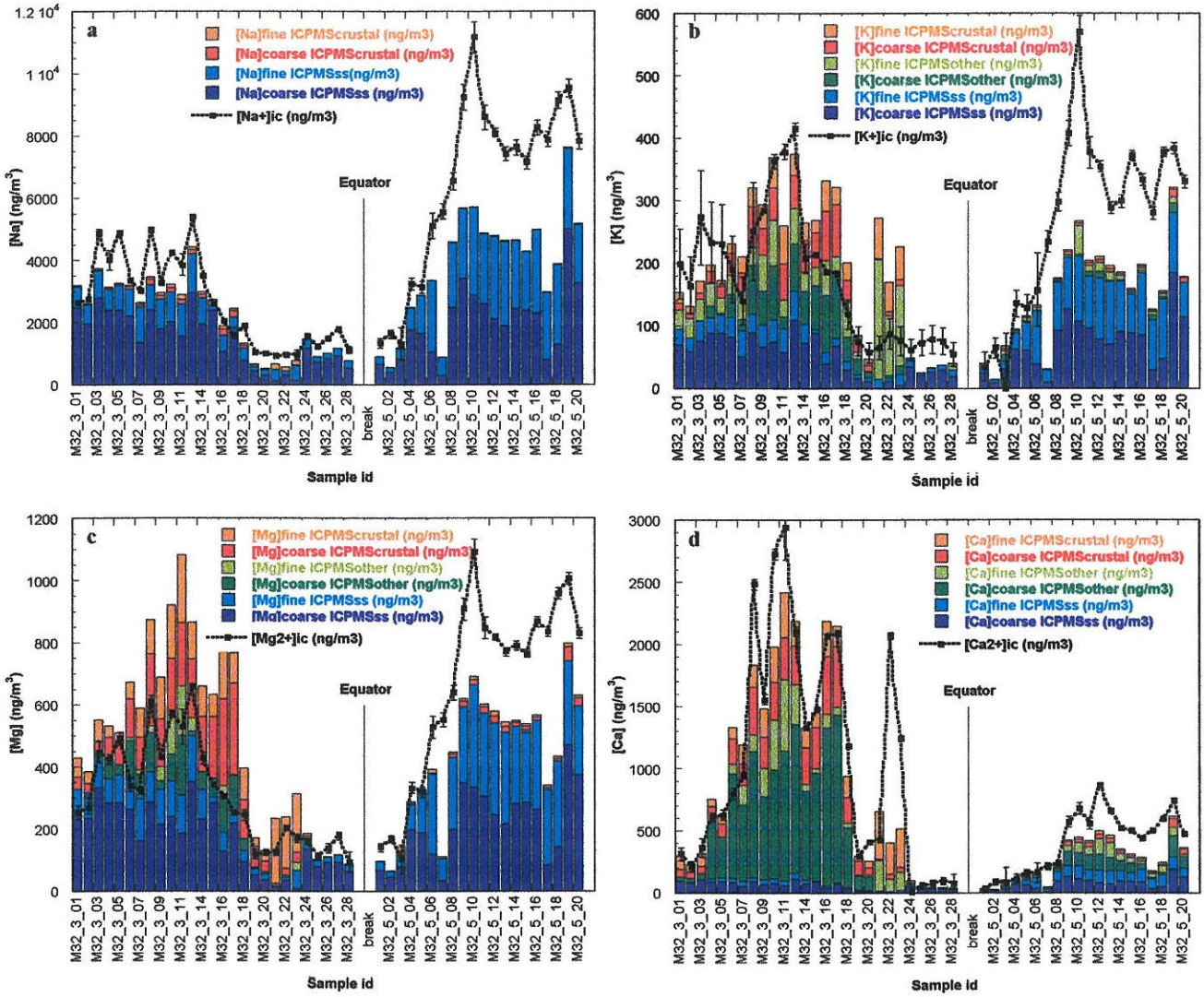
a
[Na]fine ICPMScrustal (ng/m3)
[Na]coarse ICPMScrustal (ng/m3)
[Na]fine ICPMSss(ng/m3)
[Na]coarse ICPMSss (ng/m3)
[Na+]ic (ng/m3)
Equator
[Na] (ng/m3)
1.2 10^4
1 10^4
8000
6000
4000
2000
0
b
[K]fine ICPMScrustal (ng/m3)
[K]coarse ICPMScrustal (ng/m3)
[K]fine ICPMSother (ng/m3)
[K]coarse ICPMSother (ng/m3)
[K]fine ICPMSss (ng/m3)
[K]coarse ICPMSss (ng/m3)
[K+]ic (ng/m3)
Equator
[K] (ng/m3)
600
500
400
300
200
100
0
c
[Mg]fine ICPMScrustal (ng/m3)
[Mg]coarse ICPMScrustal (ng/m3)
[Mg]fine ICPMSother (ng/m3)
[Mg]coarse ICPMSother (ng/m3)
[Mg]fine ICPMSss (ng/m3)
[Mg]coarse ICPMSss (ng/m3)
[Mg2+]ic (ng/m3)
Equator
[Mg] (ng/m3)
1200
1000
800
600
400
200
0
d
[Ca]fine ICPMScrustal (ng/m3)
[Ca]coarse ICPMScrustal (ng/m3)
[Ca]fine ICPMSother (ng/m3)
[Ca]coarse ICPMSother (ng/m3)
[Ca]fine ICPMSss (ng/m3)
[Ca]coarse ICPMSss (ng/m3)
[Ca2+]ic (ng/m3)
Equator
[Ca] (ng/m3)
3000
2500
2000
1500
1000
500
0
M32_3_01
M32_3_03
M32_3_05
M32_3_07
M32_3_09
M32_3_11
M32_3_14
M32_3_16
M32_3_18
M32_3_20
M32_3_22
M32_3_24
M32_3_26
M32_3_28
break
M32_5_02
M32_5_04
M32_5_06
M32_5_08
M32_5_10
M32_5_12
M32_5_14
M32_5_16
M32_5_18
M32_5_20
Sample id

Figure 13

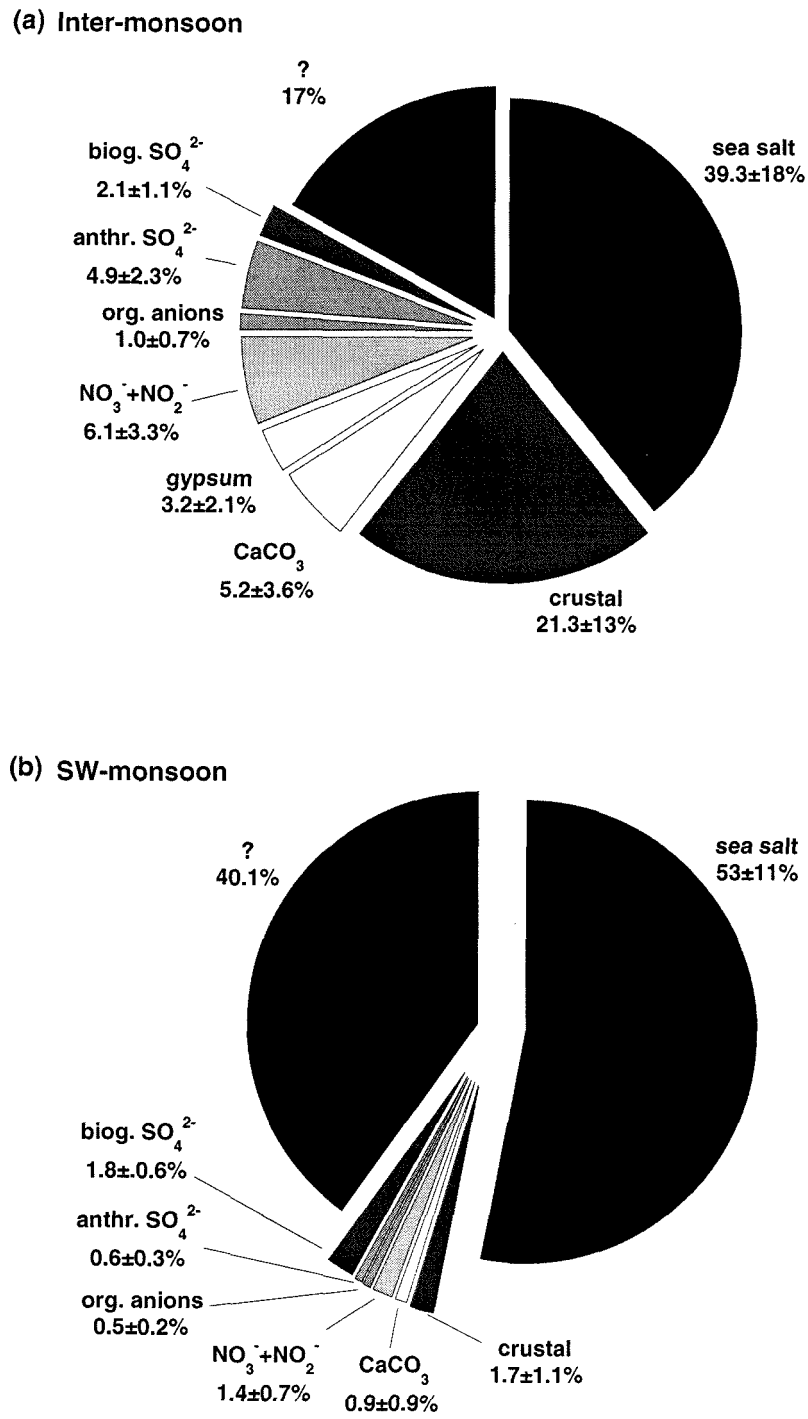
(a) Inter-monsoon
?
17%
sea salt
39.3±18%
biog. SO_4^{2-}
2.1±1.1%
anthr. SO_4^{2-}
4.9±2.3%
org. anions
1.0±0.7%
NO_3^-+NO_2^-
6.1±3.3%
gypsum
3.2±2.1%
$CaCO_3$
5.2±3.6%
crustal
21.3±13%
(b) SW-monsoon
?
40.1%
sea salt
53±11%
biog. SO_4^{2-}
1.8±.0.6%
anthr. SO_4^{2-}
0.6±0.3%
org. anions
0.5±0.2%
NO_3^-+NO_2^-
1.4±0.7%
$CaCO_3$
0.9±0.9%
crustal
1.7±1.1%

Chapter 4

Chemical composition of aerosols collected over the tropical North Atlantic Ocean

[Anne M. Johansen, Ronald L. Siefert and Michael R. Hoffmann, submitted to the *Journal of Geophysical Research*]

4.1 Abstract

Ambient aerosol samples were collected over the tropical Northern Atlantic Ocean during the month of April of 1996 onboard the R/V Seward Johnson. Dichotomous high volume collector samples were analyzed for ferrous iron immediately after collection, while trace metals, anions and cations were determined upon return to the lab. Data is analyzed with the aid of enrichment factor, principal component, and weighted multiple linear regression analyses. Average mineral aerosol concentrations amounted to 19.3 ± 16.4 μg m^{-3} whereby the chemical characteristics and air mass back trajectories indicated the dust to be of a typical shale composition and Saharan origin. Calcite accounted for 3.0 and 7.9% of the mineral aerosol during the first and second halves of the cruise, respectively. Total iron concentrations (averaging 0.84 ± 0.61 μg m^{-3}) are crustal derived, of which 0.51 ± 0.56% is readily released as Fe(II). 86% of this Fe(II) is present in the fine (< 3 μm diameter) aerosol fraction and correlates with NSS-SO_4^{2-} and oxalate. Approximately 23% of the measured NSS-SO_4^{2-} in both size fractions appears to be biogenically derived and the rest is of anthropogenic nature. Biogenic SO_4^{2-}/MSA ratios could not be easily extracted by employing a multiple linear regression analysis analogous to Johansen et al. [*Johansen et al.*, 1999], possibly due to the varying characteristics of the aerosol chemistry and air temperature during the cruise. Because of the presence of anthropogenic SO_4^{2-}, the NSS-SO_4^{2-}/MSA ratio, 37.4 ± 16.4, is elevated over what would be expected if the NSS-SO_4^{2-} were purely biogenic. Cl^- depletion is seen in all samples and averages 18.3 ± 9.1%. The release of Cl from the aerosol phase appears to occur through acid displacement reactions with primarily HNO_3 in the coarse and H_2SO_4 in the fine fraction.

4.2 Introduction

The present study focuses on the chemical characterization of the ambient aerosol over the Atlantic during the month of April of 1996. It is part of a multidisciplinary effort to observe a possible link between trace metal abundance, its speciation in the atmosphere and phytoplankton productivity. Specific focus was directed to the N_2 fixing cyanobacterium *Trichodesmium erythraeum*, which was studied by several groups aboard the ship.

The long-range atmospheric transport of weathered crustal material from the continents supplies a major portion of the non-biogenic sediments that accumulate on the sea floor. Mineralogical similarities between the composition of African dust and sediments of the North Atlantic [*Delaney et al.*, 1967] have confirmed that the arid regions of northern Africa, especially the Sahara and Sahel, are the source regions for atmospheric dust that reaches the North Atlantic Ocean. Information of the flux of mineral aerosol in marine sediments has also been used in the field of paleoclimate.

Considerable evidence, mainly provided by Prospero and colleagues, demonstrates that Saharan dust reaches the Caribbean [*Prospero et al.*, 1970; *Prospero and Carlson*, 1972; *Talbot et al.*, 1990], western North Atlantic [*Duce et al.*, 1975], southern North America [*Savoie and Prospero*, 1977] and the northeastern South America [*Prospero et al.*, 1981; *Swap et al.*, 1992; *Talbot et al.*, 1990]. The deposition of mineral aerosol is also evident in the chemistry of island soils of the Atlantic and Caribbean regions [*Chester et al.*, 1972; *Muhs et al.*, 1990; *Muhs et al.*, 1987; *Paquet et al.*, 1984; *Schütz and Sebert*, 1987]. Dust collection over the Atlantic Ocean and in the Caribbean was initiated in the late sixties [*Chester et al.*, 1972; *Delaney et al.*, 1967; *Prospero*, 1968] and continues to be the focus of many research groups. The transport mechanism by which African dust is carried to the west

seems well understood [*Chiapello et al.*, 1997; *Prospero and Nees*, 1977; *Schütz*, 1980]. Models [*D'Almeida*, 1986] and aerosol optical thickness data of the dust and its transport [*Swap et al.*, 1996] have further elucidated the seasonal and spatial variability of the mineral dust over the Atlantic Ocean.

Many atmospheric and oceanic processes are affected by the transport and deposition of mineral dust. The annual production of aeolian material from North Africa was estimated at approximately 400-700 Tg/yr [*D'Almeida*, 1987; *Schütz et al.*, 1981]. Although the mass scattering efficiency of mineral aerosol is estimated at about ¼ of that for non-sea-salt sulfate [*Li et al.*, 1996], the large mass concentrations of mineral aerosol indicate that their contribution and importance to the total burden of tropospheric aerosols has been underestimated so far, especially in regions such as the tropical and subtropical North Atlantic [*Andreae*, 1996; *D'Almeida*, 1987; *D'Almeida*, 1986; *Li et al.*, 1996; *Schollaert and Merrill*, 1998; *Tegen and Fung*, 1995; *Tegen et al.*, 1996]. In the context of biogeochemical cycles, the dissolution of mineral aerosol during atmospheric transport and after air-to-sea transfer releases important trace metals into surface waters that play an important role in phytoplantkton metabolism. Recent studies have found Fe to be a rate-limiting nutrient to primary phytoplankton growth in certain regions of the open ocean [*Cooper et al.*, 1996; *DiTullio et al.*, 1993; *Kolber et al.*, 1994; *Martin et al.*, 1994; *Martin and Fitzwater*, 1988; *Martin et al.*, 1991; *Paerl et al.*, 1994; *Price et al.*, 1994], thus it has become the most studied trace metal.

Based on laboratory studies and field measurements the photoredox chemistry of ferric oxides and (oxy)hydroxides, which are believed to be the predominant forms of iron in the atmosphere, results in the production of ferrous iron (Fe(II)) in the presence of electron

donors such as organic acids [*Erel et al.*, 1993; *Faust and Hoigné*, 1990; *Faust and Zepp*, 1993; *Pehkonen et al.*, 1993; *Siefert et al.*, 1994; *Zuo*, 1995; *Zuo and Hoigné*, 1992; *Zuo and Hoigné*, 1994]. Iron is also known to catalyze the oxidation of S(IV) by oxygen [*Berglund and Elding*, 1995; *Berglund et al.*, 1993; *Conklin and Hoffmann*, 1988; *Faust and Allen*, 1994; *Kraft and van Eldik*, 1989; *Martin and Hill*, 1987] and to undergo fast redox cycling with Cu in surface waters [*Sedlak and Hoigné*, 1993; *Sedlak and Hoigné*, 1994]. Thus, despite the thermodynamic instability of the reduced from of iron, Fe(II) may be present in considerable amounts in atmospheric and surface waters. Fe(II) is far more soluble than Fe(III) and may therefore be more bioavailable in the surface water of the ocean. Although inorganic Fe(II) in sea water is rapidly oxidized by photo-induced H_2O_2, with a reaction half-time of a few minutes [*Millero et al.*, 1991; *Moffett and Zika*, 1987a], the newly precipitated Fe(III) will be finely dispersed and may therefore still be more bioavailable than the Fe(III) trapped in large particles of rapidly sinking crustal material. Numerous studies exist on the solubility of iron and its photochemical reactions in sea water [*Duce and Tindale*, 1991; *Kuma et al.*, 1996; *Miller and Bruland*, 1994; *Millero et al.*, 1995; *Moffett and Zika*, 1987a; *O'Sullivan et al.*, 1995; *Spokes and Liss*, 1995; *Voelker and Sedlak*, 1995; *Waite and Morel*, 1984; *Zhang and Terada*, 1994; *Zhuang et al.*, 1990]. However, Wells et al. [*Wells et al.*, 1995] reaffirm the existing gap in the knowledge about the different physico-chemical forms of iron in the ocean.

Most studies of trace metals in the atmosphere have largely focused on the determination of their adundance, particle-size distribution and sources while neglecting oxidation states of the transition metal. Few studies exist on the speciation of iron in fog [*Behra and Sigg*, 1990; *Erel et al.*, 1993; *Kotronarou and Sigg*, 1993; *Siefert et al.*, 1998;

Zuo, 1995] and in aerosols [*Kopcewicz and Kopcewicz*, 1991; *Kopcewicz and Kopcewicz*, 1992; *Kopcewicz and Kopcewicz*, 1998; *Siefert et al.*, 1999; *Siefert et al.*, 1994; *Siefert et al.*, 1996; *Zhu et al.*, 1993; *Zhu et al.*, 1997; *Zhuang et al.*, 1992b]. Several of the listed aerosol iron speciation studies were performed in remote oceanic regions [*Siefert et al.*, 1999; *Zhu et al.*, 1993; *Zhu et al.*, 1997; *Zhuang et al.*, 1992b]. Ferrous iron extraction experiments in the Zhu studies were carried out at pH 1, which Zhu et al. [*Zhu et al.*, 1992] in a different study believe to be representative of marine aerosol. Furthermore, the samples analyzed in Zhu et al. [*Zhu et al.*, 1993] and Zhuang et al. [*Zhuang et al.*, 1992a] had been collected over a period of a day to a week and subsequently analyzed after storage for a considerable length of time (weeks to months) during which sample bias may have been introduced from the oxidation of Fe(II). Zhuang et al. [*Zhuang et al.*, 1992a] observed a mean of 15% (this is the corrected value, see [*Zhu et al.*, 1993]) of the total iron in the form of soluble Fe(II) in Barbados, while Zhu et al. [*Zhu et al.*, 1993] during sampling in the same location found Fe(II) to represent less than 1% of the total iron. In a later study in Barbados by Zhu et al. [*Zhu et al.*, 1997] samples were analyzed immediately after collection, the mean value for Fe(II) was 1.7%. Siefert et al. [*Siefert et al.*, 1999] measured Fe(II) concentrations during the inter- and SW-monsoon seasons of 1995 over the Indian Ocean. A sequential extraction procedure, identical to the one carried out in the present study, was performed immediately after sample collection and revealed the following Fe(II) concentration percentages: on average, only 0.3% of Fe was present as Fe(II) after the first 30 minutes of extraction and, even after 22 hours, never more than 4% of the total Fe was released as Fe(II). These values are in close agreement with both studies by Zhu et al., but they differ from the larger values found by Zhuang et al. [*Zhuang et al.*, 1992b] both in Barbados and over the central North

Pacific. In the present study we will present Fe(II) results obtained from the sequential extraction procedure [*Siefert et al.*, 1999] carried out on samples collected during a month-long cruise between Barbados and Cape Verde.

Zhuang et al. [*Zhuang et al.*, 1992b] suggest that the iron and sulfur chemical cycles in remote marine aerosols are closely coupled. By incorporating this link between iron and sulfur into the climate feedback loop proposed by Charlson et al. [*Charlson et al.*, 1987] Zhuang et al. [*Zhuang et al.*, 1992b] identify two potential positive feedback loops that would result in enhanced production of atmospheric Fe(II). The parent sulfur compound in this debate is the biogenically derived dimethyl sulfide (DMS) which is emitted from phytoplankton and outgassed into the atmosphere above the sea surface. In the atmosphere, DMS is oxidized in a series of steps which lead to the formation of non-sea-salt sulfate (NSS-SO_4^{2-}) and other sulfur-containing reaction products, such as methanesulfonic acid (CH_3SO_3H, MSA) [*Hynes et al.*, 1986; *Yin et al.*, 1986].

NSS-SO_4^{2-} can nucleate particles in the sub-micrometer size range which serve as cloud condensation nuclei (CCN) and influence the radiation balance of the atmosphere [*Charlson et al.*, 1987], thus extensive efforts have focused on elucidating the chemical and physical processes that lead to NSS-SO_4^{2-} particle formation from anthropogenic and biogenic sulfur sources. Biogenic sources are particularly important in the marine boundary layer of remote oceanic regions [*Andreae et al.*, 1995; *Berresheim et al.*, 1993; *Charlson et al.*, 1987].

Sea-salt particles may act as seeds for the uptake and oxidation of sulfur gases and deposition of condensable sulfate vapors [*Keene et al.*, 1998; *McInnes et al.*, 1994; *O'Dowd et al.*, 1997]. Sea-salt may also strongly influence the oxidative properties of aerosol

particles in the marine boundary layer through the production of halogen radicals [*Fan and Jacob*, 1992; *Finlayson-Pitts et al.*, 1989; *Graedel and Keene*, 1995; *Keene et al.*, 1996; *Pszenny et al.*, 1993; *Sander and Crutzen*, 1996; *Vogt et al.*, 1996]. These transient radical oxidants may have an effect on the biogenically emitted DMS and the speciation of trace metals.

Due to the intricate chemistry of marine aerosols it appears essential to present all available chemical and physical information of the sampled aerosol particles when trying to interpret observed Fe(II) concentrations. In the present study, we will present trace metal data along with anion and cation abundances since some of them may be directly or indirectly coupled with the iron speciation. Furthermore, these additional species elucidate the sources and source strengths of the sampled aerosol.

4.3 Experimental

4.3.1 Sampling Location and Period

Samples were collected aboard the R/V Seward Johnson during a month-long cruise from Barbados (13.2 °N, 59.5 °W) to Cape Verde (16.8 °N, 23 °W) and back to Barbados. The cruise track is outlined in Figure 1, where the southern track was initiated in Barbados on March 28, 1996; it intercepted the equator and ended in Cape Verde on April 13, 1996. The return to Barbados did not backtrack the same trace; instead, it followed a direct trajectory from Cape Verde to Barbados where it ended on April 26, 1996.

Six-day isentropic air mass back trajectories were calculated with the HYSPLIT trajectory model [*NOAA*, 1997]. Based on literature reports on the transport mechanism of African dust across the Atlantic Ocean [*Bergametti et al.*, 1989; *D'Almeida*, 1986; *Prospero and Carlson*, 1972; *Prospero and Nees*, 1977; *Schütz*, 1980], five different elevations were chosen for the trajectory calculations: 20 m, 500 m, 1500 m, 3000 m, and 6000 m. It is known that long-range transport of dust from the African deserts occurs at a high altitude, in the Saharan Air Layer (SAL), between 1.5 and 5-7 km. This is a consequence of the strong heating of the air at the desert surface, which creates a very deep isentropic mixing layer that carries dust particles into high altitudes. The dry and dust laden air masses leave Africa and move westward within a very persistent wind system towards the Caribbean, forming a strong inversion is generated at the base of the layer, when the relatively cool and moist northeast trade winds cut beneath the Saharan air as it emerges from the continent. This sublayer is initially free of dust, but as the air masses travel westward, the dust content increases by vertical downward mixing and by fallout of larger particles from the overlying

SAL. Thus, this high dust transport does not affect the dust concentrations at ground level in the eastern Atlantic.

The highest dust loadings at high altitudes are expected to occur during summer due to the temperature dependent upward motion of dust laden air [*Chiapello et al.*, 1997]. However, based on high resolution radiometer aerosol optical thickness data collected over 4 years, Swap et al. [*Swap et al.*, 1996] found that dust outbreaks are most frequent and extensive during the first 6 months of the year, with an annual peak in outbreak activity observed during February through April.

Dust transport from Africa occurs throughout the year, but the source regions and main transport pathways change in concert with movements of the Inter-Tropical Convergence Zone (ITCZ) [*D'Almeida*, 1986; *Prospero et al.*, 1981]. This seasonal north to south shift in dust storm activity in Africa from summer to winter has further been deduced from mineralogical signatures of the collected dust samples [*Arimoto et al.*, 1995; *Bergametti et al.*, 1989; *Chiapello et al.*, 1997; *Delaney et al.*, 1967; *Glaccum and Prospero*, 1980; *Schütz and Sebert*, 1987].

Thus, during the month of April, when our sampling took place, the seasonal shift to the north had initiated, and we expect the transport to take place from the northwestern part of the Sahara. The air mass back trajectories in Figure 1, however, present a more complex picture of the air mass origins during the month of April. Initially (Figure 1a), lower altitude trajectories seem to sweep around from the western Atlantic, while they change their origin towards northwest Africa and even southern Europe for the remainder of the cruise (see Figures 1b to 1d). The higher elevation trajectories also vary significantly throughout the

cruise. A similar trajectory pattern has been observed by Talbot et al. [*Talbot et al.*, 1990] and Swap et al. [*Swap et al.*, 1992] during the month of April of 1987.

4.3.2 Aerosol Collection

Ambient aerosol samples were collected with two collector types. A high volume dichotomous virtual impactor (HVDVI) served for the collection of trace metals in two size fractions ($D_{p,50}$ = 3.0 μm), analogous to sampling performed in other studies from our laboratory [*Johansen et al.*, 1999; *Siefert et al.*, 1999]. This collector was built of polycarbonate with nylon screws in order to minimize trace metal contamination. Its total flow rate amounted to 335 ± 15 l min^{-1}, whereby the fine and coarse sample fractions were collected on two 90 millimeter diameter Teflon filters (Gelman Zefluor, 1 μm pore size). Total elemental composition, Fe(II) concentrations, and anion and cation abundances were determined from those fine and coarse filter samples.

Two low volume collectors, running at flow rates of 27 l min^{-1}, were used for gravimetric analyses and for collection of total aerosol mass to be used in future experiments. For the low volume collectors, inverted high density polyethylene 2 liter bottles served as rain shields for the Nucleopore polycarbonate filter holders which were loaded with acid cleaned 47 mm diameter Gelman Zefluor filters (1 μm pore size). Anion and cation concentrations in Johansen et al. [*Johansen et al.*, 1999] were determined from aqueous extractions of the corresponding low volume filters, while in the present study, anions and cations were leached from the high volume filters. This modification seemed appropriate since sampling efficiencies of the two collector types appeared to vary substantially, especially for large particles and at high wind speeds [*Johansen et al.*, 1999].

The aerosol collectors and lab equipment were acid-cleaned before use by following similar procedures as outlined by Patterson and Settle [*Patterson and Settle*, 1976] employing ultra-pure acids from Seastar Chemicals (Sidney, B.C., Canada) and 18.2 MΩ-cm Milli-Q UV water. After Fe(II) analysis, the remaining filter portions were stored in acid-cleaned polystyrene petri dishes sealed with Teflon tape, placed inside two plastic bags and a Tupperware container and stored in a refrigerator during the cruise. After the cruise the filters were sent back to the laboratory (via air-freight, on dry ice) and stored in a freezer until analysis.

A sector sampling system controlled the operation of all the pumps, thereby stopping all aerosol collectors simultaneously when wind speed or wind direction were out of sector. The data logger was programmed to shut the pumps off when the wind speed was ≤ 0.2 m s^{-1} and when the relative wind direction was $\pm 60°$ off of the bow of the ship. In general, samples represent daily averages, but due to the ship's cruise track actual sampling duration may vary. Exact sampling intervals for each sample are listed in Table 1.

The sampling characteristics of the HVDVI are such that approximately 10% of the fine particles end up on the coarse filter. This correction has been accounted for in all coarse concentrations reported in this study. As a result, errors associated with the coarse fraction, especially for species that are present in low concentrations in the coarse fraction (e.g., NSS-SO_4^{2-}, MSA, NH_4^+), may be considerably large. This needs to be kept in mind when computing ratios such as the bio-SO_4^{2-}/MSA ratio for the coarse fraction.

4.3.3 Chemical Analyses

4.3.3.1 Fe(II) Analysis Performed On-board the Ship

Several fractions of labile Fe(II) in both the fine and coarse particle fractions were determined by a sequential extraction procedure. These measurements were initiated immediately (within 1 hour) after sample collection to minimize possible oxidation of Fe(II) otherwise conceivable to occur during sample storage. Extraction and analytical procedures are described in detail in Siefert et al. [*Siefert et al.*, 1999]. Three labile fractions of Fe(II) were determined in both the fine and coarse particle size fractions. The first portion of Fe(II) was released into a 4.2 pH formate buffer after 30 minutes of leaching; this portion is denoted as aqueous-Fe(II) ($Fe(II)_{aq}$). Ferrozine was then added to the leaching solution containing the filter and an absorption reading was made after 5 minutes. The additional Fe(II) released during this step is the 5-minute-ferrozine-Fe(II) ($Fe(II)_{FZ,5min}$). One last absorption reading was made after the ferrozine had 22 hours to act upon the filter containing the aerosol, producing a third Fe(II) fraction: 22-hour-ferrozine-Fe(II) ($Fe(II)_{FZ,22hr}$). The sum of all three Fe(II) fractions determined in such manner is defined as total-22-hour-Fe(II) ($Fe(II)_{total,22hourFZ}$). However, due to the possibility of a bias introduced through the reduction of Fe(III) by ferrozine after 22 hours, it appears more accurate to define a labile Fe(II) fraction that is composed of the first two extractable portions only, thus excluding the 22 hour reading. It is this amount of Fe(II), defined as total-5-minFZ-Fe(II) ($Fe(II)_{total,5minFZ}$), which will be used preferentially when discussing the amount of Fe(II) leached out of the aerosol material.

4.3.3.2 Elemental Analysis

Elemental analysis of 32 elements (Na, Mg, Al, K, Ca, Sc, Ti, V, Cr, Mn, Fe, Ni, Cu, Zn, Ga, Ge, As, Se, Mo, Ru, Cd, Sn, Sb, Cs, Ba, La, Ce, Sm, Eu, Hf, Pb, and Th) was performed on the high volume filters with an HP 4500 ICP-MS (Inductively Coupled Mass Spectrometer). The filter digestion technique is described in Siefert et al. [*Siefert et al.*, 1999].

4.3.3.3 Ion Analysis and Gravimetric Determination

For the ion analysis, a small section of the high volume filter was cut out, wetted with approximately 0.1 ml ethanol and then extracted overnight in 10 ml MQ water. Anions were separated and quantified with a Dionex Bio LC Ion Chromatograph (IC) using an IonPac AS11 separator column and the corresponding AG11 guard column. Organic and inorganic anions were eluted with a gradient pump and a combination of four eluents (5 mM NaOH, 100 mM NaOH, 100% MeOH, MQ H_2O) whereby the NaOH concentration was ramped from an initial 0.45 mM to a final 34.25 mM. Inorganic anions that were quantified included fluoride, chloride, nitrite, bromide, nitrate and sulfate and the organic anions were acetate, glycolate, formate, methanesulfonate, and oxalate. Propionate, pyruvate, succinate, fumarate, phthalate, phosphate and citrate were not detected.

Cations were separated and quantified isocratically with a DX 500 Ion Chromatograph (IC) with IonPac CS12/CG12 analytical and guard columns and a 20 mM MSA eluent. Sodium, ammonium, potassium, magnesium, and calcium concentrations were determined.

Daily average total suspended particulate (TSP) mass was determined by the difference in filter weights (equilibrated to 21 °C and 50% RH) before and after collection on the low volume filters.

4.3.4 Statistical Analyses

Plotted error bars represent the standard deviation calculated through propagation of error in every parameter used. Estimated errors in the volume of air sampled, the filter section cut, the volume of the extraction solution, etc., were assumed to be 10%. Average concentrations reported throughout this study are accompanied by the standard deviation of the sample population.

In addition to interpreting the data based on an element's enrichment compared to a crustal tracer [*Taylor and McLennan*, 1985] (i.e., enrichment factor analysis), a multivariate statistical analysis was performed using SPSS software [*SPSS*, 1997] (i.e., principal component analysis). The principal component analysis was performed on the whole data set, to learn about the source characteristics that make up the sampled aerosol material and to learn about possible correlations between certain chemical species. In a principal component analysis, the correlation matrix of the observed variables is examined to reduce the number of descriptive variables by linearly combining the observed ones into a smaller set of independent variables, the principal components. The principal components are orthogonal to each other and can be rotated in space to simplify interpretation of the data set. A common type of rotation is the Varimax rotation, during which orthogonality is retained. All principal components in the present study are Varimax rotated.

A principal component in this study can represent a source, such as crustal material, sea-salt, and anthropogenic pollutants. An observed variable will display a number close to 1 if it correlates with the principal component, thus two variables with numbers close to 1 in one component correlate with each other. For example, the crustal component will exhibit values close to 1 for Al and other crustal elements, while the sea-salt component will exhibit values close to 1 for variables that are characteristic for sea-salt, such as Na^+, Cl^-, and wind speed.

4.4 Results

4.4.1 Total Suspended Particulates (TSP)

Total suspended particulates (TSP) were determined for each of the low volume filters. Plots in Figure 2 represent TSP as a function of sample. The abscissa in this and all analogous concentration plots is chosen to represent the discrete samples instead of a time or location variable. This is done for simplification of the plot since sampling intervals and locations varied significantly. For reference, Table 1 lists sampling intervals and location at midpoint in time for each sample.

TSP appears to vary considerably over this part of the tropical North Atlantic Ocean during April of 1996, the mean being 46.5 $\mu g\ m^{-3}$ with a standard deviation of 26.3 $\mu g\ m^{-3}$. The maximum of 97.6 $\mu g\ m^{-3}$ is observed on April 2, for sample A96-02, and the minimum, 3.0 $\mu g\ m^{-3}$, on April 7, for sample A96-08, both on the southern leg of the cruise. A large number of studies exist on the mineral dust loadings in the same geographical area as investigated here, but since our gravimetrically determined masses are inclusive (a mixture of mineral, sea-salt, anthropogenic and biogenic aerosol), absolute values cannot be compared until each contribution is separated. Due to the relatively constant wind speeds throughout the cruise ($5.6 \pm 2.3\ m\ s^{-1}$), the sea-salt contribution is expected to be fairly constant, thus the variability observed in TSP can be attributed to the mineral dust loadings. Sea-salt and mineral dust contributions will be determined below.

4.4.2 Trace Metals

Elemental concentrations for 32 elements were determined by ICP-MS. Since four of the elements, As, Se, Ru, and Cd, were below detection limit for most of the samples, they

are omitted from further discussion. Large background concentrations for a series of elements (Cr, Ni, Cu, Ge, Mo, Sn, and Sb) are attributed to contamination from the filter material and/or from the acids used during filter digestion. Thus, these elements also had to be excluded from further analysis. Average concentrations with standard deviations, and minimum and maximum concentrations of the remaining 21 elements, are listed in Table 2.

Principal component analysis of these 21 elements reveals that the crustal tracer Al is very closely correlated with Mg, K, Ca, Sc, Ti, V, Mn, Fe, Ga, Cs, Ba, La, Ce, Sm, Eu, Hf, and Th, in both the fine and the coarse fractions. The varimax rotated principal component matrix is presented in Table 3. The first component describes 77% of total variance in the data set and is characterized by high correlations between typical crustal tracers in the fine fraction; note the large (i.e., close to one) values, in bold, in the first column. Of these elements, Mg, K, and Ca, seem to have an additional source since their component scores are not as close to 1 as for the other mentioned elements. Other potential sources of Mg, K, and Ca are sea-salt. Additional Ca sources include those of anthropogenic [*Hopke*, 1985] and additional crustal origin, in the form of $CaCO_3$ (calcite) and $CaSO_4$ (gypsum). Although, as pointed out, the first component is most notably characterized by a fine crustal source, it appears to include some of the coarse crustal portion, since the corresponding component scores are not insignificant.

The second component of this analysis describes 11% of the variance and is denoted as the coarse crustal source, although, as mentioned above, some of the coarse crustal portion already appears in the first component. Furthermore, indicative from the large value for coarse Na and coarse Mg, a strong coarse sea-salt portion is included in this component. The component scores for TSP indicate that the first two components are the major contributors

to the total mass loadings observed. Concentration plots for the mentioned crustal elements follow the same trend, as expected. Figure 3a shows Al vs. sample ID, which is representative of the other crustal elements extracted in components 1 and 2 in the principal component analysis.

The third component exhibits large scores for coarse and fine Zn as well as fine Pb. These are typical anthropogenic tracers [*Duce et al.*, 1975; *Huang et al.*, 1996], emitted from smelters and during the combustion of leaded fuel. Coarse Ca, which can have an anthropogenic source in association with the combustion of coal, oil, and fuel [*Hopke*, 1985], appears to correlate slightly with this component. To visualize the contribution of this anthropogenic source, fine and coarse Zn are plotted in stacked bars in Figure 3b. There seems to be a relatively constant background concentration of total Zn of around 4 ng m^{-3}, overlain by a sudden increase in both the fine and coarse fractions during the latter part of the cruise. The Pb concentration plot, not shown, is clearly a combination of both the Al and the Zn plots: the first half of the cruise is identical in signature to Al and the latter half of the cruise, with exception of the last sample, displays the features of Zn. This indicates that Pb is not enriched over the crustal portion during the first part of the cruise but that later another source containing Pb and Zn becomes predominant. This is in accordance with decreasing Pb concentrations since 1970 observed by Huang et al. [*Huang et al.*, 1996] who compared Pb concentrations at Bermuda to other elements typically associated with pollutants, Zn and Sb. Air mass back trajectories suggest that the anthropogenic sources are located either in northwestern Africa or southern Europe see Figures 1c and 1d.

The fourth, and last, component in this analysis with a significant component score; may be representative of a fine sea-salt component. Note the large fine Na and wind speed

scores. Other sea-salt components such as Mg, K and Ca display scores that are significant. The Na concentration plot is shown in Figure 3c. It needs to be pointed out that Na as presented here is the total Na concentration; therefore, it includes sea-salt and crustal fractions. The water-soluble fractions of Na, Mg, K and Ca are also determined and presented below.

4.4.3 Fe and Fe(II)

Principal component analysis reveals that Fe closely tracks the crustal tracers in both fine and coarse fractions. When looking at the sequentially extracted Fe(II) contributions superimposed by the total coarse and fine Fe, in Figures 4a and 4b, respectively, a weak correlation may be observed between the $Fe(II)_{total,22hourFZ}$ and the total Fe for both size fractions. The $Fe(II)_{aq}$ and $Fe(II)_{FZ,5min}$ contributions, which will be the focus in subsequent sections for reasons explained above, do not appear to display obvious correlations with the total Fe concentrations. Samples A96-01, A96-02 and A96-21 were not analyzed for Fe(II) due to time constraints aboard the ship during set up and dismantling of the lab equipment.

Absolute values for coarse-$Fe(II)_{total,5minFZ}$ range from 0 to 1.14 ng m^{-3}, averaging 0.44 ± 0.31 ng m^{-3}. This represents relative contributions to total coarse Fe of 0 to 4.2%, with a geometric mean of 0.15 ± 0.96% (the geometric mean is preferred for this number since it is a ratio). Percentages are plotted in Figure 5, which shows that the maximum percentage of 4.2% is observed for sample A96-09, near the equator, when the coarse-Fe concentration is at the detection limit encountered with the ICP-MS; see Figure 4a. Thus, this percentage is associated with large errors and may be an outlier. A more reasonable value would be somewhere close to what samples A96-08 and A96-10 display in Figure 5.

When recalculating the average percentage coarse-$Fe(II)_{total,5minFZ}$ in coarse Fe without sample A96-09, the geometric mean drops to 0.12 ± 0.19% and the maximum becomes 0.72%.

Fine-$Fe(II)_{total,5minFZ}$ varies between 0.74 and 4.91 ng m^{-3} and averages 2.70 ± 1.27 ng m^{-3}. On average, this corresponds to an increase by a factor of 6 compared to the coarse-$Fe(II)_{total,5minFZ}$. In other words, about 86% of the readily released Fe(II) is present in the fine Fe fraction. This is visualized in Figure 4c where the fine and coarse $Fe(II)_{total,5minFZ}$ fractions are plotted in stacked bars. Percentage-wise, the fine-$Fe(II)_{total,5minFZ}$ varies between 0.14 and 2.12% of total fine Fe and displays a geometric mean of 0.82 ± 0.6%.

The effect of the larger amount of Fe(II) released from the fine fraction is not obliterated when relating the fine-$Fe(II)_{total,5minFZ}$ to the combined coarse and fine Fe. Since Fe is almost evenly distributed between coarse and fine fractions, the average values being 419 ± 355 and 425 ± 366 ng m^{-3}, respectively, the effective fine and coarse percentages in total Fe are halved. This is also illustrated in Figure 5, where the percentage of total-$Fe(II)_{total,5minFZ}$ in total Fe (the solid line) is roughly evenly spaced between the coarse and fine percentages, except for sample A96-09. When considering coarse and fine fractions together, the $Fe(II)_{total,5minFZ}$ amounts to 0.51 ± 0.56% (geometric mean) of the combined total Fe. If sample A96-09 is left out, the geometric mean becomes 0.46 ± 0.36%. The average total value for $Fe(II)_{total,5minFZ}$ is 3.14 ± 1.35 ng m^{-3} with a minimum of 0.98 and a maximum of 5.05 ng m^{-3}.

Figures 6a and 6b present the average fractions extracted during the sequential extraction procedure for the coarse and fine filters, respectively. It appears that the fine Fe(II) is more readily released than the coarse Fe(II). This may be a function of the surface

area of the particles, which would be larger for the fine fraction, but it may also be a result of differential weathering processes of the size fractions, leading to different compositions of Fe phases in the two size fractions. Because of differential deposition rates of coarse and fine fractions and their diverse transport histories, their chemical transformation pathways may also be significantly different, giving rise to varying levels of available Fe(II).

Ferrous iron levels observed in this study are in the same range as those found in an analogous study by our group [*Siefert et al.*, 1999], which was carried out over the Indian Ocean. The total Fe(II) used in Siefert et al. [*Siefert et al.*, 1999] included the 3rd, 22 hour ferrozine, fraction, while in this study we decided to concentrate on the first two Fe(II) fractions only, thus, values need to be adjusted in order to be compared with each other. When considering the absolute values of Fe(II) extracted, they are very similar during the two cruises, but because the total Fe during the Indian Ocean cruise was larger than during the present cruise, the percentages are somewhat smaller. Thus, on average 0.3% of Fe was present as $Fe(II)_{total,5minFZ}$ during the Indian Ocean cruise, compared to 0.46% (A96-06 excluded) in the present study.

Compared to other studies performed over remote oceanic regions, results from this and our previous cruise [*Siefert et al.*, 1999] are in the same range as found by Zhu et al. [*Zhu et al.*, 1993; *Zhu et al.*, 1997] in Barbados. However, Zhuang et al. [*Zhuang et al.*, 1992a] reported considerable larger values (15%, corrected value, see [*Zhu et al.*, 1993]) of Fe(II) in Barbados. The absolute Fe(II) concentration is also larger by a factor of ~ 30. Because their samples had been stored over a considerable amount of time before analysis, chances exist of the introduction of artifacts.

A new principal component analysis that includes Fe(II) and ions, while omitting some of the redundant trace metals from the principal component analysis in Table 3, is shown in Table 4. The main characteristics of each principal component remain the same as for the previous analysis. The fine Fe correlates with the first component, which represents predominantly the fine crustal source, while the coarse Fe correlates with the second and with the first components. The coarse and fine $Fe(II)_{total,22hrsFZ}$ which include the 22 hour ferrozine fractions correlate with the total Fe in the corresponding fractions; the coarse-$Fe(II)_{total,22hrsFZ}$ correlates with the second component and the fine-$Fe(II)_{total,22hrsFZ}$ with the first component. This substantiates the observation previously made when visually comparing the ICP-MS Fe fractions with the $Fe(II)_{total,22hrsFZ}$ fractions in Figure 4. It is of interest to note that the $Fe(II)_{total,5min}$ fractions are not correlated with the first two crustal components, but rather with the anthropogenic component (no. 3) and component 4. The coarse $Fe(II)_{total,5min}$ correlates with component 3, which is high in coarse NO_3^-, NSS-SO_4^{2-} and oxalate, all typical anthropogenic tracers, which may have a direct effect on the speciation of Fe in the particle. The fine $Fe(II)_{total,5min}$ correlates with component 4, which may carry an anthropogenic and/or biogenic signature since the fine NSS-SO_4^{2-} scores are slightly elevated and the fine MSA scores are high. Thus, it appears that the Fe(II) that is immediately released (after 5 min with FZ) is a function of constituents in the aerosol matrix with which it may have undergone chemical and photochemical reactions and/or it shares the same source as the anthropogenic component, while the combined Fe(II) (released after 22 hours in FZ) is more a function of the total Fe available in the aerosol phase.

4.4.4 Anions

Table 5 lists the average ± one standard deviation (SD), minima and maxima of each ionic species determined in the coarse and fine filter fractions. Inorganic anions measured include F^-, Cl^-, Br^-, NO_3^-, and SO_4^{2-}. Although NO_2^- was detected in a few of the samples, values are very close to the detection limit and are therefore excluded from further analysis. Sea-salt (SS) and non-sea-salt (NSS) contributions to F^-, Cl^-, Br^-, and SO_4^{2-} are determined from measured Na^+ concentrations and the constant ratio of these species expected in sea water [*Millero and Sohn*, 1992].

Of the organic anions analyzed, acetate and formate appear to be impacted by occasional contamination that is also detected for the standards of these species and occasionally in the blanks, thus acetate and formate are not considered further. Glycolate, methanesulfonic acid (MSA) and oxalate are quantified and listed in Table 5.

4.4.4.1 NSS-SO_4^{2-} and MSA

NSS-SO_4^{2-} is believed to be derived from anthropogenic sources as a result of the oxidation of anthropogenic SO_2, and from biogenic sources, from the oxidation of the biogenically emitted dimethylsulfide (DMS). Average NSS-SO_4^{2-} concentrations observed in the present study, 1.03 ± 0.60 μg m^{-3}, are on the same order of magnitude as reported in numerous other investigations performed in the same area [*Davison et al.*, 1996; *Harrison et al.*, 1996; *Li-Jones and Prospero*, 1998; *Savoie et al.*, 1989b]. This value is a factor of two above what is observed in typical remote oceanic regions [*Saltzman et al.*, 1983], while the concentrations encountered near the equator, for samples A96-08 and 09, are much lower, around 0.15 μg m^{-3}. On average, 23% of the total SO_4^{2-} detected in the coarse fraction is

non-sea-salt derived while the corresponding number for the fine fraction is almost 3 times larger, 73%. Of the total NSS-SO_4^{2-}, 87% is present in the fine fraction. Figure 7 illustrates the various portions of SO_4^{2-}; in coarse and fine fractions and the sea-salt and non-sea-salt contributions.

Since the operationally defined fine fraction in the present study has an aerodynamic upper particle diameter cutoff of 3 μm, the observed larger contribution of NSS-SO_4^{2-} to the fine fraction may arise from a combination of effects. NSS-SO_4^{2-} particles in the sub-micrometer size range, which serve as cloud condensation nuclei (CCN), are formed from gas-to-particle conversion, and sea-salt aerosol in the 2-10 μm range, with a peak production in droplets of 4 μm diameter [*Sievering et al.*, 1992], may act as seeds for the uptake and oxidation of sulfur gases and deposition of condensable sulfate vapors [*Keene et al.*, 1998; *McInnes et al.*, 1994]. Both of these mechanisms add NSS-SO_4^{2-} to the fine particle fraction, but only the production of new CCN has an influence on the radiation balance of the atmosphere [*Charlson et al.*, 1987] while the deposition of low vapor pressure S-containing gases onto preexisting hygroscopic sea-salt particles removes S-gases that could potentially have been transformed into CCN [*O'Dowd et al.*, 1997].

Besides the presence of anthropogenic NSS-SO_4^{2-}, biogenic sources of sulfur that contribute to NSS-SO_4^{2-} are particularly important in the marine boundary layer of remote oceanic regions [*Andreae et al.*, 1995; *Berresheim et al.*, 1993; *Charlson et al.*, 1987]. MSA is one of the oxidation products of DMS that is used as a surrogate for the biogenically derived NSS-SO_4^{2-} (bio-SO_4^{2-}). Since MSA has a low vapor pressure it partitions readily into the particle phase and is therefore easily sampled. Furthermore, it is believed that the only determining factor of the bio-SO_4^{2-}/MSA ratio is temperature [*Hynes et al.*, 1986] (see

introductory section in Johansen et al. [*Johansen et al.*, 1999] for a more detailed discussion on this issue). Due to MSA's low vapor pressure and the presence of sea-salt particles in the marine environment, MSA has been found to be distributed on larger particles, in the micrometer size range, presumably as a function of sea-salt aerosol surface area [*Kerminen et al.*, 1997; *O'Dowd et al.*, 1997; *Pszenny*, 1992; *Qian and Ishizaka*, 1993; *Quinn et al.*, 1993].

MSA concentrations in both fine and coarse fractions are shown in Figure 8. On average, 79% of the MSA is present in the fine (< 3μm diameter) size fraction. This is in agreement with what has been seen by the above mentioned investigators. Total MSA concentrations vary from 8.15 to 46.9 ng m^{-3} and average 26.8 ± 9.5 ng m^{-3}. Li-Jones and Prospero [*Li-Jones and Prospero*, 1998], in a recent study performed in Barbados, observed concentrations of MSA which ranged from 7 to 33 ng m^{-3} with a mean of 22 ng m^{-3}. Other reported values for MSA over the Atlantic Ocean are also in close agreement with ours [*Bürgermeister and Georgii*, 1991; *Davison et al.*, 1996; *Huebert et al.*, 1996; *Putaud et al.*, 1993].

In Table 4, fine MSA correlates somewhat with fine NSS-SO_4^{2-} in component 4, while coarse MSA, which makes up only 1/5 of the total MSA, appears in component 5 without another significant correlation. Fine NSS-SO_4^{2-} is almost equally split between components 3 and 4, whereby component 3 is anthropogenic and component 4 possibly biogenic since MSA is used as a tracer for bio-SO_4^{2-}.

It is important to identify and quantify each contributing source of SO_4^{2-} in order to accurately determine its biogenic portion. Sea-salt is one source that can be subtracted from the total SO_4^{2-} with precision, due to the known SO_4^{2-}/Na^+ ratio in sea water and the measured Na^+ concentration. Other sources, such as anthropogenic, biogenic and crustal (in

the form of $CaSO_4$ and/or $CaCO_3$) demand an analogous such tracer, for which the corresponding ratio can be determined in a multivariate linear regression analysis. This procedure was carried out in Johansen et al. [*Johansen et al.*, 1999] and proved to be very effective in determining the relative contributions of SO_4^{2-}. In our previous study [*Johansen et al.*, 1999], Pb was used as the surrogate for anthropogenic-SO_4^{2-}, MSA for biogenic-SO_4^{2-}, Na^+ for SS-SO_4^{2-}, and NSS-Ca^{2+} for gypsum-SO_4^{2-}.

Analogous linear regression analyses are carried out in the present study and presented below.

4.4.4.2 NO_3^- and Organic Acids

Total nitrate, as indicated in Table 5, varies from < 0.24 to 1.32 μg m^{-3} with an average of 0.67 ± 0.27 μg m^{-3}. These values are in close agreement with observations by other investigators [*Berresheim et al.*, 1991; *Davison et al.*, 1996; *Galloway et al.*, 1993; *Harrison et al.*, 1996; *Huebert et al.*, 1996; *Li-Jones and Prospero*, 1998; *Savoie et al.*, 1989b] carried out in the same region, where the low concentration corresponds to a clean marine atmospheric situation and the high concentration is typical for a somewhat polluted air mass.

Slightly more than half of the total NO_3^- (53%) is typically associated with the coarse particle fraction. This is in agreement with observations made by a series of investigators [*Bassett and Seinfeld*, 1984; *Berresheim et al.*, 1991; *Huebert et al.*, 1996; *Savoie and Prospero*, 1982; *Sievering et al.*, 1990; *Sisterson*, 1989] that demonstrated that most NO_3^- is found in the supermicron mode associated with Na^+ and Cl^-, while most of the NSS-SO_4^{2-} is contained in the submicron mode. This is in strong contrast with the behavior of other

anthropogenic tracer; their content is considerably higher in the fine than in the coarse fraction: almost 3 times as much NSS-SO_4^{2-} is present in the fine fraction, while the corresponding value of Zn is 2.6 and for Pb 2.5.

Figure 9 presents NO_3^- concentrations in stacked bars in both coarse and fine fractions. The coarse NO_3^- appears to vary more strongly than the fine NO_3^- throughout the cruise. In the principal component analysis in Table 4, both size fractions correlate somewhat with the second component, which is representative of the coarse crustal component and some sea-salt. In addition, coarse NO_3^- correlates with the third component, which represents the anthropogenic source.

The mass ratio of NO_3^-/NSS-SO_4^{2-} has been used by some investigators [*Berresheim et al.*, 1991; *Li-Jones and Prospero*, 1998; *Prospero and Savoie*, 1989; *Savoie et al.*, 1989b] to identify the origin of the pollutant air masses. A ratio of 0.4 is typically found in European air masses and ratios close to 1.1 have been observed in air masses that emerge from the southwest sub-Sahara. These reported values are not corrected for possible biogenic sources of NSS-SO_4^{2-}. When comparing with the analogous ratio in the present samples, we get a value of 0.5 for the combined coarse and fine concentrations, indicating a European origin. However, when treating coarse and fine fractions separately, we obtain 2.1 and 0.3, respectively. These values are associated with considerable scatter and do not seem reliable for the use of source identification.

Glycolate varies from < 5.7 to 51.4 ng m^{-3} and averages 16.3 ± 11.3 ng m^{-3}. With exception of the sample with the maximum concentration, A96-18, and 3 samples with minimum concentrations near the equator (samples A96-08, 09, and 10), the rest of the samples display small variability.

Oxalate, plotted in Figure 10, on the other hand displays a pattern comparable to that of Zn in Figure 3b. It also correlates both in the fine and coarse fractions with the anthropogenic component in the principal component analysis in Table 4. Total oxalate concentrations vary from < 12.4 to 100.8 ng m^{-3} and average 52.2 ± 29.9 ng m^{-3}. About 60% of the total oxalate is present in the fine fraction. Oxalate is secondarily produced in the atmosphere by photochemically induced reactions involving organic precursors and it is found to be the final dicarboxylic acid to accumulate during oxidation of larger diacids [*Kawamura and Ikushima*, 1993]. It is therefore expected to correlate with the anthropogenic component.

4.4.4.3 Halogens

Concentrations for F^-, Cl^- and Br^- are summarized in Table 5 and plotted in Figures 11a, 11b and 11c, respectively. Note the negative values for the NSS contributions of Cl^- and Br^- in Table 5. This indicates that Cl^- and Br^- are depleted relative to concentrations that are expected from observed Na^+ abundances. Fluoride, on the other hand, is highly enriched over the expected sea-salt contribution: 95.8 ± 3.4% (geometric mean) of total F^- is NSS. When included in the principal component analysis (not shown), coarse F^- correlates with the crustal component while fine F^- anti-correlates with the fine MSA/sea-salt component. No obvious explanation is found for these observations.

Coarse Br^- correlates with the coarse sea-salt and crustal component (nr. 2) in the principal component analysis, showing its sea-salt origin. However, fine Br^- anti-correlates with the same component that fine F^- anti correlates with, the fine MSA/sea-salt component (nr. 4). With the exception of 2 samples (A96-08 and 09) bromide is depleted when calculating the SS contribution. The degree of depletion of Br^-, defined as the absolute value

of (observed-Br^- - SS-Br^-)/SS-Br^-, is expressed in percentages and it averages 51.6 ± 24.9% (geometric mean). The deficit varies between 3.8 and 91.8%. Large Br^- deficits have commonly been seen in marine aerosols and is the topic of great interest in conjunction with the ozone loss observed shortly after sunrise in the Arctic [*Barrie et al.*, 1988; *Bottenheim et al.*, 1990]. Bromine has been proposed to be active as the principal free radical chain carrier in an autocatalytic cycle that leads to ozone destruction and the transfer of Br species from aerosol to gas phase [*Fan and Jacob*, 1992; *McConnell et al.*, 1992; *Vogt et al.*, 1996]. In a model by Vogt et al. [*Vogt et al.*, 1996] involving the production of reactive bromine and chlorine species, the particle phase depletion of Br^- amounted to 90% and that of Cl^- to 1%.

Depletion of Cl^- in the present study is observed for all samples, and in accordance with the model by Vogt et al. [*Vogt et al.*, 1996], the Cl^- deficit is considerably smaller than that for Br^-, but still larger than the deficit predicted by the model. Absolute values for Cl^- deficits are plotted in Figure 12. Samples A96-01 and A96-02 display a very different behavior from the rest of the samples. Since they carry the characteristics of being outliers, they are excluded from the following Cl^- deficit analysis. Chloride deficits average 18.3 ± 9.1% and vary from 10.6 to 47.1%, whereby a higher percentage deficit is found in the fine fraction (29.7 ± 9.9%) compared to the coarse fraction (11.9 ± 13.3%). This may be a consequence of the relative larger surface area of smaller particles compared to larger particles, and/or it may be a function of the presence of other chemical species which may react with Cl^- and subsequently lead to its volatilization. Further mechanisms for the depletion of Cl from the aerosol phase are discussed below.

4.4.5 Cations

4.4.5.1 Na^+, K^+, Mg^{2+} and Ca^{2+}

Water-soluble portions of Na^+, K^+, Mg^{2+} and Ca^{2+} as determined by IC are presented in stacked bar plots in Figures 13a, 13b, 13c, and 13d, respectively. Their average concentrations and maxima and minima are listed in Table 5.

Typically, Na^+ is used to determine the sea-salt component in the aerosol particles since the water-soluble Na^+ is assumed to originate solely from sea water. Thus, all Na^+ in Figure 13a is sea-salt derived and is used to compute the sea-salt component of the other 3 cations in Figure 13, based on the constant concentrations encountered in sea water [*Millero and Sohn*, 1992]. A comparison between the water-soluble fraction of these alkali and alkaline earth metals and their total concentrations as determined by ICP-MS, is presented in the discussion section.

Total Na^+ concentrations vary from 0.44 to 8.52 $\mu g\ m^{-3}$ and average 3.24 ± 1.67 $\mu g\ m^{-3}$, of which 62% is present in the coarse particle fraction. The resulting sea-salt concentration varies from 1.4 to 27.8 $\mu g\ m^{-3}$ and averages 10.6 ± 5.5 $\mu g\ m^{-3}$. This falls within the range of sea-salt concentrations observed in Barbados, Cape Verde and the Atlantic [*Arimoto et al.*, 1995; *Davison et al.*, 1996; *Li-Jones and Prospero*, 1998; *Savoie and Prospero*, 1977]; however, the mean value is larger by up to a factor of 2 compared to our samples. Putaud et al. [*Putaud et al.*, 1993] reported a mean value very close to the present observation, from samples collected in calm tropical North Atlantic waters, under conditions comparable to the ones encountered during the present cruise. Compared to the TSP, which was determined from the low volume filters, the sea-salt accounts for, on average (geometric mean), 24.3 ± 9.8%.

Magnesium, as can be seen in Figure 13c, closely traces the Na^+ concentrations. The NSS-Mg^{2+} varies from small negative to small positive values, which fall within the error of the analysis techniques. Thus, water-soluble Mg^{2+} appears to be exclusively sea-salt derived implying that the Saharan dust collected on the present samples is not a significant source of water-soluble Mg. This is in agreement with observations made by Savoie and Prospero [*Savoie and Prospero*, 1980] in the same sampling area, the tropical North Atlantic. Over the Northern Indian Ocean [*Johansen et al.*, 1999], however, Mg^{2+} was slightly enriched over the sea-salt component and seemed to be of crustal origin.

Potassium, on the other hand, does exhibit a NSS water-soluble portion (see Figure 13b). The NSS contribution varies from 15.5 to 82.2% of the total water-soluble K^+, with a geometric mean of 32.5 ± 18.2%. The fine aerosol particles contain 73% of this portion of K^+.

In the case of calcium, the NSS contribution accounts for 64.9 ± 20.3% (geometric mean) of the total water-soluble Ca^{2+}; see Figure 13d. This is in perfect agreement with observations by Savoie and Prospero [*Savoie and Prospero*, 1980]. In contrast to potassium, the majority (63%) of the water-soluble NSS-Ca^{2+} is present in the coarse fraction. This indicates that the sources of NSS water-soluble potassium and calcium may not be identical. Even if the geographic source is the same, the particles releasing the potassium and the calcium are of different size ranges. The coarse size fraction is typical of crustal material. However, clay particles may be fine enough to preferentially end up in the fine filter mode (< 3μm). Thus, it is conceivable that the mineral aerosol contained a potassium rich dust of smaller particle size mixed in with larger calcite particles. In addition, potassium is a tracer for biomass burning, which would end up in the fine particle mode, as observed here.

4.4.5.2 NH_4^+ and Acid Neutralization

Ammonium has typically been observed in association with the particles in the accumulation mode, together with NSS-SO_4^{2-} and MSA [*Huebert et al.*, 1996]. Our observations are in agreement with those findings, 73% of the NH_4^+ is contained in the fine particle mode; see Figure 14a. Total ammonium concentrations vary from 68.5 to 299 ng m^{-3} and average 175 ± 62 ng m^{-3}. These concentrations are close to observations made [*Harrison et al.*, 1996; *Huebert et al.*, 1996] over the Azores in marine air masses.

Ammonia, mostly of continental origin [*Quinn et al.*, 1992], is the primary basic gas in the atmosphere and is readily absorbed by atmospheric particles whereby it neutralizes acid aerosol. First it neutralizes H_2SO_4, since the vapor pressure for H_2SO_4 is considerably smaller than that for HNO_3, and then, if sufficient ammonia is available, it will react with HNO_3 [*Seinfeld and Pandis*, 1997]. Thus, the NH_4^+/NSS-SO_4^{2-} ratio gives an estimate of the neutralization and the speciation of the acid in the aerosol. We find that the molar ratio of NH_4^+/NSS-SO_4^{2-} in the fine fraction, where 73% of the total NH_4^+ and 87% of the total NSS-SO_4^{2-} is present, is on average (geometric mean) 0.96 ± 0.46. This indicates that the particles consist mainly of bisulfate. However, as can be seen in Figure 14b, the ratio in the fine fraction (dotted line) ranges from 0.4 (near Cape Verde) to 2.1 (at the equator). A molar ratio of less than 0.5 represents a very acidic atmosphere, where the sulfate species in the aerosol particles are primarily H_2SO_4 and HSO_4^-. In the case of a molar ratio above 2, there is sufficient ammonium in the particle phase to neutralize the available sulfuric acid and some nitric acid. The coarse molar NH_4^+/NSS-SO_4^{2-} ratio is not shown, since its variability is very large due to the large associated error with the small coarse NSS-SO_4^{2-} concentrations in the denominator. However, the total ratio is plotted in Figure 14b as the solid line. It traces

closely the fine $NH_4^+/NSS\text{-}SO_4^{2-}$ curve but in general displays slightly larger values, averaging 1.03 ± 0.61.

The lowest ratios are observed near Cape Verde, when dust concentrations and especially $NSS\text{-}Ca^{2+}$ abundances are large. Since it appears (see following sections) that most of the $NSS\text{-}Ca^{2+}$ is associated with primary $CaCO_3$ rather than with primary $CaSO_4$, the CO_3^{2-} may act as an additional neutralizing species.

Due to the size cutoff of our collector (3 μm particle diameter) an appreciable amount of particulate crustal material ends up on the fine filter; 37% of total $NSS\text{-}Ca^{2+}$ is present in the fine fraction, averaging 177 ± 153 ng m^{-3}. Carbonate is available for reaction with acidic $NSS\text{-}SO_4^{2-}$, especially in the fine fraction where most of the $NSS\text{-}SO_4^{2-}$ is present. $NSS\text{-}Ca^{2+}$ peaks near Cape Verde, when the low $NH_4^+/NSS\text{-}SO_4^{2-}$ ratios indicate very acidic conditions. Inclusion of the neutralizing ability of CO_3^{2-} of one proton (as $NSS\text{-}Ca^{2+}$) in the numerator (i.e., $(NH_4^+ + NSS\text{-}Ca^{2+})/NSS\text{-}SO_4^{2-}$) of the ratio gives a new measure of the neutralization and speciation in the particle phase. As seen in Figure 15, this new ratio is generally higher than the one that does not include CO_3^{2-}, as expected. Where before the lowest ratio was 0.4 in the fine fraction, it now is 0.85. For such a value, the most abundant species is HSO_4^-. The $(NH_4^+ + NSS\text{-}Ca^{2+})/NSS\text{-}SO_4^{2-}$ for the fine fraction averages (geometric mean) 1.44 ± 0.60 (also indicative of bisulfate), and shows a maximum of 3.48 in sample A96-02. Mineral aerosol characteristics at the beginning of the cruise are considerably different from those encountered near Cape Verde; this is discussed in further detail in the discussion section below. Thus, the large ratios observed at the start and end of the cruise for the fine and for the coarse and fine fractions combined may be inaccurately elevated since the $NSS\text{-}Ca^{2+}$ may

not necessarily be present in the form of primary $CaCO_3$ in those samples. The same ratio $(NH_4^+ + NSS\text{-}Ca^{2+})/NSS\text{-}SO_4^{2-}$ for the total aerosol averages 2.0 ± 0.6.

Acid-base neutralization can also be discussed in terms of charge imbalances observed between total anionic and cationic charges. However, since both H^+ and CO_3^{2-} are not detectable with the IC, an observed charge imbalance cannot be directly attributed to the either one of the two species. In the present case, the carbonate derived from the excess $NSS\text{-}Ca^{2+}$, correlates well with the anionic charge deficit that is observed in all but one sample. The charge deficit amounts to 12% in the fine and 16% in the coarse fraction. Thus, it appears as if no additional protons are present that would acidify the aerosol over what was obtained from the ratios that include the carbonate neutralization capacity.

4.5 Discussion

4.5.1 Mineral Aerosol

Aluminum is typically used as the tracer to quantify the mineral aerosol abundance in the atmosphere, where the concentrations are computed from measured Al concentrations and Al's average concentration in bulk continental crust: 8.41 wt% Al [*Taylor and McLennan*, 1985]. Although, as will be shown below, the average crustal composition is usually a good estimate, it is not always representative of all crustal sources. For the sake of comparison of the present findings with those observed in other studies in the same area, we first report mineral dust loadings based on the 8.41% average crustal Al content. The average total dust loading thus computed amounts to 18.4 ± 15.6 μg m^{-3} ranging from 0.8 to 52.9 μg m^{-3}. The mineral dust is almost evenly distributed between the two size fractions (51% in the fine fraction). Figure 3a presents Al concentrations as a function of sample ID. It can be deduced that minimum mineral dust concentrations occur near the equator, in samples A96-08 and 09, while maximum concentrations are observed near the beginning of the cruise.

These mineral dust concentrations fall within the range of values reported by a several investigators. In Barbados, Prospero et al. [*Prospero*, 1968] found a 25 month (prior to 1968) average dust concentration of 2.5 μg m^{-3} and an average dust concentration from 1970 to 1992 of 11.0 μg m^{-3} [*Prospero et al.*, 1996]. The same group [*Prospero et al.*, 1981] reported a maximum dust loading event in Barbados in March of 1978, amounting to 104 μg m^{-3}; however, the annual maximum monthly means were typically observed in the range 15-18 μg m^{-3}. Savoie and Prospero [*Savoie and Prospero*, 1977] report a comparable mean value of 20.5 ± 17.9 μg m^{-3} in Barbados in the high dust loading season between July and

September. Arimoto et al. [*Arimoto et al.*, 1995] observed annual mean dust concentrations of 15 μg m^{-3} and median values of 8.8 and 3.8 μg m^{-3} during the month of April of 1990 and 1991, respectively. These values are lower than the ones observed in the present study, which is reasonable since our sampling occurred between the African continent and Barbados, instead of in Barbados only.

Mineral dust from the Sahara also reaches the northeastern coast of South America. Samples collected in the southern part of the present cruise track (samples A96-03 until about A96-09) may carry very similar signatures as those sampled during studies along the northeastern coast of South America. According to a study by Prospero et al. [*Prospero et al.*, 1981] performed in Cayenne, French Guiana, maximum concentrations are expected during the northern winter, when the intertropical convergence zone (ITCZ) is in its most southerly position. Annual maximum concentrations during 1978 and 1979 were 29 and 23 μg m^{-3}, respectively, but concentrations in excess of 100 μg m^{-3} were observed during the month of March. Off of the coast of northern Brazil concentrations of Saharan dust in the marine boundary layer were in the range 1-25 μg m^{-3} during February and March of 1971 [*Talbot et al.*, 1990]. These observations are in agreement with the minimum and maximum concentrations observed in the present study, during the month of April, which seems to be representative for the transitional season between large dust concentrations and low.

Over the tropical North Atlantic Ocean, dust loadings of 25 [*Losno et al.*, 1992], 22 [*Prospero and Carlson*, 1972] and 7.7 μg m^{-3} [*Aston et al.*, 1973] were observed, while concentrations near the North African coast increased to an average of 57 μg m^{-3} in the northeast trades [*Chester et al.*, 1972]. Chester et al. [*Chester et al.*, 1972] also observed a maximum of 133 μg m^{-3} south east of Cape Verde and an average of 0.23 μg m^{-3} further

south in the area of the ITCZ. Savoie et al. [*Savoie and Prospero*, 1977] reported an average mineral aerosol concentration of 29.8 ± 37.9 μg m^{-3} on Sal, Cape Verde, between July and September.

Air mass back trajectories for the maximum and minimum dust events in the present study display very similar upper elevation air mass back trajectories; compare Figures 1a and 1b. However, the lower elevation air mass back trajectories differ considerably for the two samples. During sample A96-02, the lower trajectories appear to sweep around from the middle of the Atlantic Ocean, without touching the African continent, while the corresponding trajectories for the minimum mineral dust loading event, A96-08, emanate from northwest Africa. This observation seems counterintuitive, since dust concentrations are larger when the lower level trajectories do not come in direct contact with the African continent. A possible explanation for the observed mineral dust concentration pattern may be that the high elevation trajectories carry all the dust particles, in the SAL, as previously reported [*Prospero and Carlson*, 1972; *Schütz*, 1980], and that these particles settle out later during the trajectory of an air mass.

From sample A96-13 and until the end of the cruise, trajectories display very different characteristics. Sample A96-16, in Figure 1d, illustrates trajectories that are representative for this latter part of the cruise. The upper level trajectories do not seem to be the source of mineral dust to these samples since they originate from the Caribbean, eastern North America, and/or northern South America. Samples A96-13 and A96-14 are collected in close proximity to Cape Verde and may therefore contain material from local sources, also indicated by relatively larger Pb and Zn concentrations (see Figure 3b).

The trajectories presented in Figure 1 seem very representative for the month of April over this region of the tropical North Atlantic Ocean. Swap et al. [*Swap et al.*, 1992] and Talbot et al. [*Talbot et al.*, 1990] display air mass trajectories and streamline fields over the tropical Atlantic Ocean during the month of April of 1987 which are very similar to the present trajectories. This indicates that the trajectories depend on the location of the West African Subtropical High which may vary significantly during the month of April.

It appears from the trajectories that the samples are divided into two groups with different air mass origins: one group is collected during the southern leg of the cruise and the other one during the northern leg. Of interest is to determine whether this difference is also reflected in mineralogical characteristics. Enrichment (over the crustal component) factor analyses of trace metals and the comparison of the water-soluble vs. total concentrations of alkali and alkaline earth elements serve to elucidate the mineralogical composition of the sampled mineral dust.

Ratios for the enrichment factor analysis using the crustal bulk composition according to Taylor and McLennan [*Taylor and McLennan*, 1985] are presented in Table 6. Concentrations used in this analysis are derived from the fully digested filters, thus, concentration are inclusive, regardless of the initial chemical composition of the phases present on the filter. A value above 1 signifies that the element is enriched over what would be expected if the aerosol were of average crustal composition only.

As found by the principal component analysis, Zn and Pb are of anthropogenic origin; therefore, their elevated enrichment factors: on average, 12.4 and 8.8, respectively. The rest of the trace metals, with exception of V, which may originate from the combustion of heavy fuel, are typically crustal derived, thus values close to 1 are expected. This is, however, not

the case in the present analysis. Some elements are present at levels that are too low (Sc, V, Mn, and Fe) and others at levels that are too high (Ti, Cs, Ba, La, Ce, Sm, Eu, Hf, and Th). It is also interesting to note that Ca, which has a sea-salt component and therefore should be enriched, displays a factor that is typically lower than 1. Based on the compilation in Faure [*Faure*, 1998] of the chemical composition of igneous and sedimentary rocks, several enrichment factor analyses are carried out in order to find the rock type that best matches the trace metal concentrations in the samples. Sandstone, low-Ca granite, basalt, deep-sea clay and carbonate rocks (not shown) display enrichment factors that do not match the samples well either. However, shale and high-Ca granites appear to be relatively good proxies for the trace metal composition of the samples, whereby shale is the best surrogate. The enrichment factors for shale are presented in Table 7. With the exception of Na, Mg, Ca, Zn, La, Hf, and Pb, the enrichment factors are very close to 1, indicating no enrichment. As mentioned above, Zn and Pb are of anthropogenic origin and therefore enriched over crustal concentrations. Sodium and Mg are mainly sea-salt derived, while most of the Ca has an additional, water-soluble source. Lanthanum and Hf are the only elements for which the discrepancy cannot be explained.

The typical composition of shale from Turekian and Wedephol [*Turekian and Wedepohl*, 1961], used here, not only describes the heavier trace metals in the mineral aerosol sampled, but it also accounts for the right amount of crustal-derived Na. This becomes apparent when comparing the water-soluble Na^+ concentrations as determined by the IC, with the sea-salt Na computed from the total ICP-MS Na, after subtracting the crustal (shale) contribution, see Figure 16a. Stacked bars are ICP-MS derived concentrations: the crustal component (in red and orange) is determined from the observed Al concentrations and

the composition for shale, while the remaining Na is assumed to be sea-salt (dark and light blue) derived. Overlain, in a dotted line, is the total water-soluble Na^+ concentration as determined by IC. Although not shown, the corresponding plots for Na in all the other igneous and sedimentary rocks experimented with above, exhibit crustal Na concentrations which are significantly larger than those for shale, thus increasing the discrepancy between ICP-MS and IC determined sea-salt Na concentrations. Figures 16b through 16d are plotted in an analogous manner as the Na plot. However, since both the crustal and the sea-salt (from the sea-salt ICP-MS Na) components in the ICP-MS determined concentrations can be computed, some samples display an excess or a deficit (plotted in green) compared to what would be expected if shale were the perfect crustal proxy. If the added up computed sea-salt and crustal concentration is larger than what is actually detected in the sample, the deficit is plotted as a negative bar. In that case, the shale composition must be over-predicting the concentration of the element in that sample since the sea-salt composition is assumed to be very accurate. This is especially seen for K, throughout the cruise and in both size fractions. In Figure 13, water-soluble K^+ appears to have an additional source other than sea-salt, which is mostly present in the fine fraction. This is also detected when comparing the sea-salt K determined from the ICP-MS concentrations (blue bars) with the IC determined total K^+ (dotted line). Even though shale does not satisfactorily describe the observed crustal K concentrations, it should be noted that none of the other igneous and sedimentary rocks do so in a better degree.

Either the presence of a third component or the under-prediction of the shale composition is implied when the green bars are positive. This is the case in Figure 16d, for Ca, especially during the latter part of the cruise. Sandstone and even more so carbonate

rocks significantly over-predict the Ca that should be present in the samples. High-Ca granites (not shown) and shale display very similar plots. Although shale is a good proxy for the mineral composition encountered, no one single composition would satisfactorily describe all the samples simultaneously as seen from the Ca, Mg and K plots. This is based on the observation that at the beginning of the cruise, K, Mg and Ca are over-predicted with regard to shale, while in the latter part of the cruise, the over-prediction becomes smaller for K, disappears for Mg and for Ca, shale starts under-predicting the crustal component. Thus, it is apparent that the mineral dust composition varies between the first and the second half of the cruise.

If shale is a good representation of the mineral composition in the present samples, then the plot in Figure 16d indicates that most of the Ca in the shale has to be present in a water-soluble form since concentrations of the IC determined Ca^{2+} closely follow the total Ca concentrations as determined by the ICP-MS. This water-soluble Ca is believed to be calcite ($CaCO_3$). Calcite has previously been observed in aerosol samples over the Atlantic Ocean [*Glaccum and Prospero*, 1980; *Savoie and Prospero*, 1980; *Schütz and Sebert*, 1987; *Zhu et al.*, 1992]. Furthermore, the water-soluble NSS-Ca^{2+} component in the coarse fraction, where most (63%) of the NSS-Ca^{2+} is present, correlates with the deficit in anionic charges in the principal component analysis in Table 4. The observed charge deficit is believed to arise from the CO_3^{2-} which is not detected by IC. Additional calcite appears on the samples in the second half of the cruise, not only in close proximity to Cape Verde, but along the entire northern trajectory back to Barbados. This is another indication that two somewhat distinct mineral aerosol sources prevail during the first and the second part of the cruise.

Glaccum and Prospero [*Glaccum and Prospero*, 1980] determined that the mineralogical composition of aerosols carried from Cape Verde to Barbados and Miami were very similar to that of an average shale, in agreement with our observations. Shale is made up of a number of different minerals and it carries the implication of very small particle size. The mineral composition of the aerosols over the Atlantic Ocean has been found to be made up of mica, quartz, kaolinite, chlorite, montmorillonite, plagioclase, microcline and calcite [*Anderson et al.*, 1996; *Chester et al.*, 1972; *Delaney et al.*, 1967; *Glaccum and Prospero*, 1980], which is the composition of a typical shale. Shale is a weathering product whose composition depends not only on the mineral form from which it was formed, but also on the chemical environment of weathering, which in turn is largely the result of climate. The weathering may have occurred at the location of the parent material and/or during transport by water and wind, having been sorted and possibly concentrated in the process. Resistant materials such as quartz, incompletely weathered minerals, such as feldspar, and minerals formed by precipitation from aqueous solution, notably calcite, may be present. A consequence of the differential density and shape of the distinct mineral phases in the shale aerosol would be that the composition changes as the dust is transported across the Atlantic. Greater sedimentation velocities of the larger and heavier mineral particles, such as quartz, are preferentially removed from the air mass relative to the small and flaky clay particles. Such a selective separation was observed in samples collected along the trajectory of an air mass by Glaccum and Prospero [*Glaccum and Prospero*, 1980]. In the present case, however, this does not explain the apparent different mineralogical composition encountered during the first and second halves of the present cruise.

According to a number of investigators [*Chiapello et al.*, 1997; *Paquet et al.*, 1984; *Schütz and Sebert*, 1987], a high amount of calcite in the mineral aerosol can be considered an indicator for aerosol matter originating from the northern Sahara, where calcite is the major compound of marine sedimentary deposits and outcrops [*Schütz and Sebert*, 1987]. This would imply that during the latter half of the cruise, when calcite is more abundant, the air mass trajectories should have emanated from over the northern Sahara. The present trajectories are not a clear indicator for that since some of them appear to originate from southern Europe (see Figure 1c and 1d).

Chiapello et al. [*Chiapello et al.*, 1997] investigated the relationship between Fe, Ca, K, Si and Al to identify aerosol originating from three different source regions in Africa. In comparing their air mass trajectories with ours, it seems that throughout the cruise, air masses in the present study originate from the north and west Saharan sector, which includes Spanish Sahara, Morocco and west Algeria. During the months of March and April all the dust events at Sal Island (Cape Verde) originated from this north and west Saharan sector [*Chiapello et al.*, 1997], thus, due to the apparent seasonality of the wind patterns, we expect to see the same sector as the origin for our mineral aerosol. Chiapello et al. [*Chiapello et al.*, 1997] found that the ratios of Fe/Ca, Ca/Al and K/Ca were good indicators to classify the mineral aerosol into one of the three sectors. Due to the elevated Ca concentrations in the latter part of the present cruise compared to the first half, all three of these ratios varied to an extent that would indicate two different mineralogical characteristics. The Fe/Ca geometric mean decreased from 1.71 to 0.93, the Ca/Al ratio increased from 0.31 to 0.64, and the K/Ca ratio decreased from 0.86 to 0.57, from the first half of the cruise to the latter part. Compared to Chiapello et al.'s ratios, this would classify the mineral aerosol collected during

the first half of the cruise to originate from the central Sahara, while the mineral aerosol from the latter half would have emanated from the northern Sahara.

Other investigators [*Arimoto et al.*, 1995; *Bergametti et al.*, 1989; *Chiapello et al.*, 1997; *Delaney et al.*, 1967] have used the Fe/Al ratio to determine source regions of Africa. Fe/Al is found to be higher in dust originating from a Sahelian source compared with dust from the vicinity of Morocco. This increase in Fe/Al ratios may result from changes in clay minerals [*Bergametti et al.*, 1989]: the Sahelian regions are known to present abundant ferrallitic soils, thus, iron is the dominant element in clay minerals from this region, while in clay minerals that originate from Morocco, iron only appears as a minor component. Fe/Al ratios from the Sahelian regions are in the range 1.5-1.8, while those from the northern Sahara range from 0.3 to 1.1. In the present samples we observe Fe/Al ratios on the fine and coarse fractions combined that average 0.56 ± 0.09 (geometric mean) and vary only in a very small range, from 0.47 to 0.9. The geometric mean of the first 9 samples is 0.53 while that for the rest of the samples, representing the latter part of the cruise, is insignificantly larger, 0.59. Very similar values are found when treating fine and coarse fractions separately. Thus, it appears from these observations that the Fe/Al ratio does not indicate a Sahelian source region throughout the cruise. Based on all the ratios investigated above, the mineral aerosol sampled during the entire cruise seems to originate from the Sahara, whereby it may be that the second half of the cruise is more typical of the northern Sahara, rich in calcite, and the first part of the cruise of central Sahara.

In summary, shale appears to be the best proxy for the mineral aerosol composition sampled during the present cruise. Based on the heavier trace metals, there seems be no variability in mineralogical composition between samples, thus indicating a common source

region, the Saharan desert. Mineralogical differences are only indicated in the concentrations of alkali and alkaline earth elements. Excess water-soluble Ca^{2+} (over that expected from shale and sea-salt), presumably present in the form of $CaCO_3$, is abundant in the latter part of the cruise which suggests that the air masses emanated from the northern Sahara, while the mineral aerosol during the first half of the cruise may have originated from central Saharan sources. With an average Al concentration of 8% in shale [*Turekian and Wedepohl*, 1961], the computed dust loading concentrations will increase by 5% from the values determined based on the average crustal composition presented above. Thus, the average dust loadings amount to 19.3 ± 16.4 μg m^{-3}, and range from 0.8 to 55.6 μg m^{-3}. On average, the mineral aerosol accounts for ~ 42% of the TSP. This value is most probably skewed since the TSP is determined from the low volume filters while the mineral dust loadings are derived from the Al concentrations on the high volume filters. In our previous paper [*Johansen et al.*, 1999] we showed that the sampling efficiency for the two samplers utilized in this study differ appreciably, especially during high winds and for the larger particles. The low volume sampler appears to be more efficient at collecting large particles, which leads to presently determined TSP values that are larger than TSP values that would have been determined from the high volume filters.

Calcite ranges from 0.01 to 3.47 μg m^{-3} and averages 1.27 ± 0.98 μg m^{-3} (~ 3% of TSP, note the comment made above about the different samplers used). The calcite content amounts to 3.0 and 7.9% of the mineral aerosol, during the first and second half of the cruise, respectively. The calcite content peaks in sample A96-14, showing 11.5% of calcite and it reaches a minimum near the equator, in sample A96-08, when it represents 0.6% of the mineral aerosol. Zhu et al. [*Zhu et al.*, 1992] found calcite to comprise 5.0-5.3% of the dust

in Barbados, while Glaccum and Prospero [*Glaccum and Prospero*, 1980] observed 3.9% calcite in the same location. These values are in the same range as those determined in the present study. Savoie and Prospero [*Savoie and Prospero*, 1980] measured soluble Ca concentrations in Barbados and Miami which were about a factor of 2 lower than in Sal Island (Cape Verde), accounting for 6.4, 6.6, and 11.3% of the mineral aerosol, respectively. These values are in agreement with our observations during the second part of the cruise. While the calcite content in the fine fraction does not change significantly between the two halves of the cruise, the calcite in the coarse fraction is considerably larger during the second half, 10.4 as opposed to 5.4% during the first part.

4.5.2 Sea-salt Aerosol

Although most sea-salt derived ions can be considered conservative and inert to chemical reactions occurring in the aerosol phase, the few anions that may play a role need to be studied in greater detail due to their oxidative character. Furthermore, the sole presence of the sea-salt in the atmosphere may have an effect on the uptake and oxidation of sulfur gases, which in turn play an important role in the radiation balance of the atmosphere.

Of the water-soluble cations in the collected aerosol, Na^+ is typically used as the tracer for the sea-salt component. In the present samples, sea-salt concentrations computed from Na^+ vary from 1.4 to 27.8 $\mu g\ m^{-3}$ and average 10.6 ± 5.5 $\mu g\ m^{-3}$. See Figure 13a for concentrations in coarse and fine fractions as a function of sample. Compared to the mineral aerosol, the sea-salt component varies to a much smaller extent and amounts to ~ 55% of the mass of the mineral dust component in the aerosol. The sea-salt represents ~ 23% of the TSP (again, note the different samplers used). Combining the sea-salt and crustal masses

accounts for ~ 68% of the TSP, while ~ 32% of the TSP has another source. Since anthropogenic and biogenic sources are unlikely to add the missing aerosol mass, the low volume collectors appear to be more efficient in collecting aerosol particles, particularly in the larger size range (see also [*Johansen et al.*, 1999]).

Sea-salt particles in the fine fraction appear to correlate with MSA and NSS-SO_4^{2-} in the principal component analysis presented in Table 4. This is in agreement with observations by a series of investigators [*Kerminen et al.*, 1997; *O'Dowd et al.*, 1997; *Pszenny*, 1992; *Qian and Ishizaka*, 1993; *Quinn et al.*, 1993; *Saltzman et al.*, 1983]. The low vapor pressure of the gaseous species H_2SO_4 and MSA leads to their immediate condensation onto available pre-existing aerosol surface area. The major contributor to aerosol surface area over the oceans may under most circumstances be the sea-salt particles in the size range 1-5 μm [*Sievering et al.*, 1992]. Thus, these droplets may provide the primary sink for low vapor pressure aerosol precursor species which could otherwise form and grow new particles on CCN. Furthermore, sea spray is buffered at a high pH, at which SO_2 oxidation by ozone proceeds at a substantial rate [*O'Dowd et al.*, 1997]. This may significantly modify the marine sulfur cycle by providing a rapid removal for SO_2 from the atmosphere.

Sea-salt aerosol has also been found to be the source of halogen radicals [*Fan and Jacob*, 1992; *Finlayson-Pitts*, 1983; *Finlayson-Pitts et al.*, 1989; *Graedel and Keene*, 1995; *Keene et al.*, 1996; *Pszenny et al.*, 1993; *Sander and Crutzen*, 1996; *Vogt et al.*, 1996]. These transient radical oxidants strongly influence the oxidative properties of aerosol particles in the marine boundary layer. Reactive Cl can initiate photochemical reactions in an analogous manner to $OH^{\bullet}$ and have major consequences for the oxidation of hydrocarbons and DMS [*Keene et al.*, 1996; *Keene et al.*, 1990; *Langer et al.*, 1996; *Pszenny et al.*, 1993; *Sander and*

Crutzen, 1996; *Stickel et al.*, 1992; *Vogt et al.*, 1996]. The release of reactive Cl species from the aerosol phase can be traced by examining the depletion of Cl^- compared to expected sea-salt concentrations. However, there exist additional mechanisms by which Cl^- is depleted from the aerosol phase.

Chloride deficits have typically been found to correlate with the proximity to continental landmasses and thus assumed to depend on the concentrations of anthropogenic pollutants such as NSS-SO_4^{2-} and NO_3^- [*Sturges and Shaw*, 1993]. Thermodynamically favorable acid displacement reactions between mineral acids (H_2SO_4, HNO_3) and Cl^-, with subsequent HCl volatilization [*Duce and Hoffmann*, 1976; *Duce et al.*, 1973; *Sturges and Barrie*, 1988] have been assumed responsible for these observations. In Johansen et al. [*Johansen et al.*, 1999] we found that the Cl^- deficit observed during two different seasons over the Northern Indian Ocean depended strongly on the matrix of the aerosol particles. The largest deficits were measured during the SW-monsoon, when NO_3^- and NSS-SO_4^{2-} concentrations were very small and therefore acid displacement reactions less important. Instead, the Cl^- deficit appeared to correlate well with the discrepancy between total anion and cation charges, which would be a consequence of the Cl being released in the form of reactive species, such as Cl_2, HOCl, $ClNO_2$, NOCl and BrCl. Evidence of the existence of several highly reactive Cl gases has been shown experimentally [*Finlayson-Pitts*, 1983; *Finlayson-Pitts et al.*, 1989; *Graedel and Keene*, 1995; *Keene et al.*, 1990; *Pszenny et al.*, 1993; *Vogt et al.*, 1996].

To find a possible correlation in the present samples between the Cl^- deficit on one hand and anthropogenic pollutants and charge deficits on the other, the Cl^- deficit for both size fractions is included in the principal component analysis (not shown). The chloride

deficit in the coarse fraction, and less so in the fine, correlates with component 2, which is analogous to component 2 in the principal component analysis in Table 4. This component represents the sea-salt and to a lesser degree a coarse crustal source, including coarse NO_3^-, thelatter of which may be partly responsible for the volatilization of HCl in the coarse fraction. The second component also correlates with the charge deficit observed between the anions and cations in the coarse fraction. When plotting neq concentrations of NO_3^-, NSS-SO_4^{2-} as a function of Cl^- deficit for the coarse fraction (in Figure 12b), the correlation is slight and concentrations of NO_3^- are typically 30-40% below Cl^- deficit concentrations. The line in the plot represents the 1:1 ratio of nmols of Cl^- deficit and neq of mineral acid. For the data points that fall to the lower right of the line the Cl^- deficit is larger than the mineral acid available for the acid displacement reaction. Even the addition of the available NSS-SO_4^{2-} to the NO_3^- concentrations in the coarse fraction does not bring the mineral acid abundance up to match the Cl^- deficit concentration for 76% of the samples. This is indicative of the presence of another potential mechanism that leads to the Cl^- deficit. As mentioned, the Cl^- deficit also correlates with the charge discrepancy between cations and anions. Since the release of Cl in the form of reactive species, such as Cl_2, HOCl, $ClNO_2$, NOCl and BrCl may not be replaced by a detectable ion, such as, e.g., CO_3^{2-}, it is conceivable that the charge difference may become a measure of the extent of Cl^- released in this form. However, the charge difference amounts to concentrations that are on average ~ 115% larger than the Cl^- deficit. Thus, in the coarse aerosol fraction, it seems that a combination of mechanisms are responsible for the depletion of Cl^-; both the acid displacement reaction with HNO_3 and H_2SO_4 and the Cl release in the form of reactive species. The acid displacement reactions are thermodynamically favorable:

$$2\ NaCl(s) + H_2SO_4 \rightarrow Na_2SO_4(s) + 2HCl(g) \quad (1)$$

$$NaCl(s) + HNO_3 \rightarrow NaNO_3 + HCl(g) \quad (2)$$

The depletion of Cl in the form of volatile reactive Cl species may include reactions with Br [*Fan and Jacob*, 1992; *McConnell et al.*, 1992; *Vogt et al.*, 1996] and with gas-phase species such as NO_2, $ClONO_2$, N_2O_5, and O_3 [*Finlayson-Pitts*, 1983; *Finlayson-Pitts et al.*, 1989; *Graedel and Keene*, 1995; *Keene et al.*, 1990; *Pszenny et al.*, 1993; *Vogt et al.*, 1996]:

$$H^+ + Cl^- + HOCl \rightarrow Cl_2(g) + H_2O \quad (3)$$

$$H^+ + Cl^- + HOBr \rightarrow BrCl(g) + H_2O \quad (4)$$

$$Cl^- + 2\ NO_2(g) \rightarrow NOCl(g) + NO_3^- \quad (5)$$

$$Cl^- + ClONO_2(g) \rightarrow Cl_2(g) + NO_3^- \quad (6)$$

$$Cl^- + N_2O_5(g) \rightarrow ClNO_2(g) + NO_3^- \quad (7)$$

$$2\ Cl^- + O_3(g) \rightarrow Cl_2(g) + 2\ OH^- + O_2(g) \quad (8)$$

The fine fraction Cl^- deficit correlates with the fine MSA/sea-salt component (nr. 4), which also carries a significant signature of fine NSS-SO_4^{2-}. This NSS-SO_4^{2-} appears to be the main actor for the deficit of Cl^- in the fine fraction, clearly visible in Figure 12c, where the data points representing the NSS-SO_4^{2-} neq concentrations vs. Cl^- deficit (open circles) fall around the 1:1 line. These observations are in agreement with Sievering et al.'s [*Sievering et al.*, 1990] findings from samples collected in Bermuda, where they observed that the fine fraction (< 1 μm) aerosol Cl^- displacement appears to be more likely by SO_4^{2-} than by NO_3^-.

Kerminen et al. [*Kerminen et al.*, 1998] also found that MSA and oxalate replace Cl^- from supermicron sea-salt particles. However, concentrations of MSA and oxalate are so

small compared to NSS-SO_4^{2-} and NO_3^- that their effect would be minute and undetectable in the present case.

4.5.3 SO_4^{2-} Contributions

Sulfate in the atmosphere is composed from a series of different sources. It is of special interest to determine the various contributions to NSS-SO_4^{2-} since particles in the sub-micrometer size range may serve at CCN and influence the radiation balance of the atmosphere [*Charlson et al.*, 1987].

Weighted linear regression analysis has been shown [*Johansen et al.*, 1999] to be a useful tool for identifying the sources and determining the source strengths of SO_4^{2-}. Tracers are used to represent the various sources: typically, Na^+ serves as the sea-salt, MSA as the biogenic, and Pb or NO_3^- as the anthropogenic tracer. The principal component analysis in Table 4 gives an indication of which species can be used as surrogates for the different SO_4^{2-} sources. Component 3 carries high scores for fine and coarse NSS-SO_4^{2-}, which appears to correlate strongly with fine and coarse Zn, fine Pb, and less with coarse NO_3^- and coarse NSS-Ca^{2+}. Thus, Zn, Pb and NO_3^- may be potential anthropogenic tracers, while NSS-Ca^{2+} may describe the gypsum component that was also observed over the Indian Ocean in Johansen et al. [*Johansen et al.*, 1999].

Exploration of the various tracer combinations in the regression analysis did not uncover a regression that satisfactorily describes the present system. Table 8 lists the best model runs for each of the size fractions, fine, coarse, and total. In each case, the corresponding SO_4^{2-} is the dependent variable, and the tracers used for the various sources represent the set of independent variables. The model can be tested by inspecting the

statistical information that accompanies it (refer to [*Johansen et al.*, 1999; *Zar*, 1996] for a detailed description). In addition, there is a convenient way of testing the models in the present case: the ratio of SS-SO_4^{2-}/Na^+ is constant and known, 0.252 [*Millero and Sohn*, 1992], thus, the corresponding coefficient extracted in the model should be close to 0.252. However, this is not the case in any of our models. Furthermore, in an optimal situation, the intercept with the ordinate (denoted, "constant," in the models) should be close to zero and the significance of the null hypothesis for this constant should be large if the regression can be forced through the origin. In that case the dependent variable is satisfactorily described by the selected independent variables. This is not observed in the presented models either.

The value of real interest is the coefficient for the biogenic SO_4^{2-} contribution (bio-SO_4^{2-}), bio-SO_4^{2-}/MSA, which is thought to depend only on atmospheric temperature [*Bates et al.*, 1992; *Berresheim et al.*, 1989; *Berresheim et al.*, 1991; *Bürgermeister and Georgii*, 1991; *Hynes et al.*, 1986; *Prospero et al.*, 1991; *Pszenny et al.*, 1989; *Saltzman et al.*, 1985; *Saltzman et al.*, 1983; *Savoie and Prospero*, 1989; *Savoie and Prospero*, 1994; *Savoie et al.*, 1992; *Savoie et al.*, 1989a]. *A priori* knowledge of this ratio would serve to determine the SO_4^{2-} concentrations in the atmosphere which are purely biogenically derived, from measured MSA concentrations. The bio-SO_4^{2-}/MSA ratios determined in the linear regression analyses appear underlined in Table 8; 37.4 ± 2.8 for the coarse SO_4^{2-}, 23.9 ± 4.2 for the fine SO_4^{2-}, and 33.9 ± 5.0 for the total SO_4^{2-}. These values are slightly lower than the calculated NSS-SO_4^{2-}/MSA ratio, which is the ratio typically reported in literature. The geometric mean for the NSS-SO_4^{2-}/MSA ratio in the combined fine and coarse fractions amounts to 37.4 ± 16.4 (compared to 33.9 ± 5.0 in Table 8), whereby it ranges from 11.1 to 75.1. The lowest ratio of 11.1 is observed in sample A96-09, when crustal, anthropogenic

and sea-salt abundances are very low. Thus, this value may represent a true bio-SO_4^{2-}/MSA ratio valid at the measured temperature, 26 °C. This one observation happens to be in accordance with Figure 5 in Johansen et al. [*Johansen et al.*, 1999], which presents a bio-SO_4^{2-}/MSA temperature relationship found during two seasons over the Arabian Sea.

NSS-SO_4^{2-}/MSA ratios reported in literature are not typically corrected for anthropogenic contributions, thus, very often they are higher than the true biogenic ratio. Savoie et al. [*Savoie et al.*, 1989b] found that ratios of 35.7 dropped to 15.2 when corrected for anthropogenic SO_4^{2-} contributions using NO_3^-. In the remote tropical Pacific Ocean [*Saltzman et al.*, 1985; *Saltzman et al.*, 1983] where continental inputs are believed to be minimal, low NSS-SO_4^{2-}/MSA values of ~ 15 were observed. These values are close to what the biogenic SO_4^{2-}/MSA ratio is expected to be in tropical regions. Values in the same range were found over the Arabian Sea [*Johansen et al.*, 1999] during two seasons where samples were corrected for additional inputs, other than biogenic SO_4^{2-}. In the same study, the SW-monsoon season represented very clean marine conditions, during which biogenically derived MSA concentrations were appreciable and anthropogenic sources negligible. The uncorrected NSS-SO_4^{2-}/MSA ratio in those samples averaged ~ 14, which is, as expected, very close to the real bio-SO42-/MSA, corrected for the small anthropogenic SO_4^{2-} concentrations; 13.5. NSS-SO_4^{2-}/MSA values (uncorrected for anthropogenic contributions) in the range of 30 to 40, comparable to what we determined in the present case, have been observed over the Atlantic Ocean [*Davison et al.*, 1996; *Galloway and Rodhe*, 1991; *Galloway et al.*, 1993]. They were always attributed to continental contamination.

A couple of potential reasons exist for the difficulty in extracting biogenic SO_4^{2-} /MSA ratios in the expected range (around 15 or lower) from the application of the linear

regression analysis, as done in Johansen et al. [*Johansen et al.*, 1999]. In a linear regression analysis the ratio between the tracer and the corresponding SO_4^{2-} portion needs to remain constant for each sample for it to be successful. Circumstances in which this condition may not hold true include sampling of air masses of very different source regions and large temperature variations between and within samples. During the present cruise, both the air mass characteristics and the temperature varied considerably throughout the duration of the trip. Figure 17 illustrates the temperature change from start to end of the cruise. Temperatures varied between 21 and 28 °C. In the regime of 24 to 28 °C, according to Figure 5 in Johansen et al. [*Johansen et al.*, 1999], one may expect an increase in the bio-SO_4^{2-}/MSA ratio of approximately 2 per degree increase in temperature. Thus, the outcome of the model can, therefore, not be reliable. The same argument holds for the ratio between the anthropogenic tracer and the corresponding anthropogenic-SO_4^{2-} fraction. Some investigators [*Li-Jones and Prospero*, 1998; *Savoie et al.*, 1989b] have used the magnitude of the ratio NO_3^-/NSS-SO_4^{2-} to determine whether or not the observed pollutants were of European or African origin. In analogy, it is expected that the anthropogenic SO_4^{2-} in relation to Pb and Zn will vary according to their source regions.

The insufficient number of samples prevents us from classifying samples into air mass origin and temperature groups. Due to the complex characteristics of this data set, it appears difficult to ascertain the biogenic and anthropogenic inputs of SO_4^{2-} into the atmosphere in an analogous manner as carried out in Johansen et al. [*Johansen et al.*, 1999], where air mass origins were very consistent for each season of the year.

As an alternative, the magnitude of the various SO_4^{2-} contributions can be estimated by assuming that the bio-SO_4^{2-}/MSA ratio temperature dependence in Figure 5 in Johansen et

al. [*Johansen et al.*, 1999] is a reasonable approximation for the bio-SO_4^{2-} concentrations for each sample. The bio-SO_4^{2-}/MSA ratio follows an exponential dependence: bio-SO_4^{2-}/MSA = 0.06 exp(0.198 T(C°)). In an analogous manner as performed above, weighted linear regressions with the remaining nonbiogenic SO_4^{2-} and appropriate tracers could reveal the magnitude of the other sources and prove the justified use of Figure 5 in Johansen et al. [*Johansen et al.*, 1999]. Table 9 lists the outcome of the best models for linear regressions on the coarse and fine nonbiogenic SO_4^{2-} fractions. Tracers for the nonbiogenic coarse and fine SO_4^{2-} fractions are chosen based in correlations observed in the principal component analysis, identical to the reasoning followed when the linear regressions from Table 8 were performed. Linear regressions with the total nonbiogenic SO_4^{2-} were unsuccessful, and as a consequence, they are not shown in Table 9.

The coarse NSS-SO_4^{2-} fraction includes an anthropogenic component, which appears to correlate with coarse NO_3^- and with Zn in both size fractions. Coarse NSS-Ca^{2+} also shows an indication of correlating with coarse NSS-SO_4^{2-}, thus, it is conceivable to believe that gypsum, $CaSO_4$, is present in the samples. $CaSO_4$ has been observed in aerosol particles and may be a result of the reaction between acid sulfates and silicate minerals brought together by in-cloud processes [*Andreae et al.*, 1986]. In addition, $CaSO_4$ may be associated with the combustion of fossil fuels [*Hopke*, 1985], and it may originate from crustal sources such as evaporite deposits and gyspiferous soils, as has been observed over the northern Indian Ocean [*Johansen et al.*, 1999; *Savoie et al.*, 1987]. However, $CaSO_4$ observed on samples collected over the Atlantic Ocean has been attributed to be a conversion product of calcite reacting with atmospheric sulfur species on the filter during sample collection

[*Glaccum and Prospero*, 1980]. Thus, the dust is not believed to contain any primary gypsum.

The first two models in Table 9 differ only in the choice of the anthropogenic tracer. Although the statistics show that the second model, which includes NO_3^-, is slightly better than the first one, in which Zn is the anthropogenic tracer, the coefficient for SS-SO_4^{2-}/Na^+ shows a value closer to the one expected in sea water (0.252) in the model with Zn. Since the ordinate intercept is negligible in both cases with a large significance for its null hypothesis, the linear regression is forced through the origin. Compared to the linear regression carried out on coarse SO_4^{2-}, in Table 8, the ones carried out on the coarse nonbiogenic SO_4^{2-} in Table 9 result in better models. Nevertheless, the first model in Table 9 does not perfectly describe the observed coarse SO_4^{2-} concentrations, as is visualized in Figure 18a. The anthropogenic and gypsum contributions are calculated based on the coefficients found in the first model in Table 9; the sea-salt component on the other hand is determined from the constant value 0.252, and not from the coefficient in the model. This corresponds to an overestimation of the sea-salt component by 11% compared to what the model output would predict. The biogenic fraction is determined from the observed MSA concentrations and the corresponding ratio found from the exponential temperature dependence in Figure 5 in Johansen et al. [*Johansen et al.*, 1999]. Figure 18a shows that, with exception of the first two samples, the model over-predicts total coarse SO_4^{2-} by on average 9.9%, some of which may be attributed to the larger sea-salt fraction used by assuming that the SS-SO_4^{2-}/Na^+ ratio is 0.252 instead of 0.224. Since other characteristics of the aerosol material (discussed above) have shown that the NSS-Ca^{2+} most probably is

derived from calcite instead of gypsum, the use of NSS-Ca^{2+} in the model may also lead to an over-prediction of SO_4^{2-}.

Figure 18b shows the contributions to coarse SO_4^{2-} when neglecting the existence of $CaSO_4$, corresponding to the third linear regression output in Table 9. As in the other two models, the intercept becomes negligible and the regression is forced through the origin. This time, the SS-SO_4^{2-}/Na^+ ratio that is returned by the linear regression is only 4% smaller then the expected value of 0.252. Nevertheless, the model over-predicts coarse SO_4^{2-} more than the previous model that included $CaSO_4$. The average over-prediction, excluding samples A96-08 and A96-09 (due to their large discrepancy from the model because of low concentrations and attributed large errors), amounts to 13.6%.

In both the models for the coarse SO_4^{2-} contributions (first and third in Table 9), presented in Figures 18a and 18b, the coarse biogenic SO_4^{2-} component accounts for ~ 7% (50 ± 57 ng m^{-3}) of the total coarse SO_4^{2-}, which translates into ~ 24% of the coarse NSS-SO_4^{2-}. If neglecting the presence of $CaSO_4$, the rest (~ 76%) of the NSS-SO_4^{2-} would be of anthropogenic origin, which accounts for ~ 21% (148 ± 83 ng m^{-3}) of the total SO_4^{2-}.

It is not clear which of the two models for the coarse SO_4^{2-} better fits the observed concentrations. Because gypsum has generally not been seen over the Atlantic Ocean, it may be an artifact from the reaction of $CaCO_3$ with H_2SO_4 collected on the filter, as indicated by Glaccum et al. [*Glaccum and Prospero*, 1980]. The degree of $CaCO_3$ to $CaSO_4$ conversion will depend on the availability of NSS-SO_4^{2-} and thus on the characteristics of each air mass. Since we measure the combined concentration of $CaCO_3$ and $CaSO_4$ (as NSS-Ca^{2+}), no distinction can be made between the two. Thus, although an attempt is made here to separate the temperature effect from the linear regression, there appear to be additional parameters

that influence the linear regression analyses such that no good fit of the observed coarse SO_4^{2-} concentrations is achieved. The most probable causes are in the large variability in aerosol origin, which would manifest itself in non-constant ratios for the anthropogenic tracer, and in the possibility of the presence of a small and varying quantity of $CaSO_4$ which cannot unambiguously be described by the tracer NSS-Ca^{2+}.

Fine SO_4^{2-}, as found in the linear regression analysis from Table 8 and in the principal component analysis in Table 4, does not seem to correlate with NSS-Ca^{2+}. Thus, the presence of a potential source of gypsum SO_4^{2-} does not complicate the situation for the linear regression of the fine fraction. After subtracting the biogenic SO_4^{2-} from the total fine SO_4^{2-}, the nonbiogenic SO_4^{2-} remainder is used in the linear regression analysis presented at the end of Table 9. Since the intercept is close to 0, the model is forced through the origin. The SS-SO_4^{2-}/Na^+ ratio given by the linear regression, 0.270, is 8% above what is expected for sea-salt. Figure 18c shows the predicted contributions in the stacked bars in comparison to the observed fine SO_4^{2-} concentration, represented in the dotted line. It is clear that the model overestimates the beginning, underestimates the middle, and fits nicely for the latter part of the cruise. This observation strengthens the argument about the different characteristics of the air masses sampled. On average, the model overestimates fine SO_4^{2-} by 5.8%. Approximately 16% (188 ± 97 ng m^{-3}) are of biogenic, 58% (704 ± 443 ng m^{-3}) of anthropogenic, and 26% (311 ± 144 ng m^{-3}) of sea-salt origin. The biogenic contribution to NSS-SO_4^{2-} in the fine fraction amounts to 22% while the rest is anthropogenically derived.

4.5.4 Fe(II)

Ferrous iron released after 22 hours of extraction time with added ferrozine is found to correlate with the corresponding total Fe, while Fe(II) after 5 minutes extraction with ferrozine ($Fe(II)_{total,5min}$) correlates with anthropogenic tracers such as NO_3^-, NSS-SO_4^{2-} and oxalate. This seems to suggest that the Fe(II) after 22 hours depends on the total iron that is available in the sample, regardless of its initial form, while the $Fe(II)_{total,5min}$ abundance depends on additional factors. The dependence of Fe(II) concentrations on the mentioned anthropogenic tracers is in agreement with observations made in numerous field and laboratory studies, indicating that Fe(II) is photochemically produced in the presence of organic acids and ferric oxides and (oxy)hydroxides [*Erel et al.*, 1993; *Faust and Hoigné*, 1990; *Faust and Zepp*, 1993; *Pehkonen et al.*, 1993; *Siefert et al.*, 1994; *Zuo*, 1995; *Zuo and Hoigné*, 1992; *Zuo and Hoigné*, 1994]. Iron is also known to catalyze the oxidation of S(IV) by oxygen [*Berglund and Elding*, 1995; *Berglund et al.*, 1993; *Conklin and Hoffmann*, 1988; *Faust and Allen*, 1994; *Kraft and van Eldik*, 1989; *Martin and Hill*, 1987]. Furthermore, the correlation with NO_3^- and NSS-SO_4^{2-} may also be indicative of a lower aerosol pH which increases Fe(II) stability relative to its oxidation.

The ratios NH_4^+/NSS-SO_4^{2-} and (NH_4^+ + NSS-Ca^{2+})/NSS-SO_4^{2-} are an indicator of the acidity in the aerosol particle which may serve to study the observed Fe(II) concentrations. These ratios are presented in Figures 14 and 15. When neglecting the acid neutralizing capacity of $CaCO_3$ the aerosol particles collected during several sampling periods are relatively acidic. This is reflected in the low values (close to 0.5) of the NH_4^+/NSS-SO_4^{2-} ratio seen near Cape Verde (Figure 14b). In Figure 19a, this ratio is plotted as a function of $Fe(II)_{total,5min}$ in both fine and total fractions (coarse values are not presented for reasons

given above). A relationship is apparent in Figure 19a between acidic conditions and the observed Fe(II) concentrations. After taking into account the acid neutralizing capacity of $CaCO_3$, which is especially abundant near Cape Verde, there appears to be a similar tendency in the data set (Figure 19b). This time, the increase in Fe(II) concentration as a function of a decreasing $(NH_4^+ + NSS\text{-}Ca^{2+})/NSS\text{-}SO_4^{2-}$ ratio is more pronounced in the fine fraction; this may be due to the lower $CaCO_3$ abundances in the fine fraction compared to the coarse fraction.

It is interesting to note that when comparing $Fe(II)_{total,5min}$ with total Fe (in Figure 4c), the samples appear to be divided into three groups: the first part of the cruise, where total Fe is considerable but $Fe(II)_{total,5min}$ is small, the middle part of the cruise, near the equator, when total Fe is small and Fe(II) is not negligible, and the last part of the cruise, when total Fe takes on a middle range, while $Fe(II)_{total,5min}$ is considerable. The same effect can be recognized in Figure 5, in terms of % of $Fe(II)_{total,5min}$ in total Fe. This observation is in agreement with the general mineralogical characteristics found during the present cruise. The low mineral dust concentrations near the equator may indicate that the air mass may have traveled a considerable amount of time during which most particles may have settled out of the boundary layer, but the remaining ones had sufficient time to undergo chemical transformation producing more Fe(II). Similar reasoning may be used for interpreting the $Fe(II)_{total,5min}$ vs. total Fe changes observed during the latter part of the cruise, when mineral aerosol material seems to be from one and the same source (i.e., the northern Sahara). As the aerosol is transported from Cape Verde (sample A96-14) to Barbados, both total Fe and $Fe(II)_{total,5min}$ drop off, see Figure 4c, due to sedimentation of the particles. However, during the same time, the relative contribution of Fe(II) is increasing; see Figure 5. This may, again,

be a function of the time available for the iron phases in the aerosol particle to undergo photochemical reduction that leads to increased Fe(II) concentrations. The increase in the combined percentage coarse- and fine-$Fe(II)_{total,5min}$ is a factor of 2.9 from sample A96-14 to sample A96-20. This effect is more pronounced in the coarse than in the fine fraction, where the relative $Fe(II)_{total,5min}$ increases by factors of 3.6 and 1.8, respectively.

Another interesting feature, which is revealed in the principal component analysis presented in Table 4, is that $Fe(II)_{total,5min}$ in the fine fraction, where 86% of the $Fe(II)_{total,5min}$ is present, correlates with MSA (in component nr. 4). A weak relationship is affirmed by plotting fine-$Fe(II)_{total,5minFZ}$ vs. total MSA, as shown in Figure 20. In an iron enrichment experiment in under-productive surface ocean water, Turner et al. [*Turner et al.*, 1996] observed an increase in DMS production as predicted by a number of investigators [*Martin et al.*, 1994; *Martin and Fitzwater*, 1988; *Martin et al.*, 1991; *Zhuang et al.*, 1992b]: an increase in DMS production. Since DMS is oxidized to MSA and NSS-SO_4^{2-}, it may be plausible to detect a feedback in the MSA concentration from the increased Fe(II) input into the surface waters of the ocean.

4.6 Conclusions

Mineralogical characteristics of the mineral aerosol and back trajectories of the air masses sampled in the present cruise appear to indicate a Saharan desert origin; larger calcite concentrations observed during the second-half of the cruise suggest a more northern Sahara source. Based on the observed ratios between trace metals and the abundances of alkali and alkaline earth elements, the mineralogical composition of the collected mineral dust is best described as shale. This conclusion is in agreement with observations made by other investigators [*Glaccum and Prospero*, 1980].

Mineral dust aerosol concentrations based on the composition of shale amount to an average of 19.3 ± 16.4 μg m^{-3} and range from 0.8 ± 55.6 μg m^{-3}. This value is only 5% larger than that obtained if assuming an average crustal composition, which matches well with the numerous other studies performed in the same area. The variability of the mineral dust concentrations collected during the present study is considerably larger than that of the sea-salt aerosol observed. Sea-salt aerosol concentrations average 10.6 ± 5.5 μg m^{-3} and range from 1.4 to 27.8 μg m^{-3}. Calcite and ammonium sulfate and nitrate concentrations add only small amounts to the total of the suspended particulate matter; 1.3 ± 1.0 μg m^{-3} and 1.9 ± 0.9 μg m^{-3}, respectively.

The only source of iron in the aerosol is mineral dust. Total iron concentrations average 0.84 ± 0.61 μg m^{-3} and range from < 0.05 to 2.38 μg m^{-3}. The Fe is evenly distributed between the coarse, 0.42 μg m^{-3}, and fine aerosol fractions, 0.43 μg m^{-3}. Ferrous iron accounts for only 0.51 ± 0.56% of the total iron, with an average concentration of 3.14 ± 1.35 ng m^{-3}. 86% of Fe(II) is present in the fine aerosol fraction and it appears to be more rapidly released from the particulate phase compared to the coarse fraction. These low

relative Fe(II) concentrations are in the same range as those found by Zhu et al. [*Zhu et al.*, 1993; *Zhu et al.*, 1997] in Barbados and by Siefert et al. [*Siefert et al.*, 1999] over the Northern Indian Ocean.

Ferrous iron concentrations appear to be independent of the total available Fe and instead show a correlation with NSS-SO_4^{2-}, oxalate, and MSA. The excess NSS-SO_4^{2-} adds acidity to the aerosol particles and may be responsible for the increased stability of Fe(II) with respect to oxidation to the less soluble Fe(III). Oxalate is the final product of photochemically induced reactions involving many organic precursors, and it is known to be an efficient electron donor for the photochemical reduction of Fe(II) in atmospheric waters. Thus, the observed correlation between the oxalate abundance and Fe(II) may be a direct consequence of this photoinduced reduction of solid iron phases in the aerosol particles. The extent of conversion of the Fe(III) to Fe(II) will depend on the time that the aerosol particle has spent in the atmosphere before it was sampled. Therefore, we observe an increase in the relative Fe(II) concentrations between the African continent and Barbados by a factor of 2.9.

NSS-SO_4^{2-} concentrations average 1.03 ± 0.60 μg m^{-3}, most which is present in the fine fraction (87%). From our analysis, it appears that approximately 22% of the fine NSS-SO_4^{2-} is of biogenic origin and the remainder anthropogenic. In the coarse fraction the biogenic NSS-SO_4^{2-} contribution accounts for 24% while the rest is of anthropogenic origin, if assuming that no primary $CaSO_4$ is present in the samples.

The chloride deficits range from 10.6 to 47.1% and average 18.3 ± 9.1%. In these samples, the deficit can be attributed to acid displacement reactions with HNO_3 and H_2SO_4. In the coarse fraction, which contains an appreciable amount of the NO_3^- (57% of the total), the acid displacement reaction between HNO_3 and Cl^- appears to be the main contributor to

the deficit. In the fine fraction, the reaction between H_2SO_4 and Cl^- seems to be responsible for the observed deficit.

Acknowledgments. The authors wish to thank Dr. Doug Capone from the Chesapeake Biological Laboratory, University of Maryland, Solomons, MD, for the invitation to join him and his team on the R/V Seward Johnson during the month of April of 1996. Research support was provided by the National Science Foundation and by the Environment Now Foundation. Their support is greatly appreciated.

4.7 References

Anderson, J.R., P.R. Buseck, T.L. Patterson, and R. Arimoto, Characterization of the Bermuda tropospheric aerosol by combined individual-particle and bulk-aerosol analysis, *Atmos. Environ.*, *30* (2), 319-338, 1996.

Andreae, M.O., Raising dust in the greenhouse, *Nature*, *380*, 389-390, 1996.

Andreae, M.O., R.J. Charlson, H.S. Bruynseels, R. Van Grieken, and W. Maenhaut, Internal mixture of sea salt, silicates, and excess sulfate in marine aerosols, *Science*, *232*, 1620-1623, 1986.

Andreae, M.O., W. Elbert, and S.J. de Mora, Biogenic sulfur emissions and aerosols over the tropical South Atlantic. 3. Atmospheric dimethylsulfide, aerosols and cloud condensation nuclei, *J. Geophys. Res.*, *100*, 11,335-11,356, 1995.

Arimoto, R., R.A. Duce, B.J. Ray, W.G. Ellis Jr., J.D. Cullen, and J.T. Merrill, Trace elements in the atmosphere over the North Atlantic, *J. Geophys. Res.*, *100*, 1199-1213, 1995.

Aston, S.R., R. Chester, L.R. Johnson, and R.C. Padgham, Eolian dust from the lower atmosphere of the eastern Atlantic and Indian Oceans, China Sea and Sea of Japan, *Mar. Geol.*, *14*, 15-28, 1973.

Barrie, L.A., J.W. Bottenheim, R.C. Schnell, P.J. Crutzen, and R.A. Rasmussen, Ozone destruction and photochemical reactions at polar sunrise in the lower Arctic atmosphere, *Nature*, *334*, 138-141, 1988.

Bassett, M.E., and J.H. Seinfeld, Atmospheric equilibrium model of sulfate and nitrate aerosols-II. Particle size analysis, *Atmos. Environ.*, *18* (6), 1163-1170, 1984.

Bates, T.S., J.A. Calhoun, and P.K. Quinn, Variations in the methanesulfonate to sulfate molar ratio in submicrometer marine aerosol particles over the South Pacific Ocean, *J. Geophys. Res.*, *97*, 9859-9865, 1992.

Behra, P., and L. Sigg, Evidence of redox cycling of iron in atmospheric water droplets, *Nature*, *344*, 419-421, 1990.

Bergametti, G., L. Gomes, G. Coude-Gaussen, P. Rognon, and M.-N. Le Coustumer, African dust observed over Canary Islands: Source-regions identification and transport pattern for some summer situations, *J. Geophys. Res.*, *94*, 14,855-14,864, 1989.

Berglund, J., and L.I. Elding, Manganese-catalyzed autoxidation of dissolved sulfur dioxide in the atmospheric aqueous phase, *Atmos. Environ.*, *29* (12), 1379-1391, 1995.

Berglund, J., S. Fronaeus, and L.I. Elding, Kinetics and mechanism for manganese-catalyzed oxidation of sulfur(IV) by oxygen in aqueous solution, *Inorg. Chem.*, *32*, 4527-4538, 1993.

Berresheim, H., M.O. Andreae, G.P. Ayers, and R.W. Gillett, Distribution of Biogenic Sulfur Compounds, *ACS Symposium Series*, *393*, 352-366, 1989.

Berresheim, H., M.O. Andreae, R.L. Iverson, and S.M. Li, Seasonal variations of dimethylsulfide emissions and atmospheric sulfur and nitrogen species over the western north Atlantic Ocean, *Tellus*, *43B*, 353-372, 1991.

Berresheim, H., F.L. Eisele, D.J. Tanner, L.M. McInnes, D.C. Ramsey-Bell, and D.S. Covert, Atmospheric sulfur chemistry and cloud condensation nuclei (CCN) concentrations over the northeastern Pacific coast, *J. Geophys. Res.*, *98*, 12,701-12,711, 1993.

Bottenheim, J.W., L.A. Barrie, E. Atlas, L.E. Heidt, H. Niki, R.A. Rasmussen, and P.B. Shepson, Depletion of lower tropospheric ozone during Arctic spring: the polar sunrise experiment 1988, *J. Geophys. Res.*, *95*, 18,555-18,568, 1990.

Bürgermeister, S., and H.-W. Georgii, Distribution of methanesulfonate, nss-sulfate and dimethylsulfide over the Atlantic and the North Sea, *Atmos. Environ.*, *25A* (3/4), 587-595, 1991.

Charlson, R.J., J.E. Lovelock, M.O. Andreae, and S.G. Warren, Oceanic phytoplankton, atmospheric sulphur, cloud albedo and climate, *Nature*, *326*, 655-661, 1987.

Chester, R., H. Elderfield, J.J. Griffin, L.R. Johnson, and R.C. Padgham, Eolian dust along the eastern margins of the Atlantic Ocean, *Mar. Geol*, *13*, 91-105, 1972.

Chiapello, I., G. Bergametti, and B. Chatenet, Origins of African dust transport over the northeastern tropical Atlantic, *J. Geophys. Res.*, *102*, 13,701-13,709, 1997.

Conklin, M.H., and M.R. Hoffmann, Metal ion-sulfur(IV) chemistry. 3. Thermodynamics and kinetics of transient iron(III)-sulfur(IV) complexes, *Environ. Sci. Technol.*, *22* (8), 899-907, 1988.

Cooper, D.J., A.J. Watson, and P.D. Nightingale, Large decrease in ocean-surface CO2 fugacity in response to in situ iron fertilization, *Nature*, *383*, 511-514, 1996.

D'Almeida, G., On the variability of desert aerosol radiative characteristics, *J. Geophys. Res.*, *92*, 3017-3026, 1987.

D'Almeida, G.A., A model for Saharan dust transport, *J. Clim. Appl. Meteorol.*, *25*, 903-916, 1986.

Davison, B., C. O'Dowd, C.N. Hewitt, M.H. Smith, R.M. Harrison, D.A. Peel, E. Wolf, R. Mulvaney, M. Schwikowski, and U. Baltensperger, Dimethyl sulfide and its oxidation products in the atmosphere of the Atlantic and Southern Oceans, *Atmos. Environ.*, *30* (10/11), 1895-1906, 1996.

Delaney, A.C., D.W. Parkin, J.J. Griffin, E.D. Goldberg, and B.E.F. Reiman, Airborne dust collected at Barbados, *Geochim. Cosmochim. Acta*, *31*, 885-909, 1967.

DiTullio, G.R., D.A. Hutchins, and K.W. Bruland, Interaction of iron and major nutrients controls phytoplankton growth and species composition in the tropical North Pacific Ocean, *Limnol. Oceanogr.*, *38* (3), 495-508, 1993.

Duce, R.A., G.L. Hoffman, and W.H. Zoller, Atmospheric trace metals at remote northern and southern hemisphere sites: Pollution of natural, *Science*, 59-61, 1975.

Duce, R.A., and E.J. Hoffmann, Chemical fractionation at the air/sea interface, *Annu. Rev. Earth Planet. Sci.*, *4*, 187-228, 1976.

Duce, R.A., and N.W. Tindale, Atmospheric transport of iron and its deposition in the ocean, *Limnol. Ocean.*, *36* (8), 1715-1726, 1991.

Duce, R.B., W.H. Zoller, and J.L. Moyers, Particulate and gaseous halogens in the Antarctic atmosphere, *J. Geophys. Res.*, *78*, 7802-7811, 1973.

Erel, Y., S.O. Pehkonen, and M. Hoffmann, Redox chemistry of iron in fog and stratus clouds, *J. Geophys. Res.*, *98*, 18,423-18,434, 1993.

Fan, S.-M., and D.J. Jacob, Surface ozone depletion in Arctic spring sustained by bromine reactions on aerosol, *Nature*, *359*, 522-524, 1992.

Faure, G., *Principles and Applications of Geochemistry*, Mcmillan, 1998.

Faust, B.C., and J.M. Allen, Sunlight-initiated partial inhibition of the dissolved iron(III)-catalyzed oxidation of S(IV) species by molecular oxygen in aqueous solution, *Atmos. Environ.*, *28* (4), 745-748, 1994.

Faust, B.C., and J. Hoigné, Photolysis of Fe(III)-hydroxy complexes as sources of OH radicals in clouds, fog and rain, *Atmos. Environ.*, *24A* (1), 79-89, 1990.

Faust, B.C., and R.G. Zepp, Photochemistry of aqueous iron(III)-polycarboxylate complexes: roles in the chemistry of atmospheric and surface waters, *Environ. Sci. Technol.*, *27*, 2517-2522, 1993.

Finlayson-Pitts, B.J., Reaction of NO_2 with NaCl and atmospheric implications of NOCl formation, *Nature*, *306*, 676-677, 1983.

Finlayson-Pitts, B.J., M.J. Ezell, and J.N. Pitts Jr., Formation of chemically active chlorine compounds by reactions of atmospheric NaCl particles with gaseous N_2O_5 and $ClONO_2$, *Nature*, *337*, 241-244, 1989.

Galloway, J.N., and H. Rodhe, Regional atmospheric budgets of S and N fluxes: how well can they be quantified?, *Proc. R. Soc. Edinburgh*, *97B*, 61-80, 1991.

Galloway, J.N., D.L. Savoie, W.C. Keene, and J.M. Prospero, The temporal and spatial variability of scavenging ratios for nss sulfate, nitrate, methanesulfonate and sodium in the atmosphere over the North Atlantic Ocean, *Atmos. Environ.*, *27A* (2), 235-250, 1993.

Glaccum, R.A., and J.M. Prospero, Saharan aerosols over the tropical North Atlantic-Mineralogy, *Mar. Geol.*, *37*, 295-321, 1980.

Graedel, T.E., and W.C. Keene, Tropospheric budget of reactive chlorine, *Global Biogeochem. Cycles*, *9* (1), 47-77, 1995.

Harrison, R.M., J.D. Peak, and A.D. Kaye, Atmospheric aerosol major ion composition and cloud condensation nuclei over the northeast Atlantic, *JGR*, *101* (D2), 4425-4434, 1996.

Hopke, P.K., Appendix: Selected Source Profiles, in *Receptor Modeling in Environmental Chemistry*, pp. 267-314, John Wiley & Sons, Inv., 1985.

Huang, S., R. Arimoto, and K. Rahn, Changes in atmospheric lead and other pollution elements at Bermuda, *J. Geophys. Res.*, *101*, 21,033-21,040, 1996.

Huebert, B.J., L. Zhuang, S. Howell, K. Noone, and B. Noone, Sulfate, nitrate, methanesulfonate, chloride, ammonium, and sodium measurements from ship, island, and aircraft during the Atlantic Stratocumulus Transition Experiment/Marine Aerosol Gas Exchange, *J. Geophys. Res.*, *101*, 4413-4423, 1996.

Hynes, A.J., P.H. Wine, and D.H. Semmes, Kinetics and mechanism of OH reactions with organic sulfides, *J. Phys. Chem.*, *90*, 4148-4156, 1986.

Johansen, A.M., R.L. Siefert, and M.R. Hoffmann, Chemical characterization of ambient aerosol collected during the southwest-monsoon and inter-monsoon seasons over the Arabian Sea: Anions and cations, *J. Geophys. Res.*, *submitted*, 1999.

Kawamura, K., and K. Ikushima, Seasonal changes in the distribution of dicarboxylic acids in the urban atmosphere, *Environ. Sci. Technol.*, *27*, 2227-2235, 1993.

Keene, W.C., D.J. Jacob, and S.-M. Fan, New Directions: Reactive chlorine: A potential sink for dimethylsulfide and hydrocarbons in the marine boundary layer, *Atmos. Environ.*, *30* (6), i-iii, 1996.

Keene, W.C., A.A.P. Pszenny, D.J. Jacob, R.A. Duce, J.N. Galloway, J.J. Schultz-Tokos, H. Sievering, and J.F. Boatman, The geochemical cycling of reactive chlorine through the marine troposphere, *Global Biogeochem. Cycles*, *4* (4), 407-430, 1990.

Keene, W.C., R. Sander, A.A.P. Pszenny, R. Vogt, P.J. Crutzen, and J.N. Galloway, Aerosol pH in the marine boundary layer: A review and model evaluation, *J. Aerosol Sci.*, *29* (3), 339-356, 1998.

Kerminen, V.-M., M. Aurela, R.E. Hillamo, and A. Virkkula, Formation of particulate MSA: Deductions from size distribution measurements in the Finnish Arctic, *Tellus*, *49B*, 159-171, 1997.

Kerminen, V.-M., K. Teinilä, R. Hillamo, and T. Pakkanen, Substitution of chloride in sea-salt particles by inorganic and organic anions, *J. Aerosol Sci.*, *29* (8), 929-942, 1998.

Kolber, Z.S., R.T. Barber, K.H. Coale, S.E. Fitzwater, R.M. Greene, K.S. Johnson, S. Lindley, and P.G. Falkowski, Iron limitation of phytoplankton photosynthesis in the equatorial Pacific Ocean, *Nature*, *371*, 145-149, 1994.

Kopcewicz, B., and M. Kopcewicz, Mössbauer study of iron-containing atmospheric aerosols, *Struct. Chem.*, *2* (95), 303-312, 1991.

Kopcewicz, B., and M. Kopcewicz, Seasonal variations of iron concentration in atmospheric aerosols, *Hyperfine Interactions*, *71*, 1457-1460, 1992.

Kopcewicz, B., and M. Kopcewicz, Iron-containing atmospheric aerosols, *Hyperfine Interactions*, *11*, 179-187, 1998.

Kotronarou, A., and L. Sigg, SO_2 oxidation in atmospheric water: Role of Fe(II) and effect of ligands, *Environ. Sci. Technol.*, *27*, 2725-2735, 1993.

Kraft, J., and R. van Eldik, Kinetics and mechanism of the iron(III)-catalyzed autoxidation of sulfur(IV) oxides in aqueous solution. 2. Decomposition of transient iron(III)-sulfur(IV) complexes, *Inorg. Chem.*, *28*, 2306-2312, 1989.

Kuma, K., J. Nichioka, and K. Matsunaga, Controls on iron(III) hydroxide solubility in seawater: The influence of pH and natural organic chelators, *Limnol. Oceanogr.*, *41* (3), 396-407, 1996.

Langer, S., B.T. McGovney, B.J. Finlayson-Pitts, and R.M. Moore, The dimethyl sulfide reaction with atomic chlorine and its implications for the budget of methyl chloride, *Geophys. Res. Lett.*, *23* (13), 1661-1664, 1996.

Li, X., H. Maring, D. Savoie, K. Voss, and J.M. Prospero, Dominance of mineral dust in aerosol light-scattering in the North Atlantic trace winds, *Nature*, *380*, 416-418, 1996.

Li-Jones, X., and J.M. Prospero, Variations in the size distribution of non-sea-salt sulfate aerosol in the marine boundary layer at Barbados: Impact of African dust, *J.Geophys. Res.*, *103* (D13), 16,073-16,084, 1998.

Losno, R., G. Bergametti, and P. Carlier, Origins of atmospheric particulate matter over the North Sea and the Atlantic Ocean, *J. Atmos. Chem.*, *15*, 333-352, 1992.

Martin, J.H., K.H. Coale, K.S. Johnson, S.E. Fitzwater, R.M. Gordon, and ....., Testing the iron hypothesis in ecosystems of the equatorial Pacific Ocean, *Nature*, *371*, 123-129, 1994.

Martin, J.H., and S.F. Fitzwater, Iron deficiency limits phytoplankton growth in the north-east Pacific subarctic, *Nature*, *331*, 341-342, 1988.

Martin, J.H., R.M. Gordon, and S.E. Fitzwater, The case of iron, *Limnol. Oceanogr.*, *36* (8), 1793-1802, 1991.

Martin, R.L., and M.W. Hill, The iron catalyzed oxidation of sulfur: Reconciliation of the literature rates, *Atmos. Environ.*, *21* (6), 1487-1490, 1987.

McConnell, J.C., G.S. Henderson, L. Barrie, J. Bottenheim, H. Niki, C.H. Langford, and E.M.J. Templeton, Photochemical bromine production implicated in Arctic boundary -layer ozone depletion, *Nature*, *355*, 150-152, 1992.

McInnes, L.M., D.S. Covert, P.K. Quinn, and M.S. Germani, Measurements of chloride depletion and sulfur enrichment in individual sea-salt particles collected from the remote marine boundary layer, *J. Geophys. Res.*, *99*, 8257-8268, 1994.

Miller, L.A., and K.W. Bruland, Determination of copper speciation in marine waters by competitive ligand equilibration/liquid-liquid extraction: an evaluation of the technique, *Anal. Chim. Acta*, *284*, 573-586, 1994.

Millero, F.J., and M.L. Sohn, *Chemical Oceanography*, CRC Press, 1992.

Millero, F.J., S. Sotolongo, D.J. Stade, and C.A. Vega, Effect of ionic interactions on the oxidation of Fe(II) with H_2O_2 in aqueous solutions, *J. Solution Chem.*, *20* (11), 1079-1092, 1991.

Millero, F.J., W. Yao, and J. Aicher, The speciation of Fe(II) and Fe(III) in natural waters, *Mar. Chem.*, *50*, 21-39, 1995.

Moffett, J.W., and R.G. Zika, Reaction kinetics of hydrogen peroxide with copper and iron in seawater, *Environ. Sci. Technol.*, *1* (8), 804-810, 1987a.

Muhs, D.R., C.A. Bush, K.C. Stewart, T.R. Rowland, and R.C. Crittenden, Geochemical evidence of Saharan dust parent material for soils developed on quarternary limestones of Caribbean and Western Atlantic islands, *Quart. Res.*, *33*, 157-177, 1990.

Muhs, D.R., R.C. Crittenden, J.N. Rosholt, C.A. Bush, and K.C. Stewart, Genesis of marine terrace soils, Barbados, West Indies: Evidence from mineralogy and geochemistry, *Earth Surf. Processes Landfroms*, *12*, 605-618, 1987.

NOAA, A.R.L., HYSPLIT4 (HYbrid Single-Particle Lagrangian Integrated Trajectory) Model, Silver Spring, MD, 1997.

O'Dowd, C., M.H. Smith, I.E. Consterdine, and J.A. Lowe, Marine aerosol, sea-salt, and the marine sulphur cycle: A short review, *Atmos. Environ.*, *31* (1), 73-80, 1997.

O'Sullivan, D.W., A.K. Hanson Jr., and D.R. Kester, Stopped flow luminol chemiluminescence determination of Fe(II) and reducible iron in seawater at subnanomolar levels, *Mar. Chem.*, *49*, 65-77, 1995.

Paerl, H.W., L.E. Prufert-Bebout, and C. Guo, Iron-stimulated N_2 fixation and growth on natural and cultured populations of the planktonic marine cyanobacteria *Trichodesmium* spp., *Appl. Environ. Microbiol.*, *60* (3), 1044-1047, 1994.

Paquet, H., G. Coudé-Gaussen, and P. Rognon, Mineralogical datas about desertic dusts along a saharan transect from North 19° to 35° lat, *Rev. Géol. Dynam. Géogr. Phys.*, *25* (4), 257-265, 1984.

Patterson, C.C., and D.M. Settle, The reduction of orders of magnitude errors in lead analysis of biological materials and natural waters by evaluating and controlling the extent and sources of industrial lead contamination introduced during sampling, collecting, handling and analysis, *Natl. Bur. Stand. Spec. Publ.*, *422*, 321-351, 1976.

Pehkonen, S.O., R. Siefert, Y. Erel, S. Webb, and M. Hoffmann, Photoreduction of iron oxyhydroxides in the presence of important atmospheric organic compounds, *Environ. Sci. Technol.*, *27* (10), 2056-2062, 1993.

Price, N.M., B.A. Ahner, and F.M.M. Morel, The equatorial Pacific Ocean: Grazer-controlled phytoplankton populations in an iron-limited ecosystem, *Limnol. Oceanogr.*, *39* (3), 520-534, 1994.

Prospero, J.M., Atmospheric dust studies on Barbados, *Bull. Amer. Meteorol. Soc.*, *49* (6), 645-652, 1968.

Prospero, J.M., K. Barrett, T. Church, F. Dentener, R.A. Duce, J.N. Galloway, H. Levy II, J. Moody, and P. Quinn, Atmospheric deposition of nutrients to the North Atlantic basin, *Biogeochem.*, *35*, 27-73, 1996.

Prospero, J.M., E. Bonatti, C. Schubert, and T.N. Carlson, Dust in the Caribbean atmosphere traced to an African dust storm, *Earth Planet. Sci. Lett.*, *9*, 287-293, 1970.

Prospero, J.M., and T.N. Carlson, Vertical and areal distribution of Saharan dust over the Western Equatorial North Atlantic Ocean, *J. Geophys. Res.*, *77*, 5255-5265, 1972.

Prospero, J.M., R.A. Glaccum, and R.T. Nees, Atmospheric transport of soil dust from Africa to South America, *Nature*, *289*, 570-572, 1981.

Prospero, J.M., and R.T. Nees, Dust concentration in the atmosphere of the equatorial North Atlantic: Possible relationship to the Sahelian Drought, *Science*, *196*, 1196-1198, 1977.

Prospero, J.M., and D.L. Savoie, Effect of continental sources on nitrate concentrations over the Pacific Ocean, *Nature*, *339*, 687-689, 1989.

Prospero, J.M., D.L. Savoie, E.S. Saltzman, and R. Larsen, Impact of oceanic sources of biogenic sulphur on sulphate aerosol concentrations at Mawson, Antarctica, *Nature*, *350*, 221-223, 1991.

Pszenny, A.A.P., Particle size distributions of methanesulfonate in the tropical Pacific marine boundary layer, *J. Atmos. Chem.*, *14*, 273-284, 1992.

Pszenny, A.A.P., A.J. Castelle, and J.N. Galloway, A study of the sulfur cycle in the Antarctic marine boundary layer, *J. Geophys. Res.*, *94*, 9818-9839, 1989.

Pszenny, A.A.P., W.C. Keene, D.J. Jacob, S. Fan, J.R. Maben, M.P. Zetwo, M. Springer-Young, and J.N. Galloway, Evidence of inorganic chlorine gases other than hydrogen chloride in marine surface air, *Geophys. Res. Lett.*, *20* (8), 699-702, 1993.

Putaud, J.-P., S. Belviso, B.C. Nguyen, and N. Mihalopoulos, Dimethylsulfide, aerosols, and condensation nuclei over the tropical northeastern Atlantic Ocean, *J. Geophys. Res.*, *98*, 14,863-14,871, 1993.

Qian, G.-W., and Y. Ishizaka, Electron microscope studies of methane sulfonic acid in individual aerosol particles, *J. Geophys. Res.*, *98*, 8459-8470, 1993.

Quinn, P.K., W.E. Asher, and R.J. Charlson, Equilibria of the marine mulitphase ammonia system, *J. Atmos. Chem.*, *14*, 11-30, 1992.

Quinn, P.K., D.S. Covert, T.S. Bates, V.N. Kapustin, D.C. Ramsey-Bell, and L.M. McInnes, Dimethylsulfide/cloud condensation nuclei/climate system: Relevant size-resolved measurements of the chemical and physical properties of atmospheric aerosol particles, *J. Geophys. Res.*, *98*, 10,411-10,427, 1993.

Saltzman, E.S., D.L. Savoie, J.M. Prospero, and R.G. Zika, Atmospheric methanesulfonic acid and non-sea-salt sulfate at Fanning and American Samoa, *Geophys. Res. Lett.*, *12* (7), 437-440, 1985.

Saltzman, E.S., D.L. Savoie, R.G. Zika, and J.M. Prospero, Methane sulfonic acid in the marine atmosphere, *J. Geophys. Res.*, *88*, 10,897-10,902, 1983.

Sander, R., and P.J. Crutzen, Model study indicating halogen activation and ozone destruction in polluted air masses transported to the sea, *J. Geophys. Res.*, *101*, 9121-9138, 1996.

Savoie, D.L., and J.M. Prospero, Aerosol concentration statistics for the northern tropical Atlantic, *J. Geophys. Res.*, *82*, 5954-5964, 1977.

Savoie, D.L., and J.M. Prospero, Water-soluble potassium, calcium, and magnesium in the aerosols over the tropical North Atlantic, *J. Geophys. Res.*, *85*, 385-392, 1980.

Savoie, D.L., and J.M. Prospero, Particle size distribution of nitrate and sulfate in the marine atmosphere, *Geophys. Res. Lett.*, *9* (10), 1207-1210, 1982.

Savoie, D.L., and J.M. Prospero, Comparison of oceanic and continental sources of non-sea-salt sulphate over the Pacific Ocean, *Nature*, *339*, 685-687, 1989.

Savoie, D.L., and J.M. Prospero, Non-sea-salt sulfate and methansulfonate at American Samoa, *J. Geophys. Res.*, *99*, 3587-3596, 1994.

Savoie, D.L., J.M. Prospero, R.J. Larsen, and E.S. Saltzman, Nitrogen and sulfur species in aerosols at Mawson, Antarctica, and their relationship to natural radionuclides, *J. Atmos. Chem.*, *14*, 181-204, 1992.

Savoie, D.L., J.M. Prospero, J.T. Merrill, and M. Uematsu, Nitrate in the atmospheric boundary layer of the Tropical South Pacific: Implications Regarding Sources and Transport, *J. Atmos. Chem.*, *8*, 391-415, 1989a.

Savoie, D.L., J.M. Prospero, and R.T. Nees, Nitrate, non-sea-salt sulfate, and mineral aerosol over the northwestern Indian Ocean, *J. Geophys. Res.*, *92*, 933-942, 1987.

Savoie, D.L., J.M. Prospero, and E.S. Saltzman, Non-sea-salt sulfate and nitrate in trade wind aerosols at Barbados: Evidence for long-range transport, *J. Geophys. Res.*, *94*, 5,069-5,080, 1989b.

Schollaert, S.E., and J.T. Merrill, Cooler sea surface west of the Sahara Desert, *Geophys. Res. Lett.*, *25* (18), 3529-3532, 1998.

Schütz, L., Long range transport of desert dust with special emphasis on the Sahara, *Ann. N. Y. Acad. Sci.*, *338*, 515-532, 1980.

Schütz, L., R. Jaenicke, and H. Pietrek, Saharan dust transport over the North Atlantic Ocean, *Geol. Soc. of Am., Spec. Pap.*, *186*, 87-100, 1981.

Schütz, L., and M. Sebert, Mineral aerosols and source identification, *J. Aerosol Sci.*, *18* (1), 1-10, 1987.

Sedlak, D.L., and J. Hoigné, The role of copper and oxalate in the redox cycling of iron in atmospheric waters, *Atmos. Environ.*, *27A* (14), 2173-2185, 1993.

Sedlak, D.L., and J. Hoigné, Oxidation of S(IV) in atmospheric water by photooxidants and iron in the presence of copper, *Environ. Sci. Technol.*, *28* (11), 1898-1906, 1994.

Seinfeld, J.H., and S.N. Pandis, *Atmospheric Chemistry and Physics: From Air Pollution to Climate Change*, John Wiley & Sons, Inc., 1997.

Siefert, R.L., A.M. Johansen, and M.R. Hoffmann, Measurements of trace metal (Fe, Cu, Mn, Cr) oxidation states in fog and stratus clouds, *J. Air & Waste Manage. Assoc.*, *48*, 128-143, 1998.

Siefert, R.L., A.M. Johansen, and M.R. Hoffmann, Chemical characterization of ambient aerosol collected during the southwest- and inter-monsoon seasons over the Arabian Sea: Labile-Fe(II) and other trace metals, *J. Geophys. Res.*, *104* (3511-3526), 1999.

Siefert, R.L., S.O. Pehkonen, Y. Erel, and M.R. Hoffmann, Iron photochemistry of aqueous suspensions of ambient aerosol with added organic acids, *Geochim. Cosmochim. Acta*, *58* (15), 3271-3279, 1994.

Siefert, R.L., S.M. Webb, and M.R. Hoffmann, Determination of photochemically available iron in ambient aerosols, *J. Geophys. Res.*, *101*, 14441-14449, 1996.

Sievering, H., J. Boatman, E. Gorman, Y. Kim, L. Anderson, G. Ennis, M. Luria, and S. Pandis, Removal of sulphur from the marine boundary layer by ozone oxidation in sea-salt aerosols, *Nature*, *360*, 571-573, 1992.

Sievering, H., G. Ennis, E. Gorman, and C. Nagamoto, Size distribution and statistical analysis of nitrate, excess sulfate, and chloride deficit in the marine boundary layer during GCE/CASE/WATOX, *Global Biogeochem. Cycles*, *4* (4), 395-405, 1990.

Sisterson, D.L., A method for evaluation of acidic sulfate and nitrate in precipitation, *Water, Air, and Soil Pollut.*, *43*, 61-72, 1989.

Spokes, L.J., and P.S. Liss, Photochemically induced redox reactions in seawater, I. Cations, *Mar. Chem.*, *49*, 201-213, 1995.

SPSS, SPSS for Windows, SPSS Inc., Chicago, 1997.

Stickel, R.E., J.M. Nicovich, Z. Zhao, and P.H. Wine, Kinetic and mechanistic study of the reaction of atomic chlorine with dimethyl sulfide, *J. Phys. Chem.*, *96*, 9875-9883, 1992.

Sturges, W.T., and L.A. Barrie, Chlorine, bromine and iodine in Arctic aerosols, *Atmos. Environ.*, *22* (6), 1179-1194, 1988.

Sturges, W.T., and G.E. Shaw, Halogens in aerosol in central Alaska, *Atmos. Environ.*, *27A* (17/18), 2969-2977, 1993.

Swap, R., M. Garstang, S. Greco, R. Talbot, and P. Kålleberg, Saharan dust in the Amazon Basin, *Tellus*, *44B*, 133-149, 1992.

Swap, R., S. Ulanski, M. Cobbett, and M. Garstang, Temporal and spatial characteristics of Saharan dust outbreaks, *J. Geophys. Res.*, *101*, 4205-4220, 1996.

Talbot, R.W., M.O. Andreae, H. Berresheim, P. Artaxo, M. Garstang, R.C. Harriss, K.M. Beecher, and S.M. Li, Aerosol chemistry during the wet season in Central Amazonia: The influence of long-range transport, *J. Geophys. Res.*, *95*, 16,955-16,969, 1990.

Taylor, S.R., and S.M. McLennan, *The Continental Crust: Its Composition and Evolution*, Blackwell Scientific Publ., Oxford, England, 1985.

Tegen, I., and I. Fung, Contribution to the atmospheric mineral load from land surface modification, *J. Geophys. Res.*, *100*, 18,707-18,726, 1995.

Tegen, I., A.A. Lacis, and I. Fung, The influence on climate forcing of mineral aerosols from disturbed soils, *Nature*, *380*, 419-422, 1996.

Turekian, K.K., and K.H. Wedepohl, Distribution of the elements in some major units of the Earth's crust, *Geol. Soc. Amer. Bull.*, *72*, 175-192, 1961.

Turner, S.M., P.D. Nightingale, L.J. Spokes, M.I. Liddicoat, and P.S. Liss, Increased dimethyl sulphide concentrations in sea water from *in situ* iron enrichment, *Nature*, *383*, 513-517, 1996.

Voelker, B.M., and D.L. Sedlak, Iron reduction by photoproduced superoxide in seawater, *Mar. Chem.*, *50*, 93-102, 1995.

Vogt, R., P.J. Crutzen, and R. Sander, A mechanism for halogen release in the remote marine boundary layer, *Nature*, *383*, 327-330, 1996.

Waite, D.T., and F.M.M. Morel, Coulometric study of the redox dynamics of iron in seawater, *Anal. Chem.*, *56*, 787-792, 1984.

Wells, M.L., N.M. Price, and K.W. Bruland, Iron chemistry in seawater and its relationship to phytoplankton: a workshop report, *Mar. Chem.*, *48*, 157-182, 1995.

Yin, F., D. Grosjean, and J.H. Seinfeld, Analysis of atmopheric photooxidation mechanisms for organosulfur compounds, *J. Geophys. Res.*, *91*, 14417-14438, 1986.

Zar, J.H., *Biostatistical Analysis*, Prentice-Hall, Inc., Upper Saddle River, New Jersey, 1996.

Zhang, L.-P., and K. Terada, Spectrophotometric determination of iron(II) in sea water after preconcentration by sorption of its 3-(2-pyridyl)-5,6-bis(4-phenylsulphonic acid)-1,2,4-

triazine complex with poly(chlorotrifluoroethylene) resin, *Anal. Chim. Acta*, *293*, 311-318, 1994.

Zhu, X., J.M. Prospero, F.J. Millero, D.L. Savoie, and G. Brass, The solubility of ferric ion in marine mineral aerosol solutions at ambient relative humidities, *Mar. Chem.*, *38*, 91-107, 1992.

Zhu, X., J.M. Prospero, D.L. Svoie, F.J. Millero, R.G. Zika, and E.S. Saltzman, Photoreduction of iron(III) in marine mineral aerosol solutions, *J. Geophys. Res.*, *98*, 9039-9046, 1993.

Zhu, X.R., J.M. Prospero, and F.J. Millero, Diel variability of soluble Fe(II) and soluble total Fe in North African dust in the trade winds at Barbados, *J. Geophys. Res.*, *102*, 21,297-21,305, 1997.

Zhuang, G., R.A. Duce, and D.R. Kester, The dissolution of atmospheric iron in surface seawater of the open ocean, *J. Geophys. Res.*, *95*, 16,207-16,216, 1990.

Zhuang, G., Z. Yi, and R.A. Duce, Chemistry of iron in marine aerosols, *Global Biogeochem. Cycles*, *6* (2), 161-173, 1992a.

Zhuang, G., Z. Yi, R.A. Duce, and P.R. Brown, Link between iron and sulphur cycles suggested by detection of Fe(II) in remote marine aerosols, *Nature*, *355*, 537-539, 1992b.

Zuo, Y., Kinetics of photochemical/chemical cycling of iron coupled with organic substances in cloud and fog droplets, *Geochim. Cosmochim. Acta*, *59* (15), 3123-3130, 1995.

Zuo, Y., and J. Hoigné, Formation of hydrogen peroxide and depletion of oxalic acid in atmospheric water by photolysis of iron(III)-oxalato complexes, *Environ. Sci. Technol.*, *26* (5), 1014-1022, 1992.

Zuo, Y., and J. Hoigné, Photochemical decomposition of oxalic, glyoxalic and pyruvic acid catalysed by iron in atmospheric waters, *Atmos. Environ.*, *28* (7), 1231-1239, 1994.

4.8 Figure Captions

Figure 1. Six-day air mass back trajectory calculations at five different final elevations above sea level for: a) April 2, 1996; b) April 7, 1996; c) April 10, 1996; and d) April 18, 1996.

Figure 2. Total suspended particulates (TSP) vs. sample ID. Circled symbols represent samples for which air mass back trajectories are shown in Figure 1.

Figure 3. Coarse and fine fraction trace metal concentrations vs. sample ID. for Al (a), Zn (b), and Na (c).

Figure 4. Fe(II) concentrations vs. sample ID. (a) Fe(II) in the coarse fraction, (b) Fe(II) in the fine fraction, and (c) total Fe(II) released after 5 min in ferrozine (see text for details).

Figure 5. Relative Fe(II) concentrations (in % of total Fe) vs. sample ID. for coarse, fine and total Fe(II).

Figure 6. Relative amount Fe(II) released in the sequential extraction steps for coarse (a) and fine (b) fractions.

Figure 7. Sea-salt and non-sea-salt SO_4^{2-} contributions in coarse and fine fractions vs. sample ID.

Figure 8. MSA concentrations in coarse and fine fractions vs. sample ID.

Figure 9. NO_3^- concentrations in coarse and fine fractions vs. sample ID.

Figure 10. Oxalate concentrations in coarse and fine fractions vs. sample ID.

Figure 11. Halogen concentrations in coarse and fine fractions vs. sample ID: (a) F^-, (b) Cl^-, and (c) Br^-.

Figure 12. (a) Cl^- deficit vs. sample ID. (b) neq mineral acid concentrations vs. Cl^- deficit in coarse fraction, and (c) neq mineral acid concentrations vs. Cl^- deficit in fine fraction.

Figure 13. Water-soluble sea-salt and non-sea-salt fractions of Na^+ (a), K^+ (b), Mg^{2+} (c), and Ca^{2+} (d), in coarse and fine fractions vs. sample ID.

Figure 14. (a) NH_4^+ and (b) $NH_4^+/NSS\text{-}SO_4^{2-}$ vs. sample ID., and (c) $NH_4^+/NSS\text{-}SO_4^{2-}$ vs. $NSS\text{-}SO_4^{2-}$ in fine fraction and fine and coarse combined (total).

Figure 15. (a) $(NH_4^+ + NSS\text{-}Ca^{2+})/NSS\text{-}SO_4^{2-}$ vs. sample ID. (b) $(NH_4^+ + NSS\text{-}Ca^{2+})/NSS\text{-}SO_4^{2-}$ vs. $NSS\text{-}SO_4^{2-}$ in fine fraction and fine and coarse combined (total).

Figure 16. ICP-MS and IC determined concentrations of (a) Na, (b) K, (c) Mg, and (d) Ca vs. sample ID. in coarse and fine fractions. Crustal concentrations determined from average shale composition (see text for details).

Figure 17. Air temperature vs. sample ID.

Figure 18. Model predictions (based on multiple linear regression analyses) for SO_4^{2-} contributions from different sources (in stacked bars) compared with observed SO_4^{2-} concentrations vs. sample ID.: (a) in the coarse fraction, assuming the presence of gypsum, (b) in the coarse fraction, neglecting gypsum, and (c) in the fine fraction.

Figure 19. $NH_4^+/NSS\text{-}SO_4^{2-}$ (a) and $(NH_4^+ + NSS\text{-}Ca^{2+})/NSS\text{-}SO_4^{2-}$ (b) vs. $Fe(II)_{total,5minFZ}$ concentrations in fine fraction and fine and coarse combined (total).

Figure 20. $Fe(II)_{total,5minFZ}$ in fine fraction vs. MSA.

Table 1. Aerosol sample collection times and positions.

Sample Id.	Start Date/Time (UTC)	Stop Date/Time (UTC)	Position at midpoint in time	
			Latitude N	Longitude W
A96_01	March 31, 1996 1400	April 1, 1996 0900	7.44	49.38
A96_02	April 1, 1996 1910	April 2, 1996 1730	6.27	45.00
A96_03	April 2, 1996 1745	April 3, 1996 1805	6.27	41.86
A96_04	April 3, 1996 1815	April 4, 1996 1240	6.27	39.20
A96_05	April 4, 1996 1250	April 5, 1996 1245	6.25	37.23
A96_06	April 5, 1996 1535	April 6, 1996 1225	4.58	15.27
A96_07	April 6, 1996 1240	April 7, 1996 0810	1.98	34.64
A96_08	April 7, 1996 1145	April 7, 1996 1945	0.04	34.10
A96_09	April 8, 1996 0930	April 8, 1996 2115	2.15	32.88
A96_10	April 9, 1996 0930	April 10, 1996 0730	5.31	30.88
A96_11	April 10, 1996 0740	April 11, 1996 1045	7.77	29.34
A96_12	April 11, 1996 1050	April 12, 1996 0750	10.49	27.45
A96_13	April 12, 1996 0800	April 13, 1996 1100	13.15	25.57
A96_14	April 16, 1996 0905	April 17, 1996 0850	16.31	27.86
A96_15	April 17, 1996 0900	April 18, 1996 1140	16.18	31.47
A96_16	April 18, 1996 1149	April 19, 1996 0945	15.99	34.82
A96_17	April 19, 1996 0953	April 20, 1996 1028	15.75	38.20
A96_18	April 20, 1996 1038	April 21, 1996 1022	15.44	41.77
A96_19	April 21, 1996 1033	April 22, 1996 1040	15.18	44.22
A96_20	April 22, 1996 1050	April 24, 1996 1000	14.98	46.02
A96_21	April 24, 1996 1010	April 26, 1996 1615	14.76	48.09

Table 2. Average, minimum and maximum atmospheric trace metal concentrations in coarse, fine and total aerosol fractions. Sample number is same for all: 21 samples. Concentrations in ng m^{-3} unless otherwise noted.

Element	Coarse			Fine			Total		
	Average ± SD	Min.	Max.	Average ± SD	Min.	Max.	Average ± SD	Min.	Max.
Na (μg m^{-3})	1.99 ± 1.22	< 0.0025	5.72	1.19 ± 0.58	0.15	2.21	3.18 ± 1.63	< 0.15	7.63
Mg (μg m^{-3})	0.35 ± 0.22	< 0.0002	0.92	0.25 ± 0.14	0.024	0.54	0.60 ± 0.33	< 0.025	1.25
Al (μg m^{-3})	0.75 ± 0.66	< 0.0004	2.19	0.79 ± 0.71	0.006	2.55	1.55 ± 1.32	< 0.006	4.45
K (μg m^{-3})	0.22 ± 0.15	0.0021	0.52	0.19 ± 0.12	0.003	0.46	0.41 ± 0.25	0.0047	0.81
Ca (μg m^{-3})	0.42 ± 0.31	0.0015	1.25	0.26 ± 0.18	0.0024	0.64	0.68 ± 0.46	0.0039	1.67
Sc	0.13 ± 0.11	< 0.002	0.35	0.14 ± 0.11	0.013	0.41	0.27 ± 0.21	< 0.015	0.72
Ti	49.4 ± 38.8	< 0.12	139	54.9 ± 42.5	7.52	152	104 ± 78.8	< 7.64	291
V	1.02 ± 0.80	0.098	2.58	1.54 ± 1.03	0.18	3.42	2.57 ± 1.78	0.29	5.63
Mn	8.07 ± 6.91	< 0.009	23.8	8.62 ± 7.49	0.88	26.8	16.7 ± 13.8	< 0.89	45.6
Fe (μg m^{-3})	0.42 ± 0.36	< 0.0008	1.04	0.43 ± 0.37	0.035	1.4	0.84 ± 0.61	< 0.053	2.38
Zn	2.11 ± 1.18	0.62	4.64	5.59 ± 3.50	1.58	12.7	7.69 ± 4.53	2.2	16.4
Ga	0.33 ± 0.27	< 0.0016	0.83	0.37 ± 0.30	0.025	1.15	0.67 ± 0.54	< 0.027	1.85
Cs	0.041 ± 0.032	< 0.0005	0.096	0.040 ± 0.031	0.004	0.116	0.081 ± 0.06	< 0.004	0.197
Ba	5.18 ± 4.06	< 0.018	11.5	5.19 ± 4.49	0.39	17.9	10.4 ± 8.0	< 0.40	28
La	0.40 ± 0.35	< 0.001	1.19	0.43 ± 0.41	0.029	1.4	0.84 ± 0.74	< 0.042	2.53
Ce	0.82 ± 0.76	< 0.0006	2.52	0.93 ± 0.91	0.055	3.15	1.75 ± 1.62	< 0.089	5.37
Sm	0.07 ± 0.06	< 0.001	0.2	0.07 ± 0.07	0.007	0.27	0.14 ± 0.13	< 0.008	0.42
Eu	0.015 ± 0.013	< 0.001	0.044	0.015 ± 0.014	< 0.001	0.049	0.030 ± 0.026	< 0.003	0.09
Hf	0.039 ± 0.027	< 0.002	0.11	0.041 ± 0.028	0.006	0.11	0.080 ± 0.051	< 0.053	0.2
Pb	0.29 ± 0.19	< 0.003	0.6	0.72 ± 0.46	0.12	1.69	1.01 ± 0.59	< 0.12	2.25
Th	0.11 ± 0.09	0.005	0.3	0.11 ± 0.09	0.01	0.32	0.21 ± 0.18	0.015	0.61

Table 3. Varimax rotated principal component matrix. Trace metals. Includes 21 samples.

% of variance	77.0	11.1	4.7	3.4	0.9
Element\Component	1 crustal fine	2 crustal coarse	3 anthrop. Zn&Pb	4 sea salt fine (?)	5
Na-coarse	-0.112	**0.795**	0.192	0.450	-0.258
Na-fine	0.400	0.388	-0.089	**0.796**	-0.065
Mg-coarse	0.128	**0.844**	0.343	0.272	-0.198
Mg-fine	**0.763**	0.444	0.098	0.446	0.048
Al-coarse	0.592	**0.788**	0.088	0.056	0.019
Al-fine	**0.927**	0.360	0.004	0.098	0.031
K-coarse	0.307	**0.865**	0.258	0.263	0.089
K-fine	**0.838**	0.416	0.088	0.323	0.075
Ca-coarse	0.192	**0.730**	0.533	0.265	0.216
Ca-fine	**0.775**	0.355	0.259	0.353	0.189
Sc-coarse	0.563	**0.795**	0.145	0.065	0.048
Sc-fine	**0.923**	0.358	0.054	0.117	0.032
Ti-coarse	0.614	**0.740**	-0.078	0.001	-0.106
Ti-fine	**0.857**	0.478	-0.074	0.055	-0.051
V-coarse	0.520	**0.804**	0.167	0.126	0.175
V-fine	**0.728**	0.475	0.293	0.276	0.254
Mn-coarse	0.614	**0.764**	0.057	0.077	-0.040
Mn-fine	**0.906**	0.361	-0.064	0.150	0.032
Fe-coarse	0.601	**0.768**	0.133	0.095	0.050
Fe-fine	**0.924**	0.344	0.077	0.128	0.024
Zn-coarse	-0.015	0.324	**0.862**	-0.232	-0.118
Zn-fine	-0.185	0.028	**0.944**	-0.065	-0.006
Ga-coarse	0.546	**0.791**	0.206	0.078	0.001
Ga-fine	**0.919**	0.344	0.066	0.139	0.050
Cs-coarse	0.481	**0.809**	0.214	0.175	0.172
Cs-fine	**0.890**	0.394	0.133	0.169	0.063
Ba-coarse	0.486	**0.783**	0.295	0.104	-0.010
Ba-fine	**0.902**	0.343	0.112	0.164	0.078
La-coarse	0.612	**0.771**	0.026	0.114	0.069
La-fine	**0.919**	0.378	-0.034	0.088	0.041
Ce-coarse	0.614	**0.775**	0.054	0.069	0.000
Ce-fine	**0.926**	0.362	-0.025	0.087	0.038
Sm-coarse	0.601	**0.777**	0.012	0.138	0.063
Sm-fine	**0.920**	0.374	-0.048	0.090	0.033
Eu-coarse	0.589	**0.782**	-0.014	0.136	0.083
Eu-fine	**0.912**	0.377	-0.041	0.114	0.045
Hf-coarse	0.554	**0.704**	-0.156	-0.129	-0.111
Hf-fine	**0.937**	0.232	-0.066	0.082	-0.148
Pb-coarse	0.388	**0.841**	0.124	0.103	0.120
Pb-fine	0.330	0.411	**0.732**	0.293	0.242
Th-coarse	0.579	**0.795**	0.025	0.116	0.065
Th-fine	**0.913**	0.383	-0.002	0.115	0.040
TSP	**0.621**	**0.668**	0.001	0.357	0.003
Wind speed	0.567	0.143	-0.353	**0.634**	0.198

Table 4. Varimax rotated principal component matrix. Trace metals and ions. Includes 21 samples.

% of variance	59.0	17.2	8.2	4.9	2.7
Element\Component	1 crustal fine + some coarse	2 sea salt + some crustal coarse	3 anthrop. Zn&Pb&NSS-SO_4^{2-}	4 MSA/sea salt fine	5 MSA coarse
Na-coarse	0.188	**0.927**	0.188	0.168	0.003
Na-fine	**0.675**	0.478	-0.062	**0.494**	-0.101
Mg-coarse	0.362	**0.787**	0.380	0.066	-0.057
Mg-fine	**0.913**	0.282	0.066	0.263	-0.067
Al-coarse	**0.753**	**0.547**	0.200	-0.035	-0.052
Al-fine	**0.988**	0.073	-0.021	0.022	0.009
K-coarse	0.539	**0.716**	0.348	0.145	-0.023
K-fine	**0.957**	0.206	0.060	0.170	-0.009
Ca-coarse	0.465	**0.545**	**0.620**	0.195	-0.097
Ca-fine	**0.919**	0.110	0.190	0.277	-0.108
Fe-coarse	**0.780**	**0.518**	0.206	-0.021	-0.093
Fe-fine	**0.988**	0.068	0.038	0.033	0.026
Zn-coarse	0.058	0.214	**0.844**	-0.274	0.179
Zn-fine	-0.140	0.019	**0.897**	0.003	0.128
La-coarse	**0.786**	**0.568**	0.140	0.019	-0.041
La-fine	**0.986**	0.092	-0.047	0.017	-0.002
Pb-coarse	0.590	**0.637**	0.221	-0.001	0.150
Pb-fine	0.503	0.229	**0.743**	0.307	0.016
Th-coarse	**0.751**	**0.611**	0.141	0.034	-0.040
Th-fine	**0.981**	0.109	-0.015	0.049	0.004
$FeII\text{-}coarse_{total,22hrsFZ}$	0.603	**0.641**	0.384	0.126	0.036
$FeII\text{-}fine_{total,22hrsFZ}$	**0.704**	0.313	0.301	0.349	0.291
$FeII\text{-}coarse_{total,5minFZ}$	-0.176	0.251	**0.743**	-0.149	-0.092
$FeII\text{-}fine_{total,5minFZ}$	0.375	0.143	0.348	**0.530**	0.452
Na^+-coarse	0.129	**0.945**	0.191	0.122	0.022
Na^+-fine	0.556	**0.634**	-0.095	**0.459**	-0.118
Mg^{2+}-coarse	0.126	**0.948**	0.184	0.114	0.037
Mg^{2+}-fine	**0.663**	**0.574**	-0.015	**0.408**	-0.070
K^+-coarse	0.286	**0.925**	0.082	0.097	0.087
K^+-fine	**0.765**	0.508	-0.153	0.062	-0.020
Ca^{2+}-coarse	0.481	0.543	**0.625**	0.188	-0.110
Ca^{2+}-fine	**0.864**	0.152	0.241	0.342	-0.129
NSS-Ca^{2+}-coarse	0.515	0.434	**0.664**	0.188	-0.128
NSS-Ca^{2+}-fine	**0.869**	0.073	0.280	0.308	-0.124
NH_4^+-coarse	0.068	**0.575**	0.290	**0.473**	0.404
NH_4^+-fine	0.093	0.371	**0.701**	0.255	-0.037
NO_3^--coarse	0.109	**0.676**	**0.546**	0.373	0.051
NO_3^--fine	0.400	**0.569**	0.383	0.391	-0.130
SO_4^{2-}-coarse	0.180	**0.864**	0.428	0.133	0.004
SO_4^{2-}-fine	0.387	0.427	0.523	**0.614**	-0.052
NSS-SO_4^{2-}-coarse	0.229	0.235	**0.872**	0.102	-0.046
NSS-SO_4^{2-}-fine	0.301	0.324	**0.648**	**0.596**	-0.030

Table 4. Contintued.

MSA-coarse	-0.291	0.030	-0.133	-0.109	**0.825**
MSA-fine	0.237	0.303	0.143	**0.882**	-0.062
Cl^--coarse	0.126	**0.945**	0.181	0.119	0.029
Cl^--fine	**0.613**	**0.595**	-0.202	0.343	-0.147
Oxalate-coarse	-0.170	0.013	**0.936**	0.013	-0.002
Oxalate-fine	-0.147	0.204	**0.861**	0.166	-0.144
(cation-anion)-coarse	0.537	**0.554**	**0.552**	0.173	-0.162
(cation-anion)-fine	**0.877**	0.248	-0.170	0.170	-0.026
TSP	**0.792**	**0.530**	0.116	0.193	-0.108
wind speed	**0.611**	0.091	-0.366	**0.602**	-0.142

Table 5. Average, minimum and maximum atmospheric anion and cation concentrations in coarse, fine and total aerosol fractions. Sample number is same for all: 21 samples. Concentrations in ng m^{-3} unless otherwise noted.

Element	Coarse			Fine			Total		
	Average ± SD	Min.	Max.	Average ± SD	Min.	Max.	Average ± SD	Min.	Max.
F^-	9.45 ± 15.27	0.97	71	7.07 ± 5.52	1.39	22.1	16.6 ± 18.1	3.64	83.8
NSS-F^-	9.25 ± 15.27	0.82	70.8	6.92 ± 5.51	1.2	22	16.2 ± 18.1	3.22	83.4
Br^-	4.78 ± 5.56	1.04	23.2	3.05 ± 1.43	1.32	5.39	7.83 ± 6.34	2.36	26.6
NSS-Br^-	- 7.69 ± 6.32	-20	4.08	- 4.66 ± 3.83	-11.3	2.88	- 12.4 ± 9.17	-27.6	5.03
Cl^- (μg m^{-3})	3.14 ± 2.16	0.24	10.5	1.66 ± 0.89	0.16	3.3	4.80 ± 2.69	0.42	13.7
NSS-Cl^- (μg m^{-3})	- 0.45 ± 0.40	-1.61	-0.11	- 0.56 ± 0.42	-1.08	0.79	- 1.01 ± 0.49	-2.35	-0.28
SO_4^{2-} (μg m^{-3})	0.65 ± 0.38	0.07	1.63	1.20 ± 0.60	0.19	2.35	1.82 ± 0.90	0.26	3.67
NSS-SO_4^{2-} (μg m^{-3})	0.15 ± 0.16	0.003	0.47	0.88 ± 0.51	0.14	1.99	1.03 ± 0.60	0.15	2.46
NO_3^- (μg m^{-3})	0.32 ± 0.16	< 0.11	0.74	0.36 ± 0.12	< 0.21	0.57	0.67 ± 0.27	< 0.24	1.32
Glycolate	8.59 ± 9.04	< 3.18	41.3	7.46 ± 3.09	< 2.50	13.2	16.3 ± 11.3	< 5.7	51.4
MSA	4.82 ± 3.58	0.98	16.4	22.0 ± 10.1	4.55	43.1	26.8 ± 9.5	8.15	46.9
Oxalate	18.6 ± 10.4	< 5.03	38.7	31.5 ± 19.9	< 7.0	68.9	52.2 ± 29.9	< 12.4	100.8
NH_4^+	34.4 ± 13.9	8.47	61.5	141 ± 53	49	260	175 ± 62	68.5	299
Na^+ (μg m^{-3})	2.00 ± 1.23	0.22	6.16	1.24 ± 0.57	0.18	2.36	3.24 ± 1.67	0.44	8.52
K^+	90.6 ± 45.5	24.5	247	91.2 ± 38.1	26.2	161	182 ± 75	65.7	408
Mg^{2+}	247 ± 140	43.8	725	156 ± 65	33.7	265	402 ± 189	79.3	990
Ca^{2+}	381 ± 302	10	1170	224 ± 168	8	554	605 ± 442	20	1580
NSS-Ca^{2+}	304 ± 273	0	1040	177 ± 153	-15.5	480	481 ± 402	0	1390

Table 6. Enrichment factors assuming continental bulk composition according to Taylor and McLennan [1985].

Sample Id	Na	Mg	K	Ca	Sc	Ti	V	Mn	Fe	Zn	Cs	Ba	La	Ce	Sm	Eu	Hf	Pb	Th
A96-01	12.77	1.23	2.72	0.44	0.49	1.25	0.54	0.90	0.57	1.96	3.77	1.66	3.05	3.10	2.42	1.74	1.80	5.17	3.38
A96-02	2.58	0.52	1.58	0.33	0.45	1.04	0.45	0.61	0.56	1.09	3.58	1.74	2.98	3.07	2.29	1.54	1.27	3.25	3.28
A96-03	3.06	0.59	1.75	0.46	0.45	0.97	0.47	0.63	0.66	1.60	3.84	2.19	2.88	3.09	2.23	1.47	1.28	3.73	3.09
A96-04	3.52	0.66	1.87	0.51	0.45	0.97	0.51	0.67	0.68	1.43	3.76	2.04	2.97	3.11	2.29	1.51	1.33	4.27	3.25
A96-05	7.02	0.85	2.28	0.55	0.46	0.96	0.51	0.65	0.62	1.52	4.18	2.29	2.80	2.89	2.22	1.53	1.24	4.80	3.09
A96-06	10.72	1.26	2.71	0.63	0.45	1.26	0.51	0.68	0.64	2.08	4.15	2.14	2.89	3.00	2.31	1.55	1.36	4.94	3.48
A96-07	6.66	0.88	2.36	0.47	0.46	1.74	0.59	1.00	0.61	8.13	3.58	1.89	2.72	2.79	1.97	1.41	1.89	10.88	3.03
A96-08	7.29	0.82	2.50	0.31	0.49	2.63	0.45	0.49	0.71	20.89	2.96	1.46	1.73	1.61	0.89	0.56	3.21	7.37	1.85
A96-09	8.72	1.02	6.92	0.98	0.64	1.89	1.66	0.84	0.67	73.32	5.11	2.12	3.46	3.48	2.95	3.21	13.79	19.94	5.72
A96-10	24.67	2.50	7.17	1.56	0.48	1.35	1.71	0.64	0.78	10.84	10.45	2.68	6.38	2.93	5.10	3.41	3.55	13.37	7.64
A96-11	14.49	1.69	3.34	1.39	0.53	0.99	0.79	0.69	0.68	5.12	5.02	2.79	2.65	2.72	2.11	1.41	1.31	7.79	3.16
A96-12	17.90	1.82	3.43	0.81	0.51	0.97	0.80	0.60	0.62	8.23	4.70	1.98	2.68	2.70	1.99	1.44	1.76	11.69	3.17
A96-13	6.56	0.99	2.64	0.84	0.50	0.93	0.67	0.59	0.67	3.84	4.88	2.52	2.60	2.74	2.07	1.40	0.61	8.78	3.21
A96-14	7.14	1.12	2.84	1.09	0.51	0.89	0.85	0.61	0.71	6.71	5.10	2.50	2.74	2.84	2.10	1.41	1.12	9.73	3.19
A96-15	7.41	1.17	2.90	1.03	0.51	0.95	0.71	0.63	0.71	9.14	5.25	2.42	2.77	2.80	2.09	1.42	1.21	9.94	3.23
A96-16	10.26	1.40	3.15	1.01	0.53	0.89	0.77	0.69	0.66	13.27	5.42	2.39	2.82	2.81	2.04	1.42	1.27	13.36	3.39
A96-17	12.04	1.51	3.16	0.94	0.50	0.94	0.68	0.57	0.65	13.07	5.19	3.07	2.65	2.70	2.00	1.37	1.37	11.33	3.12
A96-18	9.24	1.27	2.66	0.77	0.47	0.95	0.59	0.65	0.59	10.76	4.64	3.39	2.37	2.39	1.87	1.56	1.39	10.24	2.86
A96-19	12.52	1.56	3.23	1.20	0.62	1.32	0.67	0.56	0.71	14.67	4.46	2.31	2.57	2.60	2.07	0.58	2.93	11.29	3.58
A96-20	14.53	1.58	2.97	0.75	0.65	1.50	0.65	0.52	0.67	34.03	4.71	3.42	1.79	1.83	1.33	0.36	3.35	10.85	2.70
A96-21	34.71	3.23	4.87	0.99	0.73	4.11	0.81	0.72	1.08	18.68	4.08	1.81	1.17	0.92	1.83	0.63	7.54	15.66	3.24
Average	11.13	1.32	3.19	0.81	0.52	1.36	0.73	0.66	0.68	12.40	4.46	2.37	2.62	2.67	2.07	1.32	1.89	8.76	3.19
± SD	7.49	0.64	1.46	0.34	0.08	0.76	0.34	0.12	0.11	16.13	1.48	0.53	0.96	0.58	0.77	0.72	2.97	4.25	1.17
continental bulk comp. ($\mu g\ g^{-1}$)	23000.0	32000.0	9000.0	53000.0	30.0	5300.0	230.0	1400.0	70400.0	80.0	1.0	250.0	16.0	33.0	3.5	1.1	3.0	8.0	3.5

Table 7. Enrichment factors assuming shale composition according to Turekian and Wedepohl [1961].

Sample Id	Na	Mg	K	Ca	Sc	Ti	V	Mn	Fe	Zn	Cs	Ba	La	Ce	Sm	Eu	Hf	Pb	Th
A96-01	29.13	2.49	0.88	1.01	1.07	1.38	0.91	1.42	0.80	1.57	0.72	0.68	0.51	1.65	1.26	1.82	1.84	1.97	0.94
A96-02	5.89	1.06	0.51	0.76	0.99	1.14	0.75	0.96	0.80	0.87	0.68	0.72	0.49	1.63	1.19	1.61	1.29	1.24	0.91
A96-03	6.99	1.19	0.56	1.04	0.99	1.07	0.79	0.99	0.94	1.28	0.73	0.90	0.48	1.65	1.16	1.54	1.31	1.42	0.86
A96-04	8.04	1.34	0.60	1.16	1.00	1.06	0.86	1.05	0.96	1.15	0.72	0.84	0.49	1.66	1.19	1.58	1.35	1.63	0.90
A96-05	16.01	1.72	0.74	1.25	1.01	1.05	0.86	1.02	0.88	1.22	0.80	0.94	0.46	1.54	1.15	1.60	1.27	1.83	0.86
A96-06	24.45	2.57	0.87	1.43	0.99	1.38	0.85	1.06	0.91	1.67	0.79	0.88	0.48	1.60	1.20	1.63	1.39	1.88	0.97
A96-07	15.19	1.79	0.76	1.08	1.02	1.91	0.99	1.56	0.87	6.52	0.68	0.78	0.45	1.49	1.03	1.48	1.93	4.14	0.84
A96-08	16.64	1.67	0.81	0.71	1.08	2.88	0.76	0.76	1.00	16.75	0.56	0.60	0.29	0.86	0.46	0.59	3.28	2.81	0.51
A96-09	19.90	2.07	2.23	2.24	1.40	2.08	2.80	1.32	0.95	58.80	0.97	0.87	0.57	1.86	1.54	3.36	14.07	7.60	1.59
A96-10	56.30	5.07	2.31	3.57	1.06	1.48	2.88	1.01	1.11	8.69	1.99	1.10	1.06	1.56	2.65	3.57	3.62	5.10	2.12
A96-11	33.05	3.43	1.08	3.17	1.17	1.09	1.33	1.08	0.96	4.11	0.96	1.15	0.44	1.45	1.10	1.48	1.34	2.97	0.88
A96-12	40.85	3.71	1.11	1.86	1.11	1.06	1.34	0.95	0.88	6.60	0.90	0.81	0.44	1.44	1.04	1.51	1.80	4.45	0.88
A96-13	14.98	2.01	0.85	1.92	1.11	1.02	1.13	0.92	0.95	3.08	0.93	1.03	0.43	1.46	1.08	1.46	0.63	3.35	0.89
A96-14	16.29	2.28	0.92	2.50	1.13	0.97	1.43	0.96	1.00	5.38	0.97	1.03	0.45	1.51	1.09	1.47	1.14	3.71	0.89
A96-15	16.92	2.38	0.93	2.35	1.13	1.04	1.20	0.98	1.01	7.33	1.00	0.99	0.46	1.49	1.09	1.48	1.24	3.79	0.90
A96-16	23.40	2.85	1.01	2.32	1.16	0.97	1.29	1.08	0.94	10.64	1.03	0.98	0.47	1.50	1.06	1.49	1.29	5.09	0.94
A96-17	27.47	3.06	1.02	2.16	1.10	1.03	1.15	0.89	0.93	10.48	0.99	1.26	0.44	1.44	1.04	1.43	1.39	4.32	0.87
A96-18	21.08	2.58	0.86	1.75	1.04	1.04	0.99	1.02	0.84	8.63	0.88	1.39	0.39	1.28	0.97	1.64	1.42	3.90	0.79
A96-19	28.57	3.17	1.04	2.74	1.35	1.45	1.13	0.88	1.01	11.76	0.85	0.95	0.43	1.38	1.08	0.60	2.99	4.30	0.99
A96-20	33.14	3.21	0.96	1.72	1.42	1.64	1.09	0.82	0.95	27.29	0.90	1.41	0.30	0.97	0.69	0.37	3.42	4.13	0.75
A96-21	79.19	6.56	1.57	2.25	1.61	4.51	1.36	1.12	1.53	14.98	0.78	0.74	0.19	0.49	0.95	0.66	7.69	5.97	0.90
Average	25.40	2.68	1.03	1.86	1.14	1.49	1.23	1.04	0.96	9.94	0.85	0.97	0.43	1.42	1.08	1.38	1.93	3.34	0.89
± SD	17.09	1.30	0.47	0.78	0.17	0.84	0.57	0.19	0.15	12.94	0.28	0.22	0.16	0.31	0.40	0.76	3.03	1.62	0.32
shale comp. ($\mu g\ g^{-1}$)	9600.0	15000.0	26600.0	22100.0	13.0	4600.0	130.0	850.0	47200.0	95.0	5.0	580.0	92.0	59.0	6.4	1.0	2.8	20.0	12.0

Table 8. Model outputs from weighted linear regressions with coarse, fine and total SO_4^{2-} fractions as dependent variables.

Dependent Variable	Model summary			Independent Variables	Unstandardized Coefficients		Standardized Coefficients	t	Sig.	95% Confidence Interval for B	
	R^2	F	Sig.		B	Std. Error	b			Lower Bound	Upper Bound
SO_4^{2-}-coarse	0.990	402.981	0.000	(constant)	-169.761	33.858		-5.014	0.000	-241.537	-97.984
				Na^+-coarse	0.222	0.008	0.799	28.854	0.000	0.205	0.238
				MSA-coarse	37.442	2.764	0.369	13.544	0.000	31.581	43.302
				NSS-Ca^{2+} coarse	0.485	0.053	0.348	9.232	0.000	0.373	0.596
				Zn-coarse	23.361	11.224	0.073	2.081	0.054	-0.432	47.154
SO_4^{2-}-fine	0.940	88.564	0.000	(constant)	-98.610	121.202		-0.814	0.427	-354.324	157.103
				Na^+-fine	0.194	0.080	0.161	2.414	0.027	0.024	0.363
				MSA-fine	23.863	4.175	0.414	5.715	0.000	15.054	32.673
				Pb-fine	757.756	75.435	0.657	10.045	0.000	598.602	916.909
SO_4^{2-}-total	0.961	98.888	0.000	(constant)	-344.949	188.144		-1.833	0.085	-743.797	53.899
				Na^+-total	0.198	0.030	0.393	6.717	0.000	0.136	0.261
				MSA-total	33.901	5.047	0.361	6.717	0.000	23.202	44.600
				NSS-Ca^{2+} coarse	1.278	0.213	0.452	6.009	0.000	0.827	1.728
				Zn-total	34.757	11.123	0.210	3.125	0.007	11.179	58.336

Table 9. Model outputs from weighted linear regressions with coarse and fine nonbiog-SO_4^{2-} fractions as dependent variables.

Dependent Variable	Model summary			Independent Variables	Unstandardized Coefficients		Standardized Coefficients	t	Sig.	95% Confidence Interval for B	
	R^2	F	Sig.		B	Std. Error	b			Lower Bound	Upper Bound
nonbio-SO_4^{2-}-coarse	0.990	572.168	0.000	Na^+-coarse	0.224	0.014	0.748	16.254	0.000	0.195	0.253
				NSS-Ca^{2+} coarse	0.393	0.110	0.220	3.567	0.002	0.162	0.624
				Zn-coarse	20.372	19.393	0.062	1.022	0.320	-21.519	62.262
nonbio-SO_4^{2-}-coarse	0.991	627.703	0.000	Na^+-coarse	0.199	0.021	0.664	9.304	0.000	0.154	0.244
				NSS-Ca^{2+} coarse	0.308	0.122	0.173	2.515	0.022	0.051	0.565
				NO_3^--coarse	0.386	0.228	0.186	1.695	0.107	-0.092	0.864
nonbio-SO_4^{2-}-coarse	0.982	526.778	0.000	Na^+-coarse	0.242	0.016	0.806	14.740	0.000	0.207	0.276
				Zn-coarse	70.431	18.014	0.214	3.910	0.001	32.727	108.134
nonbio-SO_4^{2-}-fine	0.975	375.377	0.000	Na^+-fine	0.270	0.067	0.295	4.040	0.001	0.130	0.410
				Pb-fine	971.587	98.378	0.721	9.876	0.000	765.680	1177.495

Figure 1

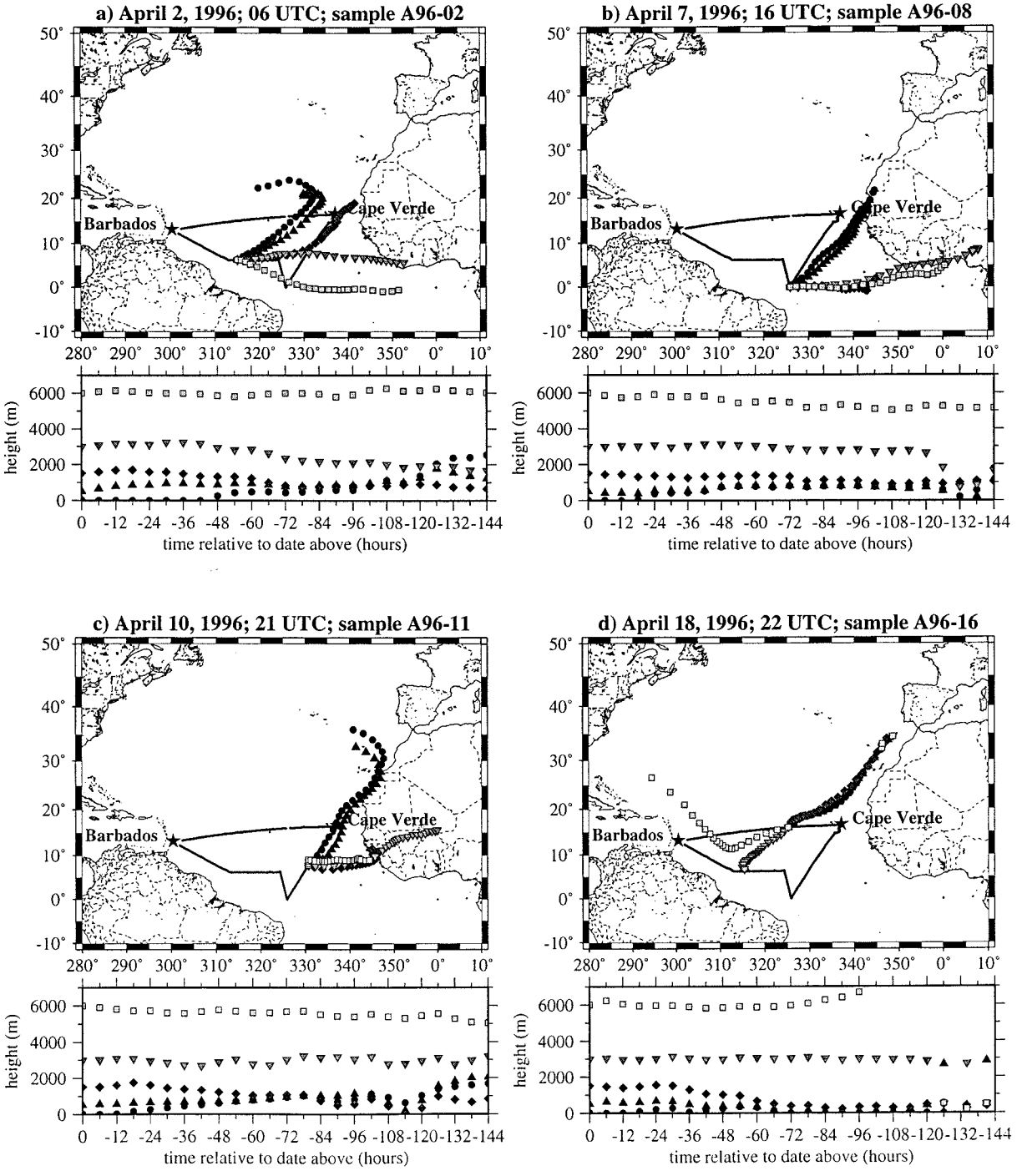
a) April 2, 1996; 06 UTC; sample A96-02
b) April 7, 1996; 16 UTC; sample A96-08
c) April 10, 1996; 21 UTC; sample A96-11
d) April 18, 1996; 22 UTC; sample A96-16
Barbados
Cape Verde
50°
40°
30°
20°
10°
0°
-10°
280° 290° 300° 310° 320° 330° 340° 350° 0° 10°
height (m)
6000
4000
2000
0
0 -12 -24 -36 -48 -60 -72 -84 -96 -108 -120 -132 -144
time relative to date above (hours)

Figure 2

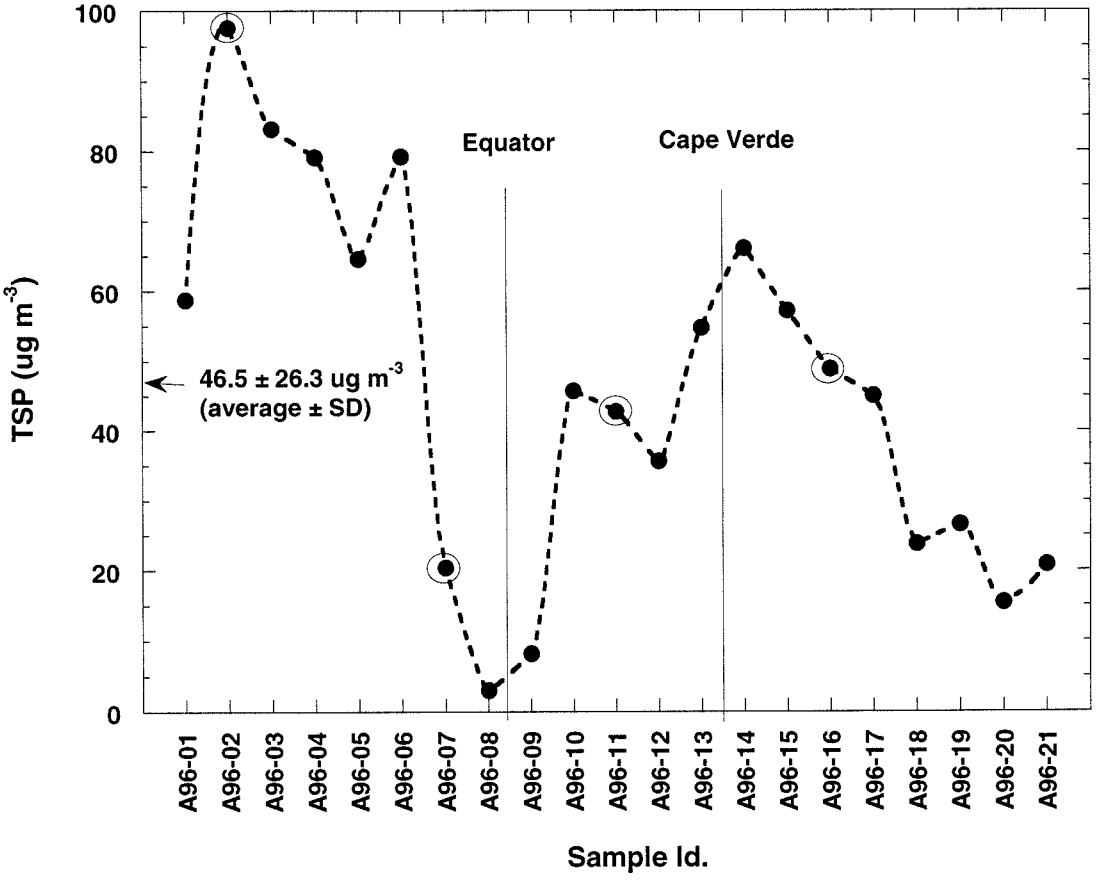
100
80
60
40
20
0
TSP (ug m-3)
46.5 ± 26.3 ug m-3
(average ± SD)
Equator
Cape Verde
A96-01
A96-02
A96-03
A96-04
A96-05
A96-06
A96-07
A96-08
A96-09
A96-10
A96-11
A96-12
A96-13
A96-14
A96-15
A96-16
A96-17
A96-18
A96-19
A96-20
A96-21
Sample Id.

Figure 3

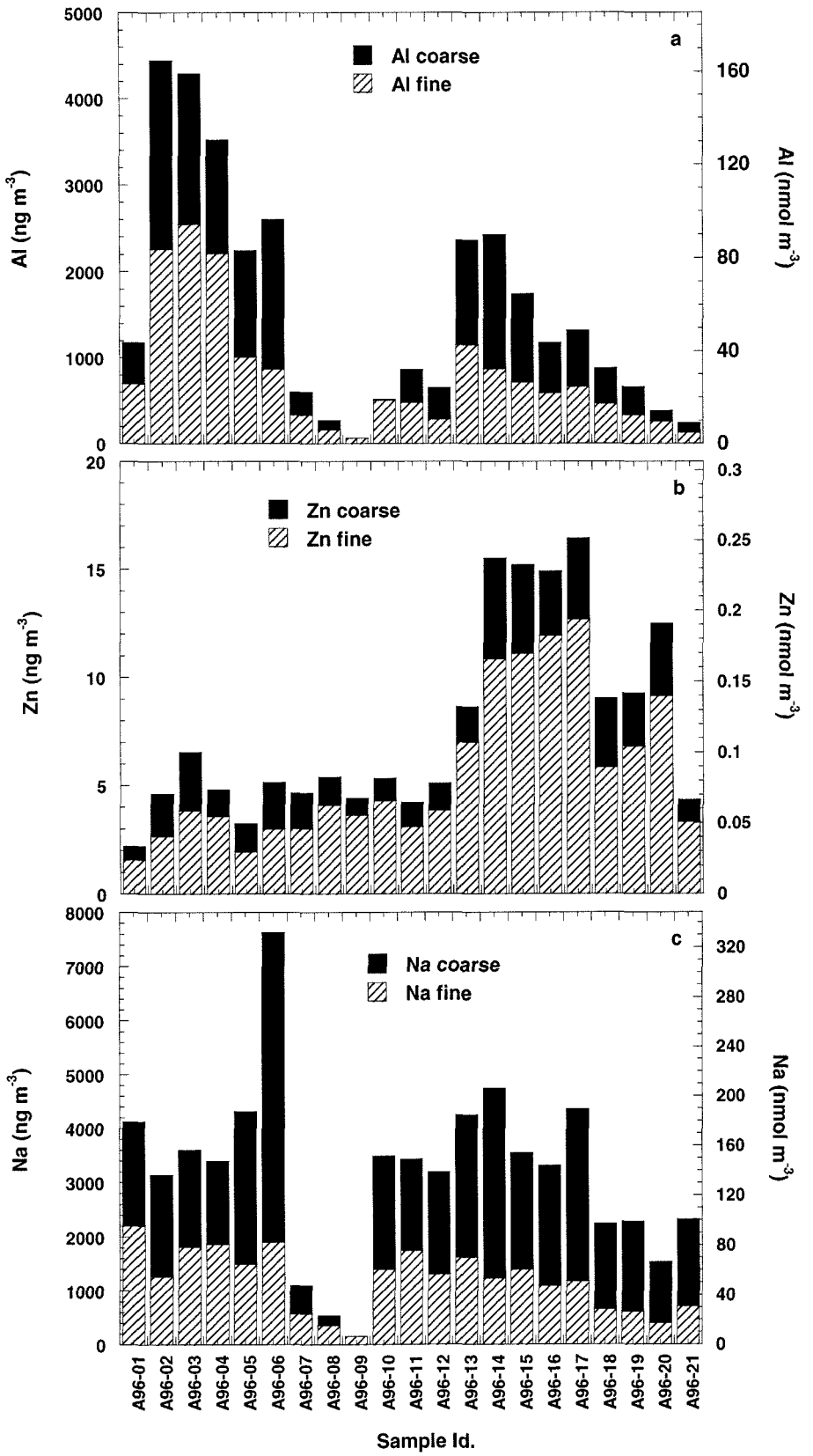
a
Al coarse
Al fine
Al (ng m-3)
Al (nmol m-3)
b
Zn coarse
Zn fine
Zn (ng m-3)
Zn (nmol m-3)
c
Na coarse
Na fine
Na (ng m-3)
Na (nmol m-3)
A96-01
A96-02
A96-03
A96-04
A96-05
A96-06
A96-07
A96-08
A96-09
A96-10
A96-11
A96-12
A96-13
A96-14
A96-15
A96-16
A96-17
A96-18
A96-19
A96-20
A96-21
Sample Id.

Figure 4

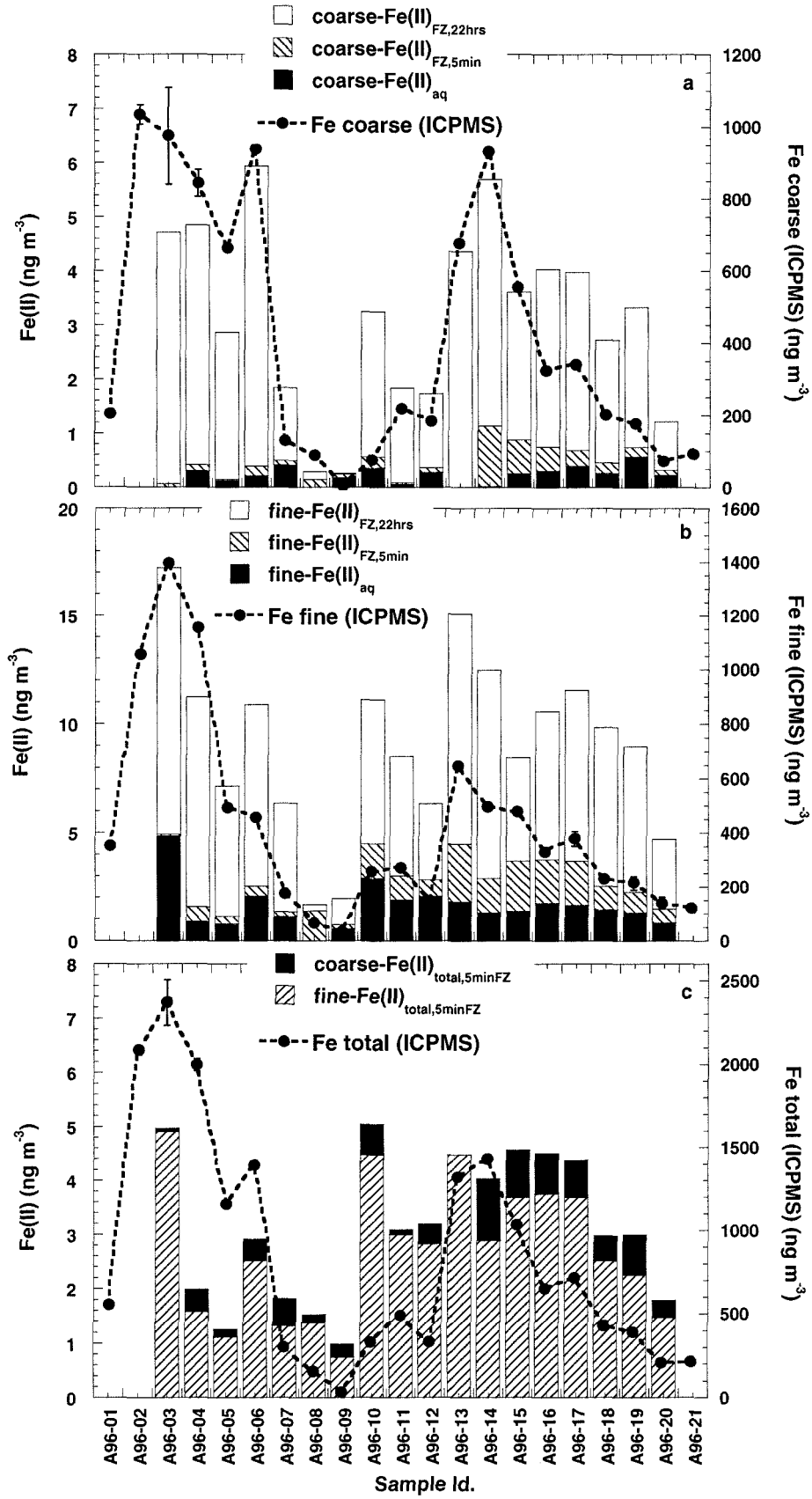
coarse-Fe(II)FZ,22hrs
coarse-Fe(II)FZ,5min
coarse-Fe(II)aq
Fe coarse (ICPMS)
a
Fe(II) (ng m-3)
Fe coarse (ICPMS) (ng m-3)
fine-Fe(II)FZ,22hrs
fine-Fe(II)FZ,5min
fine-Fe(II)aq
Fe fine (ICPMS)
b
Fe fine (ICPMS) (ng m-3)
coarse-Fe(II)total,5minFZ
fine-Fe(II)total,5minFZ
Fe total (ICPMS)
c
Fe total (ICPMS) (ng m-3)
A96-01
A96-02
A96-03
A96-04
A96-05
A96-06
A96-07
A96-08
A96-09
A96-10
A96-11
A96-12
A96-13
A96-14
A96-15
A96-16
A96-17
A96-18
A96-19
A96-20
A96-21
Sample Id.

Figure 5

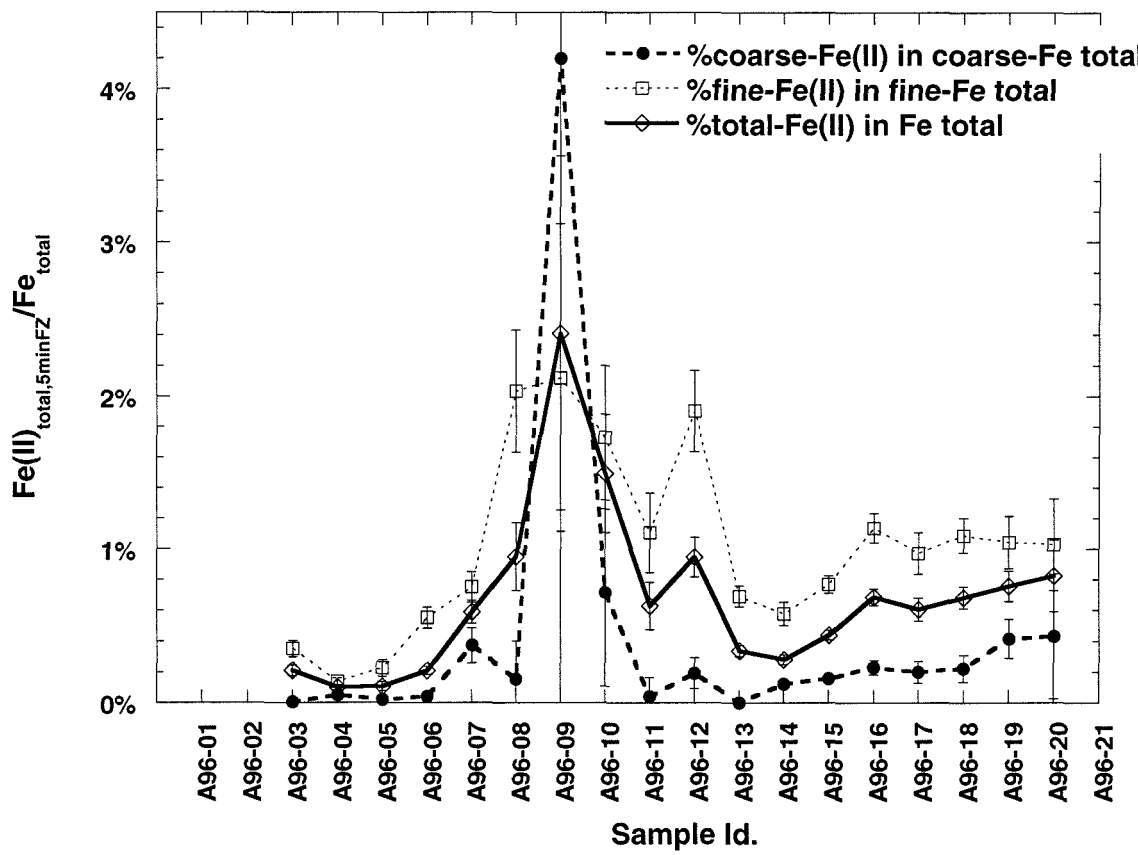
%coarse-Fe(II) in coarse-Fe total
%fine-Fe(II) in fine-Fe total
%total-Fe(II) in Fe total
Fe(II)total,5minFZ/Fetotal
4%
3%
2%
1%
0%
A96-01
A96-02
A96-03
A96-04
A96-05
A96-06
A96-07
A96-08
A96-09
A96-10
A96-11
A96-12
A96-13
A96-14
A96-15
A96-16
A96-17
A96-18
A96-19
A96-20
A96-21
Sample Id.

Figure 6

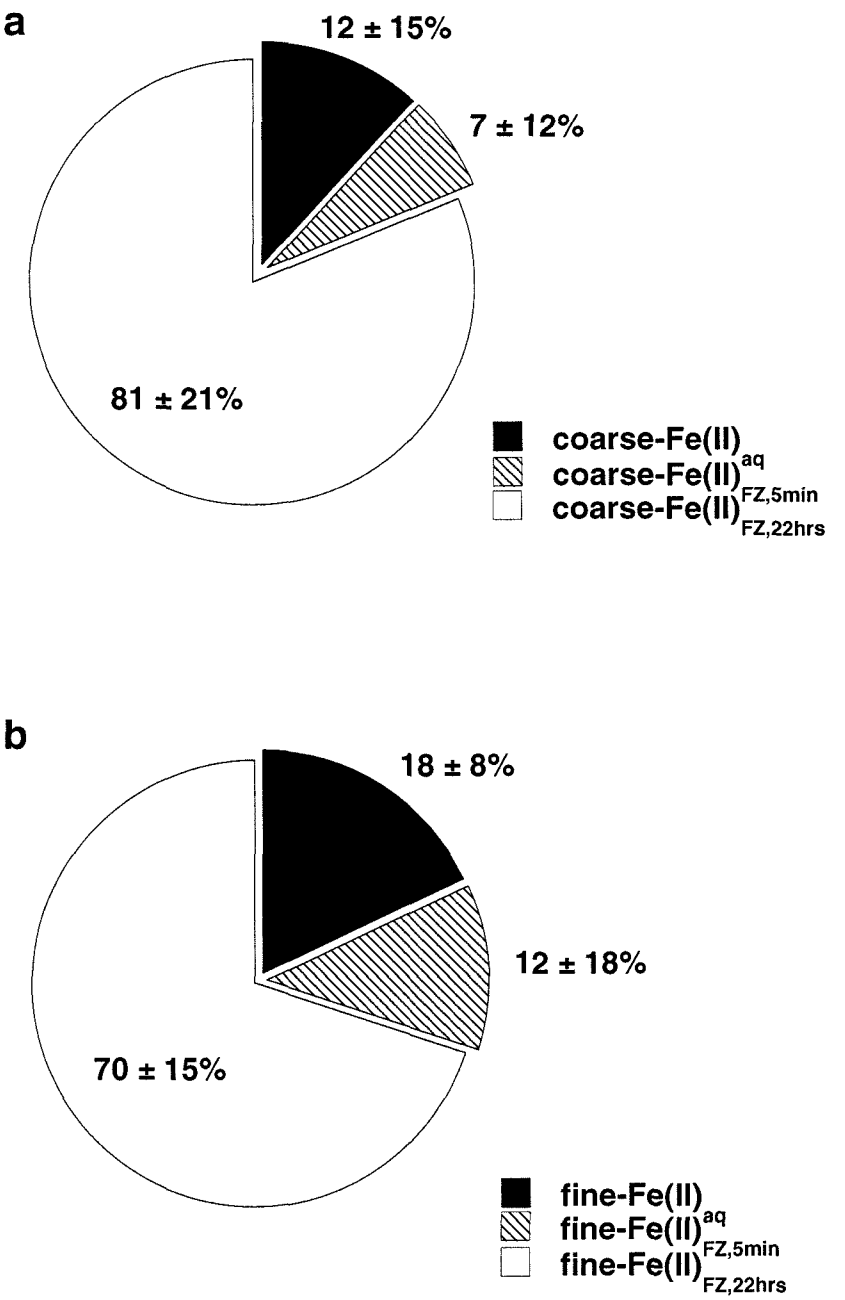
a
12 ± 15%
7 ± 12%
81 ± 21%
coarse-Fe(II)
coarse-Fe(II)aq
coarse-Fe(II)FZ,5min
coarse-Fe(II)FZ,22hrs
b
18 ± 8%
12 ± 18%
70 ± 15%
fine-Fe(II)
fine-Fe(II)aq
fine-Fe(II)FZ,5min
fine-Fe(II)FZ,22hrs

Figure 7

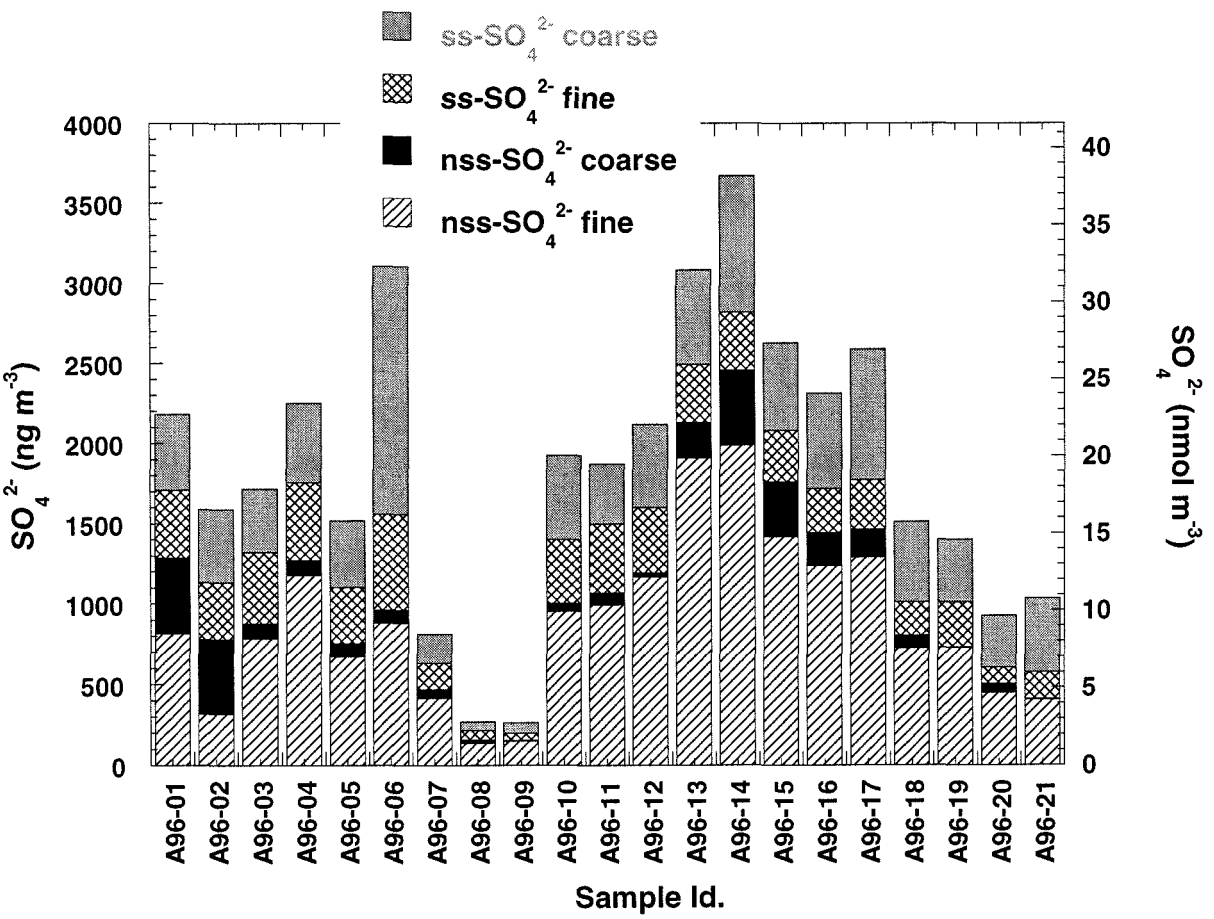
ss-SO4 2- coarse
ss-SO4 2- fine
nss-SO4 2- coarse
nss-SO4 2- fine
SO4 2- (ng m-3)
SO4 2- (nmol m-3)
4000
3500
3000
2500
2000
1500
1000
500
0
40
35
30
25
20
15
10
5
0
A96-01
A96-02
A96-03
A96-04
A96-05
A96-06
A96-07
A96-08
A96-09
A96-10
A96-11
A96-12
A96-13
A96-14
A96-15
A96-16
A96-17
A96-18
A96-19
A96-20
A96-21
Sample Id.

Figure 8

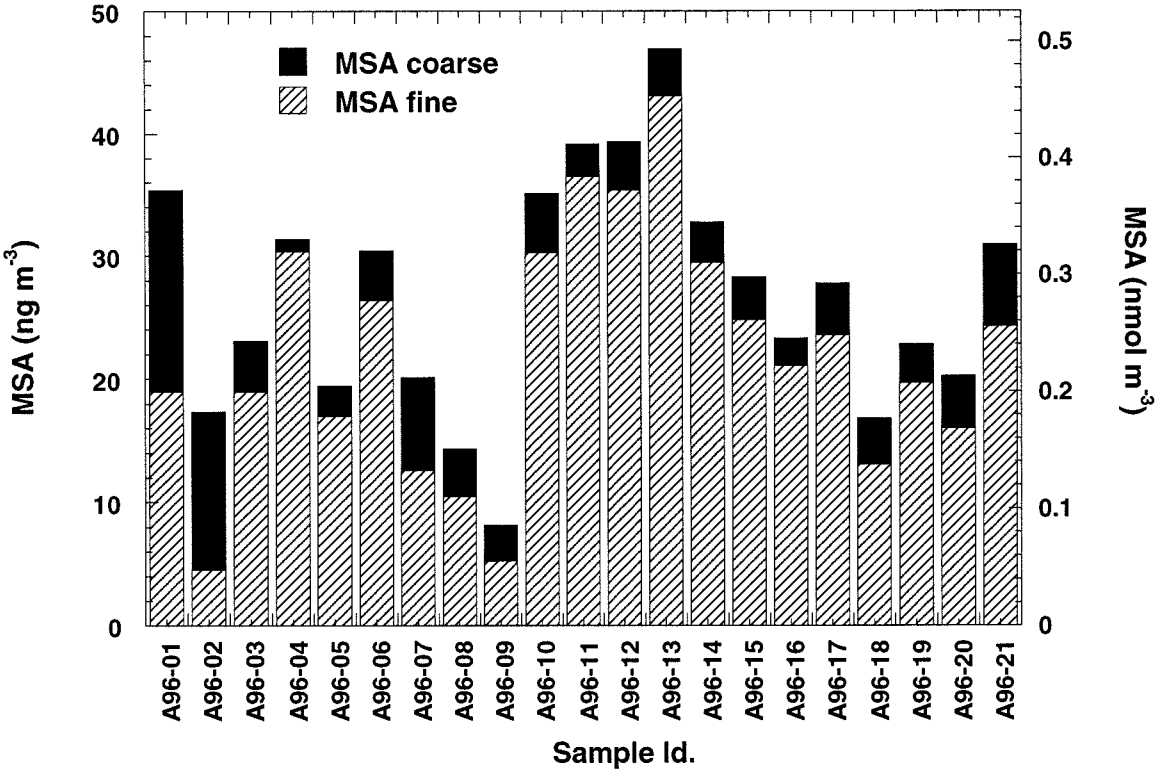
MSA coarse
MSA fine
MSA (ng m-3)
MSA (nmol m-3)
Sample Id.
0
10
20
30
40
50
0
0.1
0.2
0.3
0.4
0.5
A96-01
A96-02
A96-03
A96-04
A96-05
A96-06
A96-07
A96-08
A96-09
A96-10
A96-11
A96-12
A96-13
A96-14
A96-15
A96-16
A96-17
A96-18
A96-19
A96-20
A96-21

Figure 9

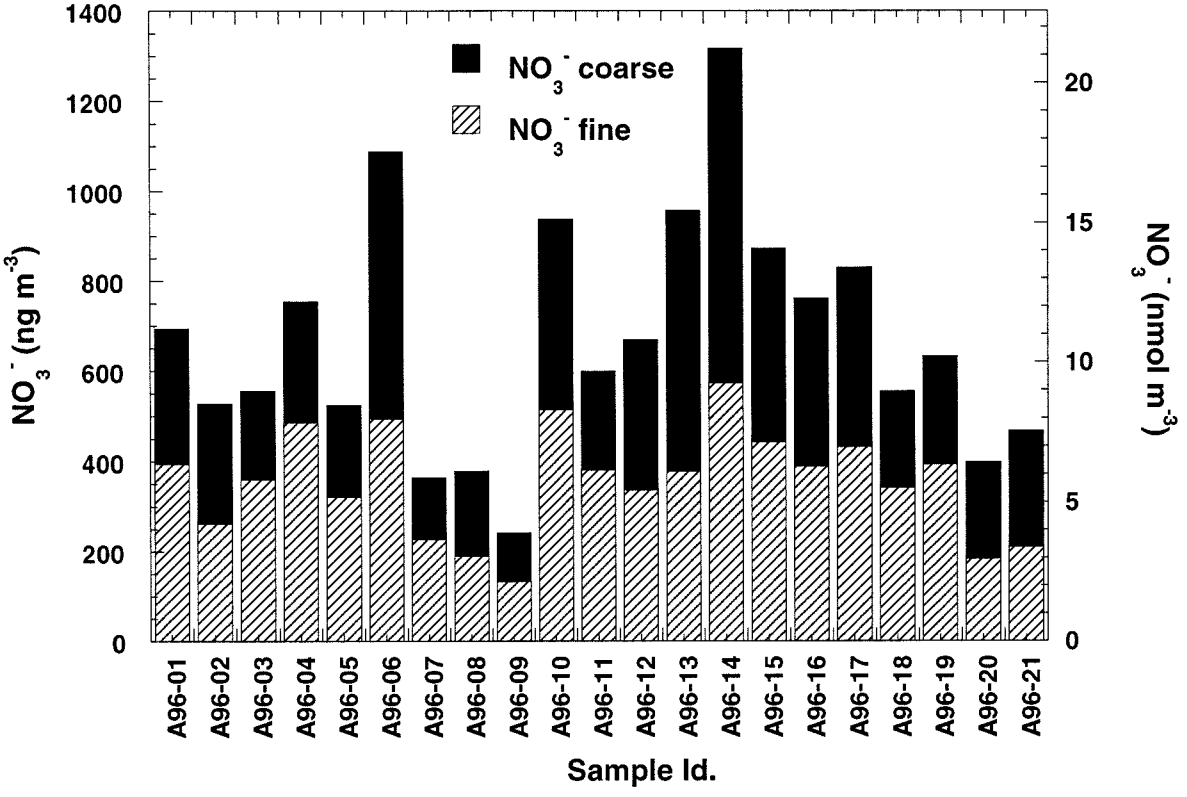
1400
1200
1000
800
600
400
200
0
NO_3^- (ng m^{-3})
20
15
10
5
0
NO_3^- (nmol m^{-3})
NO_3^- coarse
NO_3^- fine
A96-01
A96-02
A96-03
A96-04
A96-05
A96-06
A96-07
A96-08
A96-09
A96-10
A96-11
A96-12
A96-13
A96-14
A96-15
A96-16
A96-17
A96-18
A96-19
A96-20
A96-21
Sample Id.

Figure 10

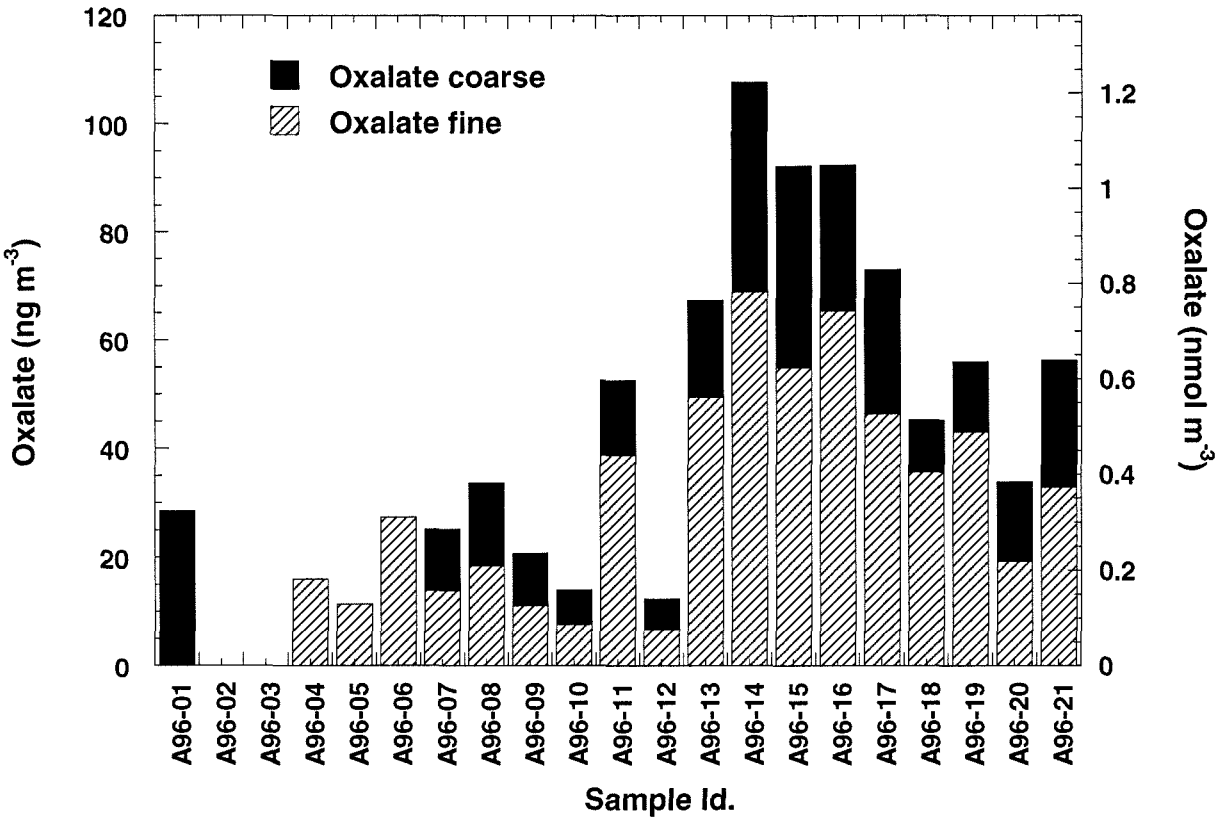
Oxalate coarse
Oxalate fine
Oxalate (ng m-3)
Oxalate (nmol m-3)
Sample Id.
0
20
40
60
80
100
120
0
0.2
0.4
0.6
0.8
1
1.2
A96-01
A96-02
A96-03
A96-04
A96-05
A96-06
A96-07
A96-08
A96-09
A96-10
A96-11
A96-12
A96-13
A96-14
A96-15
A96-16
A96-17
A96-18
A96-19
A96-20
A96-21

Figure 11

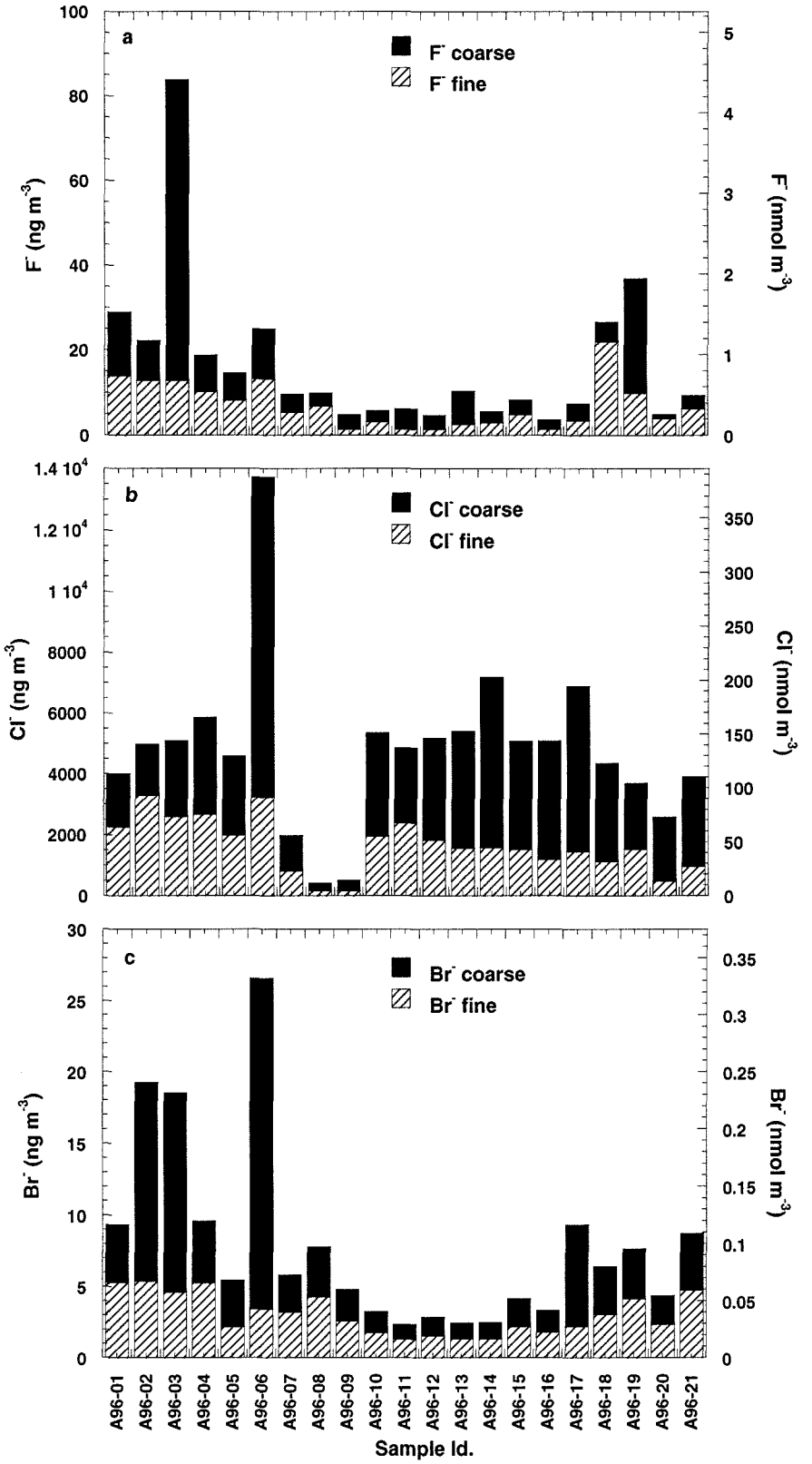
a
F⁻ coarse
F⁻ fine
F⁻ (ng m⁻³)
F⁻ (nmol m⁻³)
b
Cl⁻ coarse
Cl⁻ fine
Cl⁻ (ng m⁻³)
Cl⁻ (nmol m⁻³)
c
Br⁻ coarse
Br⁻ fine
Br⁻ (ng m⁻³)
Br⁻ (nmol m⁻³)
A96-01
A96-02
A96-03
A96-04
A96-05
A96-06
A96-07
A96-08
A96-09
A96-10
A96-11
A96-12
A96-13
A96-14
A96-15
A96-16
A96-17
A96-18
A96-19
A96-20
A96-21
Sample Id.

Figure 12

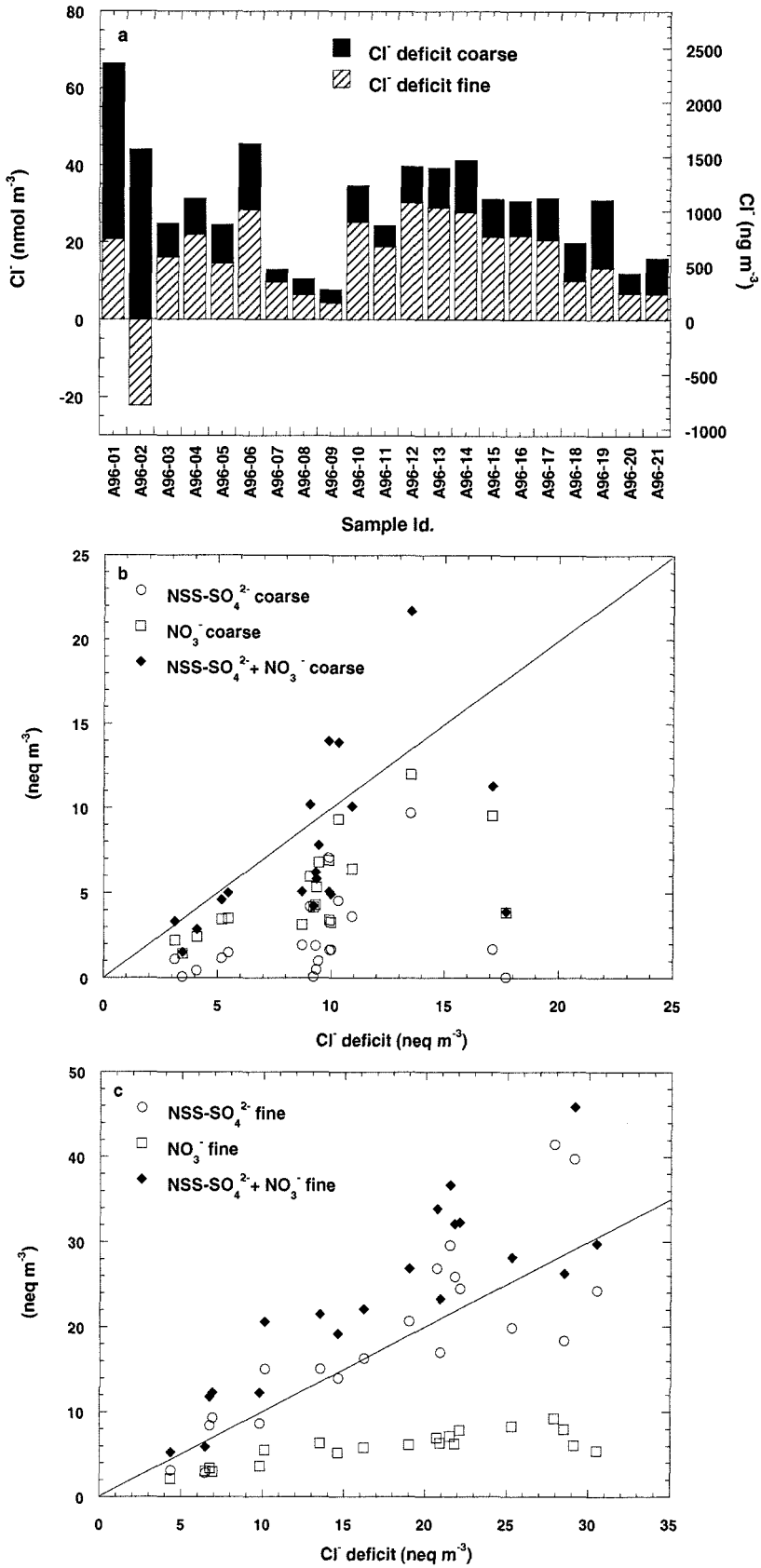
a
Cl⁻ deficit coarse
Cl⁻ deficit fine
Cl⁻ (nmol m⁻³)
Cl⁻ (ng m⁻³)
Sample Id.
A96-01
A96-02
A96-03
A96-04
A96-05
A96-06
A96-07
A96-08
A96-09
A96-10
A96-11
A96-12
A96-13
A96-14
A96-15
A96-16
A96-17
A96-18
A96-19
A96-20
A96-21
b
NSS-SO4 2- coarse
NO3⁻ coarse
NSS-SO4 2- + NO3⁻ coarse
(neq m⁻³)
Cl⁻ deficit (neq m⁻³)
c
NSS-SO4 2- fine
NO3⁻ fine
NSS-SO4 2- + NO3⁻ fine
(neq m⁻³)
Cl⁻ deficit (neq m⁻³)

Figure 13

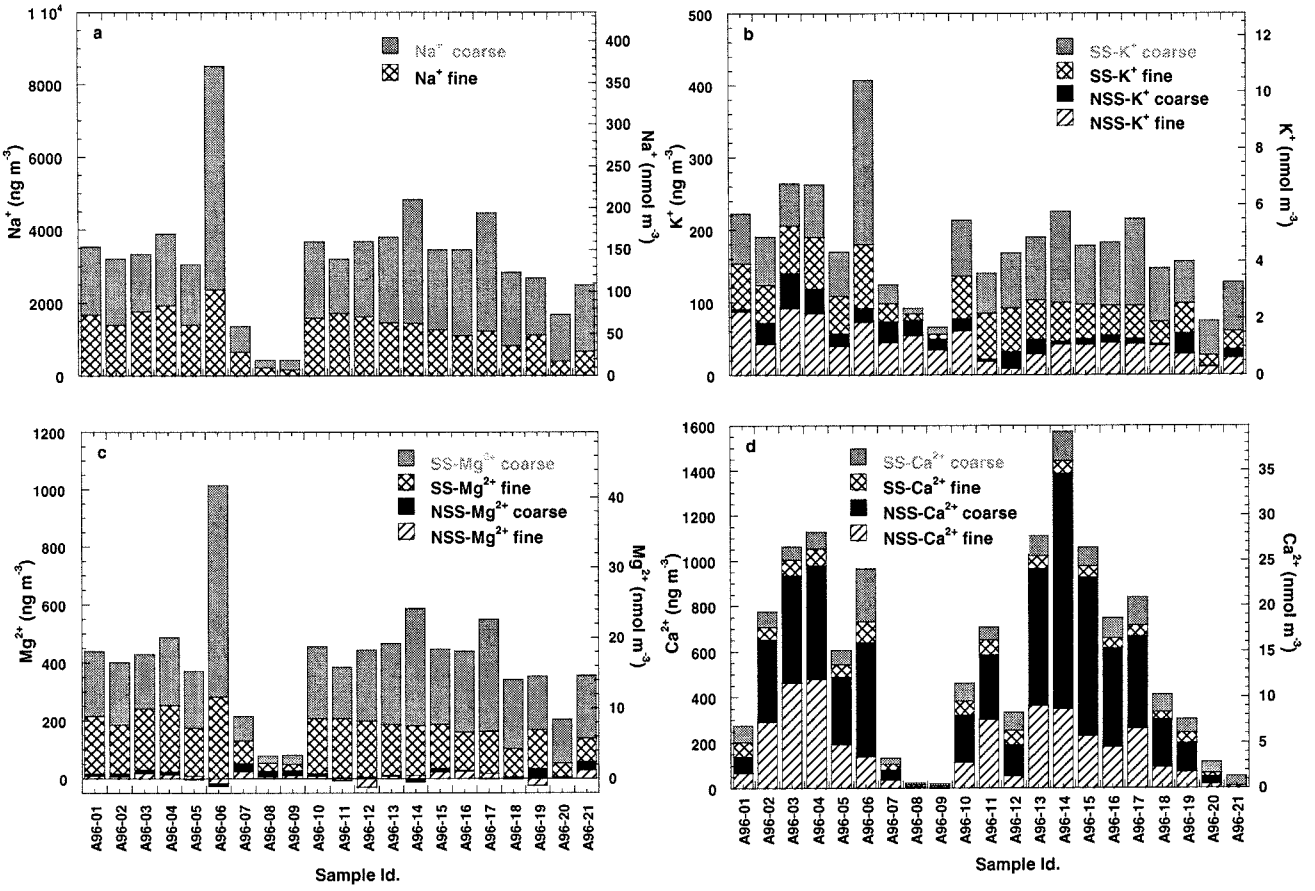
a
Na+ coarse
Na+ fine
Na+ (ng m-3)
Na+ (nmol m-3)
b
SS-K+ coarse
SS-K+ fine
NSS-K+ coarse
NSS-K+ fine
K+ (ng m-3)
K+ (nmol m-3)
c
SS-Mg2+ coarse
SS-Mg2+ fine
NSS-Mg2+ coarse
NSS-Mg2+ fine
Mg2+ (ng m-3)
Mg2+ (nmol m-3)
d
SS-Ca2+ coarse
SS-Ca2+ fine
NSS-Ca2+ coarse
NSS-Ca2+ fine
Ca2+ (ng m-3)
Ca2+ (nmol m-3)
A96-01
A96-02
A96-03
A96-04
A96-05
A96-06
A96-07
A96-08
A96-09
A96-10
A96-11
A96-12
A96-13
A96-14
A96-15
A96-16
A96-17
A96-18
A96-19
A96-20
A96-21
Sample Id.

Figure 14

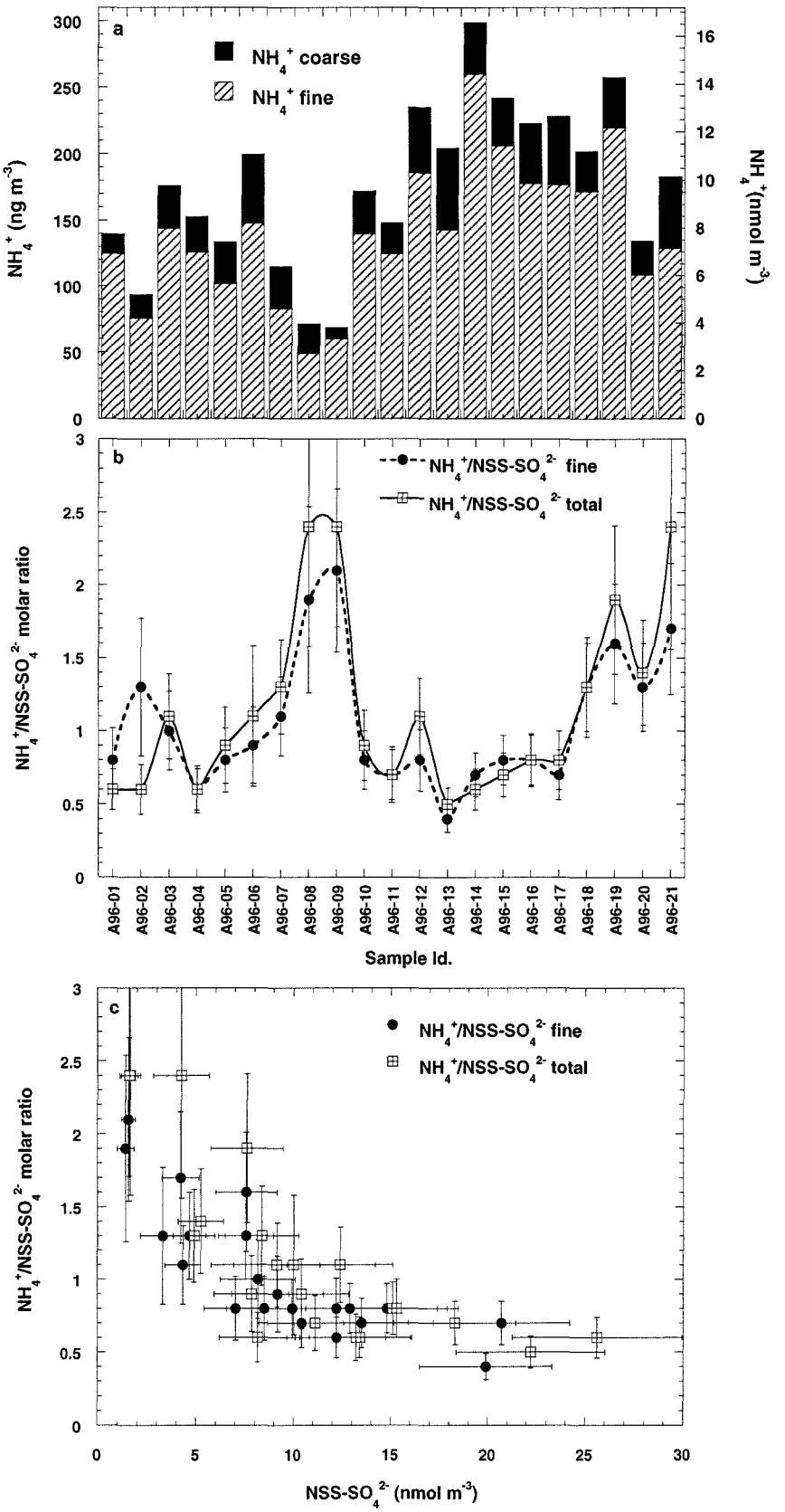
a
NH4+ coarse
NH4+ fine
NH4+ (ng m-3)
NH4+(nmol m-3)
b
NH4+/NSS-SO4 2- fine
NH4+/NSS-SO4 2- total
NH4+/NSS-SO4 2- molar ratio
A96-01
A96-02
A96-03
A96-04
A96-05
A96-06
A96-07
A96-08
A96-09
A96-10
A96-11
A96-12
A96-13
A96-14
A96-15
A96-16
A96-17
A96-18
A96-19
A96-20
A96-21
Sample Id.
c
NH4+/NSS-SO4 2- fine
NH4+/NSS-SO4 2- total
NH4+/NSS-SO4 2- molar ratio
NSS-SO4 2- (nmol m-3)

Figure 15

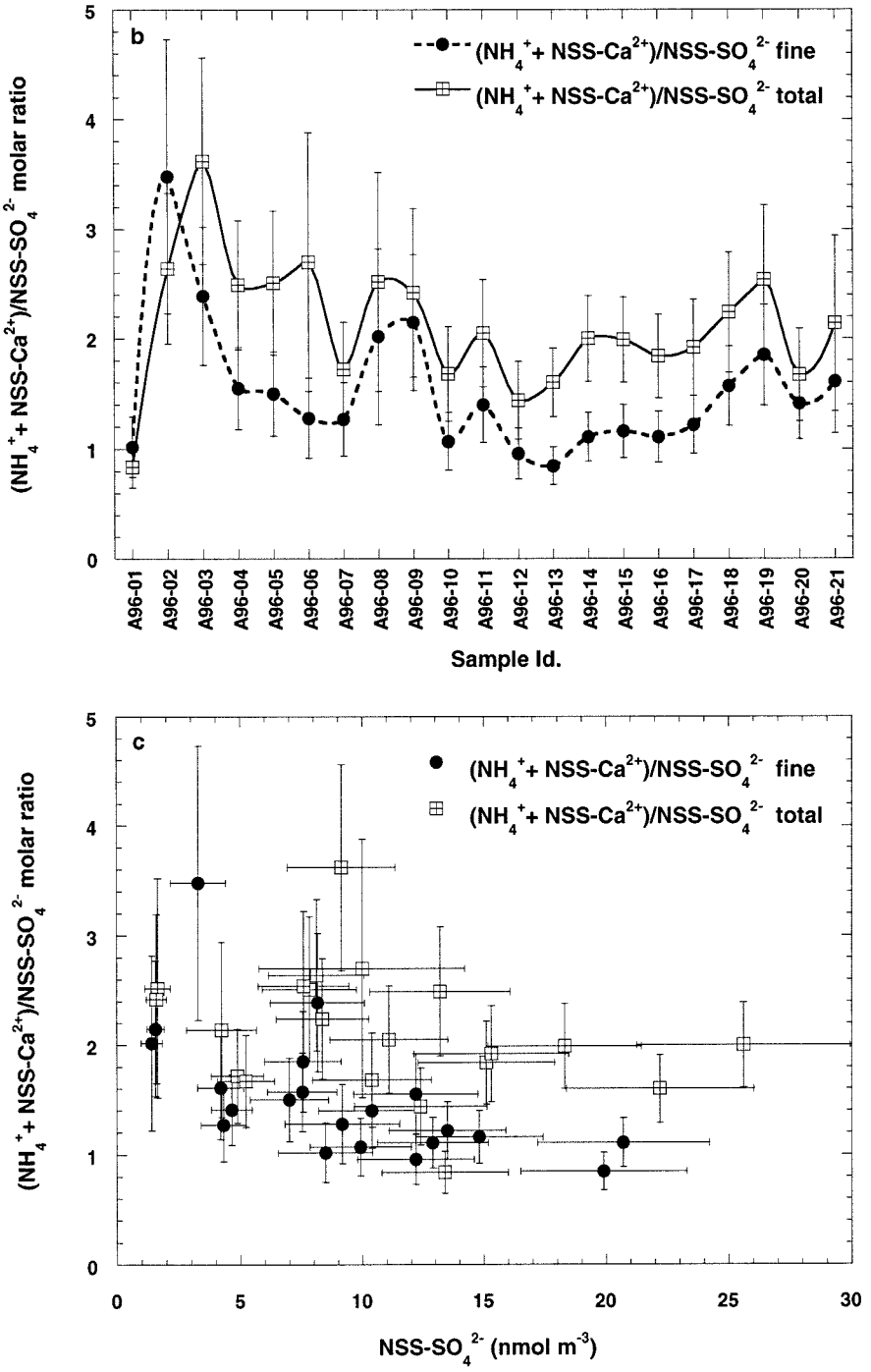
b
(NH4+ + NSS-Ca2+)/NSS-SO4 2- fine
(NH4+ + NSS-Ca2+)/NSS-SO4 2- total
(NH4+ + NSS-Ca2+)/NSS-SO4 2- molar ratio
0
1
2
3
4
5
A96-01
A96-02
A96-03
A96-04
A96-05
A96-06
A96-07
A96-08
A96-09
A96-10
A96-11
A96-12
A96-13
A96-14
A96-15
A96-16
A96-17
A96-18
A96-19
A96-20
A96-21
Sample Id.
c
(NH4+ + NSS-Ca2+)/NSS-SO4 2- fine
(NH4+ + NSS-Ca2+)/NSS-SO4 2- total
(NH4+ + NSS-Ca2+)/NSS-SO4 2- molar ratio
0
5
10
15
20
25
30
NSS-SO4 2- (nmol m-3)

Figure 16

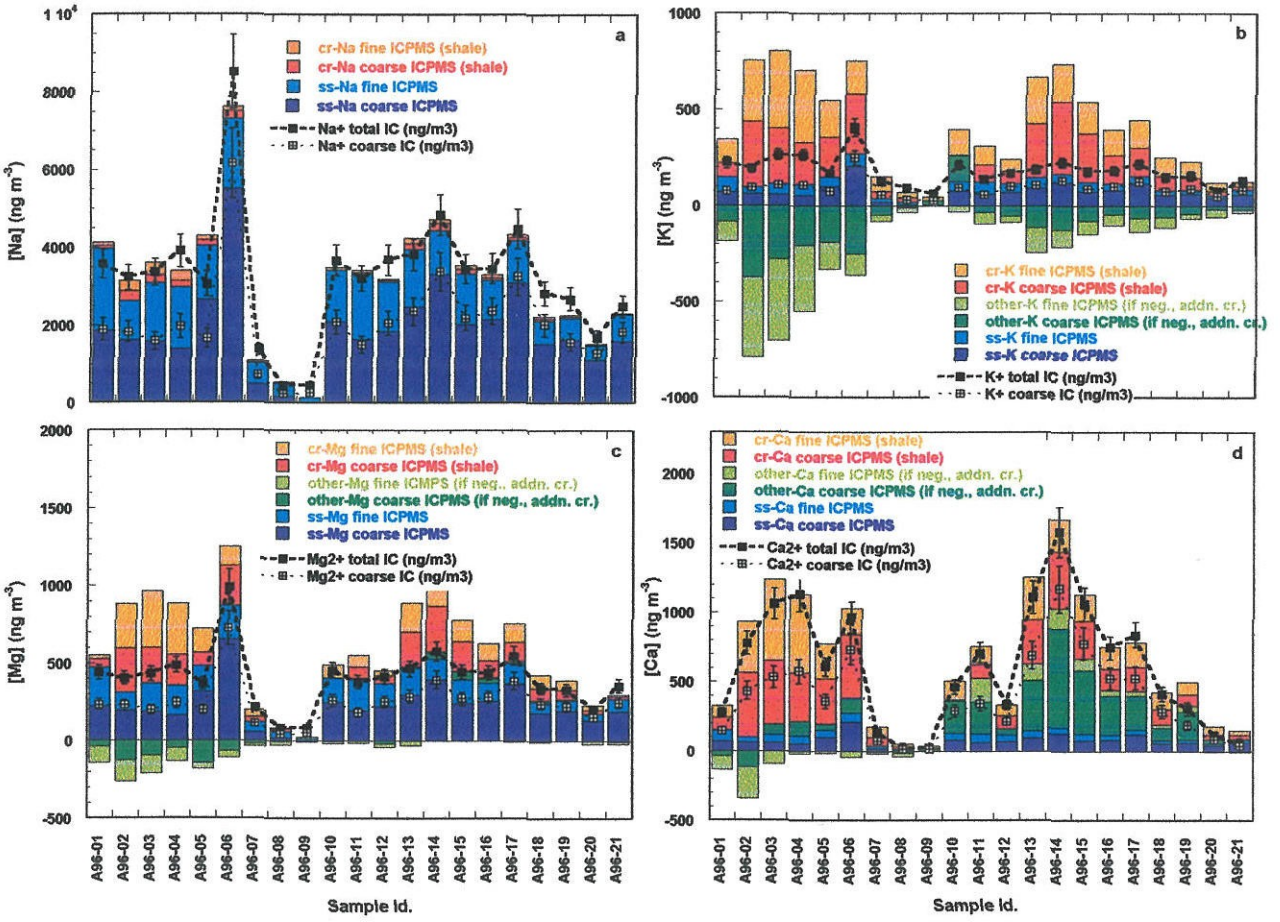
a
cr-Na fine ICPMS (shale)
cr-Na coarse ICPMS (shale)
ss-Na fine ICPMS
ss-Na coarse ICPMS
Na+ total IC (ng/m3)
Na+ coarse IC (ng/m3)
[Na] (ng m-3)
b
cr-K fine ICPMS (shale)
cr-K coarse ICPMS (shale)
other-K fine ICPMS (if neg., addn. cr.)
other-K coarse ICPMS (if neg., addn. cr.)
ss-K fine ICPMS
ss-K coarse ICPMS
K+ total IC (ng/m3)
K+ coarse IC (ng/m3)
[K] (ng m-3)
c
cr-Mg fine ICPMS (shale)
cr-Mg coarse ICPMS (shale)
other-Mg fine ICMPS (if neg., addn. cr.)
other-Mg coarse ICPMS (if neg., addn. cr.)
ss-Mg fine ICPMS
ss-Mg coarse ICPMS
Mg2+ total IC (ng/m3)
Mg2+ coarse IC (ng/m3)
[Mg] (ng m-3)
d
cr-Ca fine ICPMS (shale)
cr-Ca coarse ICPMS (shale)
other-Ca fine ICPMS (if neg., addn. cr.)
other-Ca coarse ICPMS (if neg., addn. cr.)
ss-Ca fine ICPMS
ss-Ca coarse ICPMS
Ca2+ total IC (ng/m3)
Ca2+ coarse IC (ng/m3)
[Ca] (ng m-3)
A96-01 A96-02 A96-03 A96-04 A96-05 A96-06 A96-07 A96-08 A96-09 A96-10 A96-11 A96-12 A96-13 A96-14 A96-15 A96-16 A96-17 A96-18 A96-19 A96-20 A96-21
Sample Id.

Figure 17

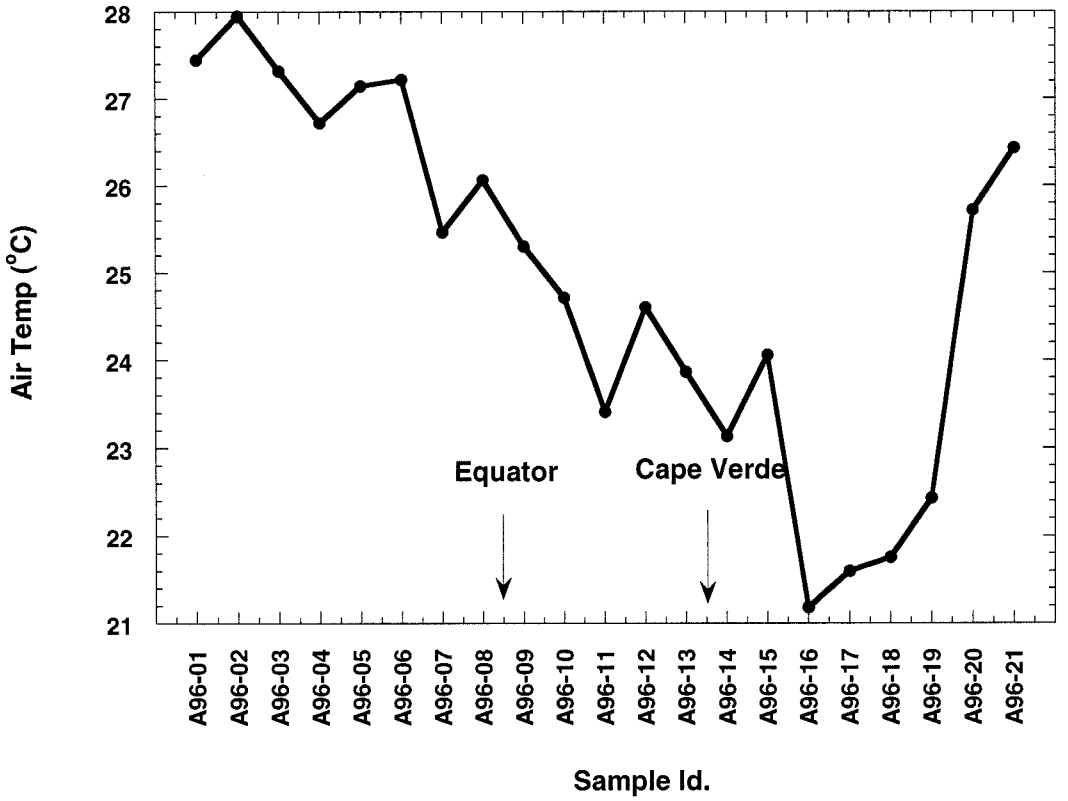
Air Temp (°C)
28
27
26
25
24
23
22
21
Equator
Cape Verde
A96-01
A96-02
A96-03
A96-04
A96-05
A96-06
A96-07
A96-08
A96-09
A96-10
A96-11
A96-12
A96-13
A96-14
A96-15
A96-16
A96-17
A96-18
A96-19
A96-20
A96-21
Sample Id.

Figure 18

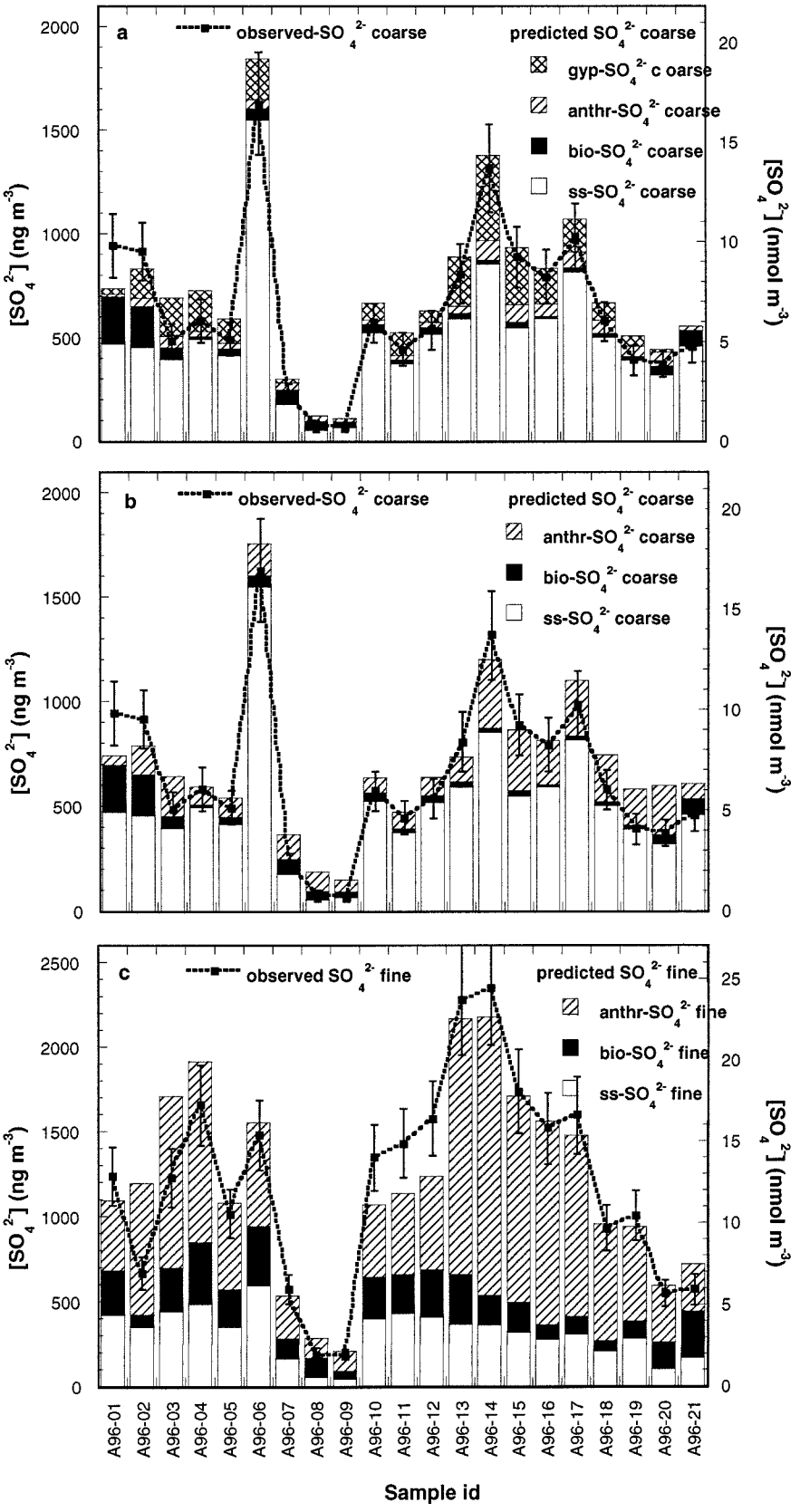
a
observed-SO4 2- coarse
predicted SO4 2- coarse
gyp-SO4 2- c oarse
anthr-SO4 2- coarse
bio-SO4 2- coarse
ss-SO4 2- coarse
[SO4 2-] (ng m-3)
[SO4 2-] (nmol m-3)
b
observed-SO4 2- coarse
predicted SO4 2- coarse
anthr-SO4 2- coarse
bio-SO4 2- coarse
ss-SO4 2- coarse
c
observed SO4 2- fine
predicted SO4 2- fine
anthr-SO4 2- fine
bio-SO4 2- fine
ss-SO4 2- fine
A96-01
A96-02
A96-03
A96-04
A96-05
A96-06
A96-07
A96-08
A96-09
A96-10
A96-11
A96-12
A96-13
A96-14
A96-15
A96-16
A96-17
A96-18
A96-19
A96-20
A96-21
Sample id

Figure 19

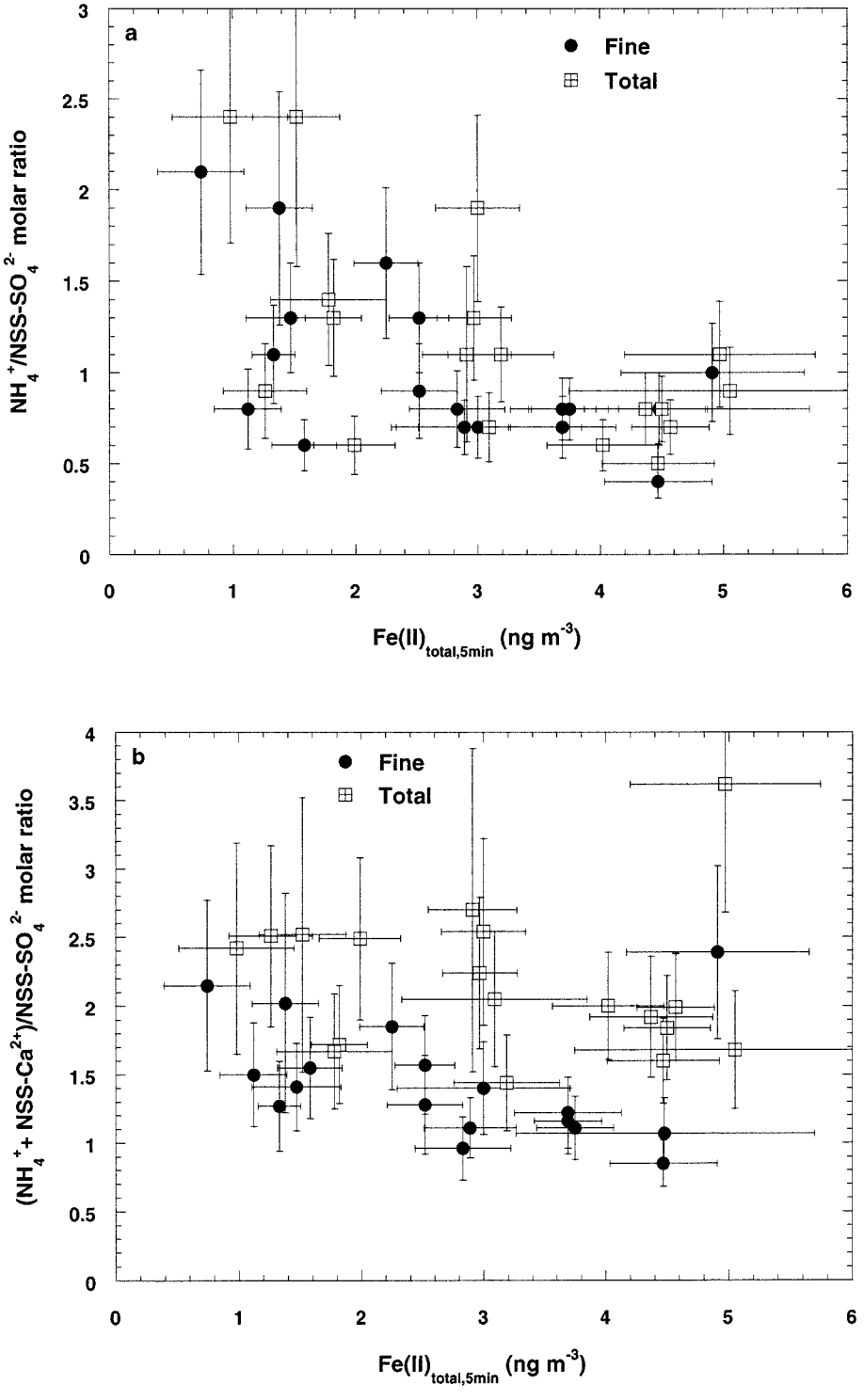
a
Fine
Total
$NH_4^+/NSS\text{-}SO_4^{2-}$ molar ratio
$Fe(II)_{total,5min}$ (ng m^{-3})
b
Fine
Total
$(NH_4^+ + NSS\text{-}Ca^{2+})/NSS\text{-}SO_4^{2-}$ molar ratio
$Fe(II)_{total,5min}$ (ng m^{-3})

Figure 20

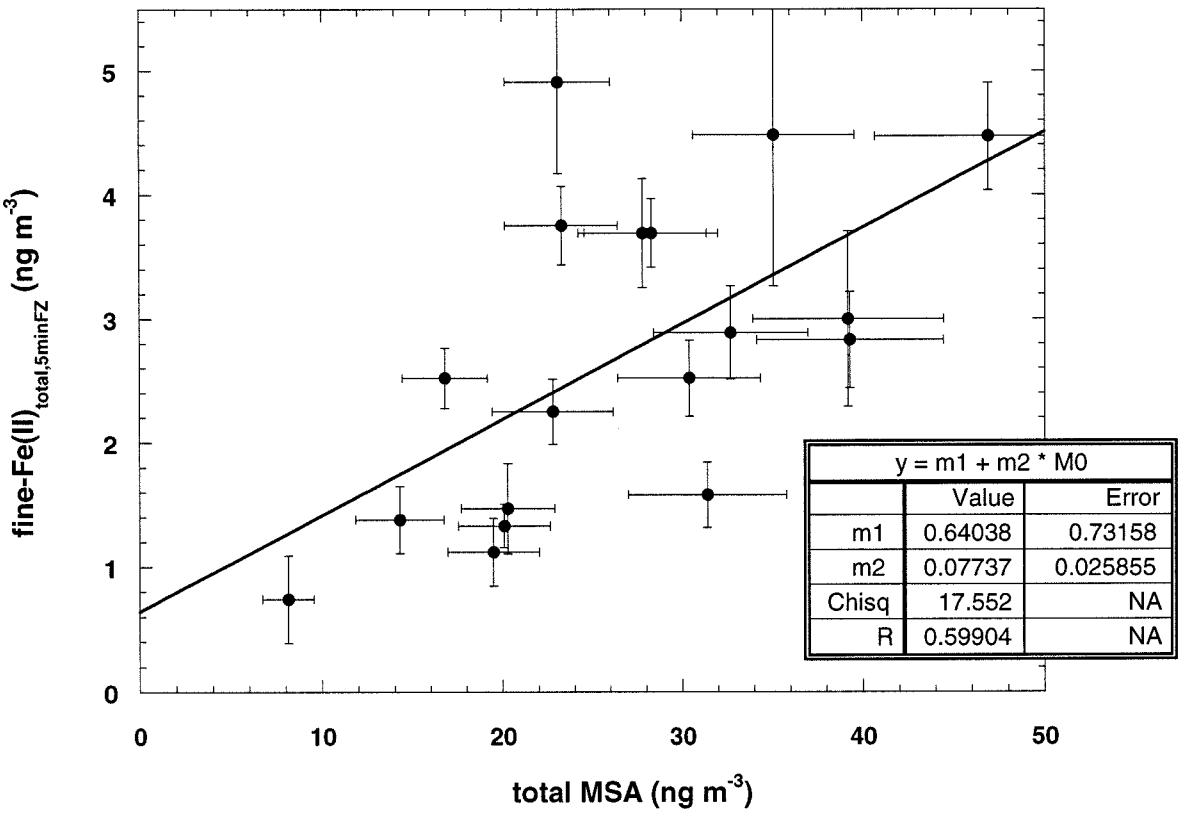
fine-Fe(II)$_{total,5minFZ}$ (ng m^{-3})
total MSA (ng m^{-3})
0
1
2
3
4
5
0
10
20
30
40
50
y = m1 + m2 * M0
Value
Error
m1
0.64038
0.73158
m2
0.07737
0.025855
Chisq
17.552
NA
R
0.59904
NA

Chapter 5

Chemical composition of aerosols collected over the Arabian Sea during the northeast-monsoon

[Anne M. Johansen and Michael R. Hoffmann, to be submitted to the *Journal of Geophysical Research*]

5.1 Abstract

Ambient aerosol samples were collected over the Arabian Sea during the month of March of 1997, aboard the German R/V Sonne, as part of the German JGOFS project (Joint Global Ocean Flux Study). This is the third study in a series of analogous measurements taken over the Arabian Sea during different seasons of the monsoon [*Johansen et al.*, 1999a; *Siefert et al.*, 1999]. Dichotomous high volume collector samples were analyzed for ferrous iron immediately after collection, while trace metals, anions and cations were determined upon return to the laboratory. Data is analyzed with the aid of enrichment factor, principal component, and weighted multiple linear regression analyses.

Average mineral dust concentrations amounted to 5.94 ± 3.08 μg m^{-3} and appeared to be geochemically well-represented by the average crustal composition according to Taylor and McLennan [*Taylor and McLennan*, 1985]. Water-soluble NSS-Ca enrichments, present in the coarse fraction and in air masses of Arabian origin, were indicative of an additional crustal component, most likely in the form of calcite, or as a mixture of calcite and gypsum. If the NSS-Ca were solely derived from calcite, it would constitute an additional contribution of 0.77 ± 0.36 μg m^{-3} of crustal material.

Total ferrous iron concentrations varied from 3.9 to 17.2 ng m^{-3} and averaged 9.8 ± 3.4 ng m^{-3}, with 87.2% of Fe(II) present in the fine aerosol fraction. The Fe(II) concentrations accounted for on average 1.3 ± 0.5% of the total Fe. Ferrous iron in the coarse fraction appeared to be correlated with the crustal component, but the fine fraction Fe(II) exhibited more complex behavior.

The anthropogenic contribution to the aerosol, as traced by Pb, Zn, NSS-K, NSS-SO_4^{2-}, NO_3^- and NH_4^+, was found to be considerably larger than previous observations from the inter-monsoon and SW-monsoon of 1995 [*Johansen et al.*, 1999a; *Siefert et al.*, 1999]. Anthropogenic pollutant concentrations were larger during the first part of the cruise, when air masses originated over the Indian subcontinent. Total NSS-SO_4^{2-} concentrations amounted to 2.94 ± 1.06 μg m^{-3} of which 92.1 ± 4.5% was present in the fine fraction. Biogenically-derived NSS-SO_4^{2-} in the fine fraction, which was traced by MSA, represented only 6% of the NSS-SO_4^{2-}, while 10% appeared to be derived from $CaSO_4$ (gyspum) and the remainder was attributed to anthropogenic sources. The biogenic NSS-SO_4^{2-} to MSA weight ratio obtained in this analysis was 9.8. This is in excellent agreement with what is expected from the temperature dependence of this ratio derived by Johansen et al. [*Johansen et al.*, 1999a]. The NSS-SO_4^{2-} and MSA concentrations present in the coarse fraction accounted for only 7.9 and 8.1% of the total aerosol concentrations, respectively. The biogenic and anthropogenic NSS-SO_4^{2-} in the coarse fraction were of equal magnitude and the corresponding biogenic NSS-SO_4^{2-}/MSA weight ratio was 52.8.

Chloride deficits up to 99.1% in the fine fraction were observed. The average Cl^- deficit in the fine fraction was 89.0 ± 9.4%, while in the coarse fraction it was 25.6 ± 21.3%. The observed Cl^- displacement appears to be related to NSS-SO_4^{2-} in the fine fraction, while in the coarse fraction NO_3^- is the preferred species for acid displacement reactions leading to HCl volatilization.

5.2 Introduction

The present study is part of a larger set of field observations collected over the Arabian Sea. The primary purpose of these investigations was to shed light on the chemical composition of atmospheric aerosol particles during different seasons of the monsoon. The Northern Indian Ocean is subject to a strong biannual reversal pattern in the low-level winds associated with the Indian monsoon [*Ackerman and Cox*, 1989; *Findlater*, 1969; *Findlater*, 1971; *Middleton*, 1986a; *Middleton*, 1986b] which not only affects the abundance and composition of aerosols over the area, but also influences the oceanic surface circulation. This flow pattern is largely driven by the heat gradient between the Indian subcontinent and the ocean.

During the northern summer a large low-pressure system builds up over the central Asian continent which allows strong winds to carry humid marine air masses from the southern Indian Ocean towards India and the Himalayas. Air masses during this SW-monsoon are characterized by clean open-ocean conditions. Our group collected aerosol samples during the SW-monsoon and inter-monsoon seasons of 1995 [*Johansen et al.*, 1999a; *Siefert et al.*, 1999]. The inter-monsoon is classified as the period between the NE- and the SW-monsoons, when no predominant wind pattern has developed.

The NE-monsoon is typified, as the name suggests, by winds from the NE (i.e., the Indian subcontinent), which are prevalent during the northern winter months. Wind patterns described by Findlater [*Findlater*, 1971] suggest the normal development of two jet streaks which emerge over the central Arabian Sea. One jet blows down over the Thar Desert, which is located in eastern Pakistan and western India, and the other jet moves out of south-west India. The air masses emerging from the Thar Desert are subject to

dust infiltration. The present paper presents data from observations collected during the tail end of the NE-monsoon of 1997. Trace metals, ferrous iron, anions and cations were determined.

The quantification and characterization of suspended aerosol particles is necessary to understand their role in the radiation budget of the earth. Aerosols can either increase or decrease the outgoing solar radiation by scattering or absorbing (direct effect) or by changing the microphysical properties of clouds (indirect effect). Due to the short residence time of aerosol particles, they are not evenly distributed over the globe and consequently their radiative forcing is subject to significant regional and seasonal variations. The spectral extinction of solar radiation passing through the atmosphere depends strongly on the size distribution and refractive index of aerosols. A number of investigators [*Jayaraman et al.*, 1998; *Moorthy et al.*, 1998; *Moorthy et al.*, 1997; *Satheesh and Krishna Moorthy*, 1997; *Satheesh et al.*, 1998] have studied the optical characteristics and size distributions of aerosols over the Indian Ocean during the NE-monsoon in the INDOEX experiment which took place in early 1996. Because air masses during the NE-monsoon have crossed arid continental regions, this season seems of special interest when studying the amount of mineral dust that reaches the Arabian Sea. Mineral dust concentrations over the northern Arabian Sea are among the highest recorded for a marine environment, only second to dust loadings observed in the Atlantic north east trades [*Chester et al.*, 1985]. The above studies found that the average aerosol optical depth for the visible wavelength region was as high as 0.5 near the western coast of India, and in the range of 0.2-0.4 over the Arabian Sea, and 0.1 and less over the Indian Ocean. For comparison, the aerosol optical depth reported for the Atlantic Ocean

ranged from 0.04 to 0.25 [*Hoppel et al.*, 1990]. Thus, the aerosol optical depth measured over the Arabian Sea is higher than the reported values for other oceanic regions with an exception of the tropical zone of the Atlantic Ocean which is affected by the Saharan dust. The high values obtained over the Arabian Sea are most likely the result of the combined effect of the influx of windblown dust from the surrounding arid and semiarid regions as well as the anthropogenic aerosols from the Indian subcontinent that are transported by the low-level flow. However, chemical analysis of aerosol samples collected over different regions of the ocean under varying wind conditions are needed to delineate the different sources and their relative significances [*Satheesh et al.*, 1998].

There are very few measurements of trace chemical species from the Indian Ocean. Savoie et al. [*Savoie et al.*, 1987] sampled nitrate, NSS-sulfate and mineral aerosol during the NE- and spring inter-monsoon of 1979 and found a strong gradient in the concentrations of the measured species, decreasing toward the south. This is in general agreement with observations made based on the aerosol optical depths mentioned above. They also detected large concentrations of NSS-Ca in the form of gypsum and suggested that the most likely sources are gypsiferous soils which are known to exist in some regions of the Thar, the Indian and the Arabian deserts. Photographs taken suggest that dust can be transported simultaneously from all these areas over the Arabian Sea. This is also indicated by Middleton [*Middleton*, 1986b] who found that the seasonality of dust storm frequency varies substantially from one part of this region to another implying that source areas vary as well. Large concentrations of NSS-Ca were also observed by Naik et al. [*Naik et al.*, 1991], Johansen et al. [*Johansen et al.*, 1999a] and Savoie et al. [*Savoie et al.*, 1987], who determined it to be of crustal origin. Johansen et al. [*Johansen*

et al., 1999a] and Savoie et al. [*Savoie et al.*, 1987] attributed it to gypsum. While Savoie et al. [*Savoie et al.*, 1987] measured mineral aerosol concentrations which averaged 1.01 ± 0.81 μg m^{-3}, that never exceeded 4 μg m^{-3} during their entire cruise, Johansen et al. [*Johansen et al.*, 1999a] found 5.9 ± 4.2 μg m^{-3} of mineral aerosol during the spring inter-monsoon, and 0.7 ± 0.4 μg m^{-3} during the SW-monsoon of 1995.

Pease et al. [*Pease et al.*, 1998] summarized the potential source areas of desert dust surrounding the Arabian Sea. Dust originates in Somalia, the southern and interior Arabian Peninsula, and in parts of Iran, Pakistan and India. During the NE-monsoon Pease et al. [*Pease et al.*, 1998] observed average dust concentrations of 40 μg m^{-3}, which ranged from 7 to 178 μg m^{-3}. Dust levels were higher over the northern and eastern Arabian Sea than over the southern sea. The large Zn enrichments observed in the dust collected over the northern and eastern regions indicate anthropogenic inputs from the Indian subcontinent. The higher dust concentrations, which were observed closer to Oman, were transported from Iran and Oman. During the spring inter-monsoon they observed average wind patterns from the northwest, with winds passing directly over Oman and the Wahiba Sand Sea area, before passing over the Arabian Sea [*Findlater*, 1971]. Geochemical evidence suggested that Oman is the most likely source for the dust loading during the spring inter-monsoon.

Chester et al. [*Chester et al.*, 1991] reported that mineral dust concentrations decreased from a range of 15-20 μg m^{-3} in the north to a range of 0.01-0.25 μg m^{-3} below 35 ^{o}S in the far southern ocean. In an earlier study, Chester et al. [*Chester et al.*, 1985] concluded that the close correspondence between the clay mineralogies of the sediments and dusts in the northern Arabian Sea provided strong evidence for the dominance of the

atmospheric pathway for deposition of land-derived material to the sediment surface. They estimated that about 75% of the land-derived material to the sediments was of an aeolian origin.

Rhoads et al. [*Rhoads et al.*, 1997] studied the chemical composition of the troposphere over the Indian Ocean during the monsoonal transition, from March to April, 1995. They found that in crossing the ITCZ from south to north, anthropogenic gaseous and particulate matter increased by a factor of 4. They concluded that this was evidence of a direct transport of anthropogenic emissions over the Indian Ocean.

In spite of the above mentioned studies of the atmospheric chemistry over the Indian Ocean, no comprehensive data base exists for this region. This is due to the large spatial and seasonal variabilities observed in the movement of air masses over the Indian Ocean. Field studies are often limited by the geographical coverage, the length of sample collection, and the specific season in which sampling took place. The present study in conjunction with our previous observations, which were made in 1995 [*Johansen et al.*, 1999a; *Siefert et al.*, 1999], clarify some aspects of the large seasonal differences that exist in the chemistry of the atmosphere over the Arabian Sea.

Air masses in the present paper were collected during the tail end of the NE-monsoon, thus they are characterized by continentally derived aerosols of crustal and anthropogenic origin, which are mixed with marine aerosols. Marine aerosols are comprised of two components, the sea-salt component, which includes aerosols produced mechanically over the sea surface by breaking bubbles and whitecaps, and a biogenically-derived non-sea-salt sulfate ($NSS\text{-}SO_4^{2-}$) produced from the $OH^{\bullet}$ and $NO_3^{\bullet}$ radical oxidation of dimethyl sulfide (DMS) [*Berresheim et al.*, 1995; *Hynes et al.*, 1986;

Turnipseed and Ravishankara, 1993; *Yin et al.*, 1990]. The interaction of continental and marine aerosols leads to a complex system. In the present study, we were interested in a geochemical characterization of the collected mineral dust, in the relative contributions of anthropogenic and biogenic sources to NSS-SO_4^{2-} and in the sea-salt component of aerosol. In addition, since Fe is thought to be the limiting nutrient for phytoplankton growth in many regions of the open oceans [*Cooper et al.*, 1996; *Kolber et al.*, 1994; *Martin et al.*, 1994; *Martin and Fitzwater*, 1988; *Paerl et al.*, 1994; *Price et al.*, 1994], the speciation of Fe was investigated. Detailed reviews on iron speciation in the atmosphere of marine environments were provided by Johansen et al. [*Johansen et al.*, 1999b] and Siefert et al. [*Siefert et al.*, 1999]. To our knowledge, the observations of ferrous iron, presented by Siefert et al. [*Siefert et al.*, 1999] and in the present paper, are the first measurements of their kind for aerosol over the Arabian Sea.

Non-sea-salt sulfate (NSS-SO_4^{2-}) particles in the sub-micrometer size range, which may be of anthropogenic and biogenic origin, serve as cloud condensation nuclei (CCN) and influence the radiation balance of the atmosphere [*Charlson et al.*, 1987]. The sea-salt aerosol may also have an effect, although of indirect nature, on the radiation budget of the earth since sea-salt particles may act as seeds for the uptake and oxidation of sulfur gases and deposition of condensable sulfate vapors [*Keene et al.*, 1998; *McInnes et al.*, 1994]. Furthermore, sea-salt may also strongly influence the oxidative properties of aerosol particles in the marine boundary layer through the production of halogen radicals [*Fan and Jacob*, 1992; *Finlayson-Pitts et al.*, 1989; *Graedel and Keene*, 1995; *Keene et al.*, 1996; *Pszenny et al.*, 1993; *Sander and Crutzen*, 1996; *Vogt et al.*, 1996]. Reactive Cl can initiate photochemical reactions in an analogous manner to $OH^{\bullet}$ and have

major consequences for the oxidation of hydrocarbons and DMS [*Keene et al.*, 1996; *Keene et al.*, 1990; *Langer et al.*, 1996; *Pszenny et al.*, 1993; *Sander and Crutzen*, 1996; *Stickel et al.*, 1992; *Vogt et al.*, 1996]. Vogt et al. [*Vogt et al.*, 1996] found in their model calculations that about 40% of the SO_2 scavenged by the aerosol is oxidized by HOCl, increasing the amount of S(IV) oxidized in sea-salt aerosol by a factor of 0.4 to 0.8. This result implies that additional SO_2 oxidation on pre-existing particles will reduce the formation of new CCN and therefore the feedback between greenhouse warming, oceanic DMS emissions and increased cloud albedo.

5.3 Experimental

5.3.1 Sampling Location and Period

Atmospheric aerosol samples were collected over the Arabian Sea during the month of March of 1997. Sampling took place on board the German Research Vessel "Sonne," which sailed as part of the German Joint Global Ocean Flux Study (JGOFS) project. The cruise track, from Cochin/India to Muscat/Oman, is delineated in the plots in Figure 1.

March is normally considered to be in the tail end of the NE-monsoon season, which develops in November and persists throughout February with winds blowing from the northeast. The NE-monsoon is developed from upper westerly air masses which have streamed over Eurasia before splitting into two streams over the Indian subcontinent to produce a northerly surface flow over Pakistan, India and the Northern Indian Ocean [*Chester et al.*, 1991]. Thus, the air masses that reach the Arabian Sea from the northeasterly direction are expected to carry pollutant-rich material from distant European and closer Indian sources, as well as mineral dust from deserts on the Indian subcontinent.

Back trajectories of air masses during this cruise are presented in Figure 1. They indicate that the first part of the cruise was predominated by such northeasterly winds; however, later in the cruise wind patterns changed such that the typical air mass originated over the Saudi Arabian peninsula.

5.3.2 Aerosol Collection

Ambient aerosol samples were collected with two different collectors. A high volume dichotomous virtual impactor (HVDVI) was used for the collection of trace metals in two discrete size fractions ($D_{p,50}$ = 3.0 μm) [*Johansen et al.*, 1999a; *Johansen et al.*, 1999b; *Siefert et al.*, 1999]. The HVDVI collector was constructed with polycarbonate using nylon screws in order to minimize trace metal contamination. The total flow rate was determined to 335 ± 15 l min^{-1}. The fine and coarse sample fractions were collected on two 90 millimeter diameter Teflon filters (Gelman Zefluor, 1 μm pore size). Total elemental composition, Fe(II) concentrations, and anion and cation abundances were determined for both fine and coarse filter samples.

Two low volume collectors, which were operated at flow rates of 27 l min^{-1}, were used for collection of total aerosol mass. Inverted high density polyethylene bottles (2 L) served as rain shields for the Nucleopore polycarbonate 47 mm diameter filter holders which were loaded with acid-cleaned Gelman Zefluor filters (1 μm pore size).

The aerosol collectors and lab equipment were acid-cleaned before use by following similar procedures as outlined by Patterson and Settle [*Patterson and Settle*, 1976] employing ultra-pure acids from Seastar Chemicals (Sidney, B.C., Canada) and 18.2 MΩ-cm Milli-Q UV water. After Fe(II) analysis, the remainder of the filters were stored in acid-cleaned polystyrene petri dishes taped shut with Teflon tape, placed inside two plastic bags inside of a Tupperware container and stored in a refrigerator during the cruise. After the cruise, the filters were sent back to Caltech (via air-freight, on dry ice) and stored in a freezer until analysis.

A sector sampling system (by Campbell Scientific) controlled the operation of all collector pumps, thereby stopping collection of the aerosol collectors simultaneously when wind speed or wind direction were out of the defined sector. The data logger (Cr10, Campbell Scientific) was programmed to shut the pumps off when the wind speed was ≤ 0.2 m s^{-1} and when the relative wind direction was more than $\pm 60°$ off of the bow of the ship. In general, collected samples represent daily averages, but resulting from the ship's cruise track actual sampling duration had some variability. Exact sampling intervals for each sample are listed in Table 1.

The sampling characteristics of the HVDVI are such that approximately 10% of the fine particles end up on the coarse filter. This correction has been accounted for in all coarse concentrations reported in this study. As a result, errors associated with the coarse fraction, especially for species that are present in low concentrations in the coarse fraction (e.g., NSS-SO_4^{2-}, MSA, NH_4^+), may be considerably large. This needs to be kept in mind when computing ratios such as the bio-SO_4^{2-}/MSA ratio for the coarse fraction.

5.3.3 Chemical Analyses

5.3.3.1 Fe(II) Analysis Performed On-board the Ship

Labile Fe(II) in both particle fractions were determined by sequential extraction. These measurements were initiated immediately (within 1 hour) after sample collection in order to minimize the oxidation of Fe(II) to Fe(III). Extraction and quantification procedures are described in detail by Siefert et al. [*Siefert et al.*, 1999]. Three labile fractions of Fe(II) were determined in each size fraction. The first portion of Fe(II) was released into a 4.2 pH formate buffer after 30 minutes of leaching; this portion is denoted

as aqueous-Fe(II) ($Fe(II)_{aq}$). Thereafter, ferrozine was added to the leaching solution containing the filter and an absorption reading was made after 5 minutes. The additional Fe(II) released during this step is the 5-minute-ferrozine-Fe(II) ($Fe(II)_{FZ,5min}$). The last absorption reading was taken after the ferrozine was in contact with the aerosol for 22 hrs. Thus produced a third Fe(II) fraction: 22-hour-ferrozine-Fe(II) ($Fe(II)_{FZ,22hr}$). The total of all three Fe(II) fractions determined in the sequential fashion is defined as total-22-hour-Fe(II) ($Fe(II)_{total,22hourFZ}$). However, due to the possibility of a bias introduced through the reduction of Fe(III) by ferrozine after 22 hours, it appears more accurate to define a labile Fe(II) fraction that is composed of the first two extractable portions only, thus excluding the 22 hour reading. It is this amount of Fe(II), which is defined as the total-5-minFZ-Fe(II) ($Fe(II)_{total,5minFZ}$) that will be used preferentially when discussing the amount of Fe(II) leached out of the aerosol material. Sample IO97-27 was not analyzed for Fe(II) because the laboratory equipment on the ship was dismantled early.

5.3.3.2 Elemental Analysis

Elemental analysis of 32 elements (Na, Mg, Al, K, Ca, Sc, Ti, V, Cr, Mn, Fe, Ni, Cu, Zn, Ga, Ge, As, Se, Mo, Ru, Cd, Sn, Sb, Cs, Ba, La, Ce, Sm, Eu, Hf, Pb, and Th) was performed on the high volume filters with an HP 4500 ICP-MS (Inductively Coupled Mass Spectrometer). The filter digestion technique was presented by Siefert et al. [*Siefert et al.*, 1999].

5.3.3.3 Ion Analysis

For the ion analyses, a small section of the high volume filter was first wetted with approximately 0.1 ml ethanol then extracted overnight in 10 ml MQ water. Anions were separated and quantified with a Dionex Bio LC Ion Chromatograph (IC) using an IonPac AS11 separator column and the corresponding AG11 guard column. Organic and inorganic anions were eluted with a gradient pump and a combination of 4 eluents (5 mM NaOH, 100 mM NaOH, 100% MeOH, MQ H_2O) whereby the NaOH concentration was ramped from an initial 0.45 mM to a final 34.25 mM. The quantified anions included methanesulfonate (MSA), chloride, nitrate and sulfate. Fluoride, acetate, glycolate, formate, nitrite, bromide and oxalate were present at very low concentrations that were near the corresponding detection limits. Due to problems with the IC, 3 samples were not run correctly (fine IO97-08, fine IO97-18, and coarse IO97-19). The missing data is clearly indicated in the plots and the samples are removed from the data set when performing statistical analyses.

Cations were separated and quantified isocratically with a DX 500 Ion Chromatograph (IC) with IonPac CS12/CG12 analytical and guard columns and a 20 mM MSA eluent. Sodium, ammonium, potassium, magnesium, and calcium concentrations were determined.

5.3.4 Statistical Analyses

Plotted error bars represent the standard deviation calculated through propagation of error in every parameter used. Estimated errors in the volume of air sampled, the filter section cut, the volume of the extraction solution, etc., were assumed to be 10%.

Average concentrations reported throughout this study are accompanied by the standard deviation of the sample population.

In addition to interpreting the data based on an element's enrichment compared to a crustal tracer (enrichment factor = EF = $(E/Al)_{obs}/(E/Al)_{crust}$) [*Taylor and McLennan*, 1985], a multivariate statistical analysis was performed using SPSS software. This PC analysis was performed on the whole data set, to learn about the source characteristics that make up the sampled aerosol material and to learn about possible correlations between certain chemical species. In a PC analysis, the correlation matrix of the observed variables is examined to reduce the number of descriptive variables by linearly combining the observed ones into a smaller set of independent variables, the PCs. The PCs are orthogonal to each other and can be rotated in space to simplify interpretation of the data set. A common type of rotation is the Varimax rotation, during which orthogonality is retained. All PCs in the present study are Varimax rotated.

A PC in this study represents a source, such as crustal material, sea-salt, anthropogenic pollutants, etc. An observed variable will display a number close to 1 if it correlates with the PC, thus two variables with numbers close to 1 in one component correlate with each other. For example, the crustal component will exhibit values close to 1 for Al and other crustal elements, while the sea-salt component will exhibit values close to 1 for variables that are characteristic for sea-salt, such as Na^+, Cl^-, and wind speed.

5.4 Results and Discussion

5.4.1 Air Mass Origins and Characteristics

Air mass back trajectories presented in Figure 1 are representative of the different atmospheric conditions encountered throughout the cruise. The beginning of the cruise was characterized by air masses that originate from the Indian subcontinent. The different air circulation patterns observed during this period are depicted in Figures 1a, 1b, and 1c, which are representative of the group of samples from IO97-01 to IO97-10. Trajectories in sample IO97-11 (not shown) appear to be transitional between the first and the second group of samples, latter of which includes samples IO97-12 through IO97-15. The distinguishing trajectory pattern observed during this second group of samples is presented in Figure 1d for sample IO97-12. These air masses were swept around in a clockwise manner from the Saudi Arabian peninsula. As a result, these air masses most likely transported mineral dust from the arid regions of that area and arrived in the middle of the Arabian Sea from a northeasterly direction. Although the wind direction observed on board the ship (see Figure 2b) is indicative of winds carrying aerosol from Pakistan, India and regions south of India, the actual air mass origin lies to the northwest; offset by as much as 180°. These air mass origins are similar to those encountered during the inter-monsoon of 1995 [*Johansen et al.*, 1999a; *Siefert et al.*, 1999].

Samples IO97-16 through IO97-18 and to a lesser degree IO97-19 display trajectories which are confined to a small area, indicating lower wind speeds and thus older continental air masses from which particles may have had sufficient time for depositional removal. As a consequence, low atmospheric concentrations of continental

species, especially in the coarse aerosol size fraction, are expected. Sample IO97-18, plotted in Figure 1e, is representative of air mass trajectories observed in this group of samples. The actual air mass origin is difficult to ascertain from this data. However, the mineralogical differences (vide infra) will shed light on the aerosol source region for the third group of samples.

Sample IO97-20 is the product of a unique circulation pattern, which has the form of large annular trajectories (Figure 1f). Wind speeds and air temperatures are at a maximum during this sample, see Figures 2a and 3, respectively. The origins of air masses for this and the rest of the samples, of which representative trajectories are presented in Figures 1g and 1h, are from the same general area, the Saudi Arabian peninsula and possibly northeastern Africa.

In summary, air mass back trajectories indicate that the collected samples could be classified into four major groups, in addition to one unique sample represented by IO97-20. The first group, up to and including sample IO97-10, is representative of a normal NE-monsoon period in which the air masses are advected over the Indian subcontinent and subsequently swept over the Arabian Sea. The remaining samples (samples IO97-11 through IO97-27) appear to be typical of the period encountered between the two major wind circulation patterns observed over the Indian Ocean (i.e., the NE- and the SW-monsoons). This intermediate period, which is known as the inter-monsoon, is characterized by air masses that originate mainly from the Saudi Arabian peninsula and may have been advected over the Thar desert of northwest India. These air masses vary considerably in their relative transport speeds. Samples IO97-11 through IO97-15 and IO97-20 through IO97-26 are representative of air masses that have traveled

from the Saudi Arabian peninsula over considerable distances in a relatively short period of time and are, therefore, expected to carry relatively more crustal material compared to air masses sampled in samples IO97-16 through IO97-19 and sample IO97-27, during which wind speeds were lower.

5.4.2 Trace Metals

Of the 33 elements detected by ICP-MS, the concentrations for elements As, Ru, Cd, Cs, and Sb were found to be below their detection limits and are, therefore, excluded from further discussion. Furthermore, principal component (PC) and enrichment factor (EF) analyses [*Johansen et al.*, 1999b; *Siefert et al.*, 1999] have shown high background concentrations for Cr, Ni, Cu, Mo, and Sn that seem to be attributable to artifacts introduced by the filter material and/or the acids used for the elemental extraction.

Average values with standard deviations, minima and maxima for the remaining 22 elements in the coarse, fine and total fractions are listed in Table 2. In order to examine the similarities among these elements, a PC analysis was performed on both the coarse and fine fractions, and the results are presented in Table 3. The first six components carry eigenvalues larger than 1 and account for a cumulative variance of 91.3% of the data set. The first component, which is representative of a coarse crustal source, has relatively "large" (i.e., values close to 1) values for typical crustal material tracers, such as Al, Sc, Ti, Ba, La, Ce, Sm, Eu, and Th. These elements are rarely enriched over what is predicted given the assumption that mineral dust is their only source. Therefore, they can be used reliably as indicators of crustal material.

Enrichment factors for the elements in the present samples are presented in Tables 4, 5 and 6, for the coarse, fine and total size fractions, respectively. Calculations are based on average crustal abundances by Taylor and McLennan [*Taylor and McLennan*, 1985]. The relatively constant EFs observed for the above mentioned crustal tracers confirm that they correlate strongly with Al. However, the fact that the EFs are smaller (e.g., for Sc) or larger (e.g., Ba, La, Ce, etc.) than 1 may be an indication that the average crustal abundance by Taylor and McLennan is not a perfect representation of the mineral aerosols collected during this cruise. As long as the EFs are constant throughout the samples, one can assume that the corresponding element is derived from a crustal source. During the inter-monsoon of 1995, Siefert et al. [*Siefert et al.*, 1999] reported EF factors for Ti, Ba, La and Ce that were similar to those observed during the NE-monsoon. Some of the elements in Tables 4, 5 and 6 (V, Mn and Ga) display crustal characteristics only in the coarse fraction (Table 4). Thus, they correlate well with the coarse crustal source, which is denoted as PC 1 in Table 3. Since the fine fraction is usually associated with gas-to-particle reactions of anthropogenic pollutants from combustion sources, the aforementioned crustal signature in the fine fraction (Table 5) could be completely masked by a possible anthropogenic contribution.

The second component in the PC analysis reflects a fine crustal source, in which fine fractions of Sc, Ti, Ga, Ba, La, Ce, Sm, Eu and Th correlate with fine Al. The same elements show constant EFs in Table 5 throughout the cruise. As a consequence, Al can be used as a tracer for both the first and second PCs. The Al concentrations are plotted as a function of sample ID (i.e., and indirect measure of time) in Figure 4a.

A series of elements in the coarse fraction (PC 1) that were clearly derived from crustal sources do not appear as crustal tracers in the fine fraction. A likely explanation for this observation is that the crustal signature of trace metals in the fine fraction can be diluted by anthropogenic sources derived from the combustion of fossil fuels. This seems to be the case for V, which exists in heavy fuel oils typically used on ships, as well as for Ge and Se, which correlate with the third PC, and for Fe and Mn, which appear in component 5. Ge and Se in the fine fraction closely follow the concentrations of Pb and Zn in both size fractions, which are reflected in component 3. Since Pb and Zn are anthropogenic tracers, Ge and Se also appear to be anthropogenically-derived. Large EFs (see Tables 4, 5 and 6) are observed for these four elements. Se displays the largest EFs, which average 379 and 2706 in the coarse and fine fractions, respectively. Since contamination from the filter material is not obvious, there is a possibility that the Se concentration in the average continental crust as cited by Taylor and McLennan [*Taylor and McLennan*, 1985] may be low.

Another element in the fine fraction that correlates with the anthropogenic PC (i.e., PC 3) is K, which may be a product of biomass burning including the products of waste incinerators [*Andreae*, 1983; *Echalar et al.*, 1995; *Fishman et al.*, 1999]. Figure 4b presents the coarse and fine Pb concentrations in stacked bars as a function of sample ID. The plots for Pb, Zn and K are all similar, and as expected for anthropogenic tracers, their concentrations are larger in the fine fraction as compared to the coarse fraction. The geometric mean for the relative abundance of Pb in the fine fraction is 89 ± 3%, while for Zn is 80 ± 8% and for K is 67 ± 16%. The largest concentrations of the anthropogenic

tracers are observed during the initial group of samples (i.e., IO97-01 through IO97-10), for which the air masses originated over the densely populated Indian subcontinent.

The fourth principal component is representative of the sea-salt. It is curious to note that Hf in the fine fraction correlates weakly with the sea-salt. Even though Na is used as the primary sea-salt tracer, the concentrations of Na, as plotted in Figure 4c, include a crustal source. With the exception of samples IO97-12 and IO97-13, which carry high concentrations of crustal material (see peaks in Figure 4a), the crustal Na is relatively small compared to its sea-salt contribution. Therefore, Na in the PC analysis does not correlate strongly with PCs 1 and 2. Upon visual inspection of the Na and wind speed plots of Figures 4c and 2a, respectively, a weak correlation is apparent. This is a result of the increased wave action on the water surface, which leads to sea-salt aerosol formation.

As mentioned above, Fe and Mn in the fine fraction correlate with each other in PC 5. Corresponding EFs given in Table 5 are not markedly elevated, which indicates that these elements are only slightly enriched. Source of fine Fe and Mn may be local incinerators or even our research vessel's smoke stack. The same elements were observed to be enriched during a previous cruise [*Siefert et al.*, 1999], which also took place over the Arabian Sea but during the inter-monsoon of 1995 [*Siefert et al.*, 1999] and on a very similar ship (the German R/V Meteor). Since both these vessels used Diesel fuel and electric power generators to propel the ship, V was not expected to be seen in the ship's plume [*Hopke*, 1985]. However, Fe and Mn during the Meteor cruise were enriched in collected samples when the sampling sector system was malfunctioning. Thus, there is a slight chance that, although the sector sampling system was working well

during the whole present cruise, minute amounts of the ship's plume may have reached the sampling setup during the ship's maneuvers. Fe concentrations are plotted in Figure 4d.

In Table 3 we see that PC 6 has large values for Ca in both fractions. The EF analysis shows that Ca is slightly enriched for most of the samples in both size fractions, but that the enrichment is especially pronounced in the coarse fraction and for sample IO97-11 and samples IO97-20 through IO97-27. Visual comparison of the Al and Ca plots, in Figures 4a and 4e, reaffirms that those samples contain another Ca component in addition to the crustal source represented by Al. As mentioned above, these samples are characterized by air masses that have been transported relatively quickly from their origin over the Saudi Arabian peninsula and northern Africa to the Arabian Sea and, therefore, can be expected to contain relatively more coarse crustal material that has not had a chance to settle out.

A slightly different PC analysis is computed in which some of the redundant trace metals are omitted and Fe(II), anions and cations are added to the matrix. The output of this analysis is presented in Table 7. Four of the typical crustal tracers (Al, Sc, La, and Sm) and four of the anthropogenic tracers (Zn, Ge, Se, and Pb) are retained in addition to V, Mn, Fe, the alkali and alkaline earth elements. In this case four samples (IO97-08, IO97-18, IO97-19, and IO97-27) were excluded because of miscellaneous data gaps in the anions and Fe(II) concentrations (vide supra).

The resulting PCs are not identically distributed compared to what was found in the first analysis (Table 3). A crustal coarse and fine source appears to be combined in PC 1, with the coarse fraction correlating stronger with this component than the fine

fraction. Two other components appear to correlate with fine crustal material, represented by PCs 3 and 5. This is indicative from the correlation of the typical crustal tracers (Al, Sc, La and Sm) in those components. In addition, fine Mg and Ca in both size fractions, as well as the corresponding water-soluble (Mg^{2+}-fine, Ca^{2+}-fine and -coarse) portions, correlate strongly with PC 3, which is one of the fine crustal components. Minor correlations with NSS-SO_4^{2-} and with the discrepancy between cationic and anionic charges seem to indicate that this water-soluble Ca may be associated with gypsum ($CaSO_4$) and calcite ($CaCO_3$).

The other fine crustal component, PC 5, correlates with fine Na and fine Mg, but not with their respective water-soluble portions. Therefore, the possibility of PC 5 being of sea-salt nature can be ruled out. This crustal source does not contain significant amounts of Ca and, therefore, is considerably different from the fine crustal source identified in PC 3. It may, however, be related to the first crustal component (PC 1), whereby the origins are the same, but due to the differential transport characteristics of coarse and fine particles may exhibit varying concentrations in each sample.

The factor scores of all three crustal PCs are plotted together in Figure 5a. Factor scores give a measure of the relative importance of a specific source across the samples. The plot of Figure 5a illustrates that each of the three crustal sources prevails at different times. The first component is predominant during the samples IO97-02 through IO97-05 and again in samples IO97-12 and IO97-13, coinciding with the large coarse Al concentrations observed in Figure 4a for the same samples. The third PC (also the second crustal source) is relatively important in samples IO97-02 through IO97-05, IO97-15, IO97-16, IO97-20, IO97-23 and IO97-24. According to the back trajectories

presented in Figure 1, this Ca and Mg rich source suggests that its geographical origins lie further west than the Thar and the Saudi Arabian peninsula. The apparently distinct chemical signatures between the two crustal components may also be a function of aerosol particle size and the different chemical transformations occurring during transport.

The third crustal component (PC 5) peaks in samples IO97-10, IO97-14 and IO97-20. No distinctly different geographical origin from the other two crustal components can be identified based on the air mass back trajectories. Again, the different chemical characteristics may be due particle size and associated different deposition velocities and chemical reactions that may have taken place during transport.

The second PC in Table 7 is clearly of anthropogenic nature: high in fine K, fine Ge, fine Se, total Zn, total Pb, NSS-water-soluble K^+, NH_4^+, NO_3^--coarse, and NSS-SO_4^{2-} -fine, which are all typical anthropogenic tracers. The factor scores for this anthropogenic component are presented in solid in Figure 5b. This component is also predominant during the first ten samples of the cruise when the air masses originated over the Indian subcontinent.

PC 4 represents the typical sea-salt source, exhibiting high correlation between Na, water-soluble Na^+, and Cl^- concentrations as well as correlating slightly with the wind speed. PC 6 is high in MSA and NSS-SO_4^{2-} in the coarse fractions.

The alkali and alkaline earth elements are plotted in the stacked bars of Figure 6. These plots are useful when evaluating the usage of the average continental crust for the representation of the crustal material sampled. Aluminum serves as the crustal tracer for the calculation of the crustal contributions in the coarse and fine fractions for each of the

four elements presented, which are plotted in red and orange. After determining the crustal contribution of Na, the remaining Na is assumed to be sea-salt derived. This sea-salt Na is then further applied to determine sea-salt concentrations of K, Mg, and Ca, plotted in light and dark blue. The remaining K, Mg and Ca concentrations are represented in green and denoted "other," since the sources are not known. Large negative values for the remainder (i.e., "other concentration") indicate that the assumed crustal composition is not an appropriate proxy for the actual sampled crustal material. This is not the case in the present samples, but it was in the samples collected over the Atlantic Ocean [*Johansen et al.*, 1999b], where large discrepancies were observed for K, Mg and Ca. For the Atlantic Ocean aerosol, shale appeared to best represent the African mineral dust component. In the present case, as in the inter-monsoon samples collected in 1995 [*Johansen et al.*, 1999a], the crustal average according to Taylor and McLennan [*Taylor and McLennan*, 1985] appears to adequately represent the sampled mineral dust; however, an additional crustal Ca source seems present in all the samples. Clays seem to play a major role in the geochemical composition of the mineral aerosol. Clays contain significant amounts of Fe, alkali and alkaline earth elements. A clay mineralogical study of the aerosol material over the Arabian Sea [*Chester et al.*, 1985] revealed that illite is the dominant clay mineral. Illite was also observed to the predominant clay mineral in most sediments from the northern Arabian Sea [*Goldberg and Griffin*, 1970].

Based on the crustal average and the observed Al concentrations, the mineral dust concentrations that we observed average 5.94 ± 3.08 μg m^{-3}. If we assume that the additional Ca, which is not accounted for by sea-salt or the crustal average, is present in the form of $CaCO_3$, it would amount to an additional 0.77 ± 0.36 μg m^{-3}. During the

inter-monsoon of 1995, Johansen et al. [*Johansen et al.*, 1999a] observed a very similar crustal average of 5.85 ± 4.24 μg m^{-3}, while during the SW-monsoon concentrations were considerably lower, 0.66 ± 0.43 μg m^{-3}. Rhoads et al. [*Rhoads et al.*, 1997] found very similar values of 6.2 ± 4.4 μg m^{-3} during the months of March and April of 1995. Chester et al. [*Chester et al.*, 1991] reported mineral dust concentrations decreasing from 15-20 μg m^{-3} in the north to 0.01-0.25 μg m^{-3} below 35 °S in the far southern ocean. Pease et al. [*Pease et al.*, 1998] obtained mineral dust concentrations of 40 μg m^{-3} during the NE-monsoon of 1995. However, observations of Pease et al. [*Pease et al.*, 1998] are in strong contrast to the observations of Savoie et al. [*Savoie et al.*, 1987] during the NE-monsoon of 1979, when the average measured dust concentrations were only 1.01 ± 0.81 μg m^{-3}.

5.4.3 Fe and Fe(II)

The PC analyses show that coarse Fe seems to be of crustal origin, while most of the fine Fe correlates with fine Mn, which are enriched over the crustal component and for which the source is not obvious. Two ferrous iron extraction fractions are included in the PC analysis in Table 7. The summed up fractions of coarse and fine Fe(II) after 22 hours of extraction with ferrozine appear to be dependent on the crustal abundance of Fe, deduced from the correlation with the corresponding coarse and fine crustal components, PC 1 and PC 3, respectively. In addition, some of the coarse $Fe(II)_{total,22hrsFZ}$ correlates with the anthropogenic component.

The combined ferrous iron released from the coarse fraction after 5 min in ferrozine is also strongly dependent on the coarse crustal component (PC 1). In addition,

it also appears to correlate with the fine crustal component, PC 5. The corresponding fine Fe(II) fraction exhibits a more complex behavior. It correlates weakly with the first two components and more strongly with the ninth component. PC 9 is also characterized by V in the fine fraction, which comes from the heavy fuels used in ships.

The three extracted Fe(II) portions for both coarse and fine fractions are presented in stacked bar plots in Figures 7a and 7b, respectively. Superimposed, in the dashed lines, are the corresponding Fe concentrations determined by ICP-MS. Visual inspection reconfirms a weak correlation between the coarse-$Fe(II)_{aq}$ and coarse-$Fe(II)_{total,5minFZ}$ fractions on the one hand and the total coarse-Fe on the other. No such dependence can be observed for the fine fraction. Thus, the complexity of the observed fine Fe(II) concentrations indicates that several factors must play important roles in the speciation of Fe in the atmosphere. Coarse- and fine-$Fe(II)_{total,5minFZ}$ are plotted in Figure 7c in the stacked bars together with the total Fe concentration.

Figure 7c shows that most (87.2 ± 6.1%) of the $Fe(II)_{total,5minFZ}$, which averages 9.76 ± 3.37 ng m^{-3}, is present in the fine fraction. Compared to the total Fe as determined by ICP-MS, the combined coarse and fine $Fe(II)_{total,5minFZ}$ account for only 1.3 ± 0.5% (geometric mean), ranging from 0.7 to 2.9%. This relative abundance is plotted in the solid line in Figure 8. The average coarse-$Fe(II)_{total,5minFZ}$ concentration of 1.16 ± 0.55 ng m^{-3} amounts to 0.3 ± 0.1% (geometric mean) of the coarse Fe, whereby the fine-$Fe(II)_{total,5minFZ}$ concentration of 8.60 ± 3.29 ng m^{-3} amounts to 2.4 ± 1.2% (geometric mean) of the fine Fe. Note that total Fe is almost evenly distributed between the fine (52.8%) and the coarse (47.2%) fractions.

Compared to previous observations reported by our group, the present samples show relative Fe(II) abundances that are slightly larger. During the inter-monsoon of 1995 [*Siefert et al.*, 1999] an average of 0.3% of the total Fe was observed as Fe(II), whereby the actual combined coarse and fine $Fe(II)_{total,5minFZ}$ amounted to 5.2 ± 4.4 ng m^{-3}. During the Atlantic Ocean cruise [*Johansen et al.*, 1999b], the measured $Fe(II)_{total,5minFZ}$ concentrations averaged 3.14 ± 1.35 ng m^{-3}, which accounted for 0.5 ± 0.4% of the total Fe. Thus, the $Fe(II)_{total,5minFZ}$ concentrations reported here are larger by a factor of 2 to 3 compared to those that we previously observed.

Few studies exist on Fe(II) concentrations measured over remote oceanic regions. Zhu et al. [*Zhu et al.*, 1993; *Zhu et al.*, 1997] reported similar concentrations as those found in the present study, while Zhuang et al. [*Zhuang et al.*, 1992] measured relative Fe(II) values that were considerably larger (15%, corrected value, see [*Zhu et al.*, 1993]) in Barbados. However, these large discrepancies may be a result of different sample handling and experimental procedures used.

Of special interest is the distinctly different behavior observed for the two size fractions with regard to the relative Fe(II) released in each extraction step. This data is visualized in Figures 9a and 9b for both size fractions, respectively. While only 22% of the total Fe(II) is released from the coarse aerosol filter after 5 minutes of exposure to ferrozine, more than 65% of the corresponding fine Fe(II) is released. This result may be a function of the surface area of the particles, the mineralogical composition of the phases present, and/or the presence of species which may reduce Fe(III) to Fe(II) over the course of the 22 hour extraction experiment.

5.4.4 Anions

The average, minimum and maximum concentrations of the detected anions in coarse and fine fractions are listed in Table 8. The non-sea-salt (NSS) concentrations of Cl^- and SO_4^{2-} are computed from the known and constant weight ratios of Cl^-/Na^+ and Na^+/SO_4^{2-} in sea-water (1.795 and 0.252, respectively [*Millero and Sohn*, 1992]) assuming that Na^+ is a conservative sea-salt tracer.

Of the 54 coarse and fine collected samples, 3 of the samples were not analyzed (vide supra). In the subsequent plots, these 3 samples are marked with crosses. Average values do not include these samples.

5.4.4.1 NSS-SO_4^{2-} and MSA

Average total NSS-SO_4^{2-} concentrations observed during the present cruise amount to 2.94 ± 1.06 μg m^{-3} and range from 1.42 to 5.38 μg m^{-3}, corresponding to 92.7 ± 3.4%. These values are in excellent agreement with those determined by Pease et al. [*Pease et al.*, 1998] (2.68 ± 0.95 μg m^{-3}) during the months of March and April of 1995 over the Arabian Sea. Compared to the average value for January to June of 1979 [*Savoie et al.*, 1987] (1.14 ± 0.75 μg m^{-3}), the present results are larger by more than a factor of 2. Total NSS-SO_4^{2-} concentrations reported by Johansen et al. [*Johansen et al.*, 1999a] during the month of May 1995, which was characterized by air masses passing over the Saudi Arabian peninsula, were slightly lower (2.08 ± 1.21 μg m^{-3}) than those reported here. However, if the samples that originated over the Indian subcontinent are excluded from the present data set, the average drops to 2.32 ± 0.70 μg m^{-3}. During the SW-monsoon [*Johansen et al.*, 1999a], average total NSS-SO_4^{2-} concentrations amounted

to only 0.80 ± 0.18 μg m^{-3}, of which only 25% could be attributed to anthropogenic sources while the rest was biogenically-derived. These results reflect the impact of air masses moving over the clean open ocean during the SW-monsoon.

NSS- and SS-SO_4^{2-} concentrations in both coarse and fine fractions are presented in stacked bars in Figure 10. Only 6.6 ± 3.4% (geometric mean) of the total SO_4^{2-} is attributed to sea-salt. From this plot, we see that most of the NSS-SO_4^{2-}, 92.1 ± 4.5% (geometric mean), is present in the fine fraction. This result is expected since both the anthropogenically- and biogenically-derived SO_4^{2-} is normally associated with submicrometer sized particles. Furthermore, since the particle size cutoff of the sampler is around 3 μm, the fine fraction should include a considerable amount of sea-salt particles. These particles may mediate the uptake and oxidation of sulfur gases and deposition of condensable sulfate vapors [*Keene et al.*, 1998; *McInnes et al.*, 1994].

Methanesulfonic acid (CH_3SO_3H, MSA) is an oxidation product [*Hynes et al.*, 1986; *Yin et al.*, 1986] of dimethyl sulfide (CH_3SCH_3, DMS), which is the primary organosulfur compound emitted to the atmosphere [*Bates et al.*, 1992]. Another oxidation product from the initial reaction of DMS with hydroxy radical ($OH^•$) and nitrate radical ($NO_3^•$) is SO_4^{2-}, which is denoted as bio-SO_4^{2-}. Hynes et al. [*Hynes et al.*, 1986] suggested that temperature determines the relative contributions of the OH-addition and H-abstraction pathways of the initial oxidation step of DMS with $OH^•$, thus fixing the bio-SO_4^{2-}/MSA ratio at a given temperature. MSA is easily sampled using filters since it partitions readily into the particle phase due to its low vapor pressure. As a consequence, MSA has been considered a quasi-conservative tracer for the marine biogenic NSS-SO_4^{2-} component. Thus, a simple relationship has been sought between the NSS-SO_4^{2-}-derived

from DMS and MSA (i.e., bio-SO_4^{2-}). Such a relationship would prove to be useful for estimating the biogenic yield of SO_4^{2-} important to the DMS-cloud-climate relationship [*Andreae et al.*, 1995; *Berresheim et al.*, 1993; *Charlson et al.*, 1987].

Average total MSA concentrations amount to 25.4 ± 6.8 ng m^{-3} and range from 12.7 to 45.0 ng m^{-3}. This value is very close to what we observed over the Arabian Sea during the inter-monsoon of 1995 [*Johansen et al.*, 1999a]. MSA in the coarse and fine fractions is plotted in Figure 11, as a function of sample ID. When comparing it with the plot for SO_4^{2-} in Figure 10, no clear correlation is seen. This is expected, since a large portion of the NSS-SO_4^{2-} is probably anthropogenic in nature. Furthermore, crustal derived gypsum can add NSS-SO_4^{2-}. This may be likely due to the large Ca enrichments measured and would be in accordance with what we observed during the inter-monsoon of 1995 [*Johansen et al.*, 1999a]. The fine fraction accounts for 91.9 ± 4% (geometric mean) of the total MSA. This trend has been observed by a series of investigators [*Johansen et al.*, 1999b; *Kerminen et al.*, 1997; *O'Dowd et al.*, 1997; *Pszenny*, 1992; *Qian and Ishizaka*, 1993; *Quinn et al.*, 1993] and is presumably a function of the surface area of the sea-salt aerosol.

The results of the PC analysis in Table 7 show that NSS-SO_4^{2-} in the fine fraction correlates strongly and exclusively with the anthropogenic component (PC 2). Compared to the anthropogenic SO_4^{2-}, the biogenically-derived SO_4^{2-} signal appears to be negligible. The coarse NSS-SO_4^{2-}, however, correlates with the coarse MSA in component 6 of Table 7. Furthermore, the coarse NSS-SO_4^{2-} correlates very slightly with the crustal components, PC 1 and PC 3, possibly indicating a contribution due to gypsum. The fine NSS-SO_4^{2-}, on the other hand, does not display such behavior.

It is of special interest to try to separate out the different contributions to NSS-SO_4^{2-} in order to get a better estimate of the biogenically-derived component. Based on observations from remote parts of the open ocean, where anthropogenic and crustal contributions are negligible [*Bürgermeister and Georgii*, 1991; *Gao et al.*, 1996; *Johansen et al.*, 1999a; *Saltzman et al.*, 1985; *Saltzman et al.*, 1983; *Savoie and Prospero*, 1989; *Savoie and Prospero*, 1994], a value close to 14 or 15 is expected. An attempt was made by Johansen et al. [*Johansen et al.*, 1999a] to find a temperature dependence for this ratio, based on data collected during the inter- and SW-monsoons of 1995 and data extracted from literature that were considered free of continental SO_4^{2-} contributions. See Figure 5 of Chapter 3. Given a mean temperature of 25.3 °C observed during the present cruise (Figure 3), a bio-SO_4^{2-}/MSA weight ratio of 9 to 10 is predicted.

The same approach as described in Chapter 3 for determining the bio-SO_4^{2-}/MSA ratio is applied here. Weighted multiple linear regression analyses were performed on the coarse and fine data sets separately. Each source of SO_4^{2-} needs to be represented by a specific tracer or independent variable. The ratio between a tracer and the corresponding SO_4^{2-} contribution is expected to be constant for all the samples. Thus, if all the SO_4^{2-} sources were correctly identified in the regression analysis, a reliable bio-SO_4^{2-}/MSA weight ratio should be obtained.

Possible tracers for each potential source can be identified from the PC analysis given in Table 7. A suitable tracer for the fine anthropogenic SO_4^{2-} (anthr-SO_4^{2-}) component could be any of the species in PC 2 that display large values, such as fine Zn, fine Ge, fine Pb, fine K^+, and fine NH_4^+. However, by way of trial and error and careful interpretation of the statistical output associated with each regression analysis, fine NH_4^+

turns out to be the best surrogate for fine anthr-SO_4^{2-}. For the coarse anthr-SO_4^{2-}, coarse NO_3^- appeared to be the best tracer. In order to check the validity of the linear regression other than by looking at the analysis of variance (ANOVA) output, the sea-salt component is initially included. A SS-SO_4^{2-}/Na^+ weight ratio extracted by the regression analysis that is close to the ratio seen in sea water (0.252) is an indication that the regression is self-consistent. The biogenic SO_4^{2-} portion is represented by MSA, and the potential crustal SO_4^{2-} contribution, in the form of gypsum, is traced by NSS-Ca^{2+}.

The outputs of a series of such a linear regression analyses for coarse SO_4^{2-} are presented in Table 9. The first model includes all the mentioned sources of SO_4^{2-}: sea-salt, biogenic, crustal, and anthropogenic, as well as a constant. The ratios of interest are unstandardized coefficients and appear as such in Table 9. From the value for the SS-SO_4^{2-}/Na^+ ratio, 0.248, and the small intercept (constant), it can be assumed that the model does an excellent job of representing the system. However, R^2 for the regression (0.596) is not satisfactory. Judging by the large value for the significance of the null-hypothesis (in the third to last column) for the y-intercept and NSS-Ca^{2+}, 63% and 44%, respectively, these two variables may not contribute to the regression. Thus, Model 2 was run without NSS-Ca^{2+}. Although the R^2 does not improve, the SS-SO_4^{2-}/Na^+ ratio becomes even more favorable than before. Upon omitting the constant from the regression analysis, in Model 3, R^2 improves substantially (0.966) and the significance for the null-hypothesis for the remaining dependent variables becomes very small. The SS-SO_4^{2-}/Na^+ ratio is slightly elevated, but since the bio-SO_4^{2-}/MSA ratios between this and Model 2 are relatively close, we assume that Model 3 represents a satisfactory fit.

The new bio-SO_4^{2-}/MSA weight ratio for the coarse fraction is 52.8, which is approximately a factor of 2 lower compared to the NSS-SO_4^{2-}/MSA ratio obtained without correction for other non-biogenic SO_4^{2-} inputs. If this model is, in fact, representative of the sulfur chemistry in the coarse aerosol particle size fraction, the NSS-Ca^{2+} measured does not seem to be attributable to gypsum, but rather to $CaCO_3$ (calcite) or maybe a mixture of the two. The magnitudes of the standardized coefficients in Table 9 give a measure of the relative contribution of each of the components. Thus, about 40% of the coarse SO_4^{2-} is sea-salt derived, 31% is of biogenic and 29% of anthropogenic nature. This implies that the coarse NSS-SO_4^{2-} is almost evenly made up of bio-SO_4^{2-} and anthr-SO_4^{2-}.

As mentioned in the statistical analysis section, the errors associated with the coarse MSA and coarse NSS-SO_4^{2-} concentrations are large as consequences of the low concentrations encountered in the coarse fraction and the subtraction of the 10% fine particle contribution. The errors are typically several times larger than the value itself. Thus, the ratio of two numbers determined with such imprecision can be regarded as an outlier.

In the fine fraction, as mentioned above, NH_4^+ appears to be the best surrogate for anthr-SO_4^{2-}. Two model runs are presented in Table 10. All potential SO_4^{2-} sources are included in the first model. The resulting SS-SO_4^{2-}/Na^+ ratio is inconsistent with the value for sea-salt and the significance of the null-hypothesis for Na^+ is 88%. It seems, therefore, that sea-salt does not contribute significantly to the fine fraction SO_4^{2-} (only 2.9% when calculating the SS-SO_4^{2-} in fine SO_4^{2-}). Model 2, which is run without the sea-salt contribution, still shows a large y-intercept. This is an indication that there may

be an additional source that has not been accounted for. Nevertheless, Model 2 represents the best fit that we encountered through trial and error with a number of different independent variables.

Based on the standardized coefficients in Model 2, 6% of the fine SO_4^{2-} (SO_4^{2-} here equals NSS-SO_4^{2-}, since the SS contributions was removed) is biogenically-derived and 84% is anthropogenically-derived. The bio-SO_4^{2-}/MSA weight ratio for the fine fraction is 9.8. This value is consistent with the temperature dependence plotted in Figure 5 of Johansen et al. [*Johansen et al.*, 1999a], given that the average temperature observed during this cruise was 25.3 °C. 10% of the SO_4^{2-} appear to be attributed to gypsum. According to some investigators [*Glaccum and Prospero*, 1980], gypsum is produced secondarily on the filter during sampling from the reaction of calcite with the abundantly available NSS-SO_4^{2-} in the fine fraction. Therefore, it is inconclusive whether the NSS-Ca^{2+} is derived from primary gypsum or calcite, or both.

5.4.4.2 NO_3^-

Total NO_3^- averages 0.93 ± 0.27 μg m^{-3} and ranges from 0.45 to 1.56 μg m^{-3}. Savoie et al. [*Savoie et al.*, 1987] reported NO_3^- aerosol concentrations over the Arabian Sea that are smaller by a factor of 2 (0.43 ± 0.34 μg m^{-3}) compared to those observed herein. However, their values for NSS-SO_4^{2-} and mineral aerosol were also small compared to our observations and those reported by other investigators. Naik et al. [*Naik et al.*, 1991] measured ~2.5 μg m^{-3} of NO_3^- during the month of May of 1983, while we [*Johansen et al.*, 1999a] detected 1.23 ± 0.41 μg m^{-3} during May of 1995. Nitrate concentrations dropped to 0.46 ± 0.12 μg m^{-3} during the SW-monsoon [*Johansen et al.*,

1999a]. Rhoads et al. [*Rhoads et al.*, 1997] found NO_3^- concentrations of 2.68 ± 0.95 μg m^{-3} during the months of March and April of 1995.

The NO_3^- concentrations in coarse and fine fractions are plotted in Figure 12 as a function of sample ID. In contrast to other anthropogenically-derived species, such as anthr-SO_4^{2-} and NH_4^+, NO_3^- is found more abundant (82.1 ± 11.4%) in the coarse fraction. This observation is in agreement with those made by other investigators [*Berresheim et al.*, 1991; *Huebert et al.*, 1996; *Johansen et al.*, 1999b; *Naik et al.*, 1991; *Savoie and Prospero*, 1982; *Sievering et al.*, 1990]. The reason is that in temperate regions and in the presence of H_2SO_4 [*Bassett and Seinfeld*, 1984; *Sisterson*, 1989], HNO_3 evaporates from small particles and is subsequently deposited on large particles, which may be marine- or soil-derived.

In the PC analysis presented in Table 7, NO_3^- in the coarse fraction correlates with the anthropogenic component, PC 2, as expected, while the fine fraction NO_3^- correlates with the fine fraction crustal component, PC 5.

5.4.4.3 Cl^-

Chloride concentrations are plotted in Figure 13a as a function of sample ID. When subtracting the sea-salt component from the coarse and fine fractions of the measured Cl^-, all concentrations are negative. Thus, all samples are deficient in Cl^- assuming that Na^+ is the appropriate sea-salt tracer. The absolute deficit is plotted in Figure 13b. On a relative scale, the deficit in the coarse fraction amounts to 25.6 ± 21.3%, in the fine fraction to 89.0 ± 9.4% and when considering coarse and fine combined, it amounts to 53.1 ± 16.0% and ranged from 27.0 to 84.9%.

In the present samples, the deficit is considerably larger than that observed by our group over the Arabian Sea [*Johansen et al.*, 1999a] during the SW- and inter-monsoons. The Cl^- deficits during those cruises were 3.5 ± 6.3% and 15 ± 9%, respectively. Over the tropical Atlantic Ocean [*Johansen et al.*, 1999b], the Cl^- deficit was 11.9 ± 13.3% in the coarse fraction and 29.7 ± 9.9% in the fine fraction.

Chloride deficits have been found to correlate with the proximity to continental landmasses, and thus are assumed to depend on the concentrations of anthropogenic pollutants such as SO_4^{2-} and NO_3^-. In heavily polluted air masses, losses of particulate Cl^- approaching 100% have been reported. Based on these observations, it is assumed that Cl^- is released solely due to the thermodynamically favorable displacement reactions between mineral acids (H_2SO_4, HNO_3) and HCl:

$$2\ NaCl(s) + H_2SO_4 \rightarrow Na_2SO_4 + 2\ HCl(g) \quad (1)$$

$$NaCl(s) + HNO_3 \rightarrow NaNO_3 + HCl(g) \quad (2)$$

Recent investigations provide evidence that in addition to HCl, highly reactive Cl gases such as Cl_2, HOCl, $ClNO_2$, and BrCl may also volatilize from sea-salt aerosol [*Fan and Jacob*, 1992; *Graedel and Keene*, 1995; *Graedel and Keene*, 1996; *Langer et al.*, 1996; *Sander and Crutzen*, 1996; *Vogt et al.*, 1996]. Photolysis of these gases during the daytime produces atomic Cl with potential implications for the atmospheric lifetimes of alkanes, methyl halides, and DMS [*Keene et al.*, 1996].

In comparison to earlier cruises [*Johansen et al.*, 1999a; *Johansen et al.*, 1999b] we found evidence for the release of Cl from the aerosol phase by both mechanisms. From the PC analysis given in Table 7, the Cl^- deficit in the coarse fraction correlates with the anthropogenic component (PC 2) which also correlates with NO_3^- in the coarse

fraction. Thus, the Cl^- deficit in the coarse fraction may be mainly a result of the acid displacement reaction with HNO_3. The plot in Figure 14a compares the concentrations of the mineral acids with the Cl^- deficit in the coarse fraction. The scatter is large, but the location of data points relative to the 1:1 drawn-in line suggests that the acids may be responsible for the displacement of HCl. The 1:1 line represents data points for which the Cl^- deficit is exactly matched with the concentration of the specific mineral acid. Thus, points to the right of the line indicate that there is not enough of the particular mineral acid present to account for the Cl^- deficit found in the samples. This is the case for the coarse NSS-SO_4^{2-}. On the other hand, NO_3^- concentrations (open squares) are always larger than the Cl^- deficit. This indicates that in the coarse aerosol fraction the concentration of NO_3^- is sufficient to be responsible for all the Cl^- displacement. This trend was also observed by Sievering et al. [*Sievering et al.*, 1990]. However, it does not exclude the possibility that H_2SO_4 and/or the reactive Cl species may have contributed to the Cl^- deficit.

The Cl^- deficit in the fine fraction is plotted in Figure 14b. In this case the deficit is smaller than the H_2SO_4 available for displacement. However, the measured deficit is 89%. The remaining 11% of the Cl^- could have been trapped inside the particles and thus was inaccessible for reaction with H_2SO_4. This plot also illustrates that the NO_3^- concentrations are not sufficient to account for the observed Cl^- deficit. Thus, H_2SO_4 seems to be the principal mineral acid affecting the displacement of Cl^- in the fine fraction. However, the possibility of Cl release due to the production of reactive Cl species cannot be ruled out.

5.4.5 Cations

The observed cation concentrations are summarized in Table 8. Assuming that all the water-soluble Na^+ is sea-salt derived, the NSS contributions for the alkali and alkaline earth elements were determined based on sea water concentrations reported by Millero and Sohn [*Millero and Sohn*, 1992].

5.4.5.1 NH_4^+

Total ammonium concentrations average 0.69 ± 0.31 μg m^{-3} and vary from 0.26 to 1.46 μg m^{-3}. These values are very close to those observed by Rhoads et al. [*Rhoads et al.*, 1997] over the Arabian Sea during March and April of 1995. During the inter-monsoon of 1995, we observed values that were smaller by more than a factor of 2 of those presently observed, and during the SW-monsoon of the same year NH_4^+ concentrations were smaller by a factor of 15 [*Johansen et al.*, 1999a].

Most (93.3 ± 3.9%) of the NH_4^+ is present in the fine fraction; this is reflected in Figure 15a. Ammonium has typically been observed in association with particles in the accumulation mode, together with NSS-SO_4^{2-} and MSA [*Huebert et al.*, 1996]. This concept is in agreement with our observations and is reaffirmed in the PC analysis presented in Table 7.

Ammonium ion in these samples appears to be of anthropogenic origin. Ammonium reaches the aerosol in the form of $NH_3(g)$ where it will neutralize acidic components of the aerosol. In ammonia-poor conditions, H_2SO_4 is first neutralized because of its extremely low vapor pressure and the acidic aerosol will tend to drive out the nitrate to the gas phase. If an excess ammonia is available (i.e., two times the

concentration of H_2SO_4) so that the aerosol phase will be neutralized to a large extent, the ammonia that does not react with H_2SO_4 and HSO_4^- will be available to react with HNO_3 to produce NH_4NO_3 [*Seinfeld and Pandis*, 1997]. Therefore, the NH_4^+/NSS-SO_4^{2-} ratio gives an estimate of the neutralization and the speciation of the acid in the aerosol. This ratio is plotted as a function of sample ID in Figure 15b. The geometric mean of the ratio in the fine fraction, where most of the NH_4^+ and the NSS-SO_4^{2-} is present, is 1.2 ± 0.2. This number indicates that the predominant species is bisulfate (HSO_4^-). The same ratio in the coarse fraction is subject to larger errors due to the small coarse aerosol fraction concentrations of the two species, but the mean (geometric) of the ratio is very close to the one found in the fine fraction, namely 1.1 ± 0.7. Thus, it appears as if in the coarse fraction, the bisulfate also prevails. However, the basicity may be enhanced by the measured NSS-Ca^{2+} if it is derived from crustal sources of calcite, especially in the coarse fraction where most of the NSS-Ca^{2+} is present. The resulting ratio ((NH_4^+ + NSS-Ca^{2+})/NSS-SO_4^{2-}) in the coarse fraction increases to 4.9 ± 2.6. In the fine fraction, the addition of NSS-Ca^{2+} has a negligible impact on the ratio, 1.3 ± 0.1. The large value in the coarse fraction implies that all of the acidic sulfate is neutralized in addition to some of the HNO_3. However, the elevated value may also be a result of some of the NSS-Ca^{2+} being derived from gypsum, which will not contribute to the neutralization of acid.

Acid-base neutralization can also be discussed in terms of charge imbalances observed between total anionic and cationic charges. However, since both H^+ and CO_3^{2-} are not detectable with the IC, an observed charge imbalance cannot be directly attributed to the either one of the two species. In the present case, the carbonate derived from the

excess NSS-Ca^{2+} in the coarse aerosol fraction, correlates well with the anionic charge deficit that is observed in the coarse fraction. In the fine fraction, anionic and cationic charges are of the same magnitude. The charge deficit in the coarse fraction amounts to 18%. Thus, it appears as if no additional protons are present in the coarse fraction that would acidify the aerosol over what was obtained from the ratios that include the carbonate neutralization capacity.

5.4.5.2 Na^+. K^+. Mg^{2+}, and Ca^{2+}

Water-soluble sodium is used as the tracer for sea-salt in the atmosphere. The total Na^+ concentration of 0.85 ± 0.28 μg m^{-3} translates into 2.76 ± 0.92 μg m^{-3} of sea-salt. Rhoads et al. [*Rhoads et al.*, 1997] and Savoie et al. [*Savoie et al.*, 1987] observed slightly higher Na^+ concentrations over the Arabian Sea, 1.11 ± 0.44 and 2.4 ± 1.2 μg m^{-3}, respectively. During the inter- and SW-monsoon of 1995 [*Johansen et al.*, 1999a], we also observed larger values, 2.6 ± 1.4 and 6.5 ± 2.9 μg m^{-3}, respectively. The difference can be attributed to the higher wind speeds observed during the SW-monsoon. Sodium correlates with the wind speed and other sea-salt components in PC 4 (Table 7). The relatively low wind speeds encountered in the present cruise (Figure 2a), resulted in the evenly distribution of sea-salt loading in the coarse and fine fractions. The plot of Figure 16a shows Na^+ in coarse and fine fractions. Data obtained from the ICP-MS is compared to that of the IC in Figure 6a. The water-soluble Na^+ values are typically larger than those determined with the ICP-MS. This is contrary to the expected since the ICP-MS measures both water-soluble and -insoluble Na.

NSS and SS contributions of water-soluble K^+ in both coarse and fine fractions are plotted in stacked bars of Figure 16b. 74.6 ± 9.1% of the total K^+, and 90.0 ± 5.2% (geometric means) of the fine K^+, is present in the fine NSS-K^+ fraction. Species that are associated with the fine fraction in such a manner are typically derived from sources, such as the combustion of wood and from waste incinerators [*Andreae*, 1983; *Echalar et al.*, 1995; *Fishman et al.*, 1999]. From the K plot of Figure 6b, we can deduce that all the enriched K observed with the ICP-MS is water-soluble. Only in samples where a considerable amount of K is classified as "other" is present in the coarse fraction (plotted in dark green), i.e., for samples IO97-02, 03, 11, 12, 13 and 20, a considerable discrepancy between the IC and the ICP-MS results are observed. The enriched K in the fine fraction is water-soluble, while the enriched K in the coarse fraction appears to be non-soluble and derived from crustal minerals.

During the inter-monsoon of 1995 [*Johansen et al.*, 1999a], when some of the air masses appear to have similar origins as during the latter part of the present cruise, the K^+ concentrations averaged 0.18 ± .11 μg m^{-3} of which 40.8 ± 16.0% were NSS. While the total K^+ concentrations are in general agreement, the contribution in the NSS fraction presently is quite large at 78.3 ± 10.0%. This is most probably a result of the influence of polluted air masses from the Indian subcontinent.

Magnesium as detected by the IC is plotted in Figure 16c. NSS and SS contributions are determined in the coarse and fine fractions, analogous to the K plot in Figure 16b. On average, excluding those samples that display negative NSS concentrations, only 16.5% of the total water-soluble Mg is NSS. The fact that we obtain negative NSS concentrations is indicative of inaccurate Na^+ (which serves to determine

the SS contribution) and/or Mg^{2+} detection by the IC. Comparing the IC and the ICP-MS results in Figure 6c seems to indicate that either some of the crustal Mg is water-soluble or that the Mg^{2+} concentrations determined by the IC are slightly elevated compared to the ICP-MS values, as it was the case for Na^{+}.

The Ca^{2+} determined by IC is plotted in Figure 16d. On average (geometric means), 66.2 ± 11.8% of all the detected Ca^{2+}, and 91.2 ± 5.9% of the coarse Ca^{2+}, is present as NSS-Ca^{2+}, which implies that it is of crustal origin. A comparison of IC and ICP-MS concentrations in Figure 6d shows that all the NSS-non-crustal (i.e., "other") Ca as well as most of the crustal Ca is water-soluble. Thus, the Ca in the average crustal composition as reported by Taylor and McLennan [*Taylor and McLennan*, 1985] seems to be in the form of a water-soluble compound, possibly calcite, gypsum or dololmite, or a mixture of these minerals. During the inter-monsoon of 1995 [*Johansen et al.*, 1999a], in which some of the air masses may have similar origins as in the present case, the NSS-Ca^{2+} seemed to be attributed mainly to gypsum. Concentrations measured during the inter-monsoon of 1995 averaged 0.96 ± 0.90 μg m^{-3} which represented 57.8 ± 25.1% of the total water-soluble Ca^{2+}. This value compares to 0.37 ± 0.21 μg m^{-3} NSS-Ca^{2+} which amounts to 89.3 ± 6.3% of the total Ca^{2+} presently found. As expected, concentrations during the SW-monsoon were considerably smaller, 0.16 ± 0.16 μg m^{-3} of which only 31.2 ± 22.4% were NSS [*Johansen et al.*, 1999a].

5.5 Conclusions

Air masses sampled during the month of March of 1997 over the Arabian Sea contain aerosols that vary considerably in their mineralogical characteristics. This is expected, since March is considered to be a transitional period between the tail end of the NE- and the inter-monsoon seasons. The mineral aerosol appears to be a composite from several arid and semiarid regions surrounding the Arabian Sea. Based on air mass back trajectories, the Thar desert and deserts of the Saudi Arabian peninsula are the most likely mineral dust sources. EF and PC analyses reveal three distinct crustal components of which one is mainly composed of a water-soluble Ca^{2+} species, possibly a mixture of gypsum and calcite. Assuming the NSS-Ca^{2+} to be solely derived from calcite, it would contribute 0.77 ± 0.36 μg m^{-3} of crustal material to the 5.94 ± 3.08 μg m^{-3} of other crustal material determined from Al concentrations and the average crustal composition by Taylor and McLennan [*Taylor and McLennan*, 1985]. The average crustal composition appears to be a good surrogate for the mineral aerosol sampled throughout the cruise.

All samples carry a strong anthropogenic signature reflected in the large enrichments in anthropogenic tracers such as Pb, Zn, fine Ge, fine Se, fine K, NSS-K^+, NSS-SO_4^{2-}, NH_4^+, and coarse NO_3^-. The anthropogenic contribution is especially pronounced in the first ten samples which exhibit air mass back trajectories that indicate a northeastern origin, from the Indian subcontinent.

Iron in the coarse fraction appears to be of a crustal origin, while the fine fraction Fe correlates with the fine fraction Mn and does not correlate with the crustal component. Although the EFs for Fe and Mn in the fine fraction are not large enrichments, contaminant sources cannot be ruled out. Ferrous iron concentrations in the coarse

fraction correlate strongly with the coarse crustal Fe; however, in the fine fraction no such simple relationship is observed. Fine $Fe(II)_{total,5minFZ}$ correlates somewhat with the main crustal and with the anthropogenic sources. Fine $Fe(II)_{total,5minFZ}$ appears to correlate slightly with the fine K and fine Mg and more strongly with the fine V. Thus, fine $Fe(II)_{total,5minFZ}$ exhibits a much more complex behavior compared to the coarse $Fe(II)_{total,5minFZ}$. This different behavior is expected due to the intricate redox chemistry that different iron phases can undergo in the presence of anthropogenic pollutants and solar radiation.

The total $Fe(II)_{total,5minFZ}$ averages 9.76 ± 3.37 μg m^{-3} which represents 1.3 ± 0.5% of the total Fe. These values are the largest observed by our group as compared to measurements taken during other seasons over the Arabian Sea [*Siefert et al.*, 1999] and over the Atlantic Ocean [*Johansen et al.*, 1999b]. While total Fe is almost evenly distributed between fine and coarse fractions, 87.2 ± 6.1% of the $Fe(II)_{total,5minFZ}$ is present in the fine fraction. Furthermore, based on the relative amounts of Fe(II) released in the sequential extraction procedure, it appears as if the Fe(II) in the fine fraction is more labile.

NSS-SO_4^{2-} concentrations vary from 1.42 to 5.38 μg m^{-3} and average 2.94 ± 1.06 μg m^{-3}. This corresponds to 92.7 ± 3.4% of the total SO_4^{2-}. Most of the NSS-SO_4^{2-} (92.1 ± 4.5%) is present in the fine fraction and is associated with other anthropogenic tracers. Weighted multiple linear regression analyses on the coarse and fine data sets reveal the relative contributions of the different SO_4^{2-} sources. In the fine fraction 6% of the NSS-SO_4^{2-} is biogenically-derived, 84% is anthropogenically-derived and the remainder

appears to be of crustal origin. In the coarse fraction, the biogenic and anthropogenic NSS-SO_4^{2-} are comparable in magnitude and no gypsum is found.

The biogenic component in the linear regression analyses is traced by methanesulfonate, MSA. The average total MSA concentration amounts to 25.4 ± 6.8 μg m^{-3} of which 91.9 ± 4.0% is present in the fine fraction. The biogenically-derived SO_4^{2-} /MSA weight ratio of 9.8 is obtained from the same linear regression analyses. This ratio fits well into the temperature dependence found for similar ratios determined over the Arabian Sea during 1995 [*Johansen et al.*, 1999a].

Cl^- deficits are observed in all the samples. They average 53.1 ± 16.0% of the expected Cl^- concentrations. In the fine fraction, however, Cl^- deficits up to 99.1% are found (average, 89.0 ± 9.4%). Acid displacement reactions with H_2SO_4 appear to be the dominant mechanism for the volatilization of HCl in the fine fraction, since the NSS-SO_4^{2-} concentrations are much larger than the displaced Cl^-. Due to possible physical transport limitations of chemical species in the aerosol particle, it may be difficult to reach 100% Cl^- deficit even in the presence of abundant NSS-SO_4^{2-}. In the coarse fraction, HNO_3 appears to be the species of preference in the displacement of Cl^-. However, in both the fine and the coarse fractions, the release of Cl^- from the particle phase by other mechanisms such as the production of reactive Cl species cannot be ruled out.

Based on the NH_4^+/NSS-SO_4^{2-} ratios of 1.2 ± 0.2 in the fine and 1.1 ± 0.7 in the coarse fractions, most of the NSS-SO_4^{2-} is expected to be present as HSO_4^- in both aerosol fractions.

Acknowledgments. The authors wish to thank Drs. Meinrat O. Andreae and Hermann W. Bange of the Max Planck Institute of Biogeochemistry in Mainz, Germany, for assistance with the cruise, which was sponsored by the German Joint Global Ocean Flux Study (JGOFS) project. Appreciation is also extended to the helpful crew of the R/V Sonne. Research support was provided by the National Science Foundation and by the Environment Now Foundation. Their support is greatly appreciated.

5.6 References

Ackerman, S.A., and S.K. Cox, Surface weather observations of atmospheric dust over the southwest summer monsoon region, *Meteorol. Atmos. Phys.*, *41*, 19-34, 1989.

Andreae, M.O., Soot carbon and exces fine potassium: Long-range transport of combustion-derived aerosols, *Science*, *220*, 1148-1151, 1983.

Andreae, M.O., W. Elbert, and S.J. de Mora, Biogenic sulfur emissions and aerosols over the tropical South Atlantic. 3. Atmospheric dimethylsulfide, aerosols and cloud condensation nuclei, *J. Geophys. Res.*, *100*, 11,335-11,356, 1995.

Bassett, M.E., and J.H. Seinfeld, Atmospheric equilibrium model of sulfate and nitrate aerosols-II. Particle size analysis, *Atmos. Environ.*, *18* (6), 1163-1170, 1984.

Bates, T.S., J.A. Calhoun, and P.K. Quinn, Variations in the methanesulfonate to sulfate molar ratio in submicrometer marine aerosol particles over the South Pacific Ocean, *J. Geophys. Res.*, *97*, 9859-9865, 1992.

Berresheim, H., M.O. Andreae, R.L. Iverson, and S.M. Li, Seasonal variations of dimethylsulfide emissions and atmospheric sulfur and nitrogen species over the western north Atlantic Ocean, *Tellus*, *43B*, 353-372, 1991.

Berresheim, H., F.L. Eisele, D.J. Tanner, L.M. McInnes, D.C. Ramsey-Bell, and D.S. Covert, Atmospheric sulfur chemistry and cloud condensation nuclei (CCN) concentrations over the northeastern Pacific coast, *J. Geophys. Res.*, *98*, 12,701-12,711, 1993.

Berresheim, H., P. Wine, and D. Davis, Sulfur in the atmosphere, in *Composition, Chemistry, and Climate of the Atmosphere*, edited by H. Singh, pp. 251-307, Van Nostrand Reinhold, New York, 1995.

Bürgermeister, S., and H.-W. Georgii, Distribution of methanesulfonate, nss-sulfate and dimethylsulfide over the Atlantic and the North Sea, *Atmos. Environ.*, *25A* (3/4), 587-595, 1991.

Charlson, R.J., J.E. Lovelock, M.O. Andreae, and S.G. Warren, Oceanic phytoplankton, atmospheric sulphur, cloud albedo and climate, *Nature*, *326*, 655-661, 1987.

Chester, R., A.S. Berry, and K.J.T. Murphy, The distributions of particulate atmospheric trace metals and mineral aerosols over the Indian Ocean, *Mar. Chem.*, *34*, 261-290, 1991.

Chester, R., E.J. Sharples, and G.S. Sanders, The concentrations of particulate aluminum and clay minerals in aerosols from the northern Arabian Sea, *J. Sedim. Petr.*, *55* (1), 37-41, 1985.

Cooper, D.J., A.J. Watson, and P.D. Nightingale, Large decrease in ocean-surface CO2 fugacity in response to in situ iron fertilization, *Nature*, *383*, 511-514, 1996.

Echalar, F., A. Gaudichet, H. Cachier, and P. Artaxo, Aerosol emissions by tropical forest and savanna biomass burning: characteristic trace elements and fluxes, *Geophys. Res. Letters*, *22* (22), 3039-3042, 1995.

Fan, S.-M., and D.J. Jacob, Surface ozone depletion in Arctic spring sustained by bromine reactions on aerosol, *Nature*, *359*, 522-524, 1992.

Findlater, J., A major low-level air current near the Indian Ocean during the northern summer, *Quart. J. R. Meteorol. Soc.*, *95*, 362-380, 1969.

Findlater, J., Mean monthly airflow at low levels over the western Indian Ocean, *Geophys. Mem. L. No. 115*, *26*, 1-53, 1971.

Finlayson-Pitts, B.J., M.J. Ezell, and J.N. Pitts Jr., Formation of chemically active chlorine compounds by reactions of atmospheric NaCl particles with gaseous N_2O_5 and $ClONO_2$, *Nature*, *337*, 241-244, 1989.

Fishman, N.S., C.A. Rice, G.N. Breit, and R.D. Johnson, Sulfur-bearing coatings in fly ash from a coal-fired power plant: composition, origin, and influence on ash alteration, *Fuel*, *78*, 187-196, 1999.

Gao, Y., R. Arimoto, R.A. Duce, L.Q. Chen, M.Y. Zhou, and D.Y. Gu, Atmospheric non-sea-salt sulfate, nitrate and methanesulfonate over the China Sea, *J. Geophys. Res.*, *101*, 12,601-12,611, 1996.

Glaccum, R.A., and J.M. Prospero, Saharan aerosols over the tropical North Atlantic-Mineralogy, *Mar. Geol.*, *37*, 295-321, 1980.

Goldberg, E.D., and J.J. Griffin, The sediments of the northern Indian Ocean, *Deep-Sea Res.*, *17*, 513-537, 1970.

Graedel, T.E., and W.C. Keene, Tropospheric budget of reactive chlorine, *Global Biogeochem. Cycles*, *9* (1), 47-77, 1995.

Graedel, T.E., and W.C. Keene, The budget and cycle of Earth's natural chlorine, *Pure Appl. Chem.*, *68* (9), 1689-1697, 1996.

Hopke, P.K., Appendix: Selected Source Profiles, in *Receptor Modeling in Environmental Chemistry*, pp. 267-314, John Wiley & Sons, Inv., 1985.

Hoppel, W.A., J.W. Fitzgerald, G.M. Frick, R.E. Larson, and E.J. Mack, Aerosol size distributions and optical properties found in the marine boundary layer over the Atlantic Ocean, *J. Geophys. Res.*, *95*, 3659-3686, 1990.

Huebert, B.J., L. Zhuang, S. Howell, K. Noone, and B. Noone, Sulfate, nitrate, methanesulfonate, chloride, ammonium, and sodium measurements from ship, island, island, and aircraft during the Atlantic Stratocumulus Transition Experiment/Marine Aerosol Gas Exchange, *J. Geophys. Res.*, *101*, 4413-4423, 1996.

Hynes, A.J., P.H. Wine, and D.H. Semmes, Kinetics and mechanism of OH reactions with organic sulfides, *J. Phys. Chem.*, *90*, 4148-4156, 1986.

Jayaraman, A., D. Lubin, S. Ramachandran, V. Ramanathan, E. Woodbridge, W.D. Collins, and K.S. Zalpuri, Direct observations of aerosol radiative forcing over the tropical Indian Ocean during the January-February 1996 pre-INDOEX, *J. Geophys. Res.*, *103*, 13,827-13,836, 1998.

Johansen, A.M., R.L. Siefert, and M.R. Hoffmann, Chemical characterization of ambient aerosol collected during the southwest-monsoon and inter-monsoon seasons over the Arabian Sea: Anions and cations, *J. Geophys. Res.*, *submitted*, 1999a.

Johansen, A.M., R.L. Siefert, and M.R. Hoffmann, Chemical composition of aerosols collected over the tropical North Atlantic Ocean, *J. Geophys. Res.*, *to be submitted*, 1999b.

Keene, W.C., D.J. Jacob, and S.-M. Fan, New Directions: Reactive chlorine: A potential sink for dimethylsulfide and hydrocarbons in the marine boundary layer, *Atmos. Environ.*, *30* (6), i-iii, 1996.

Keene, W.C., A.A.P. Pszenny, D.J. Jacob, R.A. Duce, J.N. Galloway, J.J. Schultz-Tokos, H. Sievering, and J.F. Boatman, The geochemical cycling of reactive chlorine through the marine troposphere, *Global Biogeochem. Cycles*, *4* (4), 407-430, 1990.

Keene, W.C., R. Sander, A.A.P. Pszenny, R. Vogt, P.J. Crutzen, and J.N. Galloway, Aerosol pH in the marine boundary layer: A review and model evaluation, *J. Aerosol Sci.*, *29* (3), 339-356, 1998.

Kerminen, V.-M., M. Aurela, R.E. Hillamo, and A. Virkkula, Formation of particulate MSA: Deductions from size distribution measurements in the Finnish Arctic, *Tellus*, *49B*, 159-171, 1997.

Kolber, Z.S., R.T. Barber, K.H. Coale, S.E. Fitzwater, R.M. Greene, K.S. Johnson, S. Lindley, and P.G. Falkowski, Iron limitation of phytoplankton photosynthesis in the equatorial Pacific Ocean, *Nature*, *371*, 145-149, 1994.

Langer, S., B.T. McGovney, B.J. Finlayson-Pitts, and R.M. Moore, The dimethyl sulfide reaction with atomic chlorine and its implications for the budget of methyl chloride, *Geophys. Res. Lett.*, *23* (13), 1661-1664, 1996.

Martin, J.H., K.H. Coale, K.S. Johnson, S.E. Fitzwater, R.M. Gordon, and ....., Testing the iron hypothesis in ecosystems of the equatorial Pacific Ocean, *Nature*, *371*, 123-129, 1994.

Martin, J.H., and S.F. Fitzwater, Iron deficiency limits phytoplankton growth in the north-east Pacific subarctic, *Nature*, *331*, 341-342, 1988.

McInnes, L.M., D.S. Covert, P.K. Quinn, and M.S. Germani, Measurements of chloride depletion and sulfur enrichment in individual sea-salt particles collected from the remote marine boundary layer, *J. Geophys. Res.*, *99*, 8257-8268, 1994.

Middleton, N.J., Dust storms in the Middle East, *J. Arid. Environ.*, *10*, 83-96, 1986a.

Middleton, N.J., A geography of dust storms in south-west Asia, *J. Climat.*, *6*, 183-196, 1986b.

Millero, F.J., and M.L. Sohn, *Chemical Oceanography*, CRC Press, 1992.

Moorthy, K.K., S.K. Satheesh, and B.V.K. Murthy, Characteristics of spectral optical depth and size distributions of aerosols over tropical oceanic regions, *J. Atmos. Solar-Terr. Phys.*, *60*, 981-992, 1998.

Moorthy, K.K., S.K. Satheesh, and K.B.V. Murthy, Investigations of marine aerosols over the tropical Indian Ocean, *J. Geophys. Res.*, *102*, 18,827-18,842, 1997.

Naik, M.S., L.T. Khemani, G.A. Momin, P.S. Prakasa Rao, and P.D. Safai, Origin of calcium in marine aerosol over the Arabian Sea near the west coast of India, *J. Aerosol Sci.*, *22* (3), 365-372, 1991.

O'Dowd, C., M.H. Smith, I.E. Consterdine, and J.A. Lowe, Marine aerosol, sea-salt, and the marine sulphur cycle: A short review, *Atmos. Environ.*, *31* (1), 73-80, 1997.

Paerl, H.W., L.E. Prufert-Bebout, and C. Guo, Iron-stimulated N_2 fixation and growth on natural and cultured populations of the planktonic marine cyanobacteria *Trichodesmium* spp., *Appl. Environ. Microbiol.*, *60* (3), 1044-1047, 1994.

Patterson, C.C., and D.M. Settle, The reduction of orders of magnitude errors in lead analysis of biological materials and natural waters by evaluating and controlling the extent and sources of industrial lead contamination introduced during sampling, collecting, handling and analysis, *Natl. Bur. Stand. Spec. Publ.*, *422*, 321-351, 1976.

Pease, P.P., V.P. Tchakerian, and N.W. Tindale, Aerosols over the Arabin Sea: geochemistry and source areas for aeolian desert dust, *J. Arid Environ.*, *39*, 477-496, 1998.

Price, N.M., B.A. Ahner, and F.M.M. Morel, The equatorial Pacific Ocean: Grazer-controlled phytoplankton populations in an iron-limited ecosystem, *Limnol. Oceanogr.*, *39* (3), 520-534, 1994.

Pszenny, A.A.P., Particle size distributions of methanesulfonate in the tropical Pacific marine boundary layer, *J. Atmos. Chem.*, *14*, 273-284, 1992.

Pszenny, A.A.P., W.C. Keene, D.J. Jacob, S. Fan, J.R. Maben, M.P. Zetwo, M. Springer-Young, and J.N. Galloway, Evidence of inorganic chlorine gases other than hydrogen chloride in marine surface air, *Geophys. Res. Lett.*, *20* (8), 699-702, 1993.

Qian, G.-W., and Y. Ishizaka, Electron microscope studies of methane sulfonic acid in individual aerosol particles, *J. Geophys. Res.*, *98*, 8459-8470, 1993.

Quinn, P.K., D.S. Covert, T.S. Bates, V.N. Kapustin, D.C. Ramsey-Bell, and L.M. McInnes, Dimethylsulfide/cloud condensation nuclei/climate system: Relevant size-resolved measurements of the chemical and physical properties of atmospheric aerosol particles, *J. Geophys. Res.*, *98*, 10,411-10,427, 1993.

Rhoads, K.P., P. Kelley, R.R. Dickerson, T.P. Carsey, M. Farmer, D.L. Savoie, and J.M. Porspero, Composition of the troposphere over the Indian Ocean during the monsoonal transition, *J. Geophys. Res.*, *102*, 18,981-18,995, 1997.

Saltzman, E.S., D.L. Savoie, J.M. Prospero, and R.G. Zika, Atmospheric methanesulfonic acid and non-sea-salt sulfate at Fanning and American Samoa, *Geophys. Res. Lett.*, *12* (7), 437-440, 1985.

Saltzman, E.S., D.L. Savoie, R.G. Zika, and J.M. Prospero, Methane sulfonic acid in the marine atmosphere, *J. Geophys. Res.*, *88*, 10,897-10,902, 1983.

Sander, R., and P.J. Crutzen, Model study indicating halogen activation and ozone destruction in polluted air masses transported to the sea, *J. Geophys. Res.*, *101*, 9121-9138, 1996.

Satheesh, S.K., and K. Krishna Moorthy, Aerosol characterisitcs over coastal regions of the Arabian Sea, *Tellus*, *49B*, 417-428, 1997.

Satheesh, S.K., K.K. Moorthy, and B.V. Murthy, Spatial gradients in aerosol characteristics over the Arabian Sea and Indian Ocean, *J. Geophys. Res.*, *103*, 26,183-16.192, 1998.

Savoie, D.L., and J.M. Prospero, Particle size distribution of nitrate and sulfate in the marine atmosphere, *Geophys. Res. Lett.*, *9* (10), 1207-1210, 1982.

Savoie, D.L., and J.M. Prospero, Comparison of oceanic and continental sources of non-sea-salt sulphate over the Pacific Ocean, *Nature*, *339*, 685-687, 1989.

Savoie, D.L., and J.M. Prospero, Non-sea-salt sulfate and methansulfonate at American Samoa, *J. Geophys. Res.*, *99*, 3587-3596, 1994.

Savoie, D.L., J.M. Prospero, and R.T. Nees, Nitrate, non-sea-salt sulfate, and mineral aerosol over the northwestern Indian Ocean, *J. Geophys. Res.*, *92*, 933-942, 1987.

Seinfeld, J.H., and S.N. Pandis, *Atmospheric Chemistry and Physics: From Air Pollution to Climate Change*, John Wiley & Sons, Inc., 1997.

Siefert, R.L., A.M. Johansen, and M.R. Hoffmann, Chemical characterization of ambient aerosol collected during the southwest- and inter-monsoon seasons over the Arabian Sea: Labile-Fe(II) and other trace metals, *J. Geophys. Res.*, *104* (3511-3526), 1999.

Sievering, H., G. Ennis, E. Gorman, and C. Nagamoto, Size distribution and statistical analysis of nitrate, excess sulfate, and chloride deficit in the marine boundary layer during GCE/CASE/WATOX, *Global Biogeochem. Cycles*, *4* (4), 395-405, 1990.

Sisterson, D.L., A method for evaluation of acidic sulfate and nitrate in precipitation, *Water, Air, and Soil Pollut.*, *43*, 61-72, 1989.

Stickel, R.E., J.M. Nicovich, Z. Zhao, and P.H. Wine, Kinetic and mechanistic study of the reaction of atomic chlorine with dimethyl sulfide, *J. Phys. Chem.*, *96*, 9875-9883, 1992.

Taylor, S.R., and S.M. McLennan, *The Continental Crust: Its Composition and Evolution*, Blackwell Scientific Publ., Oxford, England, 1985.

Turnipseed, A.A., and A.R. Ravishankara, The atmospheric oxidation of dimethyl sulfide: elementary steps in a complex mechanism, in *Dimethylsulfide: Oceans, Atmosphere and Climate*, edited by G.R.a.G. Angeletti, pp. 185-196, Kluwer Acad. Publ., Norwell, Mass., 1993.

Vogt, R., P.J. Crutzen, and R. Sander, A mechanism for halogen release in the remote marine boundary layer, *Nature*, *383*, 327-330, 1996.

Yin, F., D. Grosjean, and J.H. Seinfeld, Analysis of atmopheric photooxidation mechanisms for organosulfur compounds, *J. Geophys. Res.*, *91*, 14417-14438, 1986.

Yin, F., D. Grosjean, and J.H. Seinfeld, Photooxidation of dimethyl sulfide and dimethyl disulfide. I: mechanism development, *J. Atmos. Chem.*, *11*, 309-364, 1990.

Zhu, X., J.M. Prospero, D.L. Svoie, F.J. Millero, R.G. Zika, and E.S. Saltzman, Photoreduction of iron(III) in marine mineral aerosol solutions, *J. Geophys. Res.*, *98*, 9039-9046, 1993.

Zhu, X.R., J.M. Prospero, and F.J. Millero, Diel variability of soluble Fe(II) and soluble total Fe in North African dust in the trade winds at Barbados, *J. Geophys. Res.*, *102*, 21,297-21,305, 1997.

Zhuang, G., Z. Yi, R.A. Duce, and P.R. Brown, Link between iron and sulphur cycles suggested by detection of Fe(II) in remote marine aerosols, *Nature*, *355*, 537-539, 1992.

5.7 Figure Captions

Figure 1. Five-day air mass back trajectory calculations at five different final elevations (based on pressure) above sea level for: a) March 2, 1997; b) March 5, 1997; c) March 8, 1997; and d) March 12, 1997; e) March 18, 1997; f) March 20, 1997; g) March 23, 1997; h) March 27, 1997.

Figure 2. a) Average wind speed vs. sample ID; b) Average true wind direction vs. sample ID. Error bars indicate one standard deviation.

Figure 3. Air temperature and relative humidity vs. sample ID. Error bars indicate one standard deviation.

Figure 4. Coarse and fine fraction trace metal concentrations vs. sample ID. for Al (a), Pb (b), Na (c), Fe (d), and Ca (e).

Figure 5. Factor scores for the crustal (a) and other (b) principal components extracted in the principal component analysis from Table 7.

Figure 6. ICP-MS and IC determined concentrations of (a) Na, (b) K, (c) Mg, and (d) Ca vs. sample ID. in coarse and fine fractions. Crustal concentrations determined from average crustal composition (see text for details).

Figure 7. Fe(II) concentrations vs. sample ID. (a) Fe(II) in the coarse fraction, (b) Fe(II) in the fine fraction, and (c) total Fe(II) released after 5 min in ferrozine (see text for details).

Figure 8. Relative Fe(II) concentrations (in % of total Fe) vs. sample ID. for coarse, fine and total Fe(II).

Figure 9. Relative amount Fe(II) released in the sequential extraction steps for coarse (a) and fine (b) fractions.

Figure 10. Sea-salt and non-sea-salt SO_4^{2-} contributions in coarse and fine fractions vs. sample ID.

Figure 11. MSA concentrations in coarse and fine fractions vs. sample ID.

Figure 12. NO_3^- concentrations in coarse and fine fractions vs. sample ID.

Figure 13. (a) Chloride concentrations and (b) chloride deficits in coarse and fine fractions vs. sample ID.

Figure 14. (a) neq mineral acid concentrations vs. Cl^- deficit in coarse fraction, and (b) fine fraction.

Figure 15. (a) NH_4^+ and (b) $NH_4^+/NSS\text{-}SO_4^{2-}$ vs. sample ID.

Figure 16. Water-soluble sea-salt and non-sea-salt fractions of Na^+ (a), K^+ (b), Mg^{2+} (c), and Ca^{2+} (d), in coarse and fine fractions vs. sample ID.

Table 1. Aerosol sampling collection times and positions.

Sample Id	Start Date/Time (UTC)	Stop Date/Time (UTC)	Position at midpoint in time	
			Latitude N	Longitude E
IO97-01	March 1, 1997 0550	March 2, 1997 0427	6.7	67.1
IO97-02	March 2, 1997 0540	March 3, 1997 0440	6.0	64.9
IO97-03	March 3, 1997 0510	March 4, 1997 0604	6.0	64.9
IO97-04	March 4, 1997 0625	March 5, 1997 0330	5.9	64.9
IO97-05	March 5, 1997 0358	March 6, 1997 0145	6.9	65.0
IO97-06	March 6, 1997 0206	March 7, 1997 0329	9.0	65.0
IO97-07	March 7, 1997 0355	March 8, 1997 0346	10.0	64.7
IO97-08	March 8, 1997 0430	March 9, 1997 0540	10.1	64.9
IO97-09	March 9, 1997 0600	March 10, 1997 0557	11.2	65.0
IO97-10	March 10, 1997 0615	March 11, 1997 0334	12.3	64.7
IO97-11	March 11, 1997 0400	March 12, 1997 0335	14.0	64.8
IO97-12	March 12, 1997 0412	March 13, 1997 0317	14.6	64.8
IO97-13	March 13, 1997 0403	March 14, 1997 0320	14.5	64.5
IO97-14	March 14, 1997 0347	March 15, 1997 0608	15.1	64.9
IO97-15	March 15, 1997 0627	March 16, 1997 0603	16.7	65.0
IO97-16	March 16, 1997 0617	March 17, 1997 0340	17.9	65.0
IO97-17	March 17, 1997 0359	March 18, 1997 0535	17.7	64.5
IO97-18	March 18, 1997 0559	March 19, 1997 0445	18.3	65.5
IO97-19	March 19, 1997 0506	March 20, 1997 0537	16.1	68.2
IO97-20	March 20, 1997 0608	March 21, 1997 0539	15.6	67.9
IO97-21	March 21, 1997 0559	March 22, 1997 0557	15.4	67.2
IO97-22	March 22, 1997 0629	March 23, 1997 0504	14.7	64.6
IO97-23	March 23, 1997 0520	March 24, 1997 0518	15.9	62.2
IO97-24	March 24, 1997 0536	March 25, 1997 0451	16.2	60.3
IO97-25	March 25, 1997 0519	March 26, 1997 0440	16.2	60.1
IO97-26	March 26, 1997 0457	March 27, 1997 0327	16.2	59.8
IO97-27	March 27, 1997 0345	March 28, 1997 0432	17.5	59.8

Table 2. Average, minimum and maximum atmospheric trace metal concentrations in coarse, fine and total aerosol fractions. Sample number 27 for all. Concentrations in ng m^{-3} unless otherwise noted.

Element	Coarse			Fine			Total		
	Average ± SD	Min.	Max.	Average ± SD	Min.	Max.	Average ± SD	Min.	Max.
Na (μg m^{-3})	0.45 ± 0.21	0.14	0.88	0.24 ± 0.11	0.09	0.61	0.69 ± 0.31	0.23	1.49
Mg (μg m^{-3})	0.15 ± 0.08	0.07	0.39	0.094 ± 0.039	0.048	0.212	0.25 ± 0.11	0.12	0.55
Al (μg m^{-3})	0.31 ± 0.20	0.08	0.93	0.19 ± 0.08	0.1	0.4	0.50 ± 0.26	0.19	1.27
K (μg m-3)	0.08 ± 0.08	0.01	0.35	0.17 ± 0.08	0.04	0.38	0.25 ± 0.12	0.06	0.51
Ca (μg m^{-3})	0.35 ± 0.18	0.13	0.74	0.15 ± 0.07	0.08	0.39	0.51 ± 0.23	0.21	0.99
Sc	0.07 ± 0.05	0.02	0.23	0.044 ± 0.015	0.027	0.094	0.12 ± 0.06	0.049	0.299
Ti	24.8 ± 14.3	5.9	64.8	15.0 ± 6.0	8.2	32.4	39.7 ± 18.9	17.9	93.2
V	0.70 ± 0.43	0.18	1.92	1.19 ± 0.34	0.5	1.98	1.89 ± 0.66	0.68	3.43
Mn	5.61 ± 2.60	1.44	10.52	5.05 ± 1.95	2.29	9.4	10.7 ± 3.6	3.9	19.7
Fe (μg m^{-3})	0.34 ± 0.18	0.08	0.89	0.38 ± 0.21	0.15	0.89	0.72 ± 0.29	0.26	1.58
Zn	1.35 ± 0.66	0.3	2.63	6.10 ± 3.94	1.55	17.33	7.45 ± 4.39	2.05	19.25
Ga	0.13 ± 0.07	0.03	0.28	0.087 ± 0.026	0.046	0.168	0.21 ± 0.08	0.079	0.41
Ge	0.023 ± 0.094	0.007	0.045	0.037 ± 0.013	0.017	0.066	0.061 ± 0.018	0.025	0.093
Se	0.059 ± 0.036	0.02	0.142	0.27 ± 0.10	0.11	0.51	0.33 ± 0.11	0.17	0.53
Ba	1.85 ± 0.89	0.47	3.64	1.11 ± 0.35	0.62	227	2.96 ± 1.13	1.11	5.31
La	0.15 ± 0.09	0.04	0.4	0.10 ± 0.04	0.06	0.23	0.25 ± 0.12	0.1	0.63
Ce	0.34 ± 0.20	0.08	0.89	0.22 ± 0.08	0.12	0.48	0.56 ± 0.26	0.22	1.36
Sm	0.028 ± 0.015	0.008	0.067	0.017 ± 0.005	0.009	0.033	0.045 ± 0.019	0.02	0.099
Eu	0.0062 ± 0.0034	0.0018	0.0149	0.0038 ± 0.0013	0.0017	0.0069	0.010 ± 0.004	0.005	0.022
Hf	0.021 ± 0.009	0.01	0.039	0.017 ± 0.009	0.008	0.041	0.039 ± 0.015	0.02	0.074
Pb	0.54 ± 0.27	0.02	1.09	4.73 ± 2.34	1.32	10.46	5.27 ± 2.55	1.47	11.25
Th	0.049 ± 0.003	0.012	0.149	0.28 ± 0.01	0.02	0.07	0.08 ± 0.04	0.028	0.21

Table 3. Varimax rotated component matrix. Trace metals. Includes 27 samples.

variance	51.4%	17.4%	10.2%	5.7%	3.8%	2.9%
Element\Component	1 crustal coarse	2 crustal fine	3 anthrop.	4 sea salt	5 Mn&Fe fine	6 Ca
Na-coarse	0.285	-0.054	0.029	**0.926**	-0.125	0.080
Na-fine	-0.048	0.339	0.296	**0.827**	-0.150	-0.007
Mg-coarse	**0.840**	0.385	-0.240	0.193	0.130	0.073
Mg-fine	0.194	**0.799**	-0.119	0.347	0.181	0.338
Al-coarse	**0.934**	0.319	-0.008	-0.017	0.103	-0.059
Al-fine	0.396	**0.864**	-0.121	0.143	0.145	0.110
K-coarse	**0.809**	0.406	-0.170	0.254	0.122	-0.055
K-fine	0.093	0.170	**0.823**	0.296	-0.049	-0.212
Ca-coarse	**0.664**	0.371	-0.220	0.133	0.198	**0.431**
Ca-fine	-0.023	0.564	-0.094	0.239	0.308	**0.683**
Sc-coarse	**0.939**	0.247	0.001	-0.052	0.114	-0.108
Sc-fine	0.299	**0.920**	-0.049	-0.116	0.021	0.057
Ti-coarse	**0.922**	0.343	0.079	0.081	0.058	0.066
Ti-fine	0.407	**0.757**	-0.124	0.252	0.200	0.100
V-coarse	**0.923**	0.325	0.059	0.083	0.069	0.052
V-fine	0.310	0.367	0.466	0.057	0.115	-0.067
Mn-coarse	**0.861**	0.202	0.216	0.017	-0.081	0.143
Mn-fine	0.211	0.461	0.179	-0.052	**0.809**	0.114
Fe-coarse	**0.751**	0.128	0.099	-0.048	-0.075	0.093
Fe-fine	0.147	0.328	0.005	-0.180	**0.890**	0.053
Zn-coarse	**0.568**	-0.129	**0.630**	-0.197	-0.197	0.137
Zn-fine	0.014	-0.151	**0.950**	-0.077	-0.019	-0.057
Ga-coarse	**0.920**	0.273	0.219	0.073	0.025	0.114
Ga-fine	0.361	**0.757**	0.186	0.257	0.198	0.175
Ge-coarse	**0.925**	0.098	0.246	0.026	0.019	0.066
Ge-fine	0.098	0.059	**0.880**	0.001	0.407	-0.050
Se-coarse	**0.537**	-0.033	0.040	0.079	-0.254	-0.018
Se-fine	0.201	-0.110	**0.707**	0.294	0.147	-0.413
Ba-coarse	**0.905**	0.210	0.289	0.043	-0.008	0.180
Ba-fine	0.361	**0.786**	0.104	0.200	0.144	0.300
La-coarse	**0.942**	0.287	0.098	-0.008	0.036	-0.080
La-fine	0.381	**0.909**	-0.030	-0.015	0.085	-0.054
Ce-coarse	**0.934**	0.314	0.111	0.041	0.028	-0.038
Ce-fine	0.440	**0.865**	-0.090	0.105	0.132	0.009
Sm-coarse	**0.950**	0.236	0.127	0.047	0.081	-0.021
Sm-fine	0.281	**0.926**	0.039	0.031	0.125	-0.025
Eu-coarse	**0.939**	0.211	0.176	0.016	0.032	-0.037
Eu-fine	0.223	**0.904**	-0.079	0.025	0.120	-0.037
Hf-coarse	**0.623**	0.402	0.102	0.366	0.171	0.032
Hf-fine	-0.227	0.330	-0.319	**0.476**	0.361	0.229
Pb-coarse	0.480	-0.177	**0.725**	-0.067	-0.218	0.243
Pb-fine	0.030	-0.098	**0.967**	0.071	-0.028	0.150
Th-coarse	**0.922**	0.313	0.077	0.011	0.055	-0.153
Th-fine	0.324	**0.914**	-0.036	-0.138	0.018	-0.092

Table 4. Enrichment factors for the coarse aerosol fraction relative to Al, assuming continental bulk composition according to McLennan and Taylor [1985].

Sample Id	Na	Mg	Al	K	Ca	Sc	Ti	V	Mn	Fe	Zn	Ga	Ge	Se	Ba	La	Ce	Sm	Eu	Hf	Pb	Th
IO97-01	5.3	1.2	1.0	0.8	1.7	0.8	1.3	0.9	1.0	1.0	5.9	1.9	3.9	483	2.1	2.4	2.5	1.9	1.5	2.0	31.2	3.1
IO97-02	4.2	1.1	1.0	2.0	1.8	0.7	1.3	0.8	1.1	1.2	3.9	1.9	3.5	267	2.1	2.6	2.7	2.2	1.6	1.6	19.2	3.5
IO97-03	3.9	1.1	1.0	2.4	1.7	0.7	1.2	0.8	1.0	1.0	4.7	2.0	3.7	269	2.2	2.5	2.7	2.1	1.7	1.4	20.6	3.8
IO97-04	4.3	1.1	1.0	1.7	1.5	0.7	1.2	0.8	1.0	1.1	5.0	2.0	4.1	571	2.2	2.7	2.9	2.4	1.7	2.3	26.4	3.7
IO97-05	6.4	1.2	1.0	0.9	1.3	0.7	1.3	0.8	1.4	2.0	17.1	2.1	5.7	370	2.3	2.7	2.8	2.2	1.4	1.8	33.8	3.4
IO97-06	6.1	1.2	1.0	0.5	1.3	0.7	1.3	0.8	1.1	1.3	6.3	2.3	4.7	139	2.5	3.1	3.3	2.9	2.1	1.5	35.2	4.3
IO97-07	4.3	1.0	1.0	1.1	1.4	0.7	1.4	0.8	1.2	1.4	10.6	2.3	5.1	690	2.5	3.1	3.2	2.3	1.8	2.3	35.2	4.0
IO97-08	3.7	0.9	1.0	1.2	1.3	0.7	1.1	0.8	1.2	1.6	7.4	2.2	4.6	537	2.5	3.0	3.1	2.4	1.7	1.3	27.3	4.6
IO97-09	2.8	0.8	1.0	1.1	1.4	0.7	1.3	0.8	2.4	4.1	6.6	2.3	7.1	352	2.5	3.0	3.2	2.5	1.8	1.7	27.3	4.9
IO97-10	4.6	1.0	1.0	1.4	1.4	0.8	1.3	0.8	1.1	1.1	5.9	2.1	4.2	98	2.3	2.6	2.8	2.2	1.6	1.9	24.4	4.1
IO97-11	11.1	1.8	1.0	3.8	2.7	0.7	1.5	1.0	1.5	1.6	6.1	2.3	4.7	782	2.5	3.1	3.6	2.5	1.9	1.5	24.4	4.3
IO97-12	2.3	1.0	1.0	3.5	1.0	0.7	1.1	0.8	0.7	0.9	2.0	1.4	2.6	113	1.3	2.3	2.4	1.7	1.1	1.2	4.6	3.9
IO97-13	2.1	1.2	1.0	3.1	1.4	0.7	1.1	0.7	0.7	0.9	2.2	1.5	2.5	279	1.4	2.5	2.6	1.9	1.3	1.3	6.7	3.9
IO97-14	1.7	1.2	1.0	1.6	1.7	0.7	1.1	0.7	1.0	1.1	2.9	1.6	3.0	211	1.7	2.5	2.7	1.7	1.3	1.6	8.9	3.9
IO97-15	2.3	1.3	1.0	2.7	2.1	0.5	1.5	1.1	1.2	1.1	5.5	2.2	4.3	272	2.3	2.4	3.4	1.8	1.5	1.5	25.5	2.6
IO97-16	3.2	1.1	1.0	2.0	1.4	0.7	1.1	0.8	1.0	1.0	3.9	1.9	3.3	234	1.8	2.7	2.8	2.1	1.4	2.7	19.2	4.4
IO97-17	11.2	1.5	1.0	3.1	1.5	0.6	1.4	1.0	1.4	1.7	5.5	2.3	5.5	574	2.3	2.9	3.4	2.6	1.9	3.3	21.0	3.9
IO97-18	7.2	1.3	1.0	2.2	1.3	0.7	1.2	0.8	1.1	1.2	4.7	1.9	4.3	294	1.9	2.8	2.9	2.4	1.7	1.5	19.9	4.4
IO97-19	17.5	1.6	1.0	4.5	1.9	0.6	1.7	1.1	1.4	1.4	7.2	2.8	5.9	501	2.7	3.1	3.9	2.7	2.0	5.3	33.0	4.7
IO97-20	8.4	1.7	1.0	4.3	2.6	0.5	1.6	1.1	1.3	1.7	4.0	2.5	4.1	140	2.5	2.5	3.2	2.2	1.2	2.6	18.3	3.8
IO97-21	22.5	2.9	1.0	3.8	2.5	0.7	1.1	0.7	1.4	2.3	3.4	1.5	6.1	1125	1.7	2.4	2.5	2.3	1.4	3.8	16.5	3.6
IO97-22	9.4	1.7	1.0	2.9	2.5	0.7	1.2	0.8	1.0	1.1	3.9	1.9	4.7	208	2.2	2.3	2.5	1.9	1.4	3.2	18.7	3.2
IO97-23	3.6	1.7	1.0	2.3	3.8	0.7	1.1	0.7	0.8	0.9	2.8	1.8	4.3	139	1.9	2.2	2.4	2.1	1.3	2.0	12.9	2.6
IO97-24	6.6	2.2	1.0	3.7	4.7	0.7	1.5	1.0	1.6	2.4	2.7	1.9	4.0	258	2.1	1.9	2.0	2.0	1.5	3.8	1.3	2.5
IO97-25	11.2	2.2	1.0	1.6	3.3	0.7	1.2	0.8	1.2	1.6	2.8	1.9	4.9	496	2.0	2.4	2.4	2.1	1.5	2.8	14.8	3.3
IO97-26	9.4	2.0	1.0	1.5	3.1	0.7	1.2	0.8	1.1	1.4	3.3	1.9	5.0	403	2.0	2.8	2.8	2.4	1.5	2.0	16.7	3.3
IO97-27	13.6	2.2	1.0	2.1	2.6	0.8	1.2	0.9	1.1	1.2	4.5	1.9	4.4	429	2.1	2.6	2.7	2.4	2.3	3.4	21.1	3.6
Geom. mean	5.6	1.4	1.0	2.0	1.9	0.7	1.3	0.8	1.2	1.4	4.6	2.0	4.3	318	2.1	2.6	2.8	2.2	1.6	2.1	17.8	3.7
± SD	5.0	0.5	0.0	1.1	0.9	0.1	0.2	0.1	0.3	0.7	3.0	0.3	1.1	234	0.4	0.3	0.4	0.3	0.3	1.0	9.1	0.6
continental bulk comp. ($\mu g\ g^{-1}$)	23000.0	32000.0	84100.0	9100.0	52900.0	30.0	5400.0	230.0	1400.0	70700.0	80.0	18.0	1.6	0.05	250.0	16.0	33.0	3.5	1.1	3.0	8.0	3.5

Table 5. Enrichment factors for fine aerosol fraction relative to Al, assuming continental bulk composition according to McLennan and Taylor [1985].

Sample Id	Na	Mg	Al	K	Ca	Sc	Ti	V	Mn	Fe	Zn	Ga	Ge	Se	Ba	La	Ce	Sm	Eu	Hf	Pb	Th
IO97-01	4.7	1.3	1.0	4.8	1.4	0.7	1.2	2.3	1.3	1.7	33.1	2.1	7.7	2034	2.1	2.7	2.8	2.0	1.6	2.2	279.2	3.4
IO97-02	5.7	1.5	1.0	7.3	1.6	0.7	1.1	2.5	1.4	1.7	35.5	2.1	10.6	3177	2.0	2.6	2.7	2.3	1.5	1.6	297.0	3.1
IO97-03	4.9	1.3	1.0	9.3	1.5	0.7	1.1	2.4	1.4	1.5	46.3	2.2	12.1	2609	2.0	2.8	2.9	2.2	1.4	2.1	408.2	3.7
IO97-04	4.7	1.2	1.0	10.3	1.3	0.7	1.1	2.8	2.3	3.7	57.0	2.4	17.3	3344	2.1	3.0	3.0	2.8	1.4	1.8	432.4	3.4
IO97-05	6.3	1.3	1.0	12.0	1.2	0.7	1.2	3.9	2.0	2.8	73.4	2.7	19.5	3688	2.2	3.1	3.0	2.1	1.3	2.5	577.0	3.6
IO97-06	5.8	1.2	1.0	12.2	1.2	0.7	1.4	3.0	2.6	4.2	86.5	2.8	21.9	4499	2.4	3.3	3.2	2.4	1.4	2.3	556.7	3.8
IO97-07	4.1	1.1	1.0	15.9	1.2	0.7	1.1	3.2	2.2	3.3	95.4	2.7	17.5	2657	2.5	3.2	3.2	2.1	1.6	1.6	546.9	3.9
IO97-08	4.0	1.0	1.0	16.8	1.0	0.7	1.3	3.2	1.8	2.7	71.0	2.5	15.1	3583	2.4	2.8	3.0	2.2	1.4	1.9	486.5	3.9
IO97-09	3.5	1.0	1.0	13.7	1.1	0.7	1.2	2.3	1.5	1.5	68.9	2.5	13.4	2962	2.4	2.9	3.0	2.4	1.9	1.6	445.6	4.5
IO97-10	5.7	1.2	1.0	18.2	1.1	0.8	1.4	3.3	2.3	3.1	120.1	2.9	23.0	5695	2.3	3.2	3.2	2.7	2.1	2.0	725.2	4.4
IO97-11	9.1	1.7	1.0	11.0	1.8	0.6	1.3	3.0	1.5	1.7	43.5	2.4	9.0	4290	2.4	2.9	3.4	2.2	1.6	1.7	353.7	3.3
IO97-12	2.8	1.1	1.0	4.8	0.7	0.4	1.4	1.8	1.8	3.4	8.4	1.9	6.7	1747	1.7	2.4	3.0	1.5	1.2	1.5	68.8	2.7
IO97-13	1.8	1.1	1.0	3.5	0.6	0.6	1.1	1.3	0.8	0.9	6.5	1.5	3.2	903	1.4	2.9	3.0	1.9	1.3	1.3	51.8	4.2
IO97-14	4.0	1.1	1.0	3.9	1.0	0.7	1.1	1.5	1.4	2.4	14.3	1.8	6.1	1082	1.8	3.0	3.0	2.4	1.7	1.4	108.2	4.3
IO97-15	1.7	1.3	1.0	7.2	1.3	0.7	1.2	3.2	1.7	2.6	22.1	2.0	8.8	1963	2.0	2.9	3.1	2.3	1.6	1.5	180.2	4.4
IO97-16	2.4	1.2	1.0	8.3	1.1	0.7	1.1	3.4	1.7	2.6	24.7	1.9	10.7	2653	1.8	2.7	2.8	2.0	2.0	3.3	198.7	3.4
IO97-17	7.4	1.2	1.0	14.0	1.1	0.5	1.5	3.6	1.9	2.5	41.8	2.7	12.3	4018	2.4	2.5	3.1	2.2	1.5	6.0	320.4	2.8
IO97-18	6.1	1.2	1.0	12.2	0.9	0.6	1.1	3.0	2.0	3.1	37.7	2.1	13.3	4199	1.8	2.9	2.9	2.4	1.7	3.0	304.8	3.6
IO97-19	10.5	1.5	1.0	16.3	1.1	0.6	1.2	2.2	1.2	0.9	45.3	2.1	12.2	2973	1.9	2.9	3.0	2.3	1.5	2.2	339.8	3.9
IO97-20	4.9	1.5	1.0	6.2	1.7	0.4	1.4	1.6	1.2	1.3	15.2	2.1	5.9	984	2.0	2.0	2.6	1.6	1.2	3.1	193.5	2.3
IO97-21	6.5	1.3	1.0	5.9	1.2	0.6	1.4	1.8	1.0	1.3	14.9	2.7	6.7	2285	1.8	2.4	2.7	2.0	1.9	6.0	104.5	2.9
IO97-22	4.2	1.3	1.0	7.6	1.4	0.8	1.1	1.9	1.1	1.3	21.2	1.8	7.0	2086	1.9	2.8	2.9	2.2	1.6	2.3	163.5	3.3
IO97-23	2.6	1.2	1.0	4.5	1.6	0.6	1.3	1.5	2.4	4.9	15.3	1.9	10.1	1303	1.8	2.7	2.9	2.0	1.7	2.9	157.4	3.4
IO97-24	2.7	1.8	1.0	2.7	2.3	0.7	1.1	1.3	2.2	4.0	11.6	1.9	7.4	1214	1.8	2.6	2.7	2.1	1.3	3.8	122.6	3.6
IO97-25	4.4	1.4	1.0	2.3	1.5	0.7	1.1	2.0	1.2	1.7	11.2	1.8	8.0	1318	1.9	2.6	2.6	1.9	1.4	5.8	162.4	3.1
IO97-26	4.6	1.3	1.0	2.6	1.3	0.7	1.1	2.1	1.4	2.1	12.9	2.0	9.1	2733	2.0	2.9	3.0	2.3	1.9	2.1	190.5	3.5
IO97-27	7.3	1.5	1.0	3.3	1.3	0.7	1.7	1.7	1.3	1.9	19.0	2.0	8.7	3055	1.9	3.0	3.1	2.6	1.9	3.4	195.3	3.6
Geom. mean	4.5	1.3	1.0	7.4	1.2	0.7	1.2	2.3	1.6	2.2	29.1	2.2	10.2	2422	2.0	2.8	3.0	2.2	1.6	2.4	242.8	3.5
± SD	2.1	0.2	0.0	4.9	0.3	0.1	0.2	0.8	0.5	1.0	30.0	0.4	5.0	1220	0.3	0.3	0.2	0.3	0.2	1.4	176.8	0.5
continental bulk comp. ($\mu g\ g^{-1}$)	23000.0	32000.0	84100.0	9100.0	52900.0	30.0	5400.0	230.0	1400.0	70700.0	80.0	18.0	1.6	0.05	250.0	16.0	33.0	3.5	1.1	3.0	8.0	3.5

Table 6. Enrichment factors for total aerosol relative to Al, assuming continental bulk composition according to McLennan and Taylor [1985].

Sample Id	Na	Mg	Al	K	Ca	Sc	Ti	V	Mn	Fe	Zn	Ga	Ge	Se	Ba	La	Ce	Sm	Eu	Hf	Pb	Th
IO97-01	5.1	1.3	1.0	2.6	1.6	0.7	1.2	1.5	1.2	1.3	17.7	2.0	5.6	1155	2.1	2.5	2.6	2.0	1.5	2.1	138.8	3.2
IO97-02	4.6	1.2	1.0	3.3	1.8	0.7	1.2	1.2	1.2	1.3	11.4	2.0	5.2	959	2.1	2.6	2.7	2.2	1.6	1.6	85.2	3.4
IO97-03	4.2	1.2	1.0	4.3	1.6	0.7	1.2	1.3	1.1	1.2	16.1	2.1	6.0	912	2.2	2.6	2.8	2.1	1.6	1.6	127.1	3.8
IO97-04	4.4	1.1	1.0	4.2	1.4	0.7	1.2	1.4	1.4	1.8	20.3	2.1	8.0	1386	2.2	2.8	2.9	2.5	1.6	2.1	145.7	3.6
IO97-05	6.4	1.2	1.0	5.2	1.3	0.7	1.3	2.0	1.6	2.3	38.9	2.3	11.1	1657	2.3	2.8	2.9	2.2	1.4	2.1	244.5	3.5
IO97-06	6.0	1.2	1.0	5.0	1.3	0.7	1.3	1.7	1.7	2.4	36.9	2.5	11.2	1802	2.4	3.2	3.2	2.7	1.8	1.8	234.1	4.1
IO97-07	4.2	1.0	1.0	6.8	1.3	0.7	1.3	1.8	1.6	2.1	43.3	2.4	9.9	1448	2.5	3.1	3.2	2.2	1.7	2.1	232.5	4.0
IO97-08	3.8	1.0	1.0	6.2	1.2	0.7	1.2	1.6	1.4	1.9	27.9	2.3	8.0	1519	2.5	3.0	3.1	2.4	1.6	1.5	175.3	4.3
IO97-09	3.1	0.9	1.0	5.4	1.3	0.7	1.3	1.3	2.1	3.2	28.1	2.4	9.3	1251	2.4	3.0	3.1	2.5	1.8	1.7	171.4	4.7
IO97-10	4.9	1.1	1.0	6.6	1.3	0.8	1.3	1.6	1.5	1.7	41.0	2.3	9.9	1817	2.3	2.8	2.9	2.3	1.8	2.0	239.6	4.2
IO97-11	10.4	1.8	1.0	6.3	2.4	0.6	1.5	1.7	1.5	1.6	18.9	2.4	6.2	1983	2.5	3.0	3.5	2.4	1.8	1.6	137.1	3.9
IO97-12	2.5	1.1	1.0	3.8	0.9	0.6	1.2	1.0	1.0	1.5	3.6	1.5	3.6	526	1.4	2.3	2.6	1.7	1.2	1.3	20.9	3.6
IO97-13	2.0	1.1	1.0	3.2	1.1	0.7	1.1	0.9	0.7	0.9	3.6	1.5	2.7	480	1.4	2.6	2.7	1.9	1.3	1.3	21.2	4.0
IO97-14	2.8	1.2	1.0	2.7	1.4	0.7	1.1	1.1	1.1	1.7	8.3	1.7	4.5	626	1.7	2.7	2.8	2.0	1.5	1.5	56.2	4.1
IO97-15	2.0	1.3	1.0	4.7	1.8	0.6	1.4	2.1	1.4	1.7	12.9	2.1	6.3	1023	2.2	2.7	3.2	2.1	1.5	1.5	94.2	3.3
IO97-16	2.9	1.2	1.0	4.5	1.3	0.7	1.1	1.9	1.3	1.7	12.3	1.9	6.3	1214	1.8	2.7	2.8	2.1	1.6	3.0	91.9	4.0
IO97-17	9.7	1.4	1.0	7.3	1.4	0.6	1.4	2.0	1.6	2.0	19.4	2.5	8.1	1890	2.3	2.8	3.3	2.4	1.8	4.3	135.5	3.5
IO97-18	6.7	1.2	1.0	7.1	1.1	0.7	1.1	1.9	1.5	2.1	20.8	2.0	8.7	2195	1.8	2.9	2.9	2.4	1.7	2.2	158.6	4.0
IO97-19	13.8	1.6	1.0	10.9	1.5	0.6	1.4	1.7	1.3	1.2	27.6	2.4	9.3	1826	2.3	3.0	3.4	2.5	1.7	3.6	197.5	4.3
IO97-20	6.6	1.6	1.0	5.2	2.1	0.4	1.5	1.4	1.2	1.5	9.7	2.3	5.0	569	2.3	2.3	2.9	1.9	1.2	2.8	107.4	3.0
IO97-21	13.1	2.0	1.0	5.0	1.7	0.6	1.3	1.4	1.2	1.7	10.1	2.2	6.5	1806	1.7	2.4	2.6	2.1	1.7	5.1	68.1	3.2
IO97-22	6.8	1.5	1.0	5.3	1.9	0.7	1.1	1.3	1.1	1.2	12.6	1.8	5.9	1154	2.0	2.5	2.7	2.0	1.5	2.8	91.7	3.2
IO97-23	3.2	1.5	1.0	3.2	2.9	0.6	1.2	1.0	1.5	2.5	8.0	1.8	6.7	620	1.8	2.4	2.6	2.1	1.5	2.4	72.7	2.9
IO97-24	4.1	2.0	1.0	3.1	3.2	0.7	1.3	1.2	2.0	3.4	8.3	1.9	6.1	857	1.9	2.3	2.5	2.1	1.4	3.8	77.3	3.2
IO97-25	8.3	1.8	1.0	1.9	2.5	0.7	1.2	1.3	1.2	1.7	6.5	1.9	6.3	854	1.9	2.5	2.5	2.0	1.5	4.1	79.1	3.2
IO97-26	7.5	1.7	1.0	1.9	2.4	0.7	1.2	1.3	1.2	1.7	7.0	1.9	6.6	1312	2.0	2.8	2.9	2.4	1.6	2.0	84.5	3.4
IO97-27	9.9	1.8	1.0	2.8	1.8	0.8	1.5	1.3	1.2	1.6	13.0	2.0	7.0	1963	2.0	2.8	2.9	2.5	2.0	3.4	122.9	3.6
Geom. mean	5.1	1.3	1.0	4.4	1.6	0.7	1.3	1.4	1.3	1.7	14.5	2.1	6.7	1179	2.0	2.7	2.9	2.2	1.6	2.2	108.1	3.7
± SD	3.2	0.3	0.0	2.0	0.6	0.1	0.1	0.3	0.3	0.6	11.6	0.3	2.1	512	0.3	0.3	0.3	0.2	0.2	1.0	63.9	0.5
continental bulk comp. ($\mu g\ g^{-1}$)	23000.0	32000.0	84100.0	9100.0	52900.0	30.0	5400.0	230.0	1400.0	70700.0	80.0	18.0	1.6	0.05	250.0	16.0	33.0	3.5	1.1	3.0	8.0	3.5

Table 7. Varimax rotated principal component martix. Trace metals and ions. Includes 23 samples.

variance	30.3%	22.4%	10.8%	8.9%	5.3%	4.6%	3.3%	2.8%	2.1%
Element\Component	1 crustal coarse + some fine	2 anthrop.	3 crustal fine, Ca and Mg	4 sea salt coarse + some fine	5 crustal fine	6 MSA& NSS-SO_4^{2-} coarse	7	8 Fe&Mn fine	9
Na-coarse	0.244	-0.061	0.098	**0.908**	0.046	-0.094	0.136	-0.183	-0.026
Na-fine	0.118	0.092	0.312	**0.669**	**0.470**	0.184	0.081	-0.144	0.123
Mg-coarse	**0.870**	-0.276	0.205	0.227	0.078	0.074	0.023	0.111	-0.072
Mg-fine	0.345	-0.246	**0.755**	0.084	**0.423**	0.169	0.021	0.124	0.075
Al-coarse	**0.963**	-0.046	0.034	0.056	0.054	0.122	0.007	0.133	0.040
Al-fine	**0.578**	-0.261	**0.506**	-0.082	**0.486**	0.119	-0.009	0.189	0.133
K-coarse	**0.851**	-0.242	0.187	0.232	0.099	0.058	0.100	0.216	0.139
K-fine	0.262	**0.802**	-0.013	0.137	0.220	-0.049	0.119	0.077	0.362
Ca-coarse	**0.686**	-0.203	**0.540**	0.143	-0.071	0.057	-0.044	0.004	-0.294
Ca-fine	0.003	-0.097	**0.930**	0.084	0.257	0.117	-0.001	0.081	-0.063
Sc-coarse	**0.951**	-0.020	-0.055	0.041	0.024	0.155	0.001	0.120	-0.047
Sc-fine	**0.522**	-0.183	**0.449**	-0.378	**0.433**	0.212	-0.091	0.001	0.001
V-coarse	**0.942**	0.012	0.144	0.156	0.033	0.150	0.014	0.085	0.115
V-fine	0.390	0.333	0.182	0.053	0.048	0.245	-0.160	0.090	**0.693**
Mn-coarse	**0.892**	0.177	0.113	0.064	0.055	-0.026	0.110	-0.181	0.082
Mn-fine	0.278	0.128	**0.475**	-0.108	0.085	0.249	-0.123	**0.733**	0.022
Fe-coarse	**0.771**	0.055	0.021	-0.021	0.118	-0.199	0.211	-0.116	0.068
Fe-fine	0.180	-0.011	0.371	-0.180	-0.040	0.243	-0.134	**0.807**	-0.067
Zn-coarse	**0.477**	**0.613**	-0.187	-0.015	-0.128	0.184	0.199	-0.156	0.103
Zn-fine	-0.017	**0.945**	-0.234	-0.016	0.091	0.096	0.057	0.022	-0.007
Ge-coarse	**0.938**	0.226	-0.016	0.106	-0.063	-0.063	0.053	-0.025	-0.005
Ge-fine	0.137	**0.864**	0.020	-0.037	0.055	0.100	-0.222	0.356	0.014
Se-coarse	**0.509**	0.015	-0.122	0.130	-0.193	0.119	**0.432**	-0.335	0.003
Se-fine	0.279	**0.659**	-0.265	**0.407**	-0.053	0.161	-0.226	0.085	0.172
La-coarse	**0.975**	0.047	-0.008	0.070	0.041	0.123	0.036	0.061	0.069
La-fine	**0.616**	-0.194	0.364	-0.272	**0.451**	0.211	-0.028	0.146	0.071
Sm-coarse	**0.970**	0.096	0.040	0.129	-0.003	0.068	0.002	0.058	0.026
Sm-fine	**0.553**	-0.127	**0.444**	-0.280	**0.486**	0.236	-0.133	0.072	0.038
Pb-coarse	0.390	**0.757**	-0.036	0.077	-0.219	0.067	-0.024	-0.317	0.093
Pb-fine	0.003	**0.955**	-0.016	0.114	0.097	0.093	-0.039	-0.083	-0.016
FeII-coarse$_{total,22hrsFZ}$	**0.604**	**0.482**	0.196	0.198	0.120	0.369	-0.117	-0.104	-0.006
FeII-fine$_{total,22hrsFZ}$	0.384	0.308	**0.496**	-0.183	-0.250	0.212	0.206	0.229	0.382
FeII-coarse$_{total,5minFZ}$	**0.727**	0.161	0.092	0.044	**0.534**	0.197	0.029	0.001	-0.010
FeII-fine$_{total,5minFZ}$	0.319	0.334	0.151	-0.268	-0.470	0.225	0.076	0.254	**0.517**
Na^+-coarse	0.022	0.065	0.029	**0.943**	-0.114	0.072	0.125	0.040	-0.141
Na^+-fine	0.060	0.197	0.177	**0.523**	0.069	0.023	**0.773**	-0.022	0.035
Mg^{2+}-coarse	**0.448**	0.008	0.081	**0.798**	0.101	0.191	0.168	-0.041	-0.003
Mg^{2+}-fine	0.128	-0.019	**0.669**	0.376	-0.133	0.041	0.289	0.150	**0.386**
K^+-coarse	-0.019	**0.637**	-0.163	**0.647**	0.143	0.125	-0.002	-0.138	0.043
K^+-fine	-0.120	**0.878**	-0.132	-0.015	-0.118	-0.181	0.108	0.015	0.305
NSS-K^+-coarse	-0.038	**0.766**	-0.226	0.227	0.253	0.114	-0.080	-0.200	0.144
NSS-K^+-fine	-0.126	**0.874**	-0.145	-0.053	-0.126	-0.186	0.053	0.016	0.308

Table 7. (cont.) Varimax rotated principal component martix. Includes 23 samples.

variance	30.3%	22.4%	10.8%	8.9%	5.3%	4.6%	3.3%	2.8%	2.1%
Element\Component	1 crustal coarse + some fine	2 anthrop.	3 crustal fine, Ca and Mg	4 sea salt coarse + some fine	5 crustal fine	6 MSA& NSS-SO_4^{2-} coarse	7	8 Fe&Mn fine	9
Ca^{2+}-coarse	**0.634**	-0.274	**0.488**	0.160	0.085	0.385	0.077	0.113	-0.200
Ca^{2+}-fine	0.033	-0.201	**0.938**	0.117	0.039	0.017	0.157	0.129	-0.033
NSS-Ca^{2+}-coarse	**0.638**	-0.278	**0.491**	0.119	0.091	0.385	0.073	0.113	-0.195
NSS-Ca^{2+}-fine	0.029	-0.219	**0.943**	0.079	0.034	0.014	0.102	0.134	-0.037
NH_4^+-coarse	-0.163	**0.464**	-0.378	0.039	0.176	**0.516**	-0.339	0.131	0.012
NH_4^+-fine	-0.137	**0.889**	-0.111	-0.243	-0.246	-0.028	0.129	-0.013	-0.096
NO_3^--coarse	0.387	**0.640**	-0.191	0.142	-0.242	0.398	-0.134	-0.302	-0.001
NO_3^--fine	0.317	-0.321	0.179	0.277	**0.734**	0.019	0.003	0.048	-0.195
SO_4^{2-}-coarse	0.212	0.159	0.233	**0.451**	-0.070	**0.780**	0.111	0.113	0.011
SO_4^{2-}-fine	-0.158	**0.902**	0.009	-0.122	-0.335	0.004	0.103	0.037	-0.036
NSS-SO_4^{2-}-coarse	0.235	0.151	0.257	0.020	-0.021	**0.873**	0.063	0.111	0.088
NSS-SO_4^{2-}-fine	-0.161	**0.900**	0.003	-0.141	-0.338	0.003	0.079	0.038	-0.037
MSA-coarse	0.302	-0.181	0.094	-0.007	0.255	**0.613**	0.357	0.282	0.136
MSA-fine	0.410	0.229	-0.247	0.271	-0.332	0.206	0.124	-0.313	-0.033
Cl^--coarse	0.195	-0.263	0.103	**0.906**	0.065	0.067	0.200	-0.048	0.007
Cl^--fine	-0.006	-0.192	0.414	**0.452**	**0.587**	-0.323	0.077	0.076	0.045
Cl^-deficit-coarse	-0.351	**0.647**	-0.157	-0.116	-0.335	-0.005	-0.177	0.168	-0.269
Cl^-deficit-fine	0.068	0.290	0.028	0.388	-0.157	0.151	**0.808**	-0.053	0.019
(cation-anion)-coarse	0.205	-0.219	0.251	0.069	0.023	0.057	-0.161	0.282	-0.620
(cation-anion)-fine	0.176	-0.240	0.253	0.130	0.108	0.005	**0.797**	-0.116	0.058
wind speed	-0.479	0.108	0.109	**0.432**	0.212	-0.349	0.191	0.132	0.330

Table 8. Average, minimum and maximum atmospheric anion and cation concentrations in coarse, fine and total aerosol fractions. Sample number is 25 for the coarse, 26 for the fine and 24 for the total fraction of the anions and 27 for all cations. Concentrations in ng m^{-3} unless otherwise noted.

Element	Coarse			Fine			Total		
	Average ± SD	Min.	Max.	Average ± SD	Min.	Max.	Average ± SD	Min.	Max.
Cl^- (μg m^{-3})	0.65 ± 0.37	0.13	1.55	0.06 ± 0.08	0.01	0.4	0.69 ± 0.42	0.15	1.67
NSS-Cl^- (μg m^{-3})	- 0.26 ± 0.18	-0.63	0.02	- 0.54 ± 0.22	-1.14	-0.22	- 0.78 ± 0.28	-1.64	-0.32
SO_4^{2-} (μg m^{-3})	0.34 ± 0.38	0.11	0.58	2.87 ± 1.03	1.34	5.25	3.15 ± 1.07	1.61	5.65
NSS-SO_4^{2-} (μg m^{-3})	0.22 ± 0.09	0.04	0.4	2.78 ± 1.02	1.26	5.09	2.94 ± 1.06	1.42	5.38
NO_3^- (μg m^{-3})	0.78 ± 0.28	0.31	1.41	0.15 ± 0.09	0.04	0.36	0.93 ± 0.27	0.45	1.56
MSA	1.98 ± 0.96	0.54	4.01	23.9 ± 6.9	11.8	41.6	25.4 ± 6.8	12.7	45
NH_4^+	38.8 ± 19.2	11.8	84.3	655 ± 307	232	1409	693 ± 312	255	1461
Na^+ (μg m^{-3})	0.50 ± 0.19	0.19	1.01	0.35 ± 0.14	0.13	0.65	0.85 ± 0.28	0.37	1.57
K^+	28.9 ± 13.3	11.1	65.7	159 ± 82	52.6	385	187 ± 90	76	422
NSS-K^+	10.5 ± 10.5	-8	42.1	146 ± 80	43.3	361	156 ± 87	48	372
Mg^{2+}	68.2 ± 28.0	24.2	131.3	50.9 ± 16.1	25.5	88.2	119 ± 38	65.3	209
NSS-Mg^{2+}	8.9 ± 17.0	-29.9	47	9.6 ± 13.8	-22.1	43.4	18.5 ± 23.8	-28.6	62.7
Ca^{2+}	301 ± 168	591	705	103 ± 65	8.2	300	404 ± 215	119	850
NSS-Ca^{2+}	282 ± 167	44.3	680.4	89.8 ± 64.2	-1.63	288	372 ± 213	89	824

Table 9. Weighted multiple linear regression outputs for coarse SO_4^{2-} fractions as dependent variable.

Model #	Dependent Variable	Model Summary			Independent Variables	Unstandardized Coefficients		Standardized Coefficients	t	Sig.	95% Confidence Interval for B	
		R^2	F	Sig.		B	Std. Error	b			Lower Bound	Upper Bound
1	coarse-SO_4^{2-}	0.596	7.382	0.001	(constant)	30.279	63.344		0.478	0.638	-101.854	162.412
					Na^+-coarse	0.248	0.082	0.441	3.013	0.007	0.076	0.419
					MSA-coarse	41.294	18.524	0.378	2.229	0.037	2.654	79.933
					NSS-Ca^{2+}-coarse	0.089	0.112	0.137	0.795	0.436	-0.144	0.321
					NO_3^--coarse	0.104	0.056	0.274	1.848	0.079	-0.013	0.220
2	coarse-SO_4^{2-}	0.583	9.803	0.000	(constant)	31.418	62.770		0.501	0.622	-99.119	161.955
					Na^+-coarse	0.253	0.081	0.450	3.112	0.005	0.084	0.422
					MSA-coarse	49.216	15.476	0.451	3.180	0.005	17.032	81.400
					NO_3^--coarse	0.112	0.054	0.298	2.066	0.051	-0.001	0.226
3	coarse-SO_4^{2-}	0.966	208.952	0.000	Na^+-coarse	0.272	0.071	0.406	3.851	0.001	0.126	0.418
					MSA-coarse	52.753	13.532	0.320	3.899	0.001	24.691	80.816
					NO_3^--coarse	0.128	0.043	0.298	2.953	0.007	0.038	0.218

Table 10. Weighted multiple linear regression outputs for fine SO_4^{2-} fractions as dependent variable.

Model #	Dependent Variable	Model Summary			Independent Variables	Unstandardized Coefficients		Standardized Coefficients	t	Sig.	95% Confidence Interval for B	
		R^2	F	Sig.		B	Std. Error	b			Lower Bound	Upper Bound
1	fine-SO_4^{2-}	0.930	70.124	0.000	(constant)	355.619	295.541		1.203	0.242	-258.992	970.230
					Na^{2+}-fine	0.071	0.458	0.010	0.155	0.878	-0.881	1.023
					MSA-fine	10.800	9.594	0.071	1.126	0.273	-9.151	30.752
					NH_4^+-fine	3.246	0.215	0.978	15.113	0.000	2.800	3.693
					NSS-Ca^{2+}-fine	1.952	1.018	0.123	1.917	0.069	-0.166	4.069
2	fine-SO_4^{2-}	0.929	95.468	0.000	(constant)	338.441	286.953		1.179	0.251	-256.664	933.546
					MSA-fine	9.808	9.096	0.065	1.078	0.293	-9.056	28.672
					NH_4^+-fine	3.229	0.205	0.980	15.728	0.000	2.803	3.655
					NSS-Ca^{2+}-fine	1.864	0.975	0.118	1.911	0.069	-0.159	3.887

Figure 1

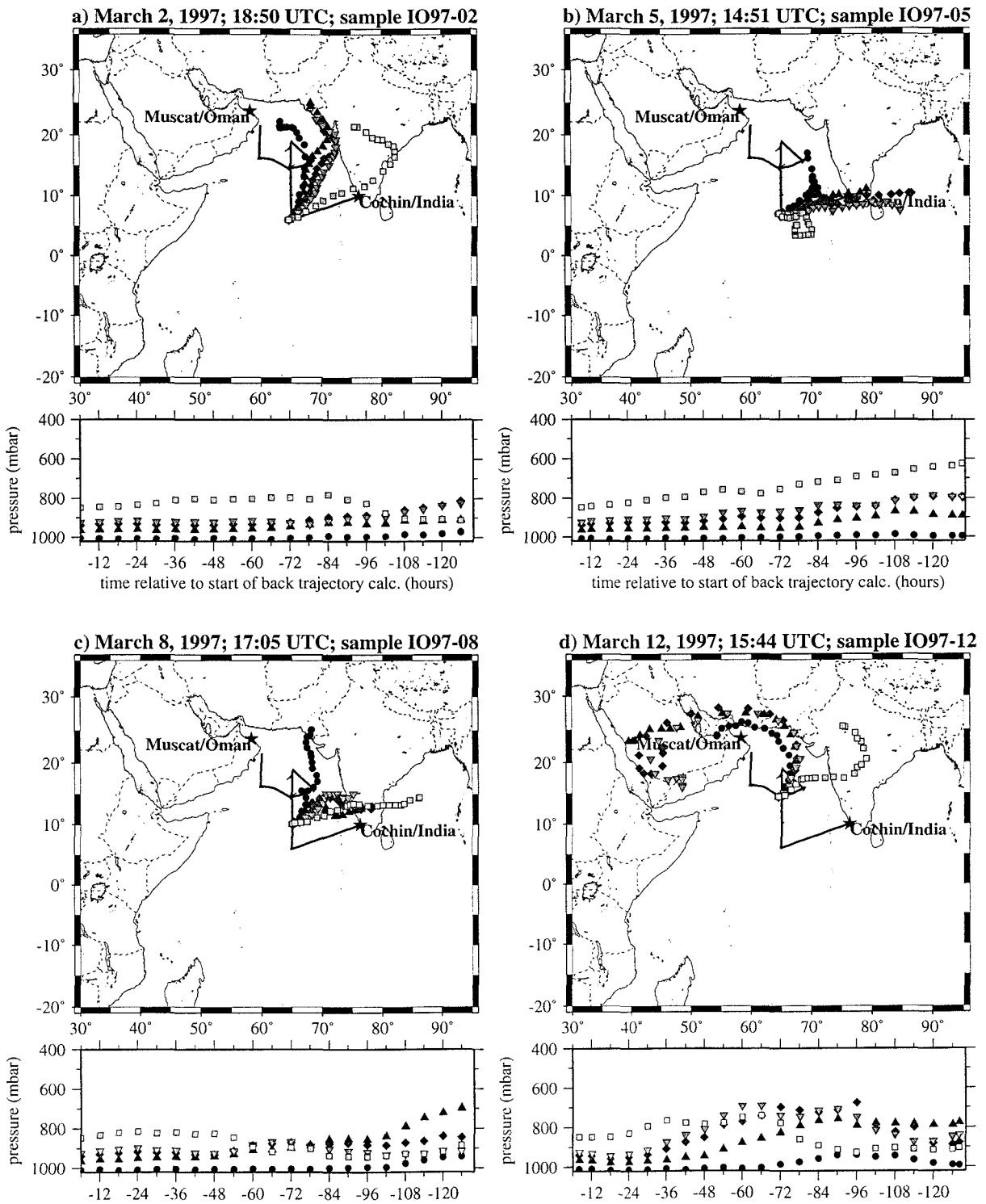
a) March 2, 1997; 18:50 UTC; sample IO97-02
b) March 5, 1997; 14:51 UTC; sample IO97-05
c) March 8, 1997; 17:05 UTC; sample IO97-08
d) March 12, 1997; 15:44 UTC; sample IO97-12
Muscat/Oman
Cochin/India
30°
20°
10°
0°
-10°
-20°
30°
40°
50°
60°
70°
80°
90°
400
600
800
1000
pressure (mbar)
-12 -24 -36 -48 -60 -72 -84 -96 -108 -120
time relative to start of back trajectory calc. (hours)

Figure 1 (continued)

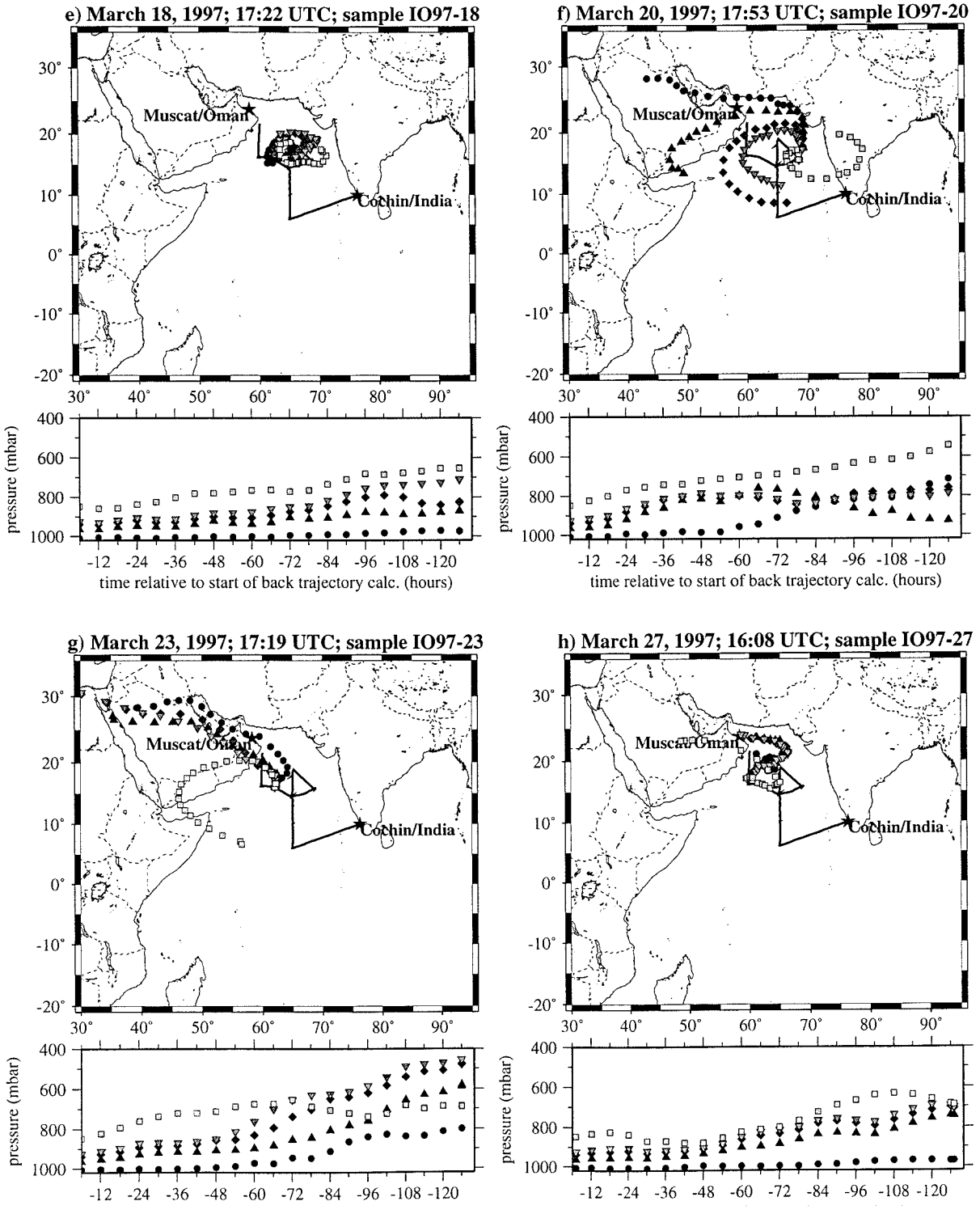

Figure 2

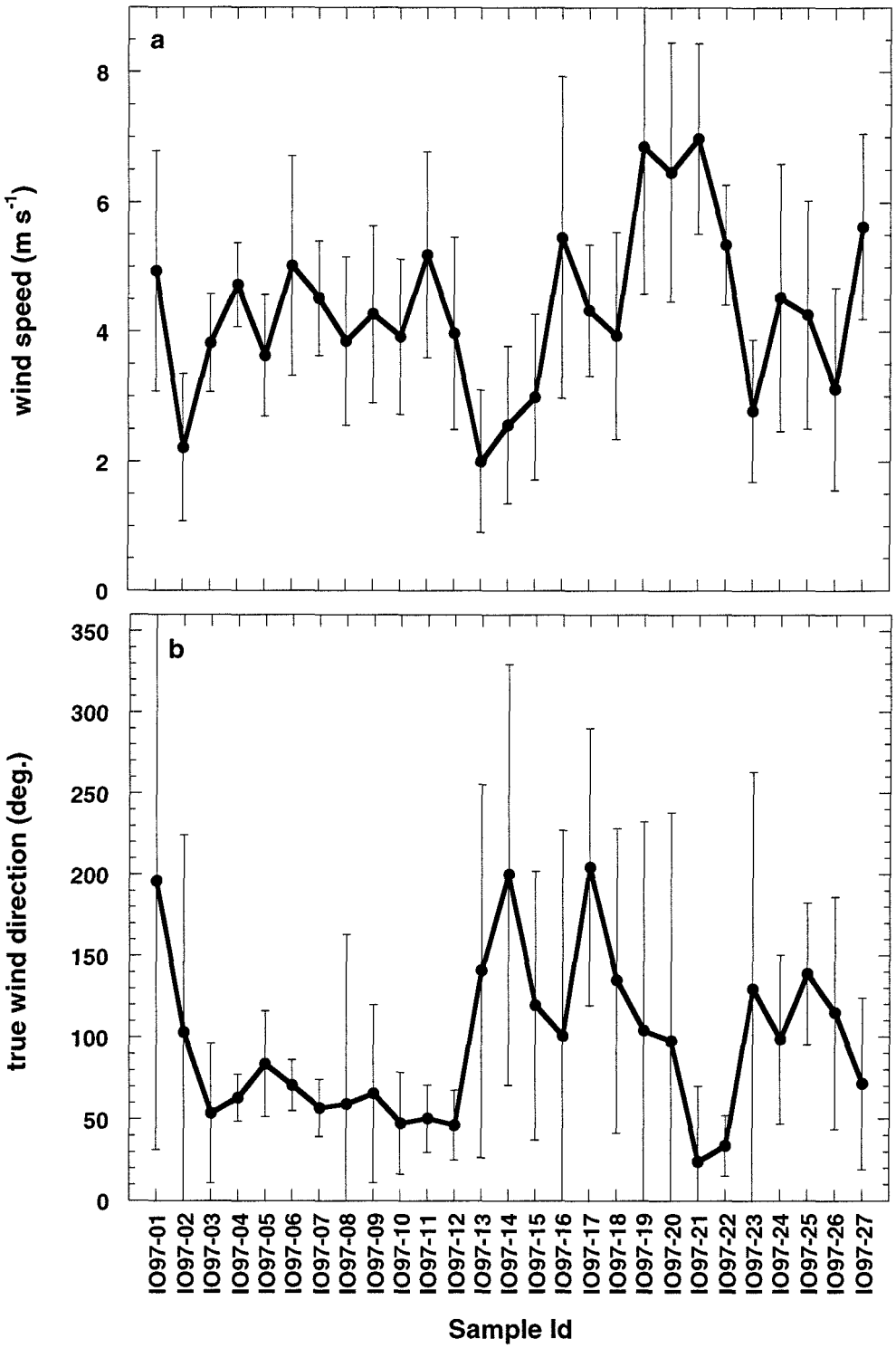
a
b
wind speed (m s-1)
true wind direction (deg.)
0
2
4
6
8
0
50
100
150
200
250
300
350
IO97-01
IO97-02
IO97-03
IO97-04
IO97-05
IO97-06
IO97-07
IO97-08
IO97-09
IO97-10
IO97-11
IO97-12
IO97-13
IO97-14
IO97-15
IO97-16
IO97-17
IO97-18
IO97-19
IO97-20
IO97-21
IO97-22
IO97-23
IO97-24
IO97-25
IO97-26
IO97-27
Sample Id

Figure 3

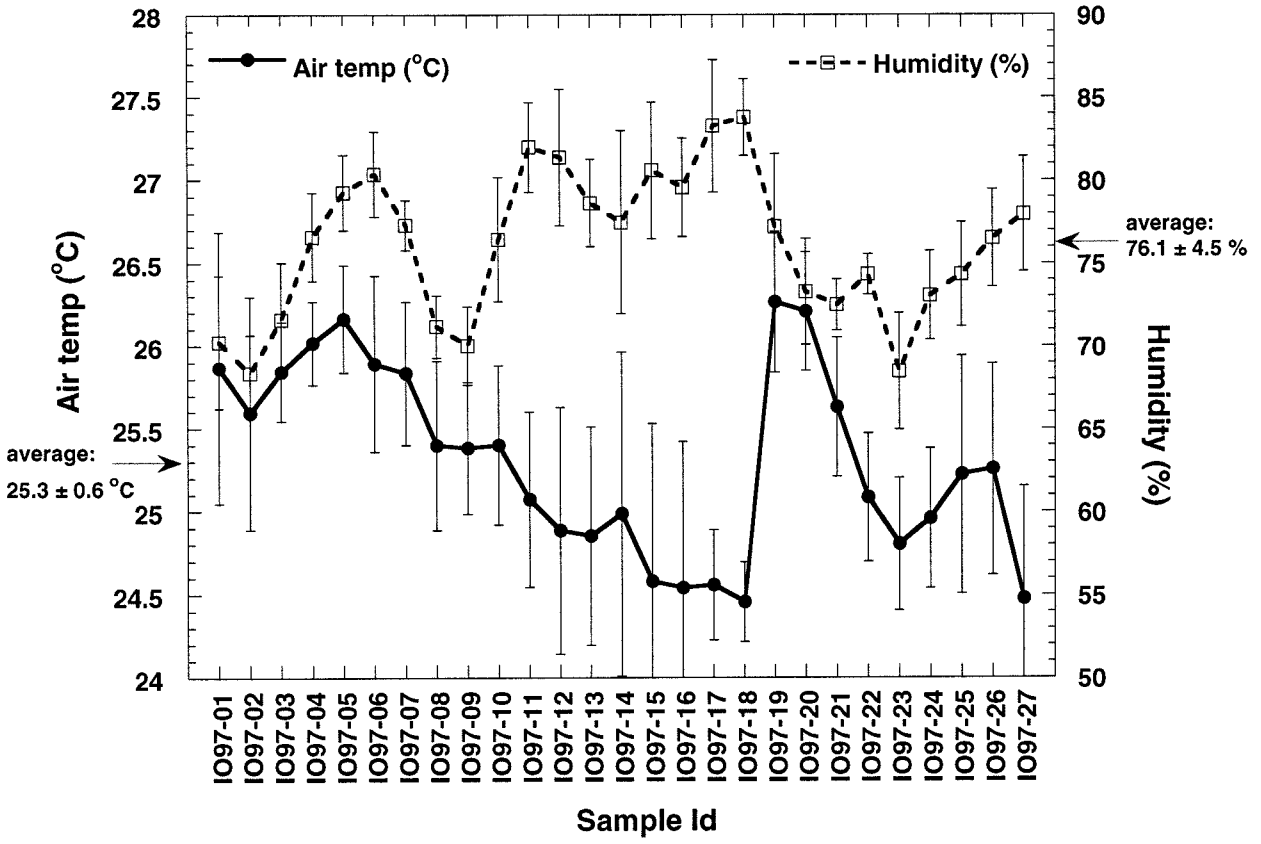
Air temp (°C)
Humidity (%)
Air temp (°C)
Humidity (%)
average:
25.3 ± 0.6 °C
average:
76.1 ± 4.5 %
28
27.5
27
26.5
26
25.5
25
24.5
24
90
85
80
75
70
65
60
55
50
IO97-01
IO97-02
IO97-03
IO97-04
IO97-05
IO97-06
IO97-07
IO97-08
IO97-09
IO97-10
IO97-11
IO97-12
IO97-13
IO97-14
IO97-15
IO97-16
IO97-17
IO97-18
IO97-19
IO97-20
IO97-21
IO97-22
IO97-23
IO97-24
IO97-25
IO97-26
IO97-27
Sample Id

Figure 4

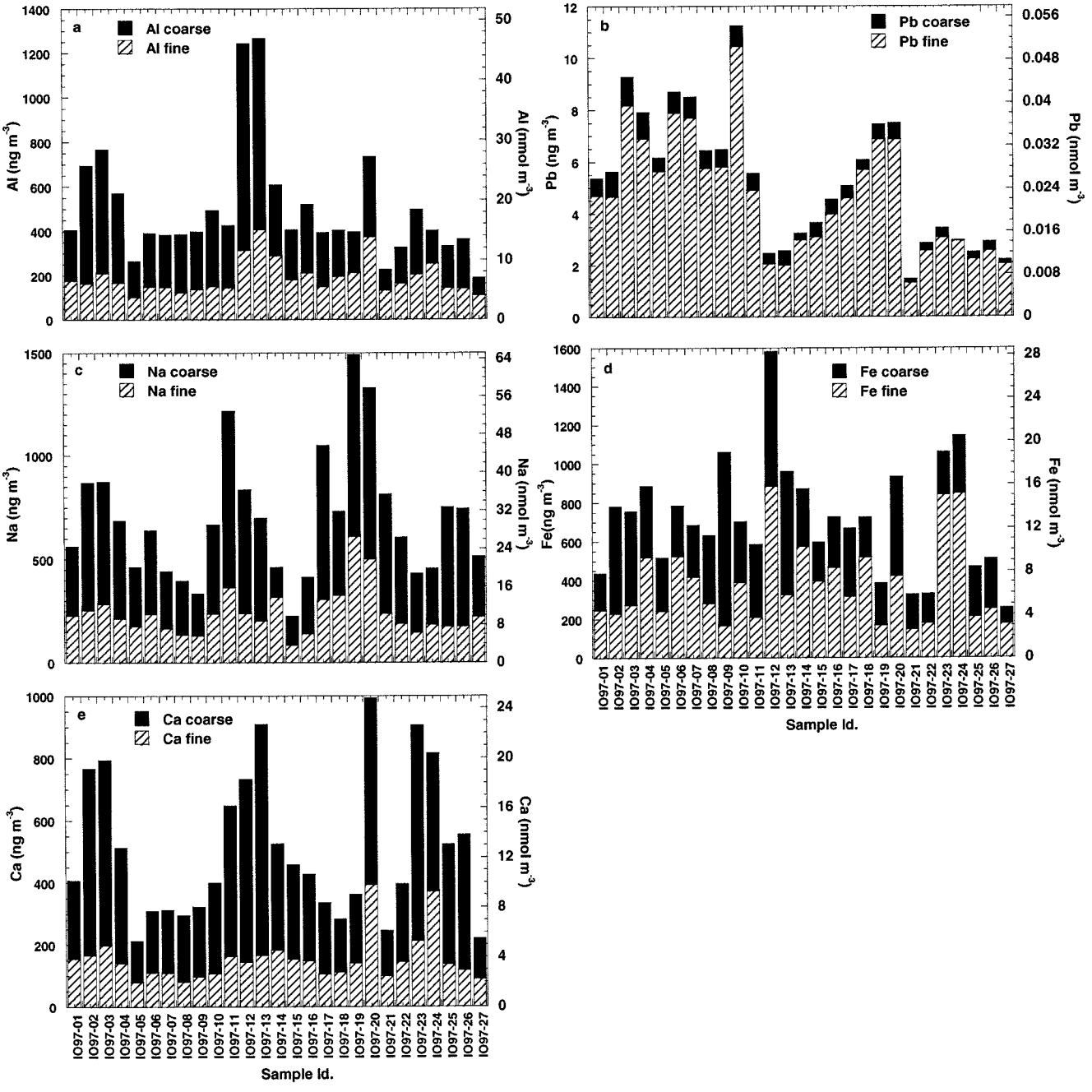
a
Al coarse
Al fine
Al (ng m-3)
Al (nmol m-3)
b
Pb coarse
Pb fine
Pb (ng m-3)
Pb (nmol m-3)
c
Na coarse
Na fine
Na (ng m-3)
Na (nmol m-3)
d
Fe coarse
Fe fine
Fe(ng m-3)
Fe (nmol m-3)
e
Ca coarse
Ca fine
Ca (ng m-3)
Ca (nmol m-3)
IO97-01
IO97-02
IO97-03
IO97-04
IO97-05
IO97-06
IO97-07
IO97-08
IO97-09
IO97-10
IO97-11
IO97-12
IO97-13
IO97-14
IO97-15
IO97-16
IO97-17
IO97-18
IO97-19
IO97-20
IO97-21
IO97-22
IO97-23
IO97-24
IO97-25
IO97-26
IO97-27
Sample Id.

Figure 5

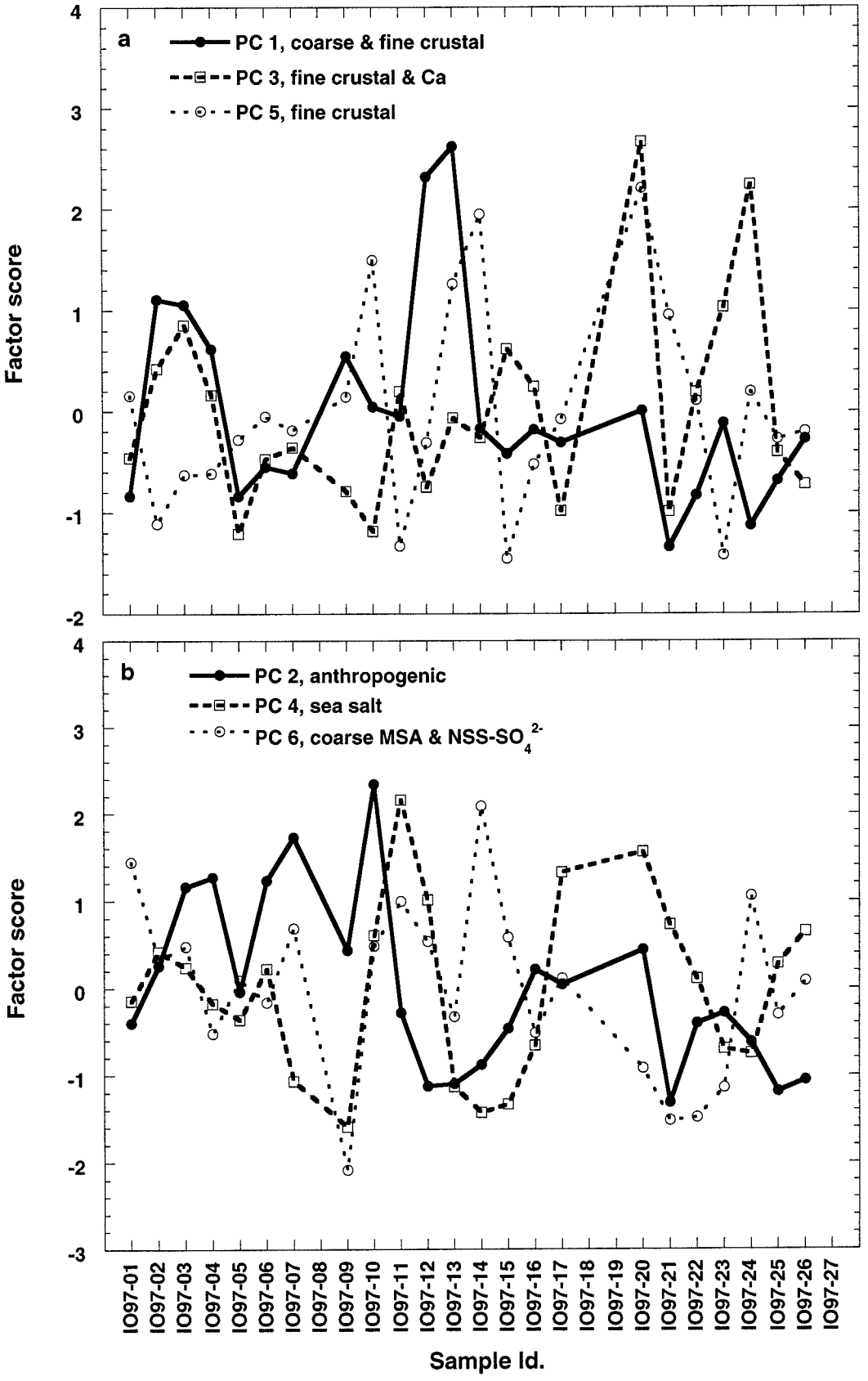
a
PC 1, coarse & fine crustal
PC 3, fine crustal & Ca
PC 5, fine crustal
b
PC 2, anthropogenic
PC 4, sea salt
PC 6, coarse MSA & NSS-SO4 2-
Factor score
Factor score
4
3
2
1
0
-1
-2
-3
IO97-01
IO97-02
IO97-03
IO97-04
IO97-05
IO97-06
IO97-07
IO97-08
IO97-09
IO97-10
IO97-11
IO97-12
IO97-13
IO97-14
IO97-15
IO97-16
IO97-17
IO97-18
IO97-19
IO97-20
IO97-21
IO97-22
IO97-23
IO97-24
IO97-25
IO97-26
IO97-27
Sample Id.

Figure 6

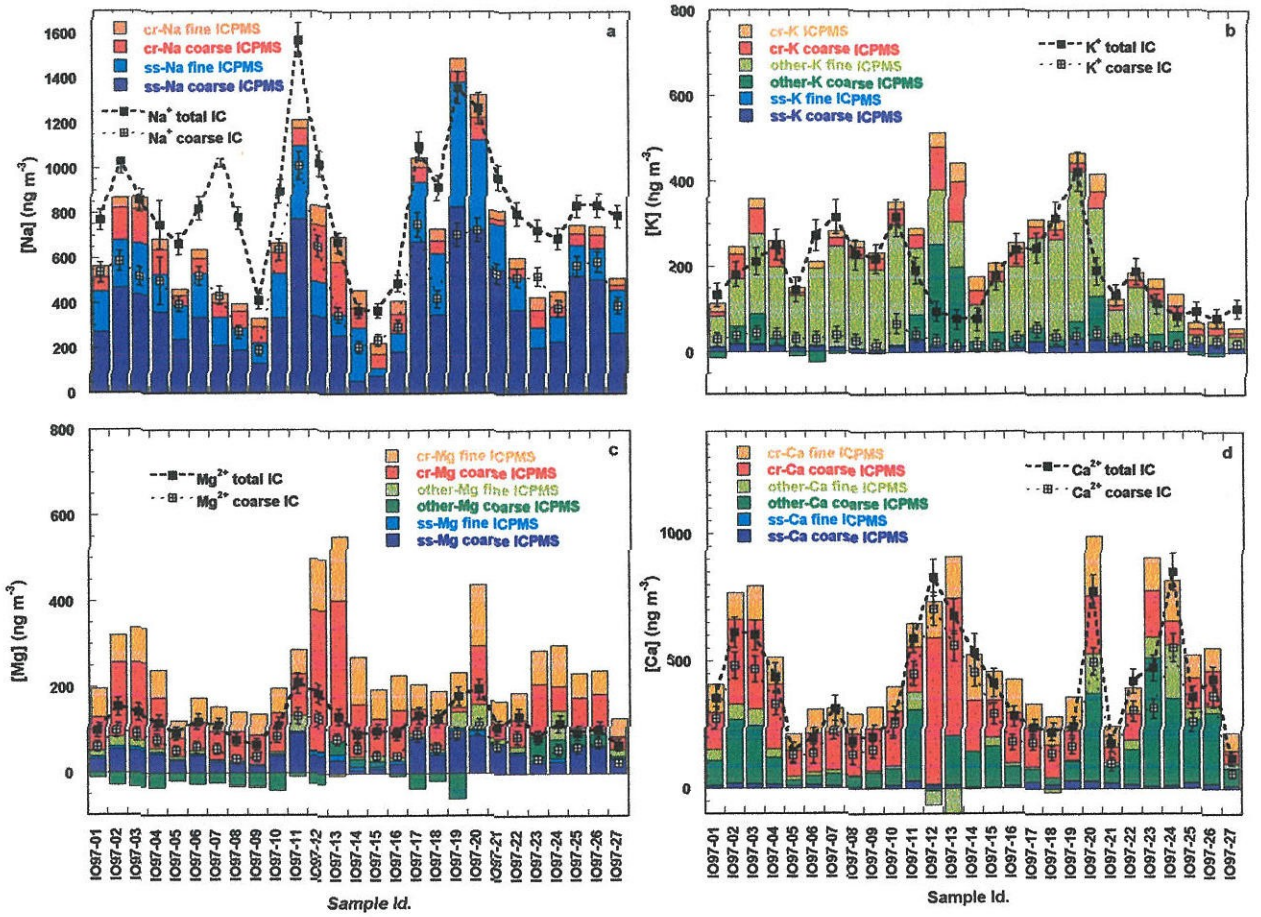
a
cr-Na fine ICPMS
cr-Na coarse ICPMS
ss-Na fine ICPMS
ss-Na coarse ICPMS
Na+ total IC
Na+ coarse IC
[Na] (ng m-3)
b
cr-K ICPMS
cr-K coarse ICPMS
other-K fine ICPMS
other-K coarse ICPMS
ss-K fine ICPMS
ss-K coarse ICPMS
K+ total IC
K+ coarse IC
[K] (ng m-3)
c
Mg2+ total IC
Mg2+ coarse IC
cr-Mg fine ICPMS
cr-Mg coarse ICPMS
other-Mg fine ICPMS
other-Mg coarse ICPMS
ss-Mg fine ICPMS
ss-Mg coarse ICPMS
[Mg] (ng m-3)
d
cr-Ca fine ICPMS
cr-Ca coarse ICPMS
other-Ca fine ICPMS
other-Ca coarse ICPMS
ss-Ca fine ICPMS
ss-Ca coarse ICPMS
Ca2+ total IC
Ca2+ coarse IC
[Ca] (ng m-3)
IO97-01 IO97-02 IO97-03 IO97-04 IO97-05 IO97-06 IO97-07 IO97-08 IO97-09 IO97-10 IO97-11 IO97-12 IO97-13 IO97-14 IO97-15 IO97-16 IO97-17 IO97-18 IO97-19 IO97-20 IO97-21 IO97-22 IO97-23 IO97-24 IO97-25 IO97-26 IO97-27
Sample Id.

Figure 7

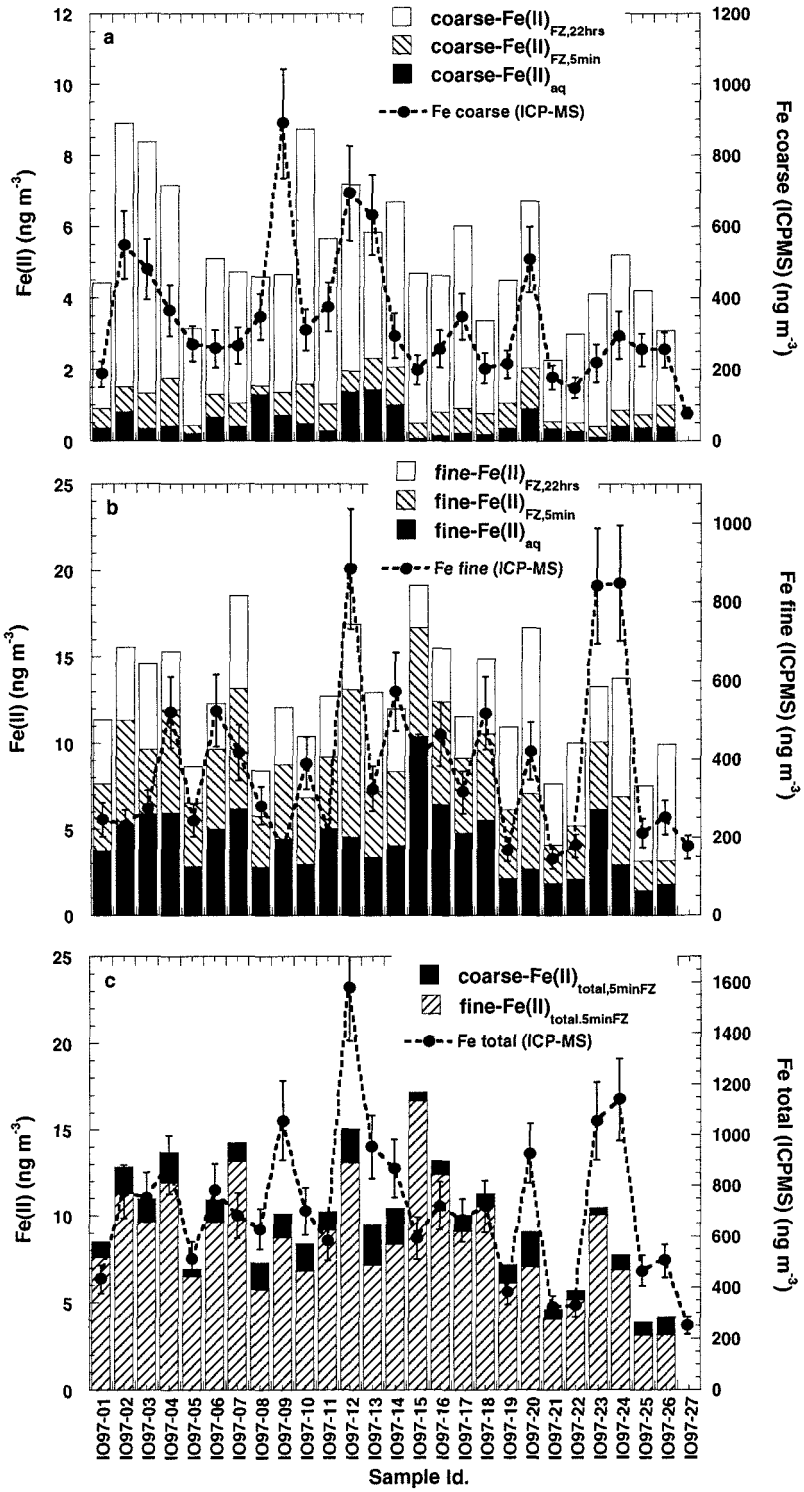
a
coarse-Fe(II)FZ,22hrs
coarse-Fe(II)FZ,5min
coarse-Fe(II)aq
Fe coarse (ICP-MS)
Fe(II) (ng m-3)
Fe coarse (ICPMS) (ng m-3)
b
fine-Fe(II)FZ,22hrs
fine-Fe(II)FZ,5min
fine-Fe(II)aq
Fe fine (ICP-MS)
Fe(II) (ng m-3)
Fe fine (ICPMS) (ng m-3)
c
coarse-Fe(II)total,5minFZ
fine-Fe(II)total,5minFZ
Fe total (ICP-MS)
Fe(II) (ng m-3)
Fe total (ICPMS) (ng m-3)
IO97-01
IO97-02
IO97-03
IO97-04
IO97-05
IO97-06
IO97-07
IO97-08
IO97-09
IO97-10
IO97-11
IO97-12
IO97-13
IO97-14
IO97-15
IO97-16
IO97-17
IO97-18
IO97-19
IO97-20
IO97-21
IO97-22
IO97-23
IO97-24
IO97-25
IO97-26
IO97-27
Sample Id.

Figure 8

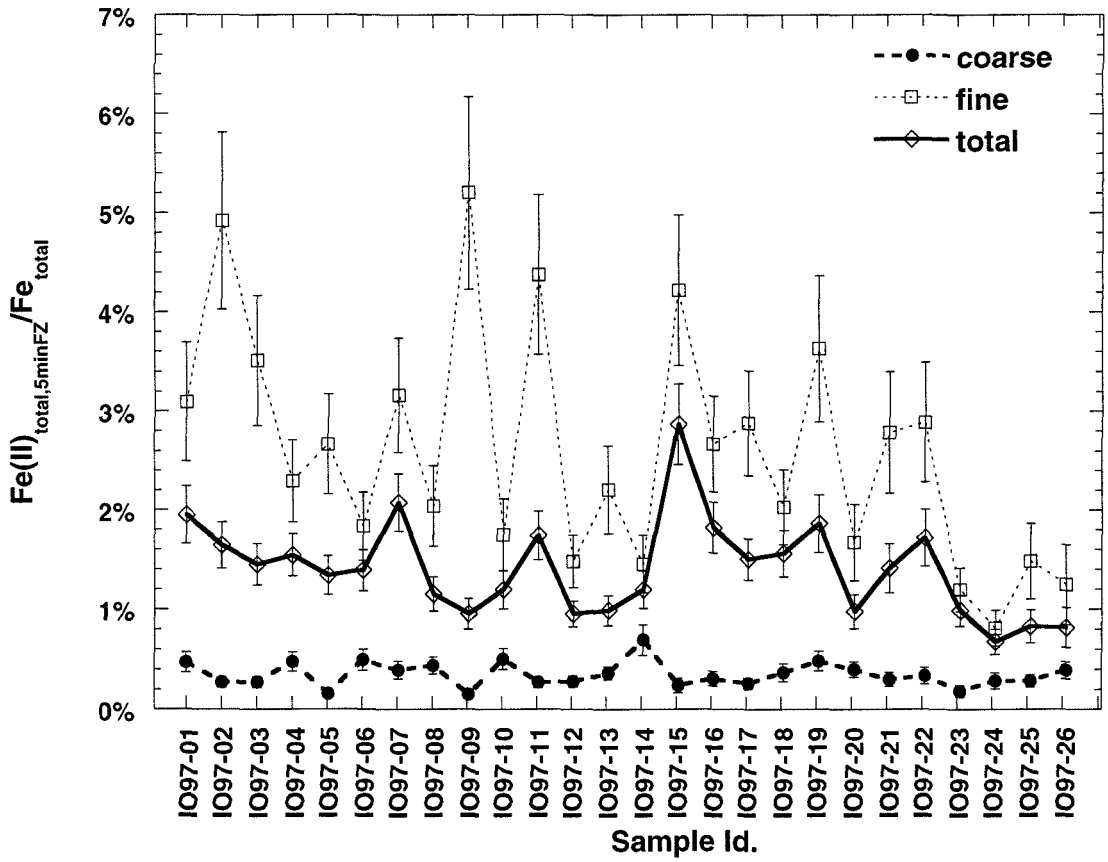
7%
6%
5%
4%
3%
2%
1%
0%
Fe(II)total,5minFZ/Fetotal
coarse
fine
total
IO97-01
IO97-02
IO97-03
IO97-04
IO97-05
IO97-06
IO97-07
IO97-08
IO97-09
IO97-10
IO97-11
IO97-12
IO97-13
IO97-14
IO97-15
IO97-16
IO97-17
IO97-18
IO97-19
IO97-20
IO97-21
IO97-22
IO97-23
IO97-24
IO97-25
IO97-26
Sample Id.

Figure 9

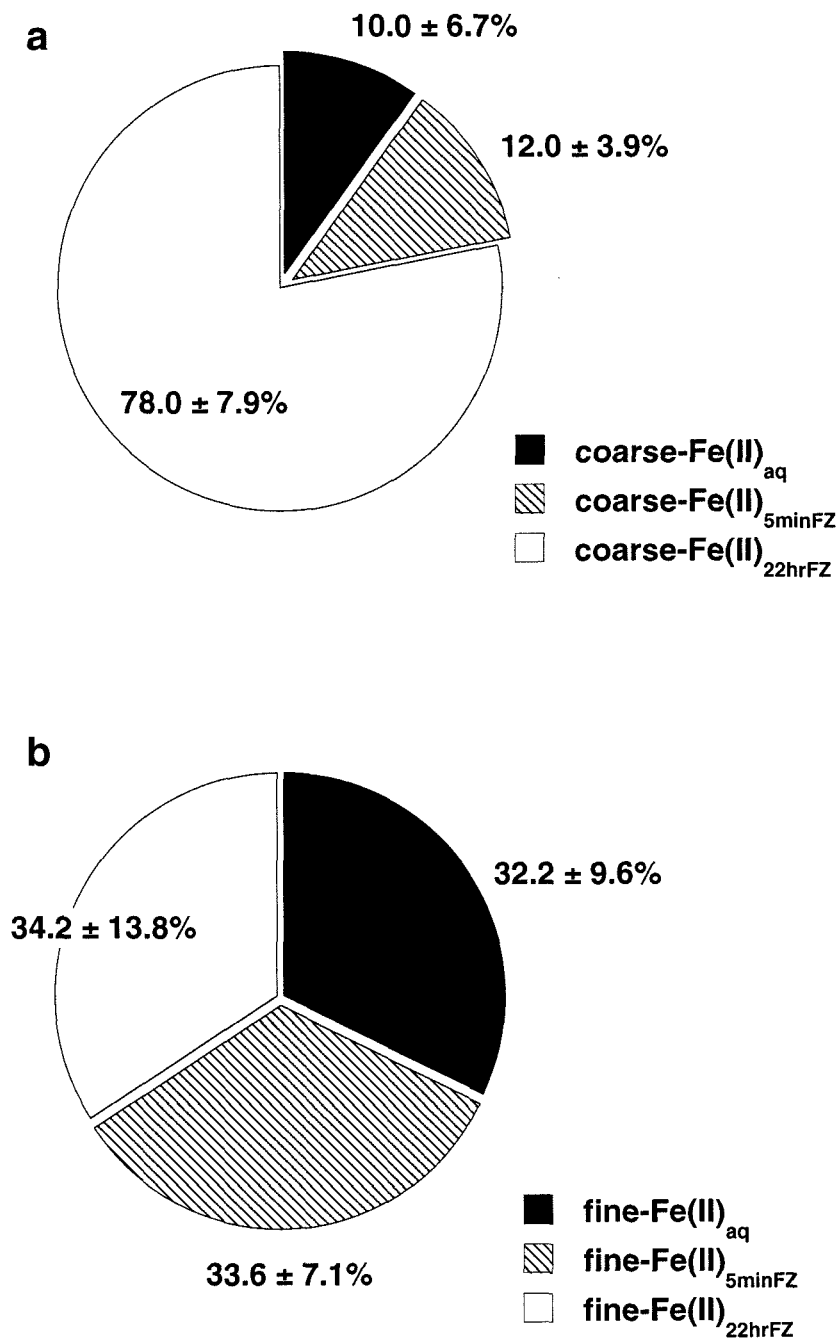
a
10.0 ± 6.7%
12.0 ± 3.9%
78.0 ± 7.9%
coarse-Fe(II)aq
coarse-Fe(II)5minFZ
coarse-Fe(II)22hrFZ
b
32.2 ± 9.6%
34.2 ± 13.8%
33.6 ± 7.1%
fine-Fe(II)aq
fine-Fe(II)5minFZ
fine-Fe(II)22hrFZ

Figure 10

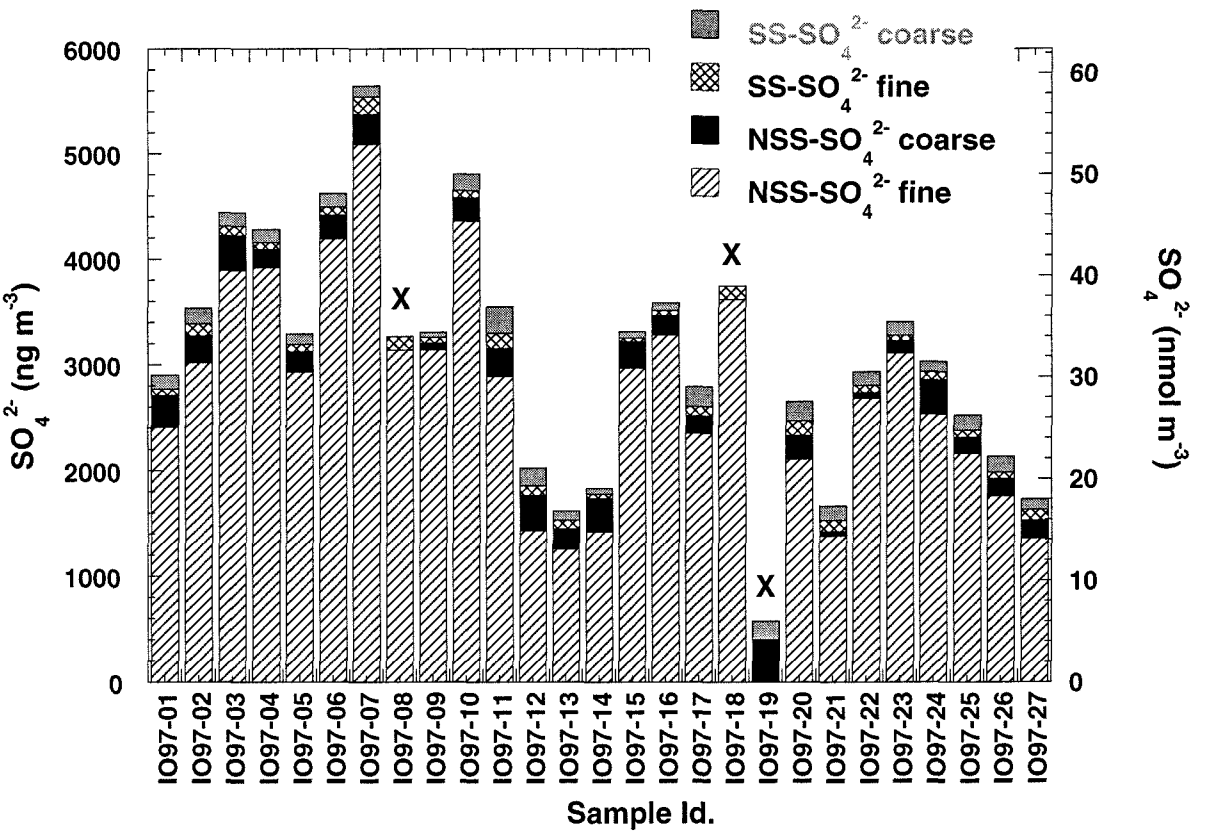
SS-SO4 2- coarse
SS-SO4 2- fine
NSS-SO4 2- coarse
NSS-SO4 2- fine
SO4 2- (ng m-3)
SO4 2- (nmol m-3)
6000
5000
4000
3000
2000
1000
0
60
50
40
30
20
10
0
X
X
X
IO97-01
IO97-02
IO97-03
IO97-04
IO97-05
IO97-06
IO97-07
IO97-08
IO97-09
IO97-10
IO97-11
IO97-12
IO97-13
IO97-14
IO97-15
IO97-16
IO97-17
IO97-18
IO97-19
IO97-20
IO97-21
IO97-22
IO97-23
IO97-24
IO97-25
IO97-26
IO97-27
Sample Id.

Figure 11

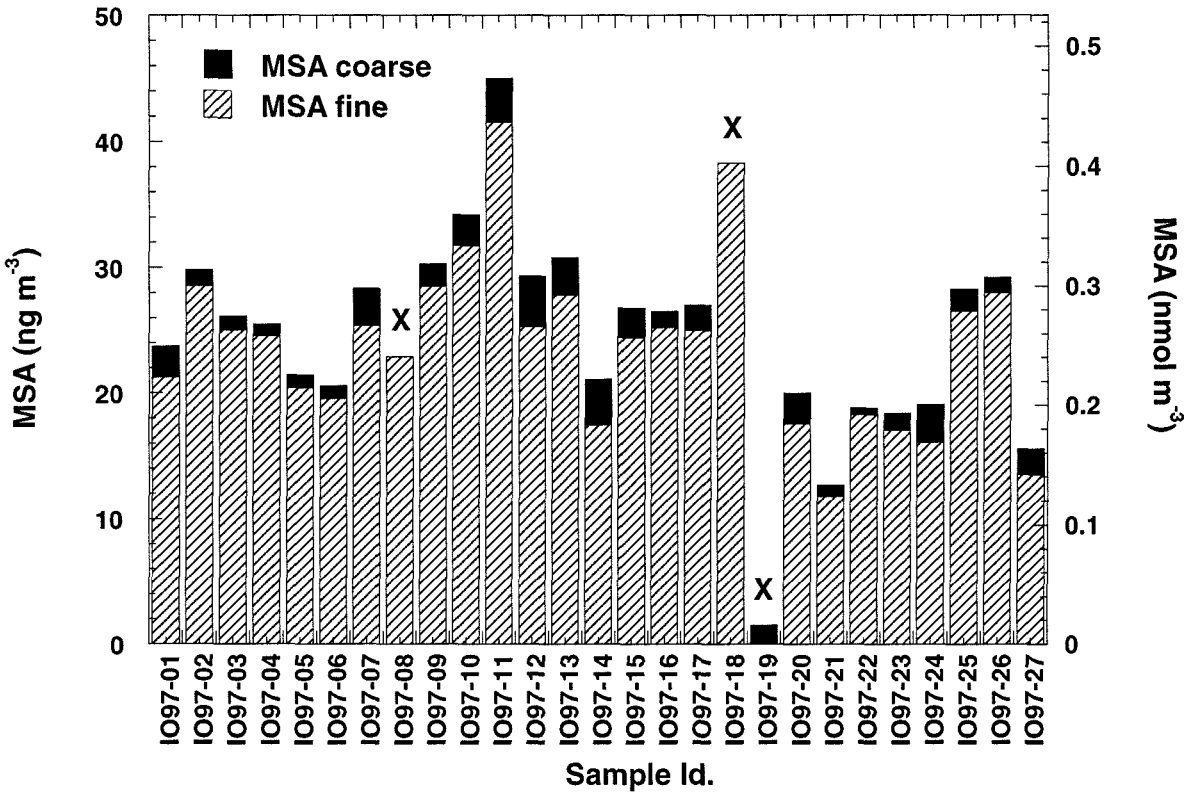
MSA coarse
MSA fine
MSA (ng m-3)
MSA (nmol m-3)
Sample Id.
X
X
X
50
40
30
20
10
0
0.5
0.4
0.3
0.2
0.1
0
IO97-01
IO97-02
IO97-03
IO97-04
IO97-05
IO97-06
IO97-07
IO97-08
IO97-09
IO97-10
IO97-11
IO97-12
IO97-13
IO97-14
IO97-15
IO97-16
IO97-17
IO97-18
IO97-19
IO97-20
IO97-21
IO97-22
IO97-23
IO97-24
IO97-25
IO97-26
IO97-27

Figure 12

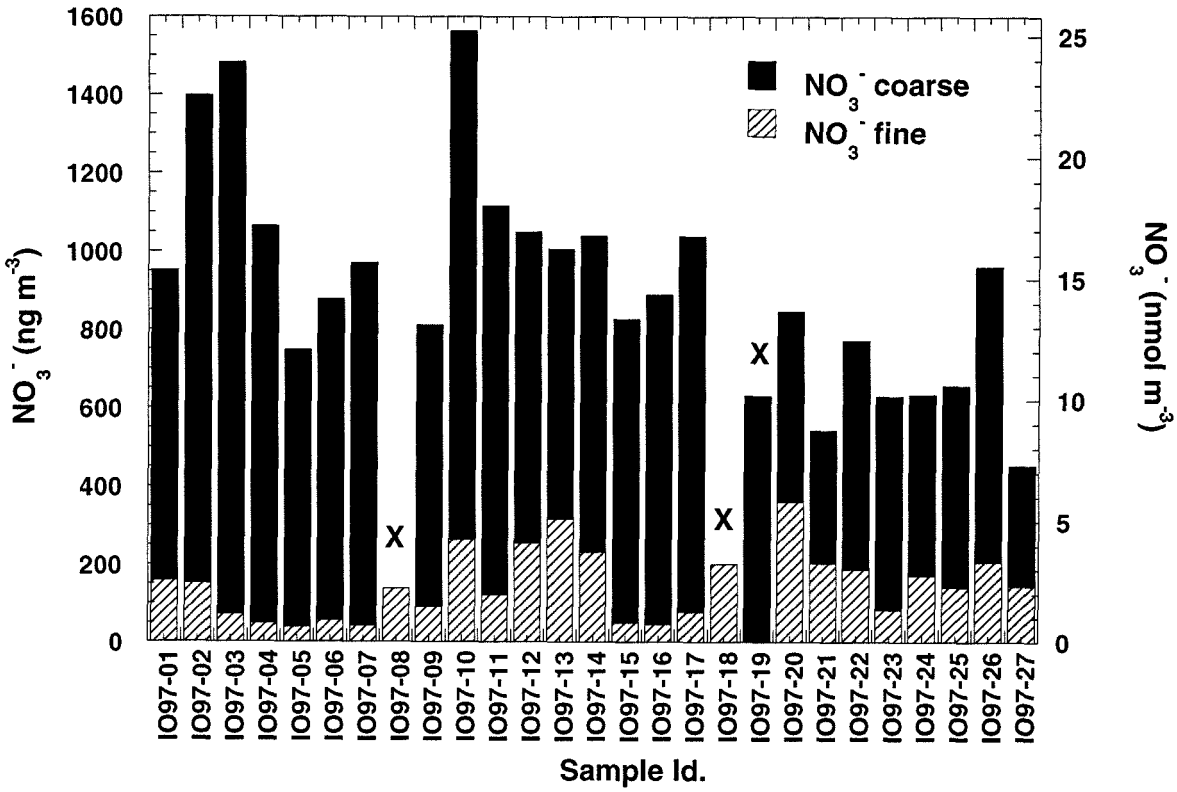
1600
1400
1200
1000
800
600
400
200
0
NO_3^- (ng m^{-3})
25
20
15
10
5
0
NO_3^- (nmol m^{-3})
NO_3^- coarse
NO_3^- fine
X
X
X
IO97-01
IO97-02
IO97-03
IO97-04
IO97-05
IO97-06
IO97-07
IO97-08
IO97-09
IO97-10
IO97-11
IO97-12
IO97-13
IO97-14
IO97-15
IO97-16
IO97-17
IO97-18
IO97-19
IO97-20
IO97-21
IO97-22
IO97-23
IO97-24
IO97-25
IO97-26
IO97-27
Sample Id.

Figure 13

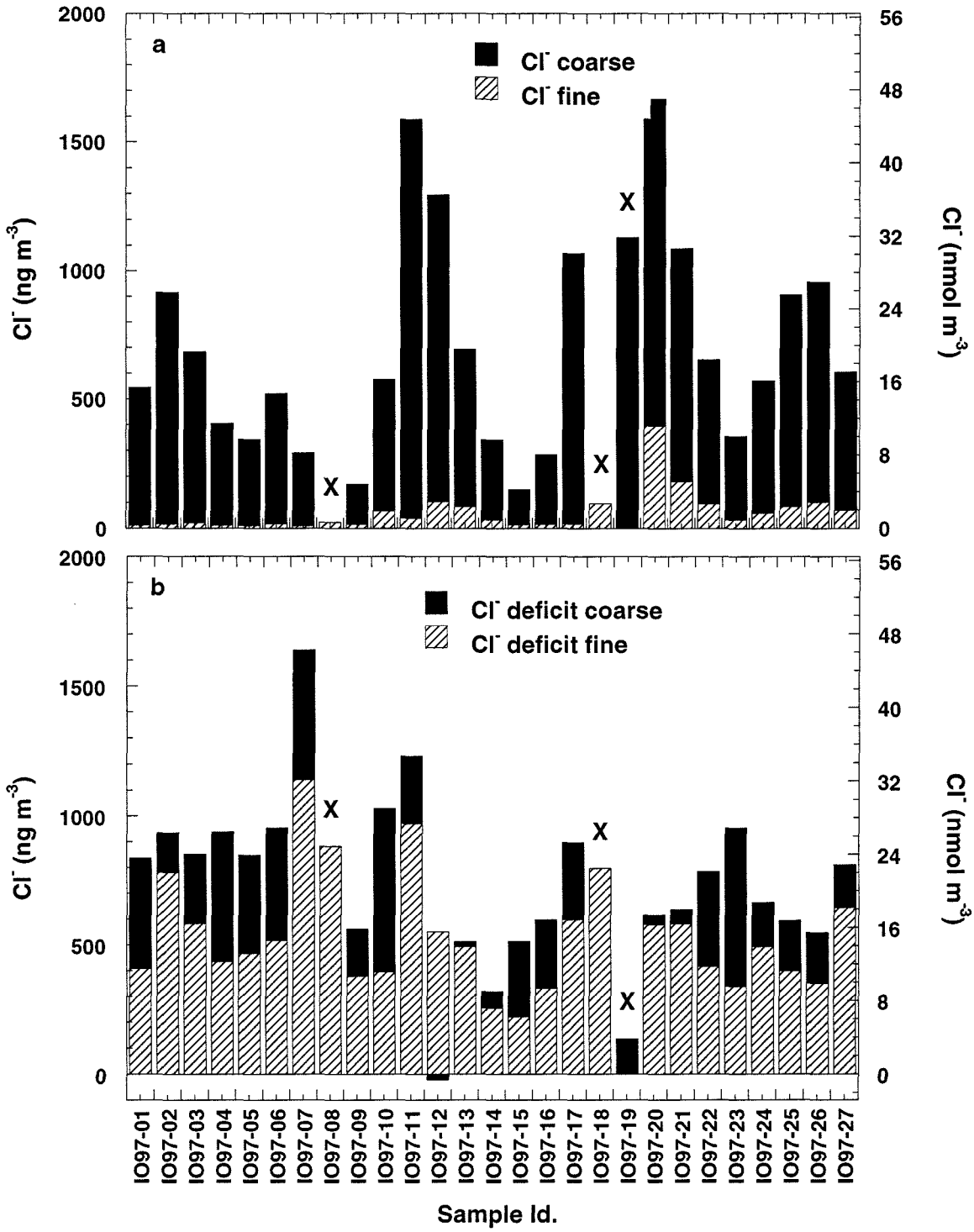
a
Cl⁻ coarse
Cl⁻ fine
Cl⁻ (ng m⁻³)
Cl⁻ (nmol m⁻³)
b
Cl⁻ deficit coarse
Cl⁻ deficit fine
Cl⁻ (ng m⁻³)
Cl⁻ (nmol m⁻³)
IO97-01
IO97-02
IO97-03
IO97-04
IO97-05
IO97-06
IO97-07
IO97-08
IO97-09
IO97-10
IO97-11
IO97-12
IO97-13
IO97-14
IO97-15
IO97-16
IO97-17
IO97-18
IO97-19
IO97-20
IO97-21
IO97-22
IO97-23
IO97-24
IO97-25
IO97-26
IO97-27
Sample Id.

Figure 14

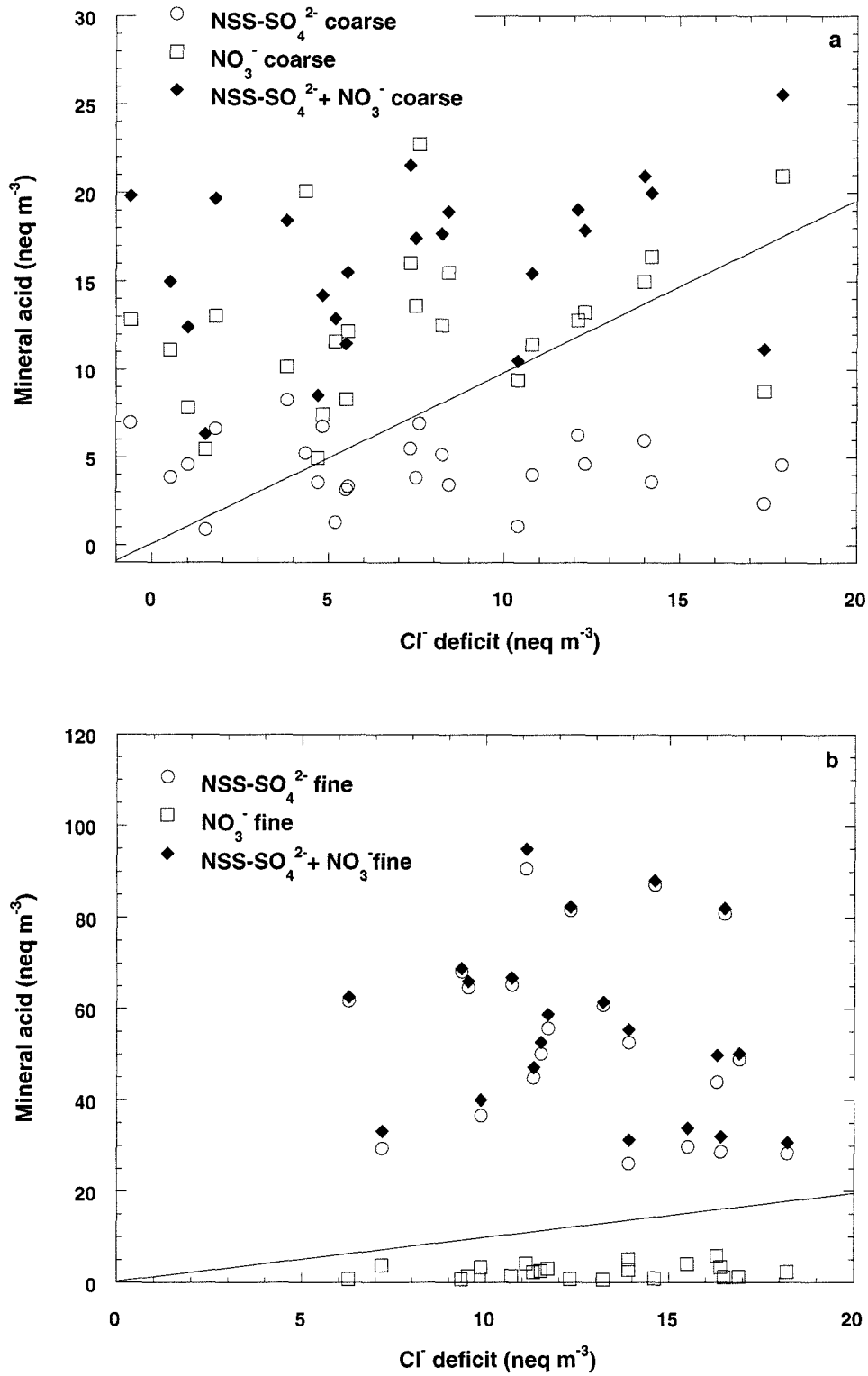
a
NSS-SO4 2- coarse
NO3 - coarse
NSS-SO4 2-+ NO3 - coarse
Mineral acid (neq m-3)
Cl- deficit (neq m-3)
0
5
10
15
20
25
30
b
NSS-SO4 2- fine
NO3 - fine
NSS-SO4 2-+ NO3 -fine
Mineral acid (neq m-3)
Cl- deficit (neq m-3)
0
20
40
60
80
100
120

Figure 15

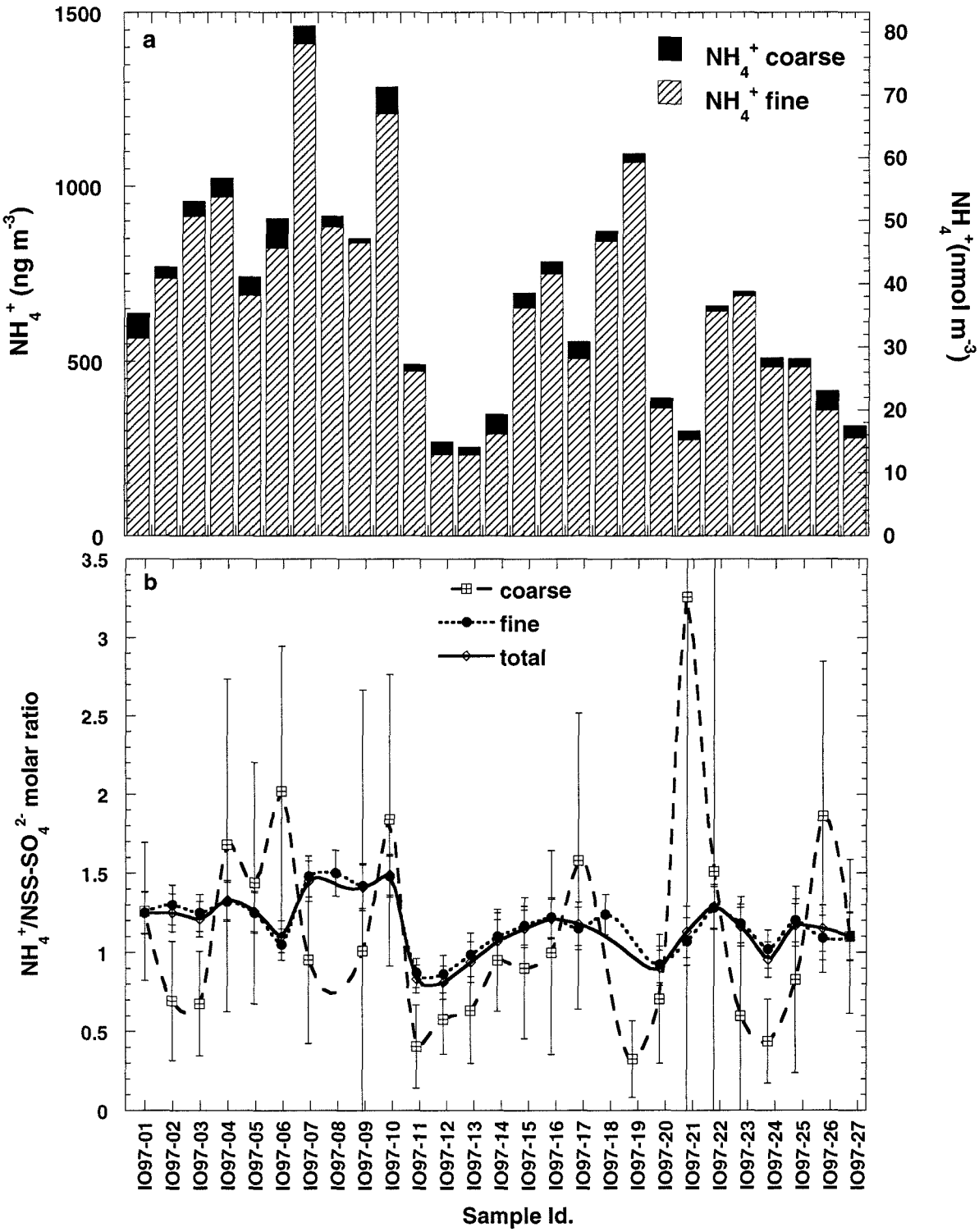
a
b
NH_4^+ coarse
NH_4^+ fine
coarse
fine
total
NH_4^+ (ng m^{-3})
NH_4^+ (nmol m^{-3})
NH_4^+/NSS-SO_4^{2-} molar ratio
Sample Id.
IO97-01
IO97-02
IO97-03
IO97-04
IO97-05
IO97-06
IO97-07
IO97-08
IO97-09
IO97-10
IO97-11
IO97-12
IO97-13
IO97-14
IO97-15
IO97-16
IO97-17
IO97-18
IO97-19
IO97-20
IO97-21
IO97-22
IO97-23
IO97-24
IO97-25
IO97-26
IO97-27

Figure 16

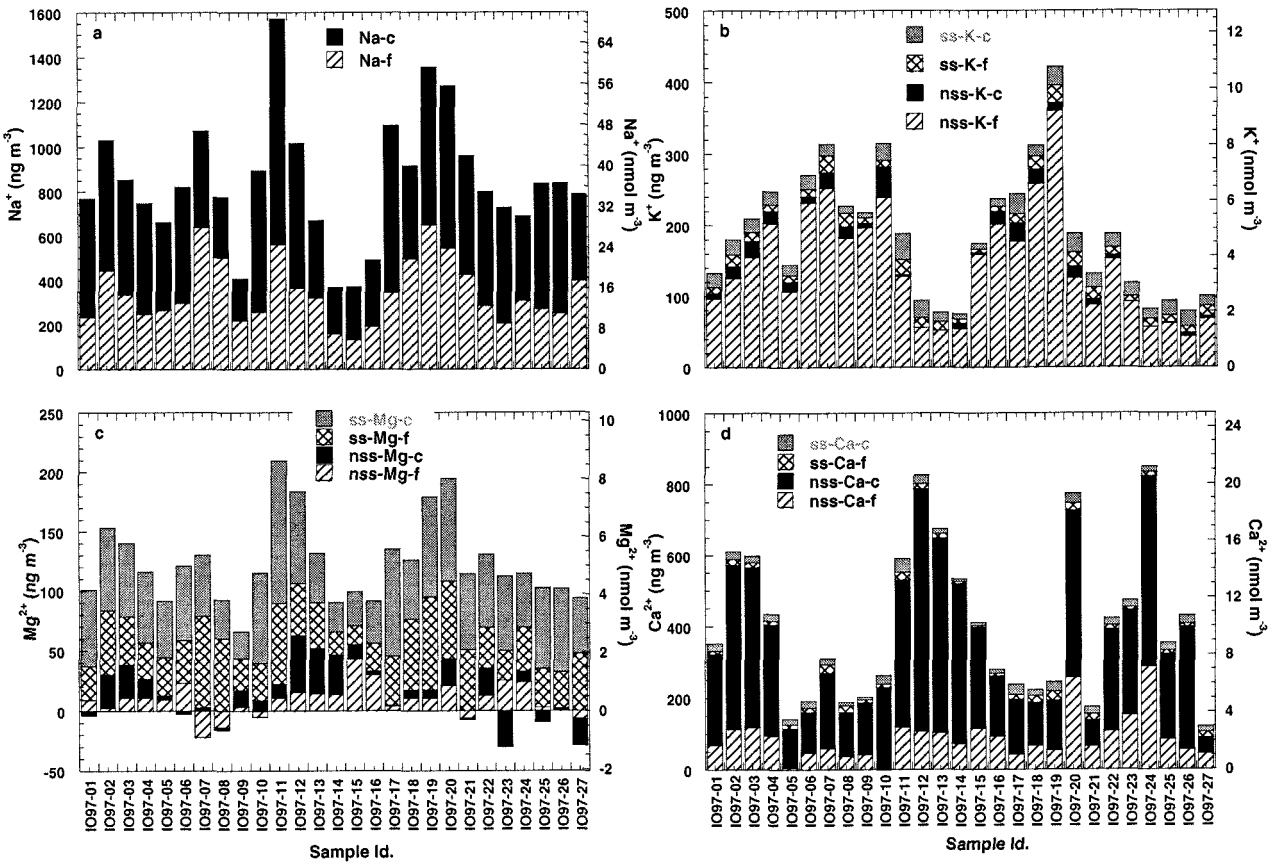
a
Na-c
Na-f
Na+ (ng m-3)
Na+ (nmol m-3)
b
ss-K-c
ss-K-f
nss-K-c
nss-K-f
K+ (ng m-3)
K+ (nmol m-3)
c
ss-Mg-c
ss-Mg-f
nss-Mg-c
nss-Mg-f
Mg2+ (ng m-3)
Mg2+ (nmol m-3)
d
ss-Ca-c
ss-Ca-f
nss-Ca-c
nss-Ca-f
Ca2+ (ng m-3)
Ca2+ (nmol m-3)
IO97-01
IO97-02
IO97-03
IO97-04
IO97-05
IO97-06
IO97-07
IO97-08
IO97-09
IO97-10
IO97-11
IO97-12
IO97-13
IO97-14
IO97-15
IO97-16
IO97-17
IO97-18
IO97-19
IO97-20
IO97-21
IO97-22
IO97-23
IO97-24
IO97-25
IO97-26
IO97-27
Sample Id.

6. Summary

The chemistry of marine aerosols has been investigated over the Arabian Sea and the tropical North Atlantic Ocean during a combined sampling period of ~ 120 days. Principal component and enrichment factor analyses proved to be useful statistical techniques to identify the sources of the particulate matter. The bulk of all the samples were found to be comprised of three major components that included crustal, sea-salt, and anthropogenic constituents. The relative contribution of each of these sources varied quite significantly with season and location.

Geochemical signatures of the major crustal component during the three months of sampling over the Arabian Sea revealed that the average crustal composition is a satisfactory representation of the mineral dust emanating from arid Saudi Arabian and Indian regions. In contrast, the mineral aerosol transported from the Northern Saharan desert to the Atlantic Ocean mostly resembled that of a typical shale. Based on these surrogate compositions and the measured Al concentrations, the average mineral dust concentrations over the Arabian Sea were estimated to be 5.9 ± 4.2, 0.7 ± 0.4, and 5.9 ± 3.1 $\mu g\ m^{-3}$, during the inter-, SW-, and NE-monsoons, respectively, and 19.3 ± 16.4 $\mu g\ m^{-3}$, over the Atlantic Ocean. An additional crustal component, which was characterized by an excess of water-soluble NSS-Ca^{2+}, was detected during the inter- and NE-monsoons over the Arabian Sea and over the Atlantic Ocean. This component appeared to be a mixture of $CaCO_3$ and $CaSO_4$ over the Arabian Sea, while over the Atlantic Ocean, $CaCO_3$ alone appeared to be responsible for the apparent excess of NSS-Ca^{2+}. These additional crustal sources averaged 2.4 and 0.8 $\mu g\ m^{-3}$ over the Arabian Sea, during the inter- and NE-monsoons, respectively, and 1.3 $\mu g\ m^{-3}$ over

the Atlantic Ocean, assuming in all cases that the excess NSS-Ca^{2+} was exclusively derived from $CaCO_3$.

Iron concentrations in both coarse and fine fractions closely followed the main crustal sources. Ferrous iron, which was released after 22 hours leaching in aqueous ferrozine, appeared to be strongly dependent on the total concentrations of this crustal derived Fe both in the coarse and fine fractions. However, the combined first two extracted fractions, $Fe(II)_{total,5minFZ}$ ($Fe(II)_{aq}$ plus $Fe(II)_{5minFZ}$), displayed a more complex behavior. Factors such as the presence of electron donors, transport history and aerosol acidity seemed to play important roles in determining the lability of the samples with respect to Fe(II). $Fe(II)_{total,5minFZ}$ concentrations were found to be below detection limit during the SW-monsoon, and amounted to 5.2 ± 4.4 and 9.8 ± 3.4 μg m^{-3} during the inter- and NE-monsoons over the Arabian Sea, respectively. These concentrations accounted for 0.3 and 1.3% of the total Fe detected during the respective seasons. Over the Atlantic Ocean, $Fe(II)_{total,5minFZ}$ concentrations were 3.1 ± 1.4 μg m^{-3} and represented 0.5% of the total Fe. For all data sets, most of the $Fe(II)_{total,5minFZ}$ (> 80%) was present in the fine fraction.

Sea-salt contributed 8.5 ± 4.6, 21.2 ± 9.5, and 2.8 ± 0.9 μg m^{-3} to the suspended particulate mass over the Arabian Sea, during the inter-, SW-, and NE-monsoons respectively, and 10.6 ± 5.5 μg m^{-3} over the Atlantic Ocean. The magnitude of the sea-salt concentrations was directly related to wind speed. Chloride deficits were observed in almost all samples. The Cl^- deficit over the Arabian Sea averaged 15.1, 3.5, and 53.1%, during the inter-, SW- and NE-monsoons, respectively. The deficit correlates with the amount of anthropogenic pollutants present in the aerosol. This result suggests that acid displacement reactions with mineral acids were the most likely pathways for volatilization of HCl from the

particulate phase. However, during the SW-monsoon, NSS-SO_4^{2-} and NO_3^- concentrations were too low to account for the measured Cl^- deficit. Due to the correlation between the anion charge deficit and the Cl^- deficit during that particular season, Cl may possibly have been released in the form of reactive Cl species generated by reactions with HOCl, HOBr, NO_2, N_2O_5, and O_3. Over the Atlantic Ocean the Cl^- deficit averaged 18.3%. While NO_3^- seemed to replace Cl^- in the coarse fraction, SO_4^{2-} appears to be responsible for the observed Cl^- deficit in the fine fraction.

Anthropogenic components were traced by the appearance of excess Pb and Zn concentrations, as well as high NO_3^-, NH_4^+ and NSS-SO_4^{2-} levels. The different sources of NSS-SO_4^{2-} were identified by using weighted multiple linear regression analyses. The anthropogenic SO_4^{2-} contributions extracted from these linear regression analyses for the samples collected over the Arabian Sea were 1.37, 0.20 and 2.44 $\mu g\ m^{-3}$, during the inter-, SW- and NE-monsoons, respectively. Over the Atlantic Ocean, the anthropogenic SO_4^{2-} amounted to 0.80 $\mu g\ m^{-3}$. These concentrations give an estimate of the relative contribution of the anthropogenic component, showing that the NE-monsoon is the most polluted and the SW-monsoon the least polluted season during which sampling took place.

The biogenically-derived SO_4^{2-}, traced by $CH_3SO_3^-$ (MSA) and extracted from the linear regression analyses, amounted to 0.44, 0.59, and 0.28 $\mu g\ m^{-3}$ over the Arabian Sea, during the inter-, SW-, and NE-monsoons, respectively. The corresponding concentration over the Atlantic Ocean was 0.23 $\mu g\ m^{-3}$. Thus, during the SW-monsoon over the Arabian Sea, when the anthropogenic SO_4^{2-} concentrations were small, the biogenic SO_4^{2-} input was the dominant contributor to total sulfate. This was the result of increased phytoplankton

activity observed in upwelling regions that are typically encountered during the SW-monsoon.

From the same linear regression analyses the biogenic SO_4^{2-}/MSA weight ratio is extracted. The ratio appears to follow an exponential temperature dependence consistent for all the Arabian Sea samples. The ratio varied from 6.8 at 24 °C to 17.7 at 28.9 °C. However, the Atlantic Ocean samples did not exhibit such a temperature dependence, possibly due to more frequent and variable temperature fluctuations.